Aggradation/incision history of a debris flow/hyperconcentrated flood dominated valley on the eastern margin of the Tibetan Plateau, China

By

Yajun Li

Submitted for the degree of Doctor of Philosophy at Royal Holloway, University of London

September 2018

Declaration

I, Yajun Li, confirm that the work presented in this thesis is my own. Where information has been derived from other sources, I confirm this has been indicated in the thesis.

Signed：_____

Date: _____

Abstract

The thesis aims to reconstruct the aggradation and incision history of a tributary valley of the Bailong River on the eastern margin of the Tibetan Plateau. To achieve this goal, geomorphological, sedimentological and chronological methods were employed. Four levels of alluvial terraces (i.e., T1, T2, T3 and T4 ranging from high-elevation to low-elevation terrace levels) were identified via field investigation. The terrace sedimentology was revealed through sedimentary logging of terrace outcrops. Channel fill sediments were investigated from two cores drilled on the channel. These sedimentological analyses indicate that the terraces and channel fill have been primarily deposited by debris flows and hyperconcentrated floods. The numerical ages of the sediments forming the alluvial terraces and channel fill were determined using the single-aliquot regenerative dose (SAR) protocol of optically stimulated luminescence (OSL) dating. By synthesizing the geomorphological, sedimentological and chronological results, the valley evolution history was classified into two aggradation periods (S1 and S3, representing the aggradation of T1 and T2, respectively), and two incision periods (S2 and S4, representing the incision of T1 and T2, respectively). The formation of T3 and T4 terraces is regarded as being due to two short aggradation events punctuating the S4 incision period. The timeframes for these stages were constrained using the OSL ages: S1 occurred before 90.0 ± 10.0 ka; S2 occurred between 90.0 ± 10.0 ka and 46.8±

5.1 ka; S3 occurred between 46.8 ± 5.1 ka and 7.1 ± 0.7 ka; and S4 occurred from 7.1 ± 0.7 ka to present. The short aggradation period which formed the T3 terraces occurred between 3.3 ± 0.3 ka and 0.6 ± 0.1 ka.

Comparison between the aggradation and incision history and regional climatic records suggests that aggradation occurred in cold and/or dry climates, whereas incision was a feature of warm and wet climates. The impact of tectonism on the valley evolution is related to the lateral displacement of a local thrust fault, which caused changes in the depositional loci of the T1 and T2 terraces. The incision during the S2 phase may be related to regional uplift because both climate and the small displacement of the local fault seem unlikely to cause the large incision(~260 m) observed. The base-level effect provided by the Bailong River valley is mainly represented by the lateral migration of the river channel which may have caused deposition and erosion of the T3 and T4 terraces at the valley mouth. The above proposed relationship between climate and valley evolution was applied to assess possible future changes in the present active channel by considering recent climatic records. The results suggest that the valley channel is expected to experience incision in the future.

Acknowledgment

At the end of the 4-year PhD study, I would like to express my sincere gratitude to those who have helped and supported me during this period.

Firstly, I would like to thank my supervisor, Dr. Simon Armitage. Simon agreed to be my supervisor in the second year of my PhD when Tom left for Uppsala University. Being an expert in OSL, he has provided the key help in guiding me through the laboratory works. Besides, he has been very patient in checking my poor logic and careless grammar mistakes in writing. He has read carefully through all my chapters and rewritten many sentences to make them become fluent. It would be impossible for me to finish the thesis without his supervision.

Secondly, I would like to thank my second supervisor, Dr. Thomas Stevens from Uppsala University. Tom has kindly accepted me as his PhD student to conduct the research on dating debris flow sediments. He took a field trip with me before I was officially accepted by Royal Holloway. In the field, he taught me the procedures in doing sedimentary logs and taking OSL samples. During the first year of my PhD study, he taught me from the very beginning the experimental procedures in OSL dating and the theories of OSL. He monitored my laboratory progress and kept everything on schedule. In the second year, before his moving to Uppsala University, he kindly transferred me to Simon and still kept an eye on

my PhD progress. In the final stage of my PhD study, he has kindly squeezed time from his already over-loaded schedule to read my chapters and provide timely insightful comments.

Thirdly, I would like to thank Professor Xingmin Meng from Lanzhou University. He has been my supervisor when I was doing a post-graduate study at Lanzhou University. The topic of this PhD study came from Xingmin's idea. During field works with him, he inspired me to conduct a study on this topic and encouraged me to pursue a PhD degree in the UK. Besides, he kindly supported my field work during my PhD study and provided all the data I required. More importantly, in the fourth year of the PhD study when my financial support from the Chinese Scholarship Council ended, he has kindly provided his house in Egham for me to stay. Without his support, I would not be able to finish the 4-year PhD study in the UK.

Fourthly, I would like to thank my parents and sisters for their support and understanding of the four-year long PhD study in abroad.

Last but not the least, I would like to thank Mr. Iñaki Valcarcel for his help in my laboratory work. Thanks for the accompanies of many Chinese friends from other departments of Royal Holloway: they are Wanpeng Li, Hongdan, Deng, Liang Liu, Bin Sheng, Jia He, Lei Zhong. I would like to thank the friends in Geography

Department: they are Jay, Jacob, Rhys, Ash, Tianshu Zhang, Xuanyu Chen, Zuyun Zang and Xuejuan Zhang. Thanks for Dr Varyl Thorndycraft, Professor Scott Alias, Professor Ian Candy, Professor Kati Wills. Many classmates from Lanzhou University have helped me during my field work and thesis writing: they are Jianbao Liu, Peng Guo, Guan Chen, Runqiang Zeng, Muqi Xiong, Yan Zhao, Feng Qing, Yi Zhang, Qingding Liu and Zhijie Cui. The Chinese Scholarship Council is acknowledged for supporting my first three year's living cost in the UK. Dr. Sven Lukas and Dr. Mattew Telfer are acknowledged for their invaluable comments and suggestions, which have greatly enhanced the quality of the thesis.

Table of Contents

List of Figures

List of Tables

Chapter 1 Introduction

1.1 Research context

On 7 August 2010, a devastating debris flow occurred in Zhouqu, a county-level town in Gansu Province, China, and killed 1765 people (Tang et al., 2011). The debris flow developed from a tributary valley of the Bailong River and swallowed the town center that was built on an alluvial fan previously formed by debris flow processes (Fig. 1.1). This event is a typical expression of the environmental conditions of the Bailong River. The Bailong River valley is characterized by high-relief steep hillslopes and deeply incised valleys. Under the influence of concentrated rainstorms during the summer, vast amounts of coarse sediments have been transported from hillslopes to form alluvial fans or terraces along the Bailong River. These aggradational landforms become major areas for people to reside. Consequently, the evolution of these landforms, i.e. alluvial fans or terraces, directly influence the safety and development of human populations settled along the Bailong River. Therefore, it is of vital importance to understand the nature of the geomorphic processes at work, as well as the evolution of these landforms.

Fig. 1.1. Zhouqu debris flow. The dashed red lines delineate the inundated area during the debris flow event which occurred on 7 August 2010.

1.2 Aims, objectives and overview

This PhD thesis aims to reconstruct the aggradation and incision history of the alluvial fans and valley fills in the Goulinping valley, a tributary valley of the Bailong River on the eastern margin of the Tibetan Plateau. Alluvial sediments in the valley are characterized by alluvial fans at the valley mouth, which were fed by the valley fills upstream. Both the fans and valley fills have been incised forming alluvial terraces along the main Goulinping channel. These alluvial terraces represent cyclic aggradation and incision in the valley, which reflects the interactions between climate, tectonism, the axial Bailong River and the specific

nature of the valley itself.

To achieve the aim of the study, the following objectives were devised: (1) to map, classify and characterize the alluvial terraces using field investigation and geomorphic analyses of a LiDAR (Light Detection And Range) image, (2) to characterize the sedimentology of the alluvial terraces using sedimentary logging of exposed terrace outcrops, (3) to obtain the depth of the channel fill by drilling boreholes on the present channel, and (4) to obtain the numerical ages for the alluvial terraces and channel fills using optically stimulated luminescence (OSL) dating. An overview of the thesis structure is provided below.

This thesis is divided into nine chapters. Chapter 1 introduces the research context and research aim. This is followed by reviews of alluvial fan and terrace research and associated studies on the broad eastern margin of the Tibetan Plateau. Chapter 2 describes the background settings of the Bailong River and the Goulinping (GLP) valley. This description includes the geographical location, geomorphology, geology and climate of the study area. Chapter 3 presents the methods employed in the thesis. Specifically, the methods used in geomorphic mapping and subsequent analyses, sedimentary logging, borehole drilling and OSL dating are described. Chapters 4, 5, 6 and 7 provides the detailed results of geomorphic mapping, sedimentary logging, borehole drilling and OSL dating, respectively. Chapter 8 is a chapter discussing the timing of the valley

aggradation and incision phases. The impacts of climate, tectonism and base-level on the valley evolution and implications for the future trend of valley evolution are also discussed. Chapter 9 summarizes the main conclusions of the study, and highlights some areas where future research should be focused.

1.3 A review of alluvial fan research

1.3.1 A general introduction to alluvial fans

Alluvial fans are important landforms in mountainous environments and record valuable information of past environmental conditions (Bull, 1977; Blair and McPherson, 1994; Harvey, 1996; Harvey et al., 2005; Owen et al., 2014; Harvey et al., 2016; Mather et al., 2017). Alluvial fans refer to the sedimentary body of a cone shape that radiates from a point where a channel starts to expand from an upland (Bull, 1977). The typical morphological features of alluvial fans include drainage basin, feeder channel, apex, incised channel, distributary channels, intersection point, active depositional lobe, and headward-eroding gullies (Fig. 1.2), though not all these features are necessarily present in each individual alluvial fan (Blair and McPherson, 1994). Alluvial fans form where there is (1) a sudden reduction in slope which enables the rapid deposition of coarse sediments, and (2) adequate accommodation space in which sediments can be deposited (Blair and MacPherson, 1994). Consequently, alluvial fans are usually present in tectonically-extensive mountain fronts (Beaty, 1963; Bull, 1977; Spelz et al., 2008; Harvey, 2011; Owen et al., 2014), intramontane basins (Suresh et

al.,, 2002; Owen et al., 2006; Suresh et al., 2007; Singh and Tandon, 2010; Giano, 2011) and tributary-junctions (Harvey, 1997; Al-Farraj and Harvey, 2000, 2005; Mather et al., 2017; Takahashi and Sugai, 2017).

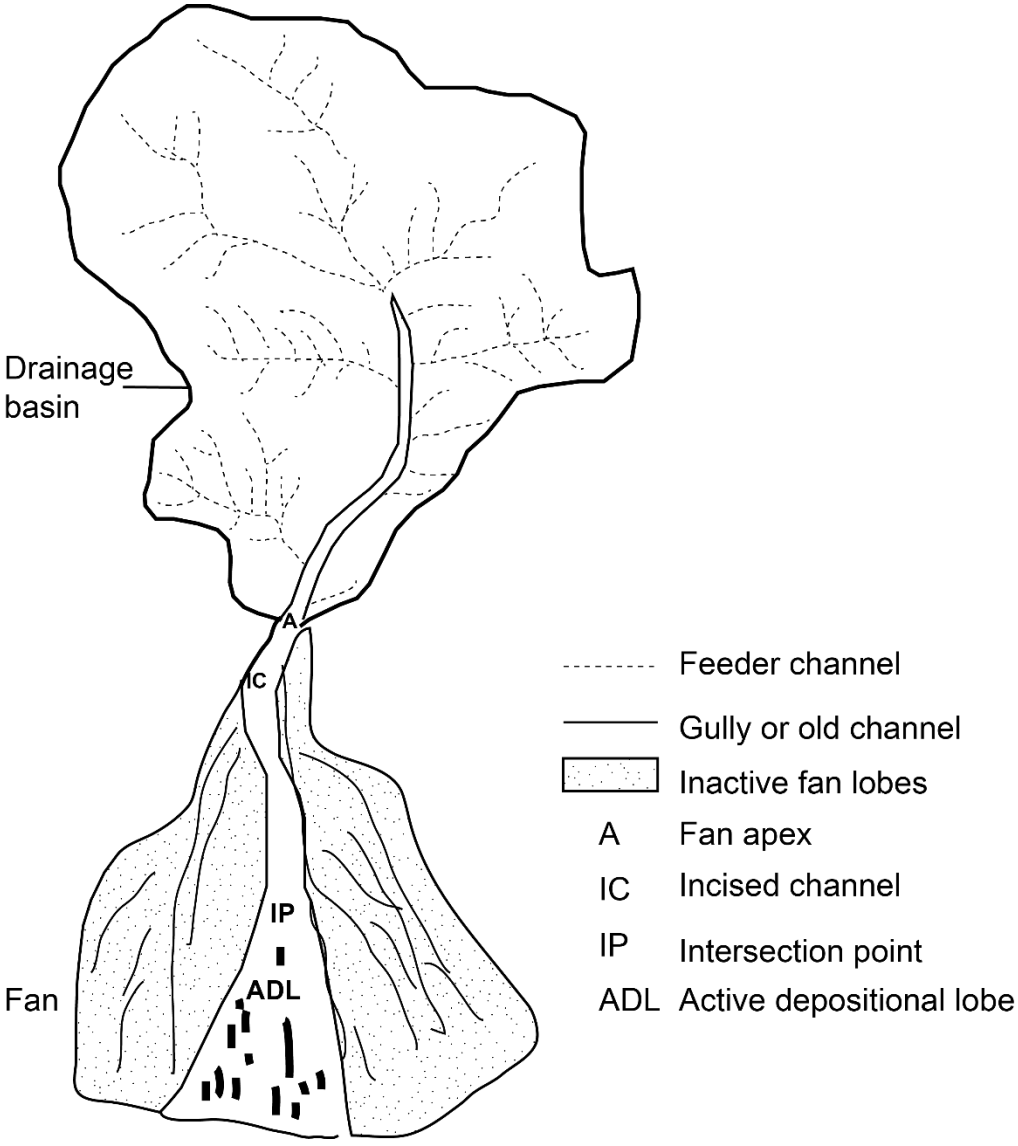

Fig. 1.2. A planview sketch showing the different geomorphic units of an alluvial fan. After Blair and McPherson (1994), their Fig. 14.3.

1.3.2 Evolution of alluvial fans

The evolution of alluvial fans was divided into four phases by Blair and Mcpherson

(1994): (1) talus cone formation (precursor fan stage), (2) development of fan foundation (incipient fans), (3) development of common composite fan morphology, and (4) fan progradation. These four phases were classified based on the primary processes which occur and the landforms which are present in each stage. The precursor stage is characterized by rock falls, the incipient fan stages by rock avalanches, gravity slides and clast-rich debris flows, the composite fan phase by debris flows and some secondary processes, e.g., rill erosion and gulling, and the progradation stage by debris flows or floods. The development of alluvial fan morphology is accompanied by a progressive decrease of fan slopes and an increase of fan lengths and areas. This model of alluvial fan development only depicts the period of fan formation, and the fan dissection phase is not considered. Harvey (2012) summarized several types of fan status (Fig. 1.3), providing a comprehensive classification of fan evolution stages. Fans dominated by deposition, either by debris flows, sheet floods or a combination of both, equate to the stage of common composite fans, while fans exhibiting combinations of erosion and deposition equate to the progradation stage. Alluvial fan dissection or incision, here specifically regarded as through-fan trenching, is achieved through the combination of fan-head trenching, mid-fan trenching and distal incision (Harvey, 2012). The fan-head trenching is equivalent to the progradation stage, representing fan-head trenching and distal aggradation. Mid-fan trenching is associated with the sudden increase of fan slopes immediately downstream of the intersection point. This usually occurs

when debris flows or floods emerge from the relatively low-gradient fan channel onto the steeper fan-surface gradient at the intersection point. If the flow is still partially confined, the unit stream power will surpass the critical power, causing intersection-point incision (Harvey, 1996). Distal incision is caused by the erosion of axial streams, leading to steepened distal fan-channel and fan headward incision (Harvey, 2012). Both lateral migration (Larson et al., 2015) and vertical incision (Harvey, 2002b) of the axial streams have been discovered to cause distal fan incision. All these types of fan deposition/erosion were concluded based on field evidence, and hence, this classification is an important reference for recognizing the fan evolution stages in the field.

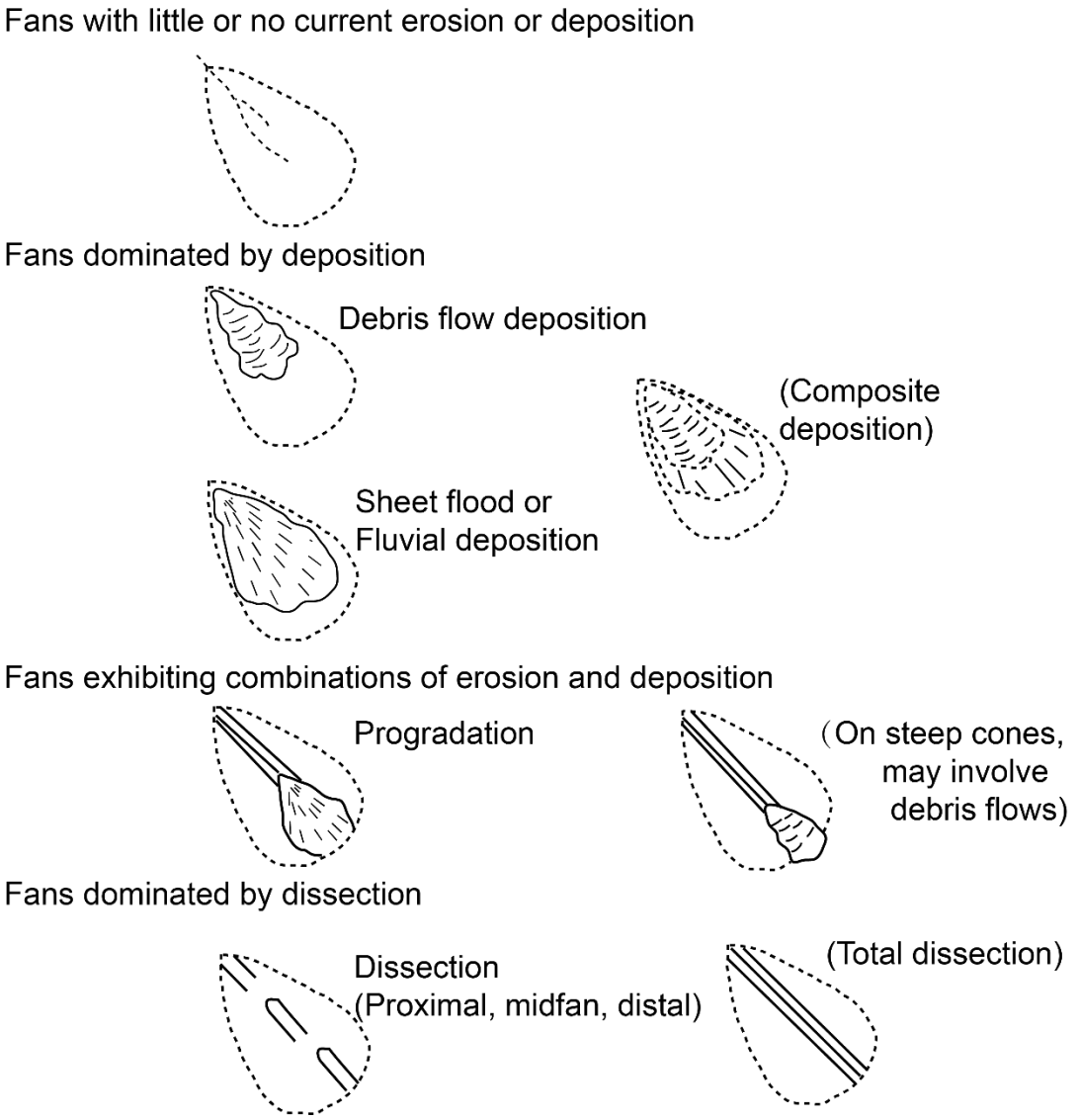

Fig. 1.3. Fan deposition or erosion style. After Harvey (2012), his Fig. 6.

Fans which only exhibit stacked deposition style are usually of relatively young ages indicating an initial period of fan development (e.g., Al-Farraj and Harvey, 2005). In contrast, most of the fans described in the literature are in a progradation stage, forming telescopic fans (e.g., Eckis, 1928; Bull, 1977; Harvey, 1996; Blair, 1999). Fans which show through-fan dissection were also identified (e.g., Harvey, 1978, 1996; Ritter et al., 1995; Al-Farraj and Harvey, 2005; Mather et al., 2017). In the case of multiple times of through-fan dissection, fans usually develop various surface levels representing cyclic fan aggradation and incision.

More recently, De Haas et al. (2018) examined the processes of fan evolution from the perspective of debris flow avulsion. Specifically, two mechanisms for channel avulsion are identified: (1) an abrupt change in channel position driven by the occurrence of channel plugs and back filling, and (2) a gradual shift in the predominant transport pathway over the course of multiple flows, allowing fan-scale compensation in response to surface gradients. Based on these two mechanisms, the authors (De Haas et al., 2018) proposed three scenarios regarding debris flow avulsion (Fig. 1.4), and these three scenarios depict detailed fan forming processes resulting from debris flow avulsion. The alluvial fans in the GLP valley have a long and wide channel upstream. It is likely that the fan formation in GLP has been associated with gradual lateral shifts of deposition locus at the valley mouth (Fig. 1.4c).

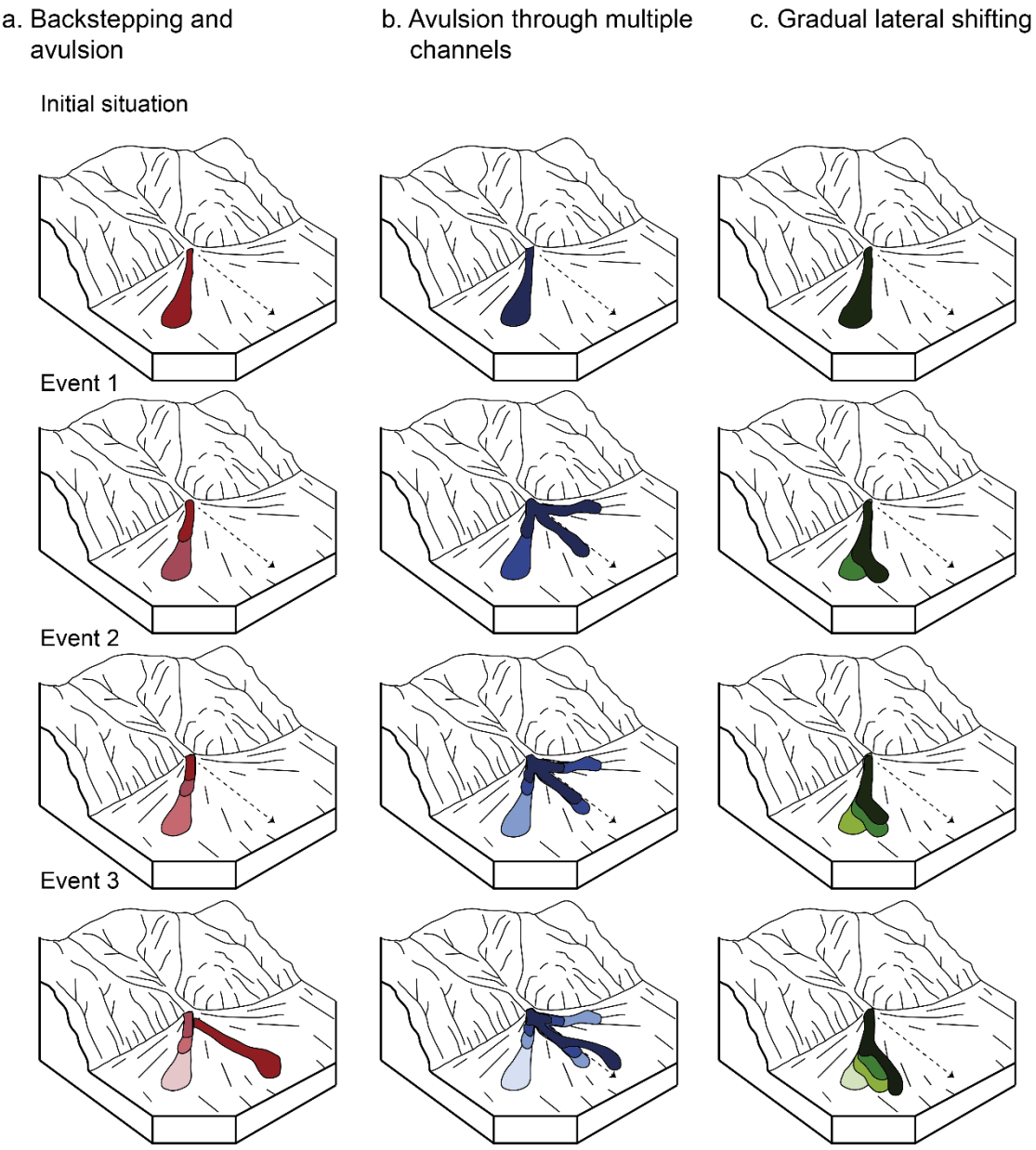

Fig. 1.4. Conceptual diagram illustrating three different avulsion patterns. Panel a illustrates a typical backstepping and avulsion sequence, wherein channel plug deposition and backstepping occurs during small to moderate-sized flows followed by avulsion during a large flow. Panel b illustrates how a large flow can overtop the main channel to occupy and open (or close off) multiple channels. The most topographically favorable channel is enlarged in subsequent flows, while the other channels are closed off by plug deposition and backstepping. Panel c illustrates how flows can shift laterally toward a topographic depression on the fan during a sequence of similar-sized flows. After De Haas et al (2018), their Fig. 17.

1.3.3 Factors controlling aggradation and incision

The switch between aggradation and incision of alluvial fans occurs when the geomorphic thresholds of the fan systems are exceeded (Schumm, 1979). Specifically, Bull (1979) used the critical power threshold, i.e. the power needed to transport sediment load, to explain the transition between fluvial aggradation and incision. He suggested that when this threshold is exceeded, an incision will be triggered; when it is approximated, net lateral erosion will be caused during high discharge conditions; when the threshold is not approached, aggradation will occur. Harvey (2012) suggested that the critical power threshold is also applicable to understanding alluvial fans which are dominated by debris flows or sheetfloods. Both intrinsic and extrinsic mechanisms may cause the critical power threshold to be exceeded (e.g., Schumm et al., 1987; Harvey, 1996; Nicholas and Quine, 2007; Spelz et al., 2008).

The intrinsic mechanism considers the internal process-form feedbacks, i.e. the interaction between fan topography, flow patterns, channel migration and avulsion etc., in a constant environment (Nicholas and Quine, 2007). Evidence for the operation of these intrinsic mechanisms generally comes from experiment-based physical modelling (e.g., Schumm et al., 1987; Whipple et al., 1998; Nicholas et al., 2009; Clarke et al., 2010) and numerical modeling (e.g., Coulthard et al., 2002; Coulthard et al., 2005; Nicholas and Quine, 2007). Both methods have demonstrated the importance of autogenic feedbacks in influencing fan

development. These internal feedbacks between fan parameters (e.g., fan slope, flow width, aggradation rate etc.) are important in characterizing the geomorphic thresholds of fan systems (Clarke et al., 2010), which is key to understanding the response of alluvial fans to external factors.

The extrinsic mechanisms are related to the change of environmental conditions which lead to geomorphic thresholds being exceeded. Three key factors, climatic change, tectonism and base-level change, have been extensively studied (e.g., Hooke, 1972; Harvey, 1984, 2002a; Wells et al., 1987; Ritter et al., 1995; Owen et al., 1997; Viseras et al., 2003; Singh et al., 2016).

Climate is an important extrinsic factor in controlling the critical power threshold because it influences flood discharge and sediment supply by determining precipitation amounts and patterns as well as temperature (Bull, 1979; Blair and McPherson, 1994). Mean annual precipitation affects weathering rates and vegetation, which controls the production of clastic sediment. More importantly, the change of the magnitude and frequency of individual precipitation events can be a critical control on fan dynamics (Dorn, 2009). Temperature is associated with bedrock weathering rate, therefore determining the amount and type of sediment supply (Blair and McPherson, 1994). In mountainous environments, the orographic conditions cause a decrease of temperatures at higher elevations, leading to a decrease of chemical/biological weathering rate, and an increase in

physical weathering of bedrock via freeze shattering processes (Matsuoka, 2001; Hall, 2004; Tan et al., 2011).

Past Quaternary climate is characterized by glacial and interglacial periods during which large changes in climate have occurred (Tzedakis, 1994; Tudhope et al., 2001; Yang and Ding, 2008). The expression of these changes in different climatic zones varies. For example, the American Southwest is characterized by cold-wet glacial climate and warm-dry interglacial climate (Roy et al., 2010), while in the regions of the Mediterranean basin and the Tibetan Plateau the glacial and interglacial periods were characterized by dry-cold and wet-warm, respectively (Pope et al., 2016). These regional variations of climate, together with some more local factors, such as the influence of glacial activities, base-level change and valley settings, have led to the existence of distinct climate-alluvial fan response models. Generally, three climate-alluvial fan response models have been widely recognized:

(1) the American Southwest arid model, which suggests that fan aggradation occurs during the transition from the wet and cold glacial periods to the warm and dry interglacial periods (Bull, 1991). This model considers that reduced annual rainfall and increased temperature in the transition towards an interglacial climate decreased soil moisture and vegetation density, leading to an increase in erodibility and therefore of sediment supply. Subsequently, these sediments were transported by infrequent rainfall storms, leading to fan aggradation. Much

research in the American southwest has supported this model (e.g., McDonald et al., 2003; Spelz et al., 2008; Owen et al., 2014;). However, the timing of these alluvial fans generally falls to the transition period from Late Pleistocene to Holocene. Few studies have produced ages of earlier glacial/interglacial transitions, e.g., MIS 6/5. Instead, some old ages of alluvial fans generally occupy a lengthy period covering both glacial and interglacial periods (e.g., Sowers et al., 1989; Benn et al., 2006; Frankel et al., 2007a; Owen et al., 2014). This condition is considered to result from the larger uncertainties inherent in older ages (Owen et al., 2014). Consequently, it is difficult to identify whether the arid model is applicable to the whole Quaternary period in these areas.

(2) the American Southwest humid model, which suggests that alluvial fan aggradation occurred during the lengthy wet and cold glacial period, with fan incision occurring during the warm and dry interglacial periods (Dorn et al., 1987; Harvey et al., 1999b). This model considers the competence of stream floods. During the humid glacial periods, an extensive vegetation cover results in fine particles to be generated on the hill-slopes and be transported to streams. These hillslope-hydrological conditions were considered to reduce the intensity and competence of stream floods, leading to fan aggradation (Dorn et al., 1987). In contrast, during the arid interglacial periods, progressively more regolith cover was stripped from the hillslopes, leading to more erosive stream flows with greater stream competence and fan erosion. This model has been supported by fewer studies compared to the American Southwest arid model, though some

relative old ages dating back to LGM or MIS 4 have been reported (Matmon et al., 2005; Le et al., 2007; Armstrong et al., 2010). Again, these ages cannot be used to support this model unequivocally due to their large uncertainties.

(3) the southeast Spain model, in which fan aggradation occurred during wet-cold glacial periods and incision in warm-wet interglacial periods (Harvey et al., 1999a). In this model aggradation during glacial periods is generally associated with the higher rates of sediment supply resulting from the increased physical weathering rate, reduced vegetation cover and weak soil development. These sediments are generally released by infrequent rain storms. This model generally fits to the broad Mediterranean basin (Macklin et al., 2002; Candy et al., 2004; Pope and Wilkinson, 2005; Pope et al., 2008) and also applies to the alluvial fans in the east and south of Asia (Harvey, 1997; Kumar Singh et al., 2001; Suresh et al., 2007).

Apart from these three broadly recognized climate-alluvial fan response models, there are many other studies which find distinct alluvial fan responses to climatic changes in nearby or far-off areas (e.g., Juyal et al., 2010; Kar et al., 2014). Generally, the spatial variation of alluvial fan responses to climatic change can result from the difference in geomorphic thresholds and the climate itself. The differences in geomorphic thresholds may be determined by vegetation cover (Harvey et al., 1999b), watershed area, relief and lithology etc. The climate condition may be different even in nearby areas (Harvey et al., 1999b; Liang et

al., 2010; Miller et al., 2010). After all, the existence of various climate-alluvial fan response models does not devalue the climatic control on alluvial fan dynamics because definite relationships between fan dynamics and climate conditions generally exist in the specific regions. However, some other studies which identified alluvial fan aggradation under different climatic conditions within the same valleys (e.g., Candy et al., 2004; Pope et al., 2016) may suggest that it is the geologic and geomorphic settings that determine fan aggradation. In these conditions, the climate's role in influencing fan aggradation may lie in a subordinate position.

Tectonism poses a fundamental control on alluvial fan development because it determines the geomorphic conditions for fan formation, i.e. a sudden drop in slope and the relatively flat accommodation space (Blair and McPherson, 1994). Consequently, the presence of alluvial fans across the world is generally related to specific tectonic settings such as the extensional mountain front (e.g., Beaty, 1963; Bull, 1977; Spelz et al., 2008; Harvey, 2011; Owen et al., 2014) or the intramontane basins (e.g., Suresh et al., 2002; Owen et al., 2006; Suresh et al., 2007; Singh and Tandon, 2010; Giano, 2011). The detailed characteristics of tectonism include rates and occurrence of uplift, down-thrown, and lateral displacement (Blair and Mcpherson, 1994). These types of tectonism have been regarded as mainly influencing the overall form of alluvial fans (e.g., Hooke, 1972; Silva et al., 1992; Ritter et al., 1995; Viseras et al., 2003; Singh and Tandon, 2010).

For example, the tilting of the headwater mountain ranges in the Death Valley led to the segmentation of alluvial fans (Hooke, 1972). The varying tectonic subsidence rates in the Granada and Bajo Segura basins of Southeast Spain also appear to have resulted in distinct fan morphologies (Viseras et al., 2003). However, generally the change between aggradation and incision of alluvial fans may not be directly controlled by tectonism because these changes occurred over timescales (10^2 - 10^3 yrs) much shorter than those of tectonism (Ritter et al., 1995; Burbank and Anderson, 2011). Nonetheless, in some occasions, the indirect effect of tectonism may pose some controls on the dynamics of fan erosion and deposition. One example is presented by Harvey et al. (2016) in the southeast of Spain. In the Neogene sedimentary basins within the Betic Cordillera, regional uplift since the Pliocene Epoch caused a relative base-level fall in the basin outlets, and this base-level fall initiated drainage incision from the basin outlet towards the basin headwaters. Consequently, alluvial fans in different parts of the basin experienced variable evolution stages (Wells and Harvey, 1987; Harvey et al., 1999a). This variability relates to the rate of headward progression of the wave of dissection through the basin (Geach et al., 2015; Harvey et al., 2016; Mather et al., 2017).

Base-level change has a major influence on fan dynamics (Harvey, 2002a). The change of base-level itself can be caused by tectonic or climatic associated factors. The uplift-induced base-level fall in the sedimentary basins within the

Betic Cordillera, southeast Spain, is an example of tectonism-induced base-level fall (Mather et al., 2017). In contrast, when alluvial fans toe out onto lakes, seas or rivers, the base-level change is generally induced by climatic changes. Conventionally, a fall in base-level would be expected to cause incision of the fan toe, and this incision may be propagated upstream through the fan. However, the reverse may occur, with fan progradation taking place in response to a base-level fall, and dissection occurring in response to a base-level rise (Harvey, 2002a). Harvey (2002a) summarized several ways of alluvial fan response to different types of base-level dynamics (Fig. 1.5).

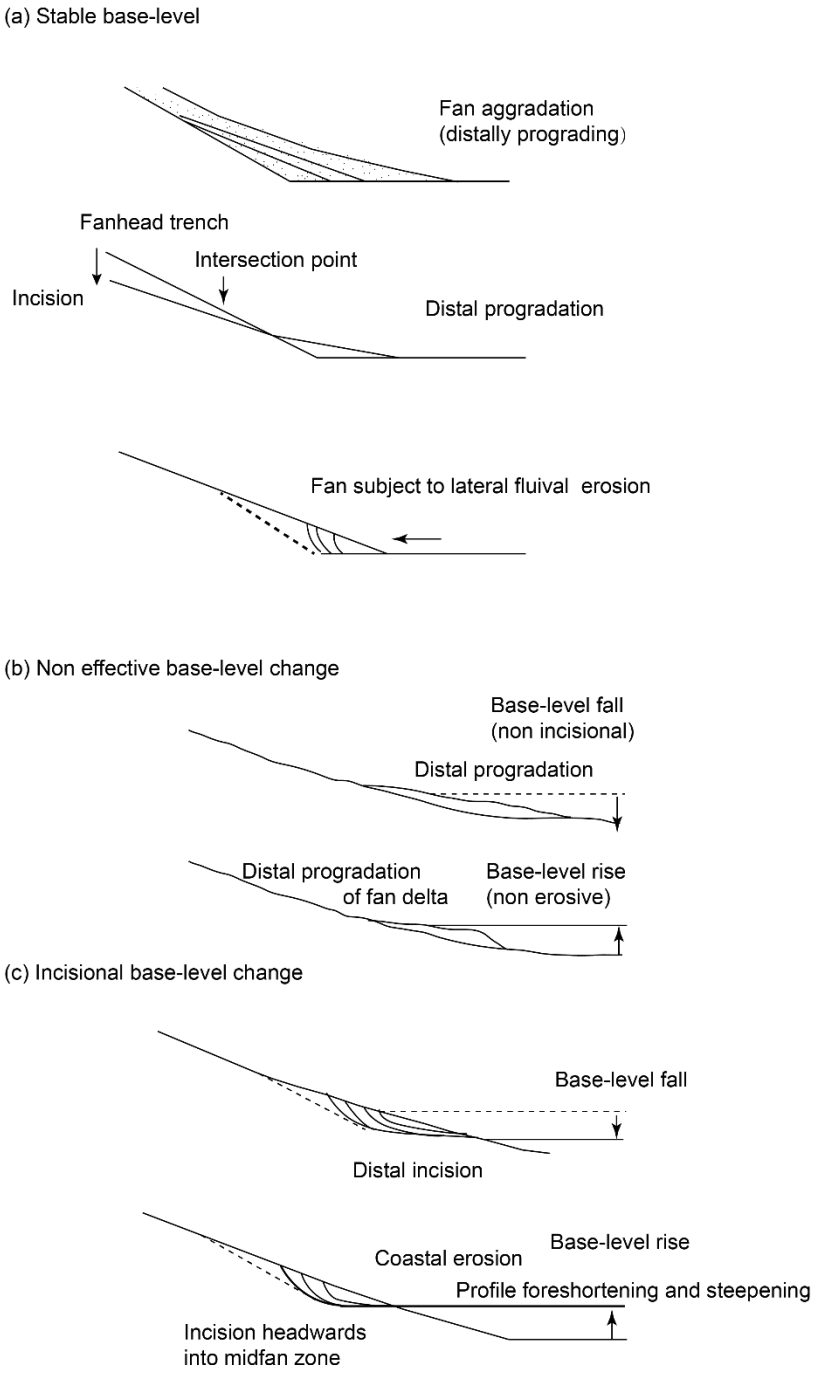

Fig. 1.5. Postulated schematic profile relationships on alluvial fans under a range of base-level conditions. After Harvey (2002a), his Fig. 2

Alluvial fans may aggradate or experience distal progradation under a stable base level condition (Fig. 1.5a). The Cabo de Gata west-coast fans in the southeast Spain and the Cold Springs fans in Nevada represent two examples of fan

development under a stable base-level (Harvey et al., 1999a; Harvey, 2002a) . In these cases, older fans are generally small and are mainly distributed close to fan apices, while younger fans are large and are generally in the fan distal areas. In some conditions, fan incision may be caused under stable base-levels by lateral fluvial erosion (Fig. 1.5a), which foreshortens the alluvial fans and causes an apparent relative base-level fall. Alluvial fans in the Big Lost River and the Rio Grand rift basin in New Mexico have been reported to experience lateral-erosion which caused fan incisions (Leeder and Mack, 2001; Mather et al., 2017). In cases of base-level fall, distal-fan incision is generally caused (Fig. 1.4c), which has been reported by many researchers (e.g., Harvey et al., 1999a; Harvey, 2002a; Owen et al., 2006; Mather et al., 2017). Besides, distal-fan incision can also be associated with base-level rise (Fig. 1.5c). This generally occurs to coastal alluvial fans which may be laterally-eroded by the elevated water-level, leading to the foreshortening and incision of alluvial fans. The fans in the Cabo de Gata ranges, southeast Spain was reported to represent such conditions (Harvey et al., 1999a). However, there are some conditions where base-level change does not affect fan development in terms of fan dissection (Fig. 1.5b). In the Dead Sea, a rapid fall in base-level during the Holocene did not cause a headward-cutting feedback (Bowman, 1988; Klinger et al., 2003). In the northern Great Basin, USA, the fall of pluvial lake levels also did not cause fan dissection (Harvey, 2005). The distinct response of alluvial fans to base-level change is related to various factors such as the rate and magnitude of base-level change

(Heller et al., 2001; Harvey, 2002a; Petter and Muto, 2008), and the hydrological conditions (Bonneau and Snow, 1992; Sinha and Parker, 1996; Bowen et al., 2007). Regarding base-level change, a lowering can only be effective in causing fan incision when the slope gradient of the exposed segment, following the level drop, is steeper than that of the former channel (Bowman, 1988; Harvey, 2002a). Regarding hydrological conditions, whether alluvial fans respond to base-level change effectively may be determined by stream discharge, with higher discharge systems being more prone to incision (Bowman et al., 2007).

1.4 A review of river terrace research

Because the alluvial fans and valley fills present in the GLP valley have mostly been incised, forming terraces above the modern floodplain, a brief review of river terraces is now presented here. River terraces are low-relief surfaces standing above the channel, formed by deposition and erosion of valley-fill sediments (i.e., fill terraces) or erosion of bedrock (i.e., strath terraces) (Leopold et al., 1964; Pazzaglia, 2013). The two key geomorphic features of river terraces are flat terrace surfaces, which may be a previous river channel, floodplain or alluvial fan (Stokes et al., 2012), and intervening slopes connecting to either a river floodplain or an adjacent terrace (Leopold et al., 1964). For fill terraces, the alluvium of the terraces represents a period of valley-wide aggradation, and the formation of the intervening slopes represents a switch from fluvial aggradation to incision. Conversely, for strath terraces the alluvium represents syn-bedrock erosion and

bedload transport (Pazzaglia, 2013). As has been mentioned before, the switch between aggradation and incision required for fill terraces to form is generally explained using Bull (1979)'s critical power threshold. Similar to alluvial fans, the factors governing the critical power threshold for fill terraces are also generally summarized into external factors, i.e., climate, tectonism and base-level, and internal factors (Vandenberghe, 2003; Eriksson et al., 2006; Erkens et al., 2009).

Climate has a profound effect upon the geomorphic properties of the fluvial system. A general consensus regarding the relationship between terrace formation and climate in Europe and Asia is that fluvial aggradation occurred during glacial periods while incision during interglacial or glacial-interglacial transition periods (Bridgland, 2000; Macklin et al., 2002; Vandenberghe, 2003; Bridgland and Westaway, 2008, 2014; Olszak, 2017; Wu et al., 2018). The cold-dry glacial climate acts to decrease slope vegetation cover and slope stability, leading to an increase in sediment supply and the onset of terrace aggradation, while the wet-warm interglacial climate causes recovery of vegetation cover and increase in water discharge, promoting channel incision (Bull, 1991; Fuller et al., 1998; Macklin et al., 2002). This perspective has been contested by much evidence showing a discrepancy between the prevailing climate and fluvial activity, such as the discovery of incision during warm-cold transitions (Vandenberghe, 2015; Soria-Jáuregui et al., 2016) and the generally thin fluvial deposits which were in contrast to the long duration of glacial periods

(Vandenberghe, 1995). These variations may suggest that the incision or aggradation may be related to a response to a Milankovitch substage fluctuation (Westaway, 2006; Bridgland and Westaway, 2008), though a paucity of high-precision numerical ages, as well as the discontinuous terrace records, generally impedes the correlation between sub-Milankovitch climatic events and terrace formation (Kasse et al., 2003). Besides, spatial variations of terrace formation under same climatic cycles, representing complex responses of fluvial processes to climatic change (Schumm, 1977; Bogaart et al., 2003;), have been identified by many studies (e.g., Mol et al., 2000; Houben, 2003; Vandenberghe, 2003; Erkens et al., 2009; Notebaert and Verstraeten, 2010; Homolová et al., 2012; Houben et al., 2013). The factors causing these complex responses were summarized by Vandenberghe (2003), who separated them into: (1) basin properties, (2) the proximity to threshold values, and (3) the different response times to a changing external condition. The basin properties include the basin relief, valley width and lithology etc. These properties determine energy conditions, hydrological connectivity, or accommodation space for terraces to be preserved (Antoine et al., 2000; Mol et al., 2000; Knox, 2001). The proximity to threshold values of different fluvial systems is related to sediment textures and channel longitudinal profiles (Vandenberghe, 2003). For example, catchments with coarse-grained bedload and steep longitudinal gradients are closer to the channel erosion threshold than those with relatively fine-grained bedload and flat longitudinal gradients (Schumm, 1979; Huisink et al., 2002; Kasse et al., 2003;

Pastre et al., 2003). In addition, fluvial systems need time to respond to the changing external condition (Schumm, 1977; Bull, 1991). For example, vegetation of different types may need different lengths of time to adapt to climatic changes (Williams et al., 2002). This suggests that the duration of climatic oscillations must be long enough to allow a particular system to react to the forcing process (van Huissteden et al., 2001). As a conclusion, it is crucial to examine the various internal factors of the fluvial systems before discussing the relationships between climate and terrace formation.

Tectonism promotes variations in surface elevation and changes in river gradient, altering the amount of available power within the active system (Bull, 1991; Demir et al., 2009; Yanites et al., 2010; DiBiase et al., 2015). Generally, tectonic uplift causes channel incision, while subsidence leads to channel aggradation. There is some consensus that tectonic uplift is a key process in the formation of terraces (e.g., Maddy et al., 2001; Starkel, 2003; Bridgland and Westaway, 2008; Pan et al., 2013; Schanz et al., 2018), and either the effect of regional or localized differential uplift has been identified for terrace formation. For example, by examining the river terrace sequences in Europe, Bridgland and Westaway (2008) found a contrast between the characteristics of river terraces that were developed before and after Middle Pleistocene: the pre-Middle Pleistocene river terraces are generally wide while the post-Middle Pleistocene terraces are narrow and steep. This pattern was attributed to accelerated regional uplift caused by the climatic

change after the Mid-Pleistocene. This view is rooted in the idea that isostatic equilibrium is maintained by flow in the weak lower crust in response to erosion and sedimentation on the ground surface, such that climate-induced erosion causes regional uplift (Westaway, 2006). Apart from regional uplift that causes terrace incision, differential uplift, which is related to the movement of local faults, may lead to erosion and deposition within the same catchment. For example, in the catchment of the Huangshui River, northeast of the Tibetan Plateau, differential rates of uplift and subsidence resulted in the simultaneous development of strath and fill terraces within the same catchment (Vandenberghe et al., 2011). In the eastern Qilian Shan Mountain, northeastern Tibetan Plateau, differential uplift controlled by active thrust or strike-slip faults has formed different sequences of river terraces (Pan et al., 2013). The control of tectonism on terrace formation can also be seen in tectonically quiescent regions. In these regions, river systems are often constrained by the inherited geological structures (Westaway et al., 2009). For example, fault-controlled corridors can determine the drainage pathways, and faulted basins can exert a control on sediment budgets between different sedimentary basins (Stokes, 2008). The river terraces preserved in regions with low tectonic activity are commonly of complex fill architectures and/or strath forms with little altitudinal spacing (Starkel, 2003).

Base-level refers to the elevation below which a stream cannot downcut. The cessation of an incision is usually due to a reduction of the hydraulic gradient into

zero when rivers flow into oceans or lakes (Leopold and Bull, 1979). The base-level can be the level of lakes, oceans, some resistant outcrops or the master stream which a tributary flows into. The role of sea level, which is the ultimate base-level for all fluvial systems, has been explored by many studies (e.g., Posamentier and Vail, 1988; Maddy, 1997; Blum and Törnqvist, 2000; Maddy et al., 2001; Holbrook et al., 2006; Bridgland and Westaway, 2008). In many cases, the change of sea level is essentially controlled by climatic cycles over Quaternary timescales (Blum and Törnqvist, 2000). Generally, a continuous sea-level fall is expected to cause firstly progradation of fluvial sediments in a seaward direction and then valley incision. The relative rise of sea level will cause valley wide filling (Posamentier and Vail, 1988). However, the configurations of the offshore shelf are also important factors which determine the distance the base-level induced fluvial response can reach upstream (Blum and Törnqvist, 2000). Generally, downstream base-level effects rarely propagate more than a few tens to a couple of hundreds of kilometers upstream because more upstream controls like climate and tectonism gain the principal influence on those portions of the river profile (Blum and Törnqvist, 2000). Holbrook et al. (2006) introduced the concept of upstream discharge-related base-level control on river longitudinal profiles. The downstream and upstream base-level control together determine a buffer area defined by the top profile of the highest possible aggradation and the base profile of maximum possible incision (Fig. 1.6). This buffer area envelopes the available fluvial preservation space.

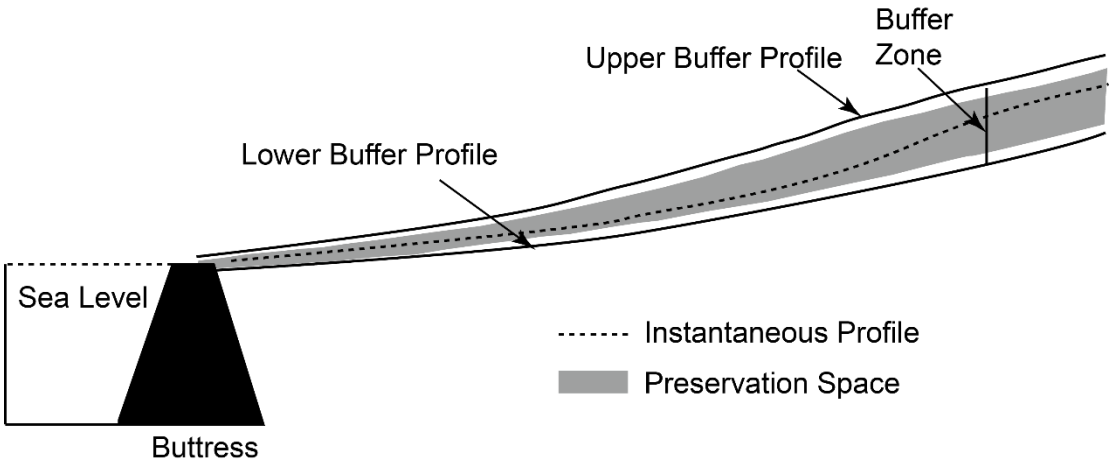

Fig. 1.6. A sketch displaying the upper and lower buffer profiles which are adjusted to a stable sea level (buttress). After Holbrook et al (2006), their Fig. 7.

Tectonic uplift usually causes a relative fall of the base-level for many rivers developing in inland regions, causing fluvial incision (e.g., Finnegan and Balco, 2013). For example, the uplift of the Tibetan Plateau caused the incision of the Yellow River into the plateau inland (Craddock et al., 2010). Fluvial terraces of same levels of the Yellow River provide progressively younger ages upstream, indicating the progressive propagation of the effect of base-level fall at the plateau margins (Craddock et al., 2010; Perrineau et al., 2011). However, there are significant lags between the growth of high topography and fluvial incision. In the northeast Tibetan Plateau, the initiation of Yellow River incision postdated the mountain building processes by nearly 10 Myr (Craddock et al., 2010). Besides, for tributary rivers, the level of the master stream into which the tributary flows act as a local base-level. However, because of the co-existence of the downstream base-level control and the upstream climate-related discharge control on river terraces, it is usually difficult to ascertain whether any observed changes were

caused by the base-level effect or the upstream climate-related discharge effect (Leopold and Bull, 1979). Because the GLP river, which is the focus of this study, is a tributary to the Bailong River, the base-level effect of the Bailong River on the tributary evolution will be discussed in Chapter 8.

Terrace sequence can also form as a result of an autogenic evolution of river systems (Schumm, 1977; Bull, 1991; Lewin and Macklin, 2003; Limaye and Lamb, 2016). The autogenic mechanisms, referring to the redistribution of sediment within a depositional system as a result of the processes inherent to the system, may reduce or enhance the impact of external forces (Schumm and Parker, 1973; Schumm, 1977; Bull, 1991; Veldkamp and van Dijke, 2000; Miall, 2006). Channel avulsion and stream capture are two important autogenic processes (Schumm, 1979; Miall, 2006). Channel avulsion is usually driven by sedimentation, usually at high rates, which produce local super elevation of some part of the channel above its surroundings (Bryant et al., 1995; Slingerland and Smith, 2004). River capture is associated with the beheading and re-routing of a less active fluvial system by an actively incising and headward-eroding fluvial system (Stokes et al., 2002). Either the avulsed channel or the rerouted fluvial system may introduce some dramatic changes in stream power, enhancing or reducing the impact of external environmental changes. Autogenic processes generally induce trends and events capable of forming valley floor landforms (e.g., terraced surfaces). Although operating over relatively small spatial and temporal scales (Houben,

2003), the autogenic processes are important mechanisms for understanding the response of fluvial processes to external changes, e.g., climatic and tectonic changes (Mol et al., 2000; Veldkamp and Tebbens, 2001).

1.5 Previous studies in the eastern margin of the Tibetan Plateau

The eastern margin of the Tibetan Plateau is characterized by large rivers incising the uplifted topography which results from the continued convergence of the Indian and Eurasian plates (Clark and Royden, 2000; Kirby et al., 2002; Ouimet et al., 2007). The sources of the two important Chinese rivers, the Yellow River and the Yangtze River, are located in the Tibetan Plateau, and numerous tributaries of these rivers incised the plateau (Clark et al., 2004; Craddock et al., 2010; Perrineau et al., 2011; Kong et al., 2012). Many river terraces have formed during these headward incising process under the influence of the Asian Summer Monsoon, and these fluvial deposits have been used as key records in reconstructing the past climate and tectonic activity.

On the northeastern margin of the Tibetan Plateau, specifically along the Yellow River and many of its tributaries, approximately seven levels of fluvial terraces are generally identified (Li et al., 1997a; Gao et al., 2008). The terrace chronology was constrained using a variety of dating methods including magnetostratigraphic techniques, ^{14}C, electron spin resonance (ESR) and thermoluminescence (TL) or optically stimulated luminescence (OSL) dating (Gao et al., 2008; Pan et al., 2009;

Wang et al., 2010). These ages generally indicate that terrace incision occurred at glacial-interglacial transitions, with an increasingly high but intermittent fluvial incision rate since 1.66 Ma (Li et al., 1997b; Lu et al., 2004; Gao et al., 2008; Pan et al., 2009). However, these studies above are generally based on a specific section of a river, and the space-time pattern of terrace distribution along the whole section of a river has not been discussed. Craddock et al (2010) noticed that the timing of the highest terrace levels across different parts of the Yellow River was not the same: terraces in the plateau inland are generally younger than the terraces in the plateau margin. Harkins et al. (2007) also revealed an ongoing pulse of transient fluvial incision across the Anyemaqen Shan (see Fig. 2.1 for its location), further upstream of the Yellow River. Together these pieces of evidence together suggest that fluvial incision was initiated at the plateau margin and progressed headward (Craddock et al., 2010; Perrineau et al., 2011). In contrast to the well-developed river terraces in the Yellow River, the upstream portion of the Yangtze River developed few terraces. This may be due to their differences in geological settings. The upstream portion of the Yellow River passes through some Neogene sedimentary basins (Li et al., 1997b; Fang et al., 2005), which provide the accommodation space for terraces to form. In contrast, the Yangtze River mostly developed in steeply-incised fault-controlled valleys (Clark et al., 2004), with little space provided for terraces to form. The research focus in the upstream portion of the Yangtze River has been on the river geometry, emphasizing changes in river patterns due to river capture, drainage direction

reversal and impact of the tectonic uplift (e.g., Barbour, 1936; Koons, 1995; Brookfield, 1998; Hallet and Molnar, 2001; Clark et al., 2004; Kong et al., 2012). Nevertheless, the river terraces along the Yalong River, a secondary tributary of the Yangtze River, were studied by He et al. (2015a). A maximum of six terrace levels were described and dated using a combination of OSL and ESR dating. The correlation between terrace formation and climate, as well as the incision rates of the Yalong River, indicates a similar pattern to the rivers on the northeastern margin of the Tibetan Plateau. Collectively, present research in both the northeastern and southeastern margin of the Tibetan Plateau suggests that (1) fluvial aggradation occurred during glacial periods while incision occurred during glacial-interglacial transitions and (2) the incision rates have been intermittently accelerated during Quaternary.

In contrast to the research on fluvial terraces which have been well characterized and chronologically constrained, the study of alluvial fans or terraces which developed from relatively small tributary valleys on the eastern margin of the Tibetan Plateau is still in its infancy. The study of alluvial fans in this region is concentrated in two primary rivers, the Xiaojiang River in the south and the Bailong River in the north of the eastern Tibetan Plateau margin. Early studies focused on fan geomorphology in the Xiaojiang River (e.g., Tang, 1990; Tang et al., 1991; Liu et al., 1992). The convex fan surfaces with hummock features and the steep fan margins were recognized by Tang (1990). Liu et al. (1992)

discussed the relationships between fan planview forms and the unit weight of debris flows based on physically modelled experiments. Chen et al. (2005b) analyzed the relationship between drainage areas, fan areas and channel slopes using regression methods and found that the fan area varies as a power function of the drainage area and that the channel slope varies as a negative power function of the drainage area. These relationships are consistent with the general findings relating to alluvial fans (Mather et al., 2017). Yang and Liang (2007) analyzed the slopes of fan surfaces formed by cohesive debris flows and cohesionless debris flows in the Bailong River. They found that the fan surfaces formed by cohesive debris flows are steeper than those formed by cohesionless debris flows.

The tributary alluvial fans or terraces are generally formed by processes which may cause a hazard to human populations, such as debris flows or hyperconcentrated floods. Consequently the sedimentary characteristics of the alluvial deposits have been studied to extract information on the characteristics of the hazardous processes. Cui and Xiong (1990) examined several sedimentary profiles of the alluvial fans along the Bailong River and the Xiaojiang River and interpreted the poorly sorted gravelly deposits collectively as deposits of debris flows. Liu and Cui (1999) further distinguished the sedimentary structures of these poorly sorted gravelly deposits and interpreted each into distinct types of debris flows (Table 1.1). Notably, the term, debris flow, has been

used slightly different between the Chinese scholars (Liu and Cui, 1999) and international scholars (Hungr et al., 2001; Hungr et al., 2014). The cohesive and non-cohesive debris flows in Table 1.1, are generally equivalent to the widely-accepted definitions of debris flows (Pierson and Costa, 1987; Hungr et al., 2014), whereas the transitional debris flows is equivalent to hyperconcentrated floods (Pierson and Costa, 1987; Hungr et al., 2014).

Table 1.1 Sedimentary structures of different types of debris flows. After Liu and Cui (1999).

Processes	Depositional mechanism	Structures
Non-cohesive debris flows ($1.3 – 1.7$ T/m^3)	Fluid flow model	Stone line; Imbrication; Gravel supporting-superimposed structure
	Granular flow model	Inverse graded bedding Inverse-normal graded bedding Imbricated-vertical structure Circling linear structure
Transitional debris flows ($1.7 – 1.9$ T/m^3)		
Cohesive debris flows ($1.9 – 2.3$ T/m^3)	Viscos-plastic model	Inverse graded-chaotic structure Bottom-mud chaotic structure Out-wedging structure Circling linear structure

Fan deposits have been dated using a number of methods including ESR, thermoluminescence (TL), OSL and ^{14}C. Ye et al. (1998) used the ESR technique to date paleo-debris flow sediments in the Jiangjia Ravine, a tributary of the Xiaojiang River, and obtained relatively old ages between 98.3 – 22.7 ka. The sample which produced an age of 22.7 ka was validated by a ^{14}C age (20.13 ±

1.48 ka). Kuang et al. (2002) also used the ESR technique to provide more age controls for the paleo-debris flow sediments in the valley. However, these two studies did not present the uncertainties of the ages produced. Chen et al. (2013) used OSL to date the fine alluvial silts intercalated between debris flow sediments in a relatively small-sized tributary valley of the Xiaojiang River. These deposits produced ages between 10.6 - 4.5 ka, a period of warm and wet conditions. In the Bailong River, only one TL date (Chen and Chai, 1993) and four ^{14}C dates (Wang et al., 2000; Li, 2003) for fan sediments are available. The TL date, which is 116.8 ± 9.9 ka, provides the oldest radiometric ages for the debris flow deposits in this region. The four ^{14}C dates are within the Holocene period and were taken from different tributary valleys. In the absence of radiometric ages, the ages of older deposits were estimated by estimating the ages of the fluvial terraces of the Bailong River upon which the debris flow deposits are located.

In both the Bailong and Xiaojiang River regions, the history of alluvial fan/terrace aggradation and incision has not been studied. Instead, the focus has been upon recognizing periods of debris flow activity and upon identifying periods in which favorable climatic conditions for debris flow formation existed (Chen and Chai, 1993; Chen and Li, 1997; Wang et al., 2000; Li et al., 2002; Wang et al., 2002; Li, 2003). In these analyses, debris flow deposits distributed at different elevation levels are regarded as representing different periods of activity. A typical example of this approach is illustrated in Fig. 1.7 (Liang et al., 2010).

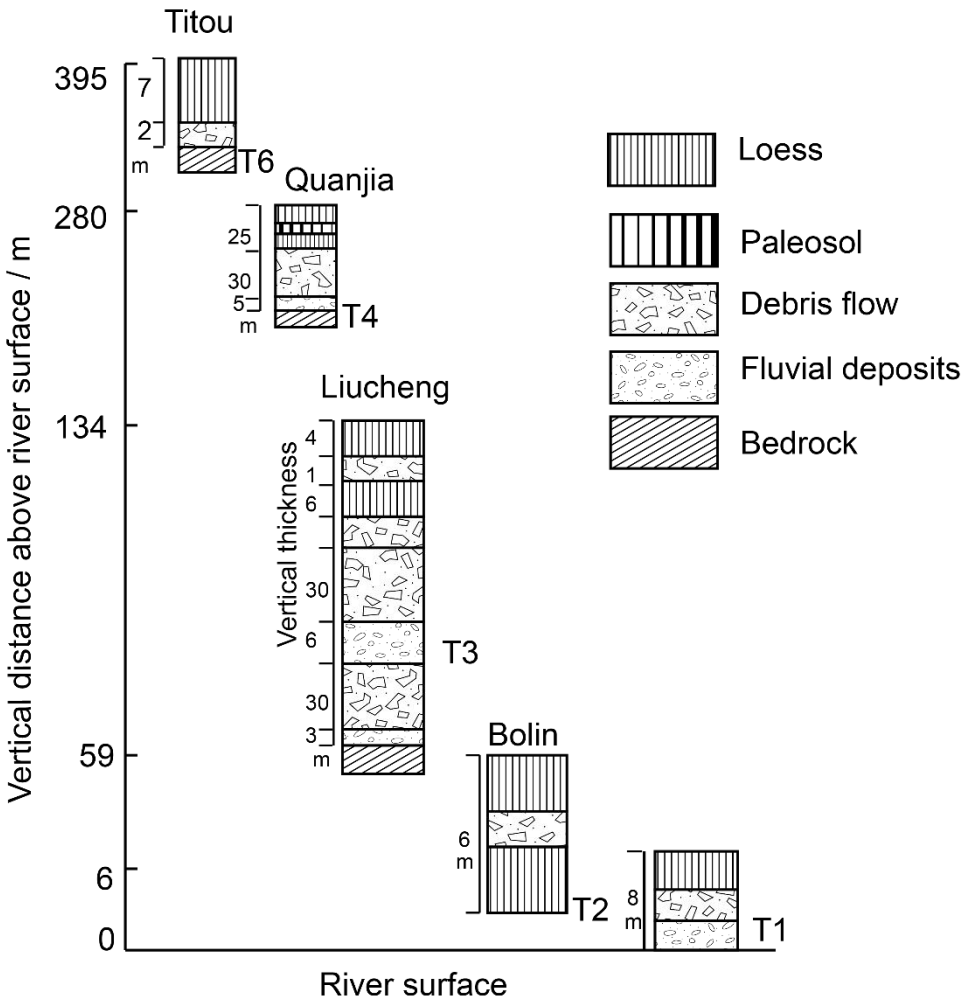

Fig. 1.7. Distribution of debris flow sediments along the Bailong River terraces. T1, T2, T3, T4 and T6 represent the different terrace levels of the Bailong River. Each profile was located at different areas within the watershed of the Bailong River. The labels, Bolin, Liucheng, Quanjia, and Titou are local names of the corresponding profile. After Liang et al (2010), their Fig.1.

In Fig. 1.7, the debris flow deposits in the Titou profile lies on the bedrock that has been regarded as the bed of the T6 terrace of the Bailong River. The debris flow deposits in the Quanjia, Liucheng and Bolin profiles were regarded as relying on the beds of the Bailong T4, T3 and T2 terraces respectively. The ages of the Bailong River terraces were estimated by the regional correlation between the terraces of the Bailong River and those of the Yellow River. Consequently, periods

of debris flow activity in tributaries of the Bailong River are currently constrained by using ages for Bailong River terraces which are themselves inferred from directly dated deposits of the Yellow River. This double correlation is not considered to be sufficient when determining the geomorphic evolution and consequent geomorphic hazards (associated with debris flows in the tributaries of the Bailong River) since there are too many opportunities for incorrect correlation.

Beside the insecure nature of the correlative dating scheme described above, several other issues exist in these studies. Firstly, because the debris flows developed from tributary valleys with varying characteristics (e.g., watershed areas, morphology and lithology etc.), the environmental conditions necessary to trigger debris flow events differ between valleys (Schumm, 1979). Consequently, the climatic conditions conducive to debris flows in one tributary might not be the same as in others, meaning that it is beneficial to discuss debris flow activity within a single tributary valley and to consider the specific conditions of that tributary. Secondly, the idea of regarding the existence of debris flow deposits as an indicator of a period of debris flow activity is questionable since it implies that the absence of debris flow deposits indicates the absence of debris flow activity. This is not the case. The poorly sorted gravelly sediments identified along the Bailong River are formed by debris flows or hyperconcentrated floods. These events are usually triggered by heavy rainfall storm during summer seasons

(Tang et al., 2011), and have been reported to be highly erosive in other similar regions of the world. For example, field monitoring in the high mountainous regions in Taiwan and American Southwest suggests that the motion of a thin sediment mantle are more erosive than the normal streamflow processes, indicating that debris flows or hyperconcentrated floods can be more erosive than stream floods at some portions of a channel (Stock and Dietrich, 2003; Stock and Dietrich, 2006). Pierson (1980) reported a rain-storm triggered debris flow event in an uplifted mountain in New Zealand, and the pulsed surges of the debris flow caused wide fan-head entrenchment of the stream channel. Based on long-term measurement of cross-channel transects in the Jiangjia Ravine, a typical and intensely studied debris flow valley in China, Chen et al. (2005a) found that: when debris flow magnitude was small, deposition in the channel increased with the magnitude; when the magnitude reached a threshold, the deposition began to decrease, and eventually erosion took place. From these pieces of reported field evidence, it is obvious that debris flows can be responsible for both valley erosion and aggradation. Consequently, the absence of debris flow deposits representing valley incision phases might not signify a period of low-debris flow activity but may instead represent poor preservation. Lastly, the lack of securely radiometrically dated debris flows has made it difficult to determine what climatic conditions may be associated with periods of intense debris-flow activity.

Considering the issues associated with determining the periods of debris flow

activity, this study proposes a new way of understanding the debris flow deposits of the area. Instead of stating that the presence of debris flow deposits indicates a period of debris flow activity, the presence of such deposits is regarded as an aggradational/depositional period of debris flows. Debris flow deposition on alluvial fans is important in understanding the potential hazards associated with active debris flow processes on fans and equally important in regards to fan evolution (Staley et al., 2006; Iverson, 2014; Pederson et al., 2015; De Haas et al., 2018). On time scales of several events, the research focus is on the spatial variation of debris flow deposition on alluvial fans. Both field-based (Okuda and Suwa, 1981; Suwa, 1983; Whipple and Dunne, 1992; Marchi et al., 2002; May and Gresswell, 2004; Staley et al., 2006; Schürch et al., 2011) and modeling-based studies (Major and Iverson, 1999; Lancaster et al., 2003) have contributed to this knowledge. The spatial variation of debris flow deposition means that (1) debris flow deposition at different parts of alluvial fans may form distinct fan topographic features because of the transition of debris flow characteristics, e.g., rheology, sediment concentration and grain size etc., during its development (2) sequential debris flow events with distinct powers and characteristics may lead to distinct loci of deposition and erosion (Benda, 1990; May and Gresswell, 2004; Imaizumi et al., 2005). Specifically, De Haas et al. (2018) proposed two mechanisms of channel avulsion during sequential debris flow events that are related to fan formation. One mechanism is related to the stochastic channel plugging during individual events, backstepping of deposition towards fan apex

over subsequent flows, avulsion and the establishment of a new active channel. The other mechanism is related to the gradual shifts of deposition loci towards topographically lower parts of a fan, i.e. the effect of topographic compensation. Studies which used dendrogeomorphological methods allow the discussion of debris flow deposition over time scales of hundreds of years (Stoffel and Beniston, 2006; Stoffel et al., 2008; Stoffel, 2010), though the majority of the study focuses on the dating of individual events and the reconstruction of magnitude and/or frequencies (Stefanini, 2003; Stoffel et al., 2005). An exception is the research conducted by Bollschweiler et al. (2007) who reconstructed the spatio-temporal patterns of debris flow activity in a forested cone in the Swiss Alps. They found frequent avulsion of debris flow events forming deposition and erosion by subsequent surges on different parts of alluvial fans. On time scales of 10^3 – 10^4 yrs, debris flow deposition generally forms relatively large-scale landforms, both in terms of area and deposit thickness e.g., alluvial fans or terraces. Over these temporal scales, the spatial variation of deposition and erosion for individual debris flow event is obscured. Instead, debris flow aggradation is regarded as a gross trend in the specific time scales, and the focus lies in the response of fan or terrace formation to the gross climatic conditions, as has been discussed in Sections 1.3 and 1.4.

This PhD thesis focuses on debris flow/hyperconcentrated flood aggradation in one tributary to the Bailong River. These flows formed alluvial terraces and fans,

which were subsequently incised, with the resulting sedimentary sequence covering the last 10^3 - 10^4 yrs. Through landform mapping, sedimentological analyses and OSL dating, the aggradation and incision periods of the valley have been identified. The Goulinping (GLP) valley was chosen for detailed investigation since the alluvial terraces/fans here support intense agriculture and several large residential areas, making them typical of those found in many Bailong River tributaries. In addition, the GLP valley is currently subject to intense study as a part of a research project aimed at monitoring and providing early-warning of debris flow events in the Bailong River catchment. The project is led by Professor Xingmin Meng at Lanzhou University and supported by the Minister of Science and Technology, China. As a result of this project, considerable amounts of extra data, including high-resolution DEM, satellite images and some borehole data were available which facilitated the study.

Chapter 2 Study Area

2.1 Introduction

This chapter provides the background context of the study area, i.e., the wider Bailong River and the GLP valley. It is divided into three sections. Sections 2.2 and 2.3 introduce the location, geology and topography of the Bailong River and the GLP valley, respectively. Section 2.4 introduces the present and paleoclimate of the Bailong River.

2.2 Background setting of the Bailong River

2.2.1 Location

The Bailong River is a secondary tributary of the Yangtze River and is located on the eastern margin of the Tibetan Plateau (TP) (Fig. 2.1). It originated from the TP at an elevation of about 6000 m and flows southeast through many parts of Gansu Province including Diebu, Zhouqu, Wudu, and Wen, and flows out of Gansu at Bikou (Fig. 2.2). The watershed covers an area of ~ 18670 km^2. The relief is ~ 4400 m over a horizontal distance of ~ 570 km. Geologically, the area belongs to the Western Qinling[1], a mountain range bounded by the TP to its west, the Linxia Basin to its north, and Sichuan Basin to its south (Fig. 2.1).

[1] Western Qinling is the western extent of the Qinling orogeny, which is an east-west trending mountain range in central China.

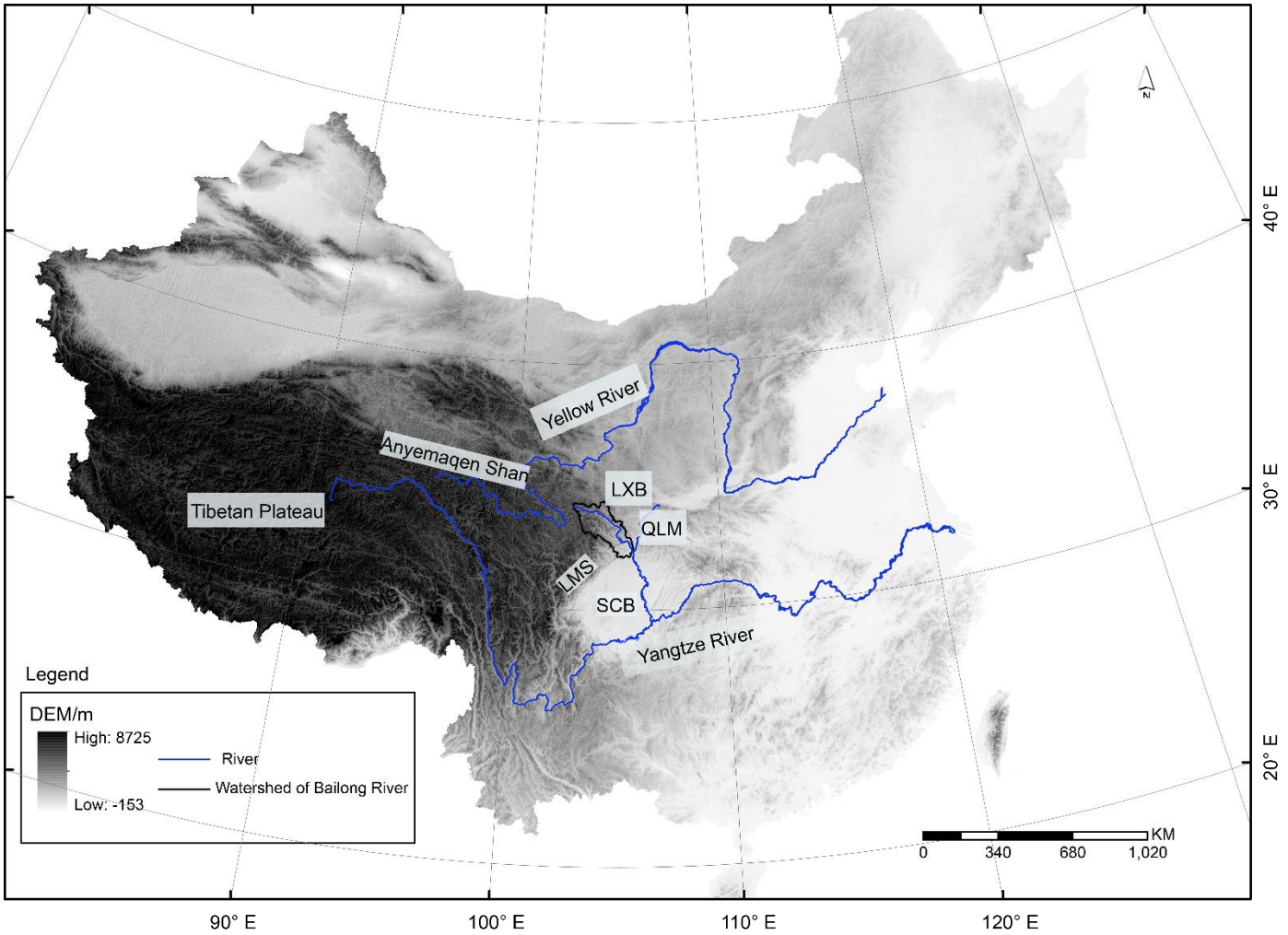

Fig. 2.1. The geographical location of the Bailong River (outlined in black lines) in China. The background map is a 90-m resolution SRTM DEM. Meaning of abbreviations: SCB = Sichuan Basin, QLM = Qinling Mountain, LXB = Linxia Basin, LMS = Longmen Shan

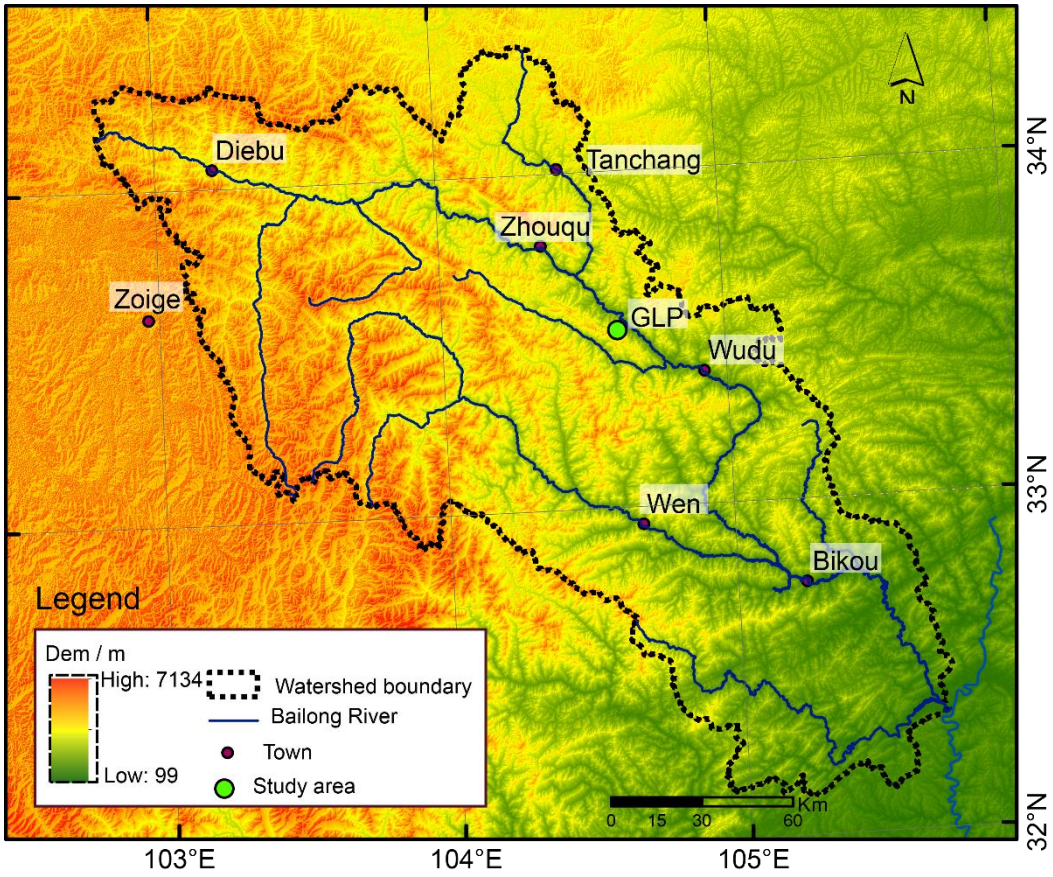

Fig. 2.2. Watershed of the Bailong River. The background image is a 30-m resolution ASTER DEM. The blue lines represent the channel of the Bailong River. The filled green dot denotes the location of the GLP valley.

2.2.2 Geology

A geological map (Fig. 2.3) was produced by digitalizing the 1: 200,000 papery geology maps from the Gansu Provincial Mapping Bureau. Three paper maps covering the Gansu part of the Bailong River were obtained from the Bureau and were digitized and integrated into one map. I digitalized one of the paper maps, the area around Bikou (Fig. 2.3), and the other two maps were drawn by Dr. Runqiang Zeng, Dr. Liang Qiao, Dr. Peng Guo and Dr. Guan Chen from Lanzhou University. The following section introduces the existing strata and the primary fault series of the region.

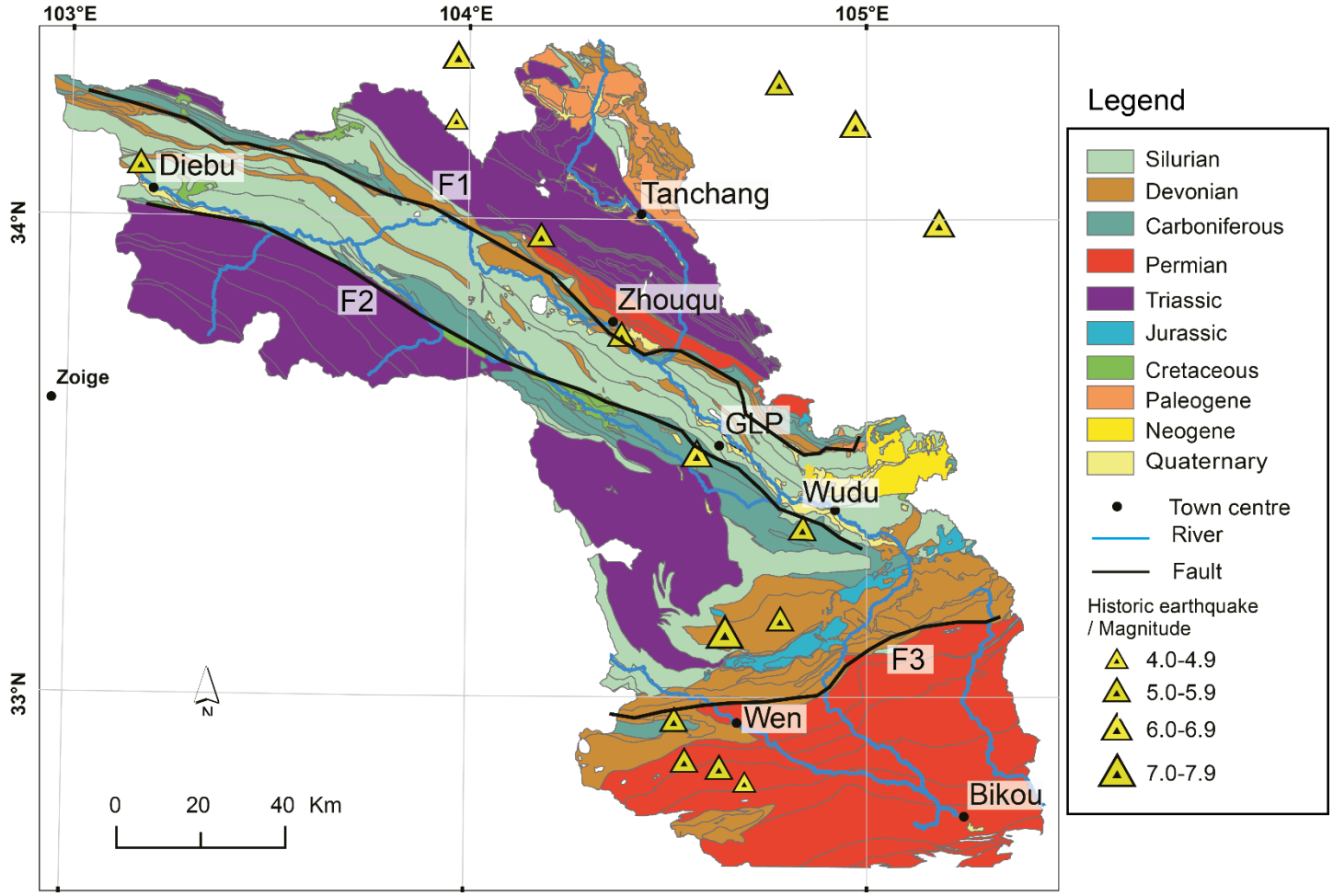

Fig. 2.3. Geology map of the Bailong River in the Gansu part compiled from three paper maps from the Gansu Provincial Mapping Bureau. The sites of historic earthquake were after Yu et al., (2012).

Strata and distribution

The geological strata in the Bailong valley cover the Silurian to the Quaternary. The characteristic rocks are phyllites, limestones and slates. Specifically, Silurian strata, with the primary lithology being phyllite, are the major set of strata in the region, while the Devonian, Carboniferous, Permian and Triassic, represented mostly by limestones, are distributed to the north and south of the Silurian strata (Fig. 2.3), forming an anticline structure. The Jurassic, Cretaceous, Paleogene and Neogene strata are composed of sandstones and conglomerates which are only present in some local basins in Wudu, Tanchang and Zhouqu. The Quaternary strata, including a series of alluvial, colluvial and aeolian deposits, are distributed along the banks of the Bailong River, in topographically low areas and flat hill-slopes.

Table 2.1 Strata, lithology and distribution alone the Bailong river (see Fig. 2.3 for location names).

Era	Period	Major rock	Distribution
Cenozoic	Quaternary	Colluvium, alluvium and loess	Sporadically distributed along the banks of the Bailong River and topographically low areas and flat slopes
	Neogene	Red sandstones and conglomerates	Tanchang and Wudu
	Paleogene		
Mesozoic	Cretaceous	Thick sandstones, marlstones, calcareous shales, and coals	Sporadically distributed in the Neogene basins in Wudu and Tanchang
	Jurassic	Thick sandstones, marlstones, calcareous shales	
	Triassic	Slates, thick quartz, sandstones, phyllites and limestones	Distributed symmetrically along both sides of the Bailong River in the section between Zhouqu to Wudu
Upper Paleozoic	Permian	Carbonaceous phyllite and sandy phyllites, argillaceous slates, slates, thick limestones, fine and silty-sandstones	
	Carboniferous		
	Devonian		
Lower-Paleozoic	Silurian	carbonaceous phyllite, fine sandstones, thin-layered limestones, quartz sandstones, and siliceous rocks	Distributed along the Bailong River in the section between Zhouqu to Wudu

Faults and earthquakes

Three major fault systems (F1, F2, F3) are identified from the geological map and have been highlighted by others (Li, 1994; Guo et al., 2009).

The F1 is a fault series called the Guanggaishan-Dieshan fault series distributed along the north bank of the Bailong River. It trends NW 70˚ and extends for around 160 km. Yu et al. (2012)’s study on the fault in the region of Zhouqu demonstrates

that the F1 has been active during the Holocene.

The F2 is called Diebu-Bailong fault series and extends parallel to the F2 on the south bank of the Bailong River. It is ~160 km in length and is composed of a series of reverse faults. The middle part of F2 was the epicenter of a 7-7.25 magnitude earthquake, a large historical event occurred in 186 BC which caused landslides and killed 760 people (Yuan et al., 2007).

The F3 is called Wenxian-Wudu fault series and extends in the NE direction. Its length is 180 km. A magnitude 8.0 earthquake which is centered on the mid of F3 (Yuan et al., 2014) occurred on July 1st of 1879 and killed ~ 20,000 people.

Noticeably, the valley of the Bailong River was confined between the F1 and the F2 fault series and is fault-guided.

2.2.3 Topography

This part focuses on the topographic features of the midsection of the Bailong River, which is defined here as the section between Zhouqu and Wudu (Fig. 2.4). There are two reasons for choosing this section. Firstly, this part bears the densest residential areas in the watershed of the Bailong River. The county centers of Zhouqu and Wudu and various town centers are distributed in the alluvial fans and fluvial terraces in this section. Secondly, the geologic and

geomorphic settings are relatively consistent in this part. The midsection has developed in an anticline in which the normal sequence of strata (Silurian to Triassic) has been folded and eroded at its hinge zone (Li, 1994). This formed the broad Bailong corridor consisting of relatively low-relief phyllite terrains and river valleys (Zhang et al., 2011), as well as the limestone high-relief high-elevation areas.

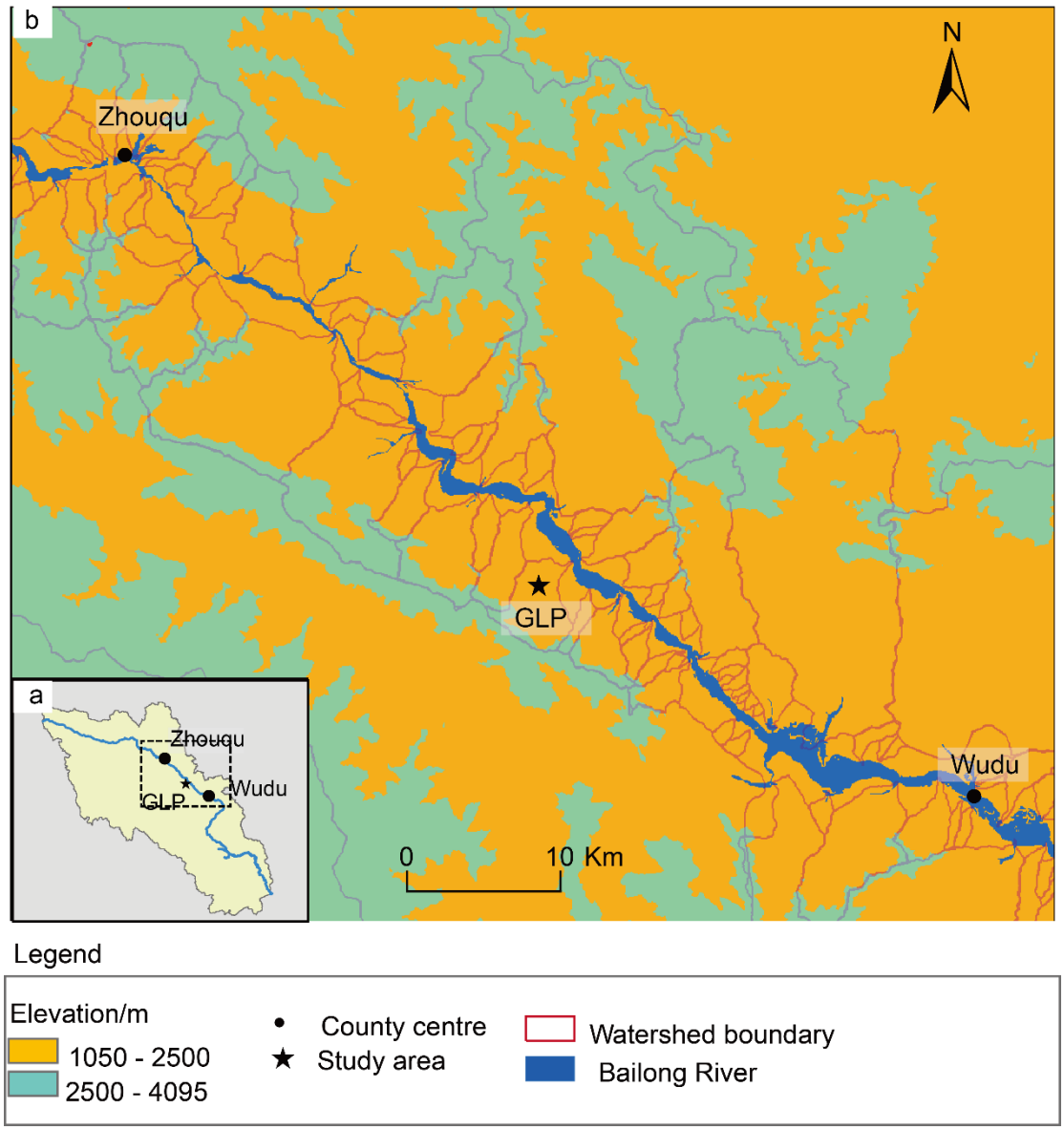

Fig. 2.4 Geomorphic characteristics of the midsection of the Bailong River. The inset map (panel a) shows the watershed boundary of the Bailong River and the midsection delineated by the dashed box. The area with an elevation between 1050 – 2500 m is shown in dark yellow, and the area above 2500 in light blue. This classification generally distinguishes the high-elevation limestone area and the low-elevation phyllite area. The red lines show the boundaries of the tributary valleys.

Fig. 2.4 is a simplified topographic map of the midsection of the Bailong River. The elevation is classified into two classes: 1050 – 2500 m and 2500 – 4095 m, generally representing the phyllite low-elevation ranges and the limestone high-

elevation ranges respectively. The high-elevation limestone areas form the divides of the tributary valleys of the Bailong River. The Bailong River developed in the middle of the phyllite ranges. It is a U-shaped valley and has formed a wide floodplain (Fig. 2.5). The channel is of an alluvial type where thick alluvial deposits as deep as 62 m can be found (according to the borehole data in the Bailong River channel in Zhouqu conducted by Gansu Provincial Bureau of Earthquakes).

Fig. 2.5. Floodplain of the Bailong River and the phyllite hillslope. The photograph was taken at a place (N 33° 32′ 28″ E 104° 38′ 54″, elevation: 1277 m) on the top of a phyllite hillslope in the downstream portion of the GLP valley.

2.3 Background setting of the GLP valley

The GLP valley, with a watershed area of ~ 20 km^2, is located at N 33°32′24″, E 104°39′13″ in the mid-section of the Bailong River (Fig. 2.2). Two major channels

exist in the valley: the Xiaogou valley and the Dagou valley (local names meaning small valley and large valley respectively, Fig. 2.6). Three villages are distributed in the topographically high areas: Yaodao, Jiudun and Zhaojiaping village, and one, the Goulinping village, is located at the mouth of the valley (Fig. 2.6).

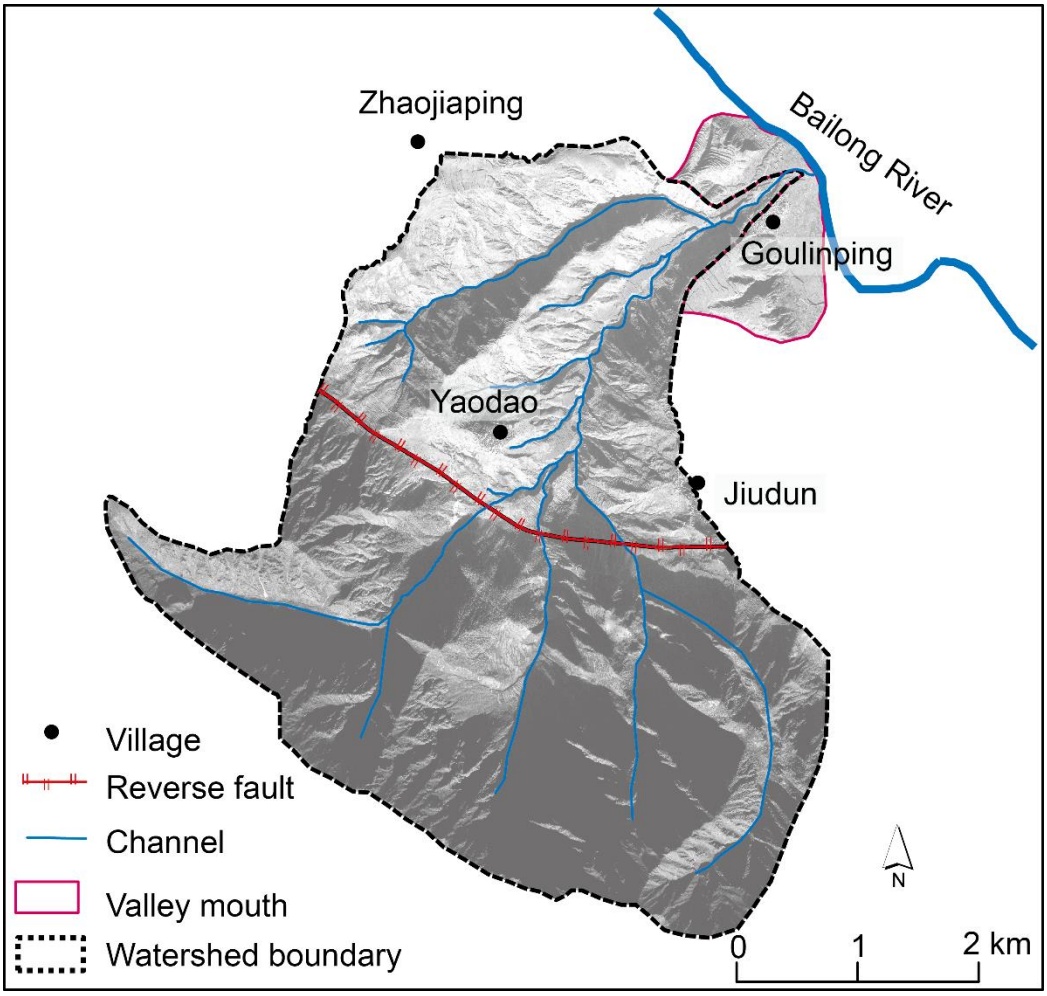

Fig. 2.6. Map of the GLP valley. The background image was obtained by the China Source Satellite in 2013.

In the GLP valley, the lithology is composed of two types: the Carboniferous limestone which forms the upstream high-relief, high-elevation ranges and the Silurian phyllite which forms the midstream low-relief, low-elevation area. Quartz dykes can be found in some parts of the phyllite areas (Fig. 2.7b). The two

bedrock types are bounded by a reverse fault (Fig. 2.6 and Fig. 2.7a), which belongs to the F2 fault series (Fig. 2.3).

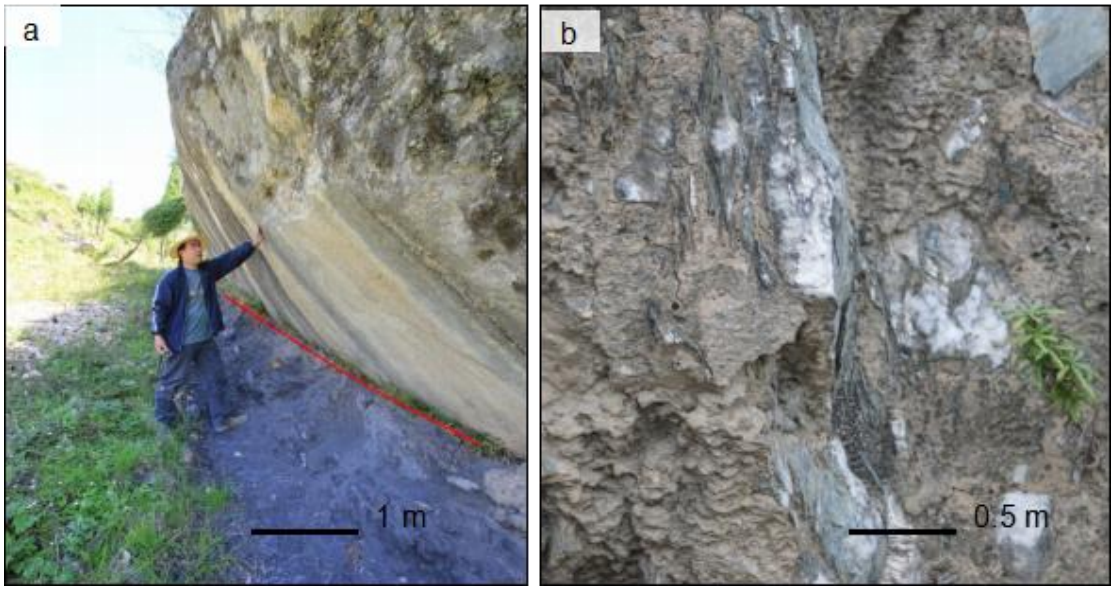

Fig. 2.7. Photographs showing the reverse fault plane (a) and the quartzite veins in phyllites (b). Photographs were taken by Professor Xingmin Meng from Lanzhou University.

The limestone area is mostly covered by coniferous trees and shrubs (Fig. 2.8 and Fig. 2.9a). The vegetation changes from farmlands (Fig. 2.9b) on the alluvial terraces to grasslands (Fig. 2.9c) on the phyllite hillslopes. At the mouth of the valley, farmlands and broad-leaved trees (Fig. 2.9d) become the primary vegetation cover.

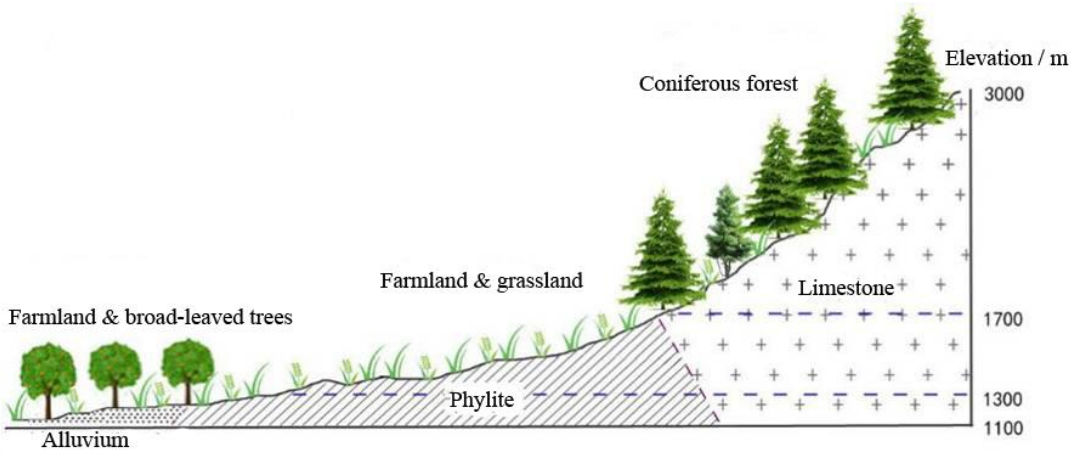

Fig. 2.8. Longitudinal profile and vegetation along the GLP channel. The figure is provided by Mr. Kai Li from Lanzhou University.

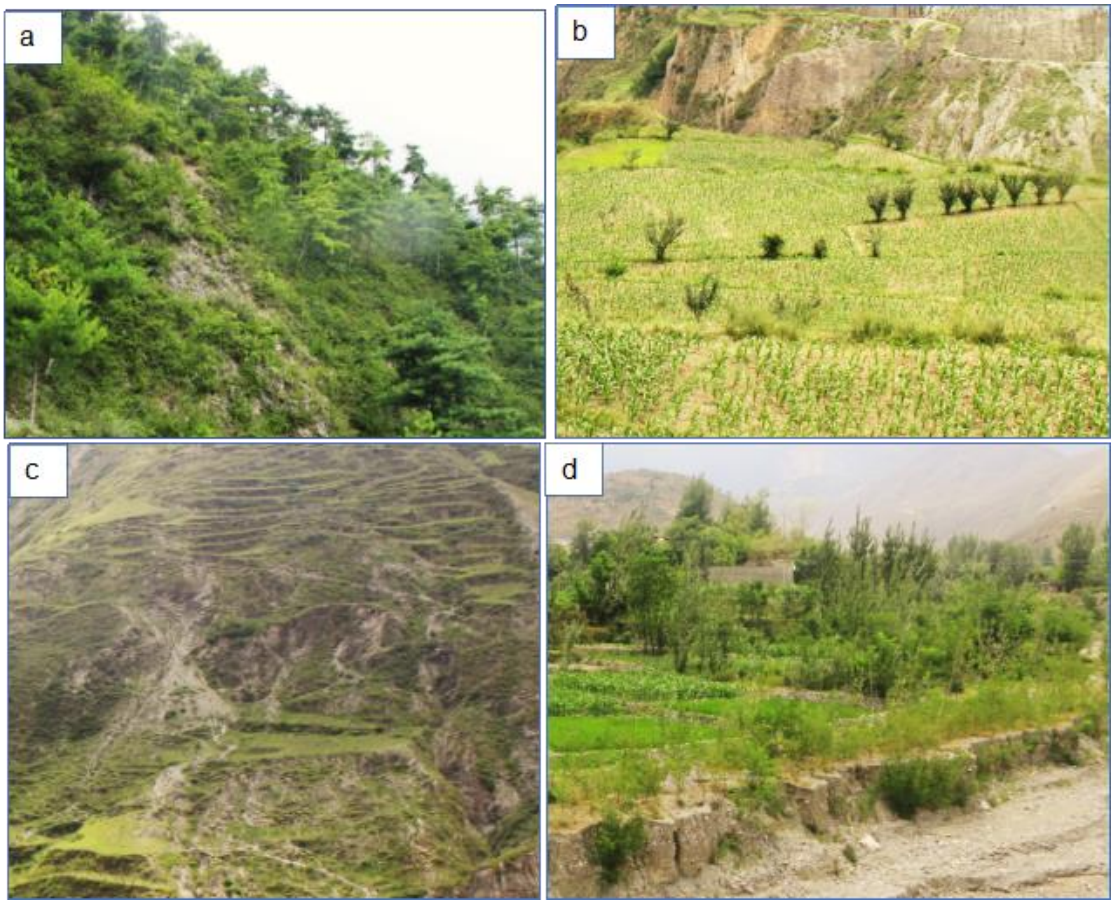

Fig. 2.9. Vegetation cover in different sections of the GLP valley. a. Coniferous trees and shrubs in the limestone area; b. Xerophytic crop distributed on the alluvial terraces in the mid-stream section of the valley. c. Sparse grasslands distributed on the hill-slopes of the phyllite areas. d. Crops and broad-leaved trees distributed at the mouth of the valley.

2.4 Present- and paleo-climate

2.4.1 Present climate

The present climatic settings of the area are shown in Fig. 2.10. The region is subject to a variety of air masses, including the dry-cold airs transported by the westerlies and the winter monsoon from the west and north of the inland region, and the warm-humid airs coming from the South China Sea, the Pacific Ocean and the Indian Ocean. The alternation between the warm-humid airs and cold-dry airs is driven by the thermal difference between the Asian landmass and the Ocean during different seasons. Consequently, the area is characterized by prominent seasonal changes in wind direction, precipitation and air temperature between winter (cold and dry) and summer (hot and humid) (An, 2000). During winter, the Siberian-Mongolian High and westerlies maintain cold and dry conditions and carry airborne dust to the site (Zhang et al., 2008), while in summer, winds bring warm and humid air masses from the oceans to the area. This alteration of the dominant wind leads to strong seasonal variation in rainfall during each individual year. According to the monitoring data from the weather station in Wudu, the area received an annual average precipitation of 487.2 mm, of which 75 to 85% falls between May and September. The average minimum and maximum temperatures are −14 °C to 3 °C in January and 11 °C to 27 °C in July (Johnson et al., 2006).

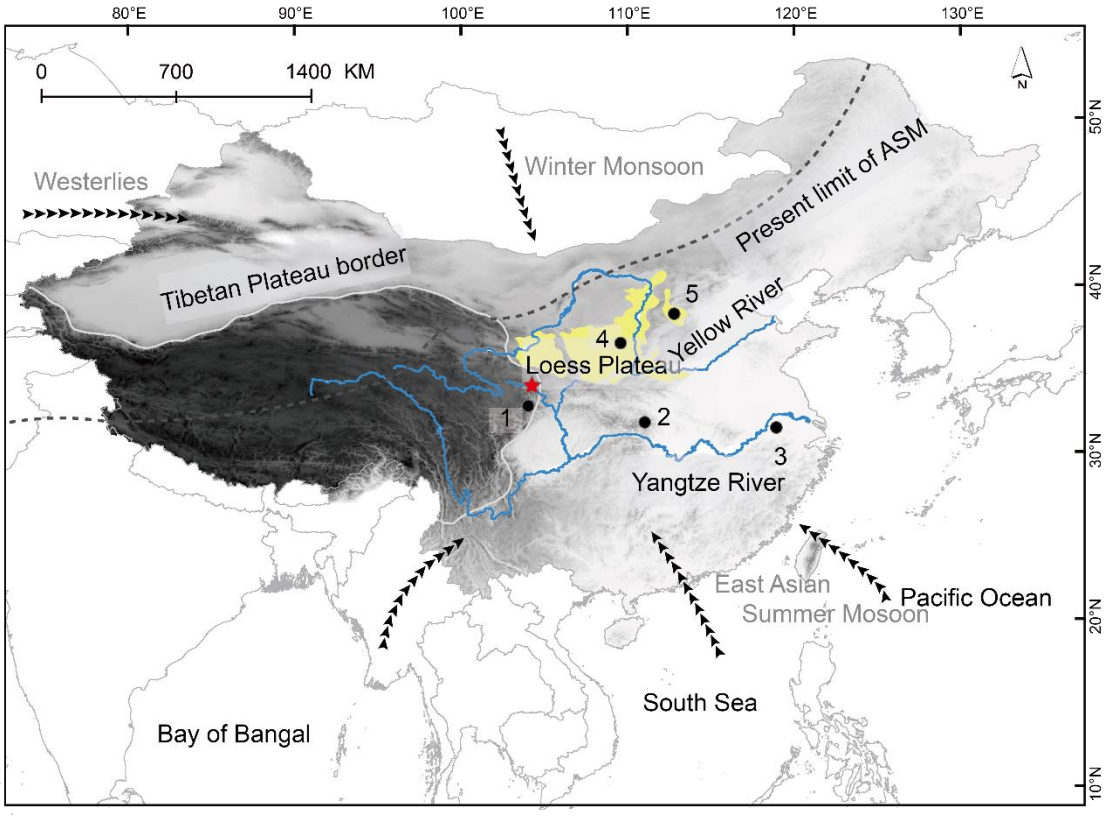

Fig. 2.10. Present climatic conditions of the Bailong River. The red star shows the location of the Bailong River. The dashed arrows show modern wind patterns. The blue lines show the two major rivers of China. The area shaded in yellow denotes the Chinese Loess Plateau. The dashed black line shows the modern northern limit of the Asian Summer Monsoon (ASM). The filled dots show the location of the climatic records mentioned below: 1 = Wanxiang Cave, 2 = Sanbao Cave, 3 = Hulu Cave, 4 = Luochuan, and 5 = Gonghai Lake. The wind direction and the present northern limit of ASM are from Railsback et al. (2014).

In addition to the impact of regional climatic systems, orographic effects on rainfall distribution have been reported by a number of researchers (Zhang et al., 2011; Bai et al., 2014). The annual precipitation has been reported by Bai et al. (2014) as varying from 400 mm in the low elevation Bailong River valley to around 600 mm in the mountains above 2000 m.

A rainfall gauge was established at the mouth of GLP, which recorded the rainfall

events from 2012 to 2014 (Fig. 2.11). The total rainfall for 2012 and 2013 is 511 and 480 mm respectively of which 88% and 86% fell between May and October. This precipitation record follows the general precipitation pattern of the Bailong River.

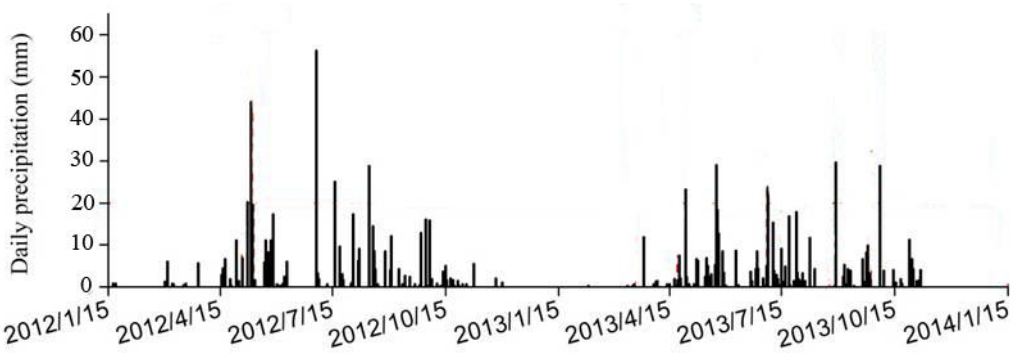

Fig. 2.11. Daily rainfall record between 2012 and 2014. The data was compiled by Dr. Muqi Xiong from Lanzhou University.

2.4.2 Paleoclimate

This section firstly introduces the long-term evolution pattern of the paleoclimate in the study area. The aim is to provide a general sense of the characteristics of the climate of the area and its relationship to the global climate. There are currently no continuous long-term climatic index records available within the watershed of the Bailong River, and so the long-term climatic history of the region is inferred from nearby sites with well-established climatic indexes. These include the loess-paleosol sequence in Luochuan (Balsam et al., 2004), the composite speleothem records from Sanbao Cave and Hulu Cave (Wang et al., 2008) and the pollen-based precipitation records from Gonghai Lake (Chen et al., 2015). The loess-paleosol sequence from Luochuan (Balsam et al., 2004) covers the whole Quaternary period, the speleothem records (Wang et al., 2008) cover a

period of 22.4 ka, and the lacustrine records (Chen et al., 2015) cover a period of 14.7 ka. Secondly, local climatic proxies including some short-period speleothem records from Wanxiang Cave (Johnson et al., 2006; Zhang et al., 2008; Railsback et al., 2014) and pollen records (Li et al., 1988) which are close to the watershed of the Bailong River are summarized. The aim is to highlight the particularity of the climate in the area.

2.4.2.1 Long-term climatic records.

1) **Loess-paleosol sequence in Luochuan.** The loess profile in Luochuan is provided in Fig. 2.12. The loess component is silt-sized material transported and deposited by the northerly winter monsoon, while the paleosols develop in this material under the southerly moisture-bearing summer monsoon (An et., 1990). The alterations between loess and paleosol sequences indicate the dominance between the summer monsoon and the winter monsoon. In Fig. 2.12, loess layers are designated as L and paleosols as S. S0 is the soil layer developed in Holocene. L1 (up to 10 m thick) is the loess layer developed in the last glacial period, equivalent to period between MIS 4 and MIS 2 (Kukla, 1987); S1 is the paleosol developed in the last interglacial period and is equivalent to the period of MIS 5. Along with the loess-paleosol sequence is the magnetic susceptibility (MS) record. The MS is associated with the ultrafine magnetic minerals, such as hematite and goethite, which are formed under warm-humid conditions. Consequently, the change of the MS values indicates the change of the climates, with increased MS indicating a predominantly warm wet condition. The MS record of the Luochuan profile has been compared with the oxygen-isotope oscillations in the oceans (Heller

and Liu, 1982; Kukla et al., 1988) indicating a synchronized pattern of climatic change, and this synchronization of climatic change suggests that the climate in China is controlled by the general circulations of the North Hemisphere.

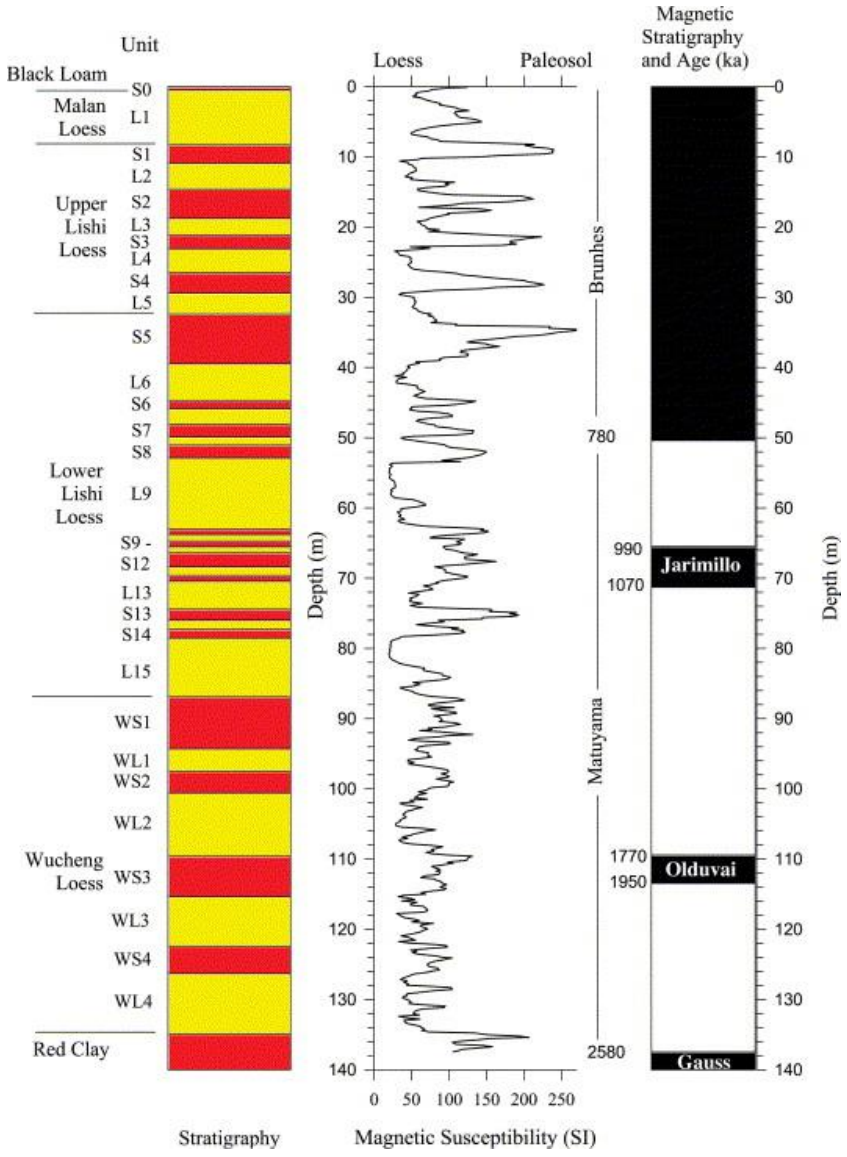

Fig. 2.12. Stratigraphy, magnetic susceptibility and magnetic reversals of the Luochuan section. After Balsam et al. (2004), their Fig. 2.

2) **Composite speleothem records from Sanbao & Hulu Cave.** The $\delta^{18}O$ records measured from speleothems have been interpreted as a

representation of the strength of the Asian Summer Monsoon (Wang et al., 2008). The advantage of the speleothem records lies in the fact that they can be precisely dated using the uranium-series disequilibrium (U-series) methods (Johnson et al., 2006). A composite speleothem $\delta^{18}O$ record from Sanbao Cave (black curve) and Hulu Cave (grey curve) is displayed in Fig. 2.13a and covers the past 22.4 ka (Wang et al., 2008). This record indicates that the monsoon cycle has been associated with the changes in Northern Hemisphere mid-latitude summer insolation on orbital time scales (Wang et al., 2008).

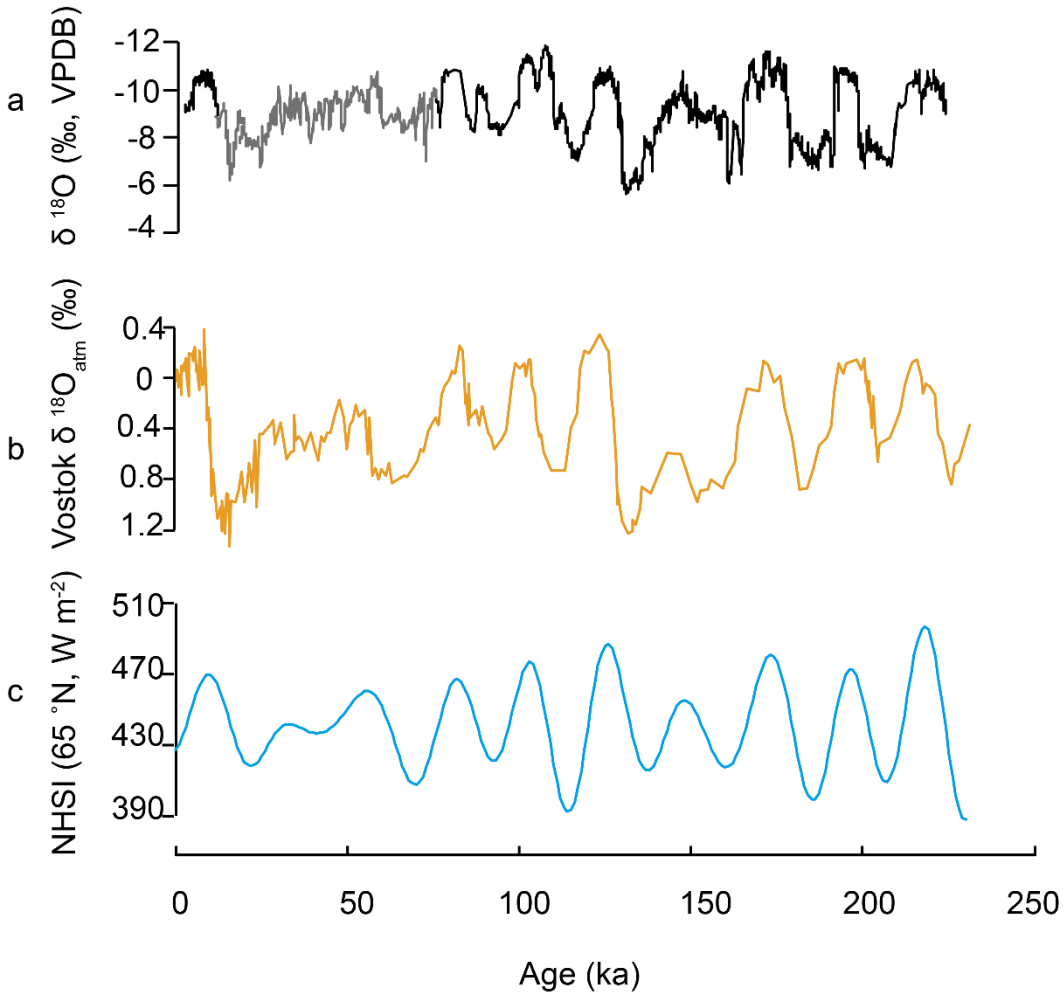

Fig. 2.13. Comparison of Sanbao/Hulu $\delta^{18}O$ records with NHSI (Northern Hemisphere summer insolation) and atmospheric $\delta^{18}O$ over the past 224 ka. a. Time versus Sanbao speleothem $\delta^{18}O$ records (black) and Hulu speleothem $\delta^{18}O$ records (grey). After Wang et al (2008). b. Time versus the atmospheric $\delta^{18}O$ record from Vostok ice core, Antarctica. After Petit et al (1999). c. Time versus NHSI, 21 July at 65 ˚N. After Berger and Loute (1991).

3) **Pollen-constructed rainfall records from Gonghai Lake.** Though the speleothem $\delta^{18}O$ records have high-precision age controls, its climatic indication has been contested recently (Liu et al., 2017) because they do not have satisfactory correlations with precipitations, which are considered as a major index of the Asian Summer Monsoon. In contrast, modern pollen records have been compared with gauge-measured precipitation (Chen et al., 2015), and are considered as a good indicator of the monsoon strength. Chen et al. (2015) produced a well-dated ~20-y-resolution, pollen-based precipitation record from Gonghai Lake in Northern China (Fig. 2.14). Although the precipitation records, which were reconstructed based on transfer-functions, may subject to certain potential pitfalls (Telford and Birks, 2011), the strength of the East Asian Summer Monsoon (EASM) suggested by this record is consistent with the records of the paleosol development (Wang et al., 2014) and the aeolian deposits (Li et al., 2014) in Northern China, indicating that the precipitation record by Chen et al. (2015) may be a satisfactory indicator of the EASM strength. This pollen-based record (Fig. 2.14a) suggests a gradually intensifying monsoon during the early Holocene (14.7-7.0 ka) and a maximum monsoon during the mid-Holocene (~7.8-5.3 ka). In contrast, the speleothem record (Fig. 2.14b) shows a maximum monsoon since the early Holocene.

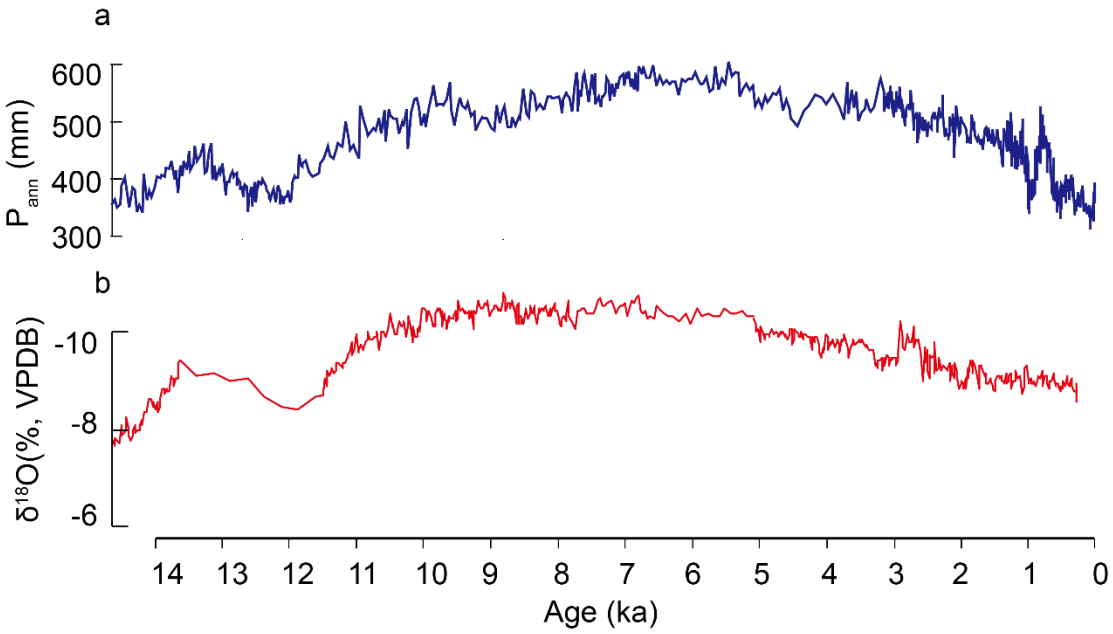

Fig. 2.14. Climatic records after Last Deglaciation. a. Pollen-based precipitation records from Gonghai Lake (Chen et al., 2015). b. Sanbao speleothem $\delta^{18}O$ records (Wang et al., 2008).

2.4.2.2 Local climatic records

1) Speleothem records from Wanxiang Cave. Within the watershed of the Bailong River, several intermittent speleothem records have been provided from Wanxiang Cave (near Wudu). These records were provided by Johnson et al. (2006) who examined the climatic conditions in the period MIS 5d-5a, by Zhang et al. (2008) who focused on the last 1810 years, and by Railsback et al. (2014) who focused on Penultimate Glacial Maximum (149 – 140 ka). Both Railsback et al. (2014) and Johnson et al. (2006) found that the climatic conditions, inferred from either the growth rate of stalagmites or the $\delta^{18}O$ values, were wetter than as is suggested by the global climatic records such as the benthic and the ice-sheet $\delta^{18}O$ records during these periods. For example, Johnson et al (2006) found that the transition from MIS 5b–5a (90 – 79 ka) was exceptionally favorable for the growth of stalagmites, and that the $\delta^{18}O$ value decreased sharply during the

period indicating a sharp increase of the summer monsoon at that time. However, the global climatic records such as the $\delta^{18}O$ values from ice cores and the N 65° summer insolation during the corresponding period do not show such a sharp change. Railsback et al. (2014) found an exceptionally wet condition during the Penultimate Glacial Maximum (MIS 6b). They attributed the exceptional moisture conditions to contributions from the Westerlies because they thought that the Westerlies at that time attached to the study area due to the southward shift of the Siberian High and transported more moisture than that at present. The wetter condition of the Westerlies during the PGM was inferred from the elevated level of Lake Lisan during the Last Glacial Maximum.

2) Pollen records. Li et al. (1988) summarized the climatic conditions in the late Pleistocene period based on pollen records and animal fossils, and they classified the climate near the study area into three types.

a) Full-glacial monsoon pattern characterized by dry and cold conditions and steppe landscape.
b) Interglacial monsoon pattern featuring a humid and warm condition and a forest or forest steppe landscape with the growth of broad-leaved trees such as Betula and Quercus, as well as coniferous trees such as Pinus.
c) Transitional or interstadial monsoon pattern characterized by a combination of glacial cold and interglacial humidity. The landscape is covered by coniferous forest and steppe with a lack of broad-leaved trees.

Chapter 3 Methodology

3.1 Introduction

The aim of this chapter is to elaborate on the methods that were adopted in this study. These methods include: (1) field mapping of alluvial terraces, supplemented by geomorphic analyses using a LiDAR (Light Detection And Ranging) DEM (Digital Elevation Model), (2) sedimentary logging of terrace outcrops, (3) borehole drill on the present channel and core sediment description, and (4) optically stimulated luminescence (OSL) dating of alluvial sediments and loess.

3.2 Field mapping of alluvial terraces and geomorphic analyses of terrace characteristics using a LiDAR DEM

3.2.1 Field mapping

Field mapping, aided by remotely-sensed images, has been a common method in the research of alluvial landforms (e.g., Viseras et al., 2003; Al-Farraj and Harvey, 2005; Owen et al., 2006; Meetei et al., 2007; Pope et al., 2008; Spelz et al., 2008; Chakrabarti Goswami et al., 2013; Owen et al., 2014). This study adopted this method to map the alluvial terraces in GLP. During my fieldwork in 2014, I used a China Resource Satellite image (Appendix 3.1, Fig. A3.1) to aid field mapping. It was scaled into 1:10000 and printed out onto several A4-sized paper sheets. The boundaries of alluvial terraces were drawn on these printed sheets in the field. The thickness of terraces was measured at the same time using a laser range finder (model PKI 3100) and a measuring tape. Alluvial

terraces with similar exposed thickness or grading at the same surface (Bull, 1991, 2000) were classified as one level. The results of this field mapping were drawn onto a polygon file in the ArcMap environment, and the boundaries of each terrace were revised further by referring to a UAV (Unmanned Aerial Vehicle) image (Appendix 3.1, Fig. A3.2) of the valley. These steps finally produced the distribution map of alluvial terraces of the GLP valley.

3.2.2 Geomorphic analyses using a LiDAR image

LiDAR (i.e. Light Detection And Ranging) images provide high-resolution topographical data, which have been widely used in extracting geomorphic parameters (e.g., Staley et al., 2006; Frankel et al., 2007b; Cavalli and Marchi, 2008; Jaboyedoff et al., 2012; Blasone et al., 2014; Qiao et al., 2017). In this study, I used a terrestrial-based LiDAR system (Riegle LPM-321 Long Range Scanner) to obtain the topographic information of the valley. This system works by emitting and receiving laser beams towards an object. The position of the object is recorded by computing the distance between the scanner and the object. The scanner was connected to a Trimble GPS to measure its geographic location. This allows data obtained from different scanning locations to be matched and merged to provide a full image of the study area. The spatial resolution of the data is determined by the distance between the scanner and the object. The LiDAR data presented in this chapter were obtained by me and colleagues at Lanzhou University in May 2012 and cover the majority of the valley. The measured data were exported into an ASCII file which was imported later into ArcGIS, version 10.2, and a TIN (Triangulated Irregular Network) file was generated accordingly (Fig. 3.1). In Fig. 3.1, the TIN has a relatively high

resolution in the midstream and downstream portions of the valley, mostly between one to two meters, which is sufficient for distinguishing terrace levels, whereas the resolution of the upstream portion of the valley is rather low due to a lack of scanning positions in this portion (Fig. 3.1). Based on this TIN image and the derived grid-based DEM, three important geomorphic features of alluvial terraces, i.e. sediment volume, longitudinal profiles, and cross-section profiles, were extracted using the spatial analyst tools of ArcGIS 10.2.

To facilitate the description of alluvial terraces, the valley was divided into three sections: upstream, midstream and downstream (Fig. 3.1). The upstream section refers to the limestone headwaters of the GLP valley, and it is bounded in its downstream end by the reverse fault of the GLP valley. The upstream section is comparable to an initiation zone which provides clastic materials and potential energies for debris flows. The average slope in the upstream area is 36˚, and hillslopes are prone to debris avalanches, slumps or rock falls. The midstream section is defined by the reverse fault at its upstream end and the place where the flow starts to be unconfined at its downstream end. Likewise, the midstream is comparable to a transport zone where well-developed channels form. The downstream section of the valley is the remaining section where flows form fan-shaped sediment bodies.

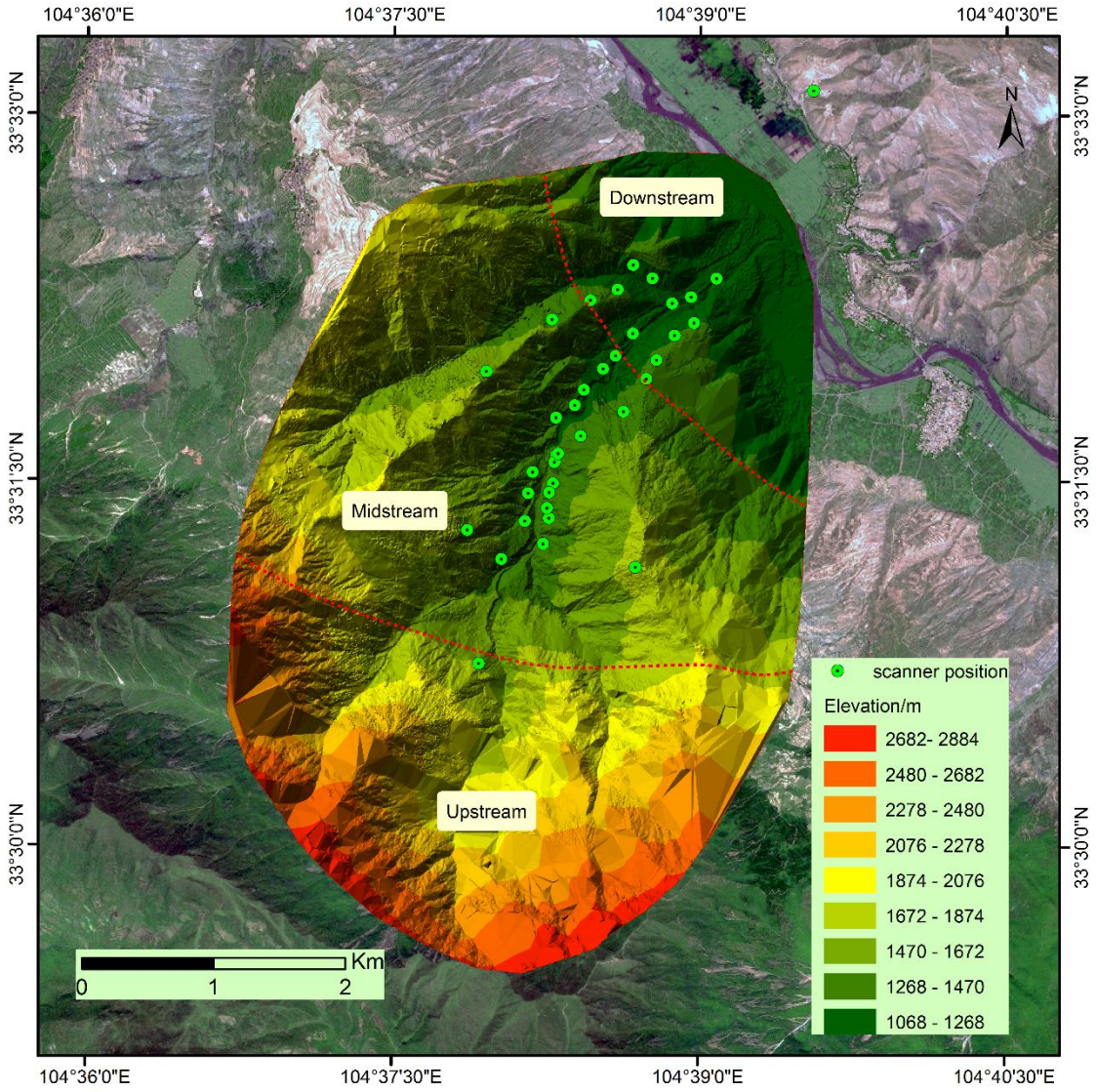

Fig. 3.1. TIN (triangulated irregular network) of the GLP valley, obtained using a terrestrial LiDAR system. Dashed red lines separate the channel into downstream, midstream and upstream sections. The background image is a SPOT image.

1) Sediment volume

Sediment volume is an important factor that reflects sediment storage and erosion in a catchment (Trimble, 1983; Oguchi, 1997; Van Balen et al., 2000; Hinderer, 2012; Jolivet et al., 2014)**.** The key step in calculating sediment volume is to determine the sediment thickness by estimating the elevations of the base and the top of the sediment body (Fischer, 2009; Djuric et al., 2011). The sediment volume is then obtained as the product of cell area and thickness. This can be

conducted solely using the “polygon volume” tool of the 3D Analyst toolboxes in ArcGIS 10.2, where the base plane is taken as a horizontal flat plane (Fig. 3.2). For terraces without exposed phyllite bedrocks (Fig. 3.2, Terrace 1), the base plane is taken as the level of the nearby channel, while for terraces with exposed bedrock channels (Fig. 3.2, Terrace 2), the base plane is taken as the level of the exposed bedrock.

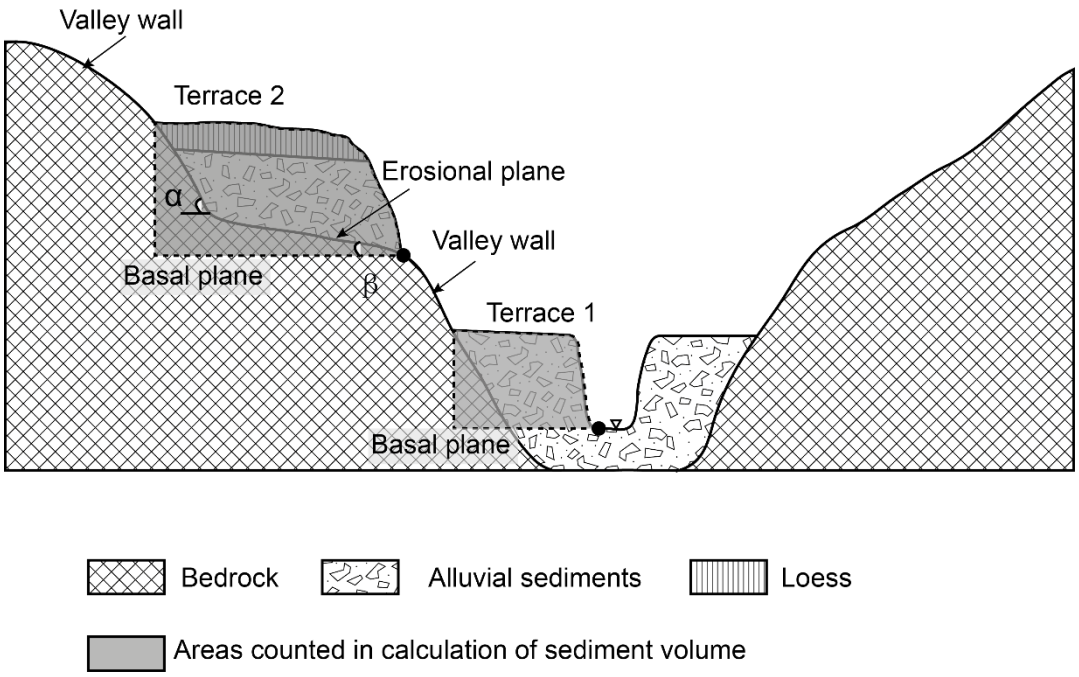

Fig. 3.2. A 2-D schematic sketch illustrating the cross-sectional area (shaded in grey) that is counted in the calculation of sediment volume in ArcGIS. For Terrace 2 (with exposed bedrock), a horizontal plane at the level of the sediment-bedrock contact was drawn to calculate the sediment volume. For Terrace 1, the horizontal basal plane was taken as the level of the present channel floor.

This method gives an over-estimate of the sediment volumes for each terrace, with the over-estimated part due to the dips of the erosional plane and the valley wall (Fig. 3.2). Steep valley walls (large α value in Fig. 3.2) and flat erosional planes (small β value in Fig. 3.2) will lead to small over-estimations of the

sediment volume. As the sediment volumes for different terrace levels (see Table 4.1 later) vary by orders of magnitude, far greater than any overestimations, this accuracy level of the calculated sediment volume is not a limiting factor in the study.

2) Longitudinal profiles

Longitudinal profiles, or radial profiles, in alluvial fans and river channels, are important features that reflect sediment size, water discharge, and watershed evolution (Gilbert, 1877; Blair and McPherson, 1994; Sinha and Parker, 1996; Pazzaglia et al., 1998; Kirby and Whipple, 2001). In this study, the longitudinal profiles of the surface of each terrace level, as well as the major channel, were obtained using the standard procedures in ArcGIS 10.2. The procedure is as follows: (1) A polyline representing the major channel was firstly extracted from the DEM by using the 'Hydrology Analyst' toolset in ArcMap. (2) The vertices of the polyline were then exported to a point file by using the 'feature vertices to points" tool. This created a series of points along the channel. (3) Elevation information was attached to these points using the 'extracting values to points' tool. (4) The distance to the valley divides of each point was calculated in Excel based on their geographic coordinates. (5) The longitudinal profile was generated based on the elevation and distance to the valley divides. Determination of the longitudinal profiles of the terrace surfaces followed a similar procedure, except that in step (1) the profile line was drawn manually following the flow direction on the terrace surface.

3) Cross-valley profiles

Cross-valley profiles have been used to represent valley erosional processes and evolution (Rosgen, 1994; Montgomery, 2002; Marston et al., 2011). They are useful sketches for illustrating the spatial relationships between different landforms or geologic units (e.g., Kirby et al., 2000; Wang et al., 2009; Vandenberghe et al., 2011; Bridgland and Westaway, 2014; Huang et al., 2014; He et al., 2015b). The cross-sectional profiles along the major channel were used to compare the relative height of different levels of alluvial terraces. These were extracted using the 3D Analyst toolbars in ArcGIS 10.2.

3.3 Sedimentary logging of terrace outcrops

Sedimentary logging of outcrops is a common method in the study of alluvial fans or river terraces (e.g., Kar et al., 2014; Owen et al., 2014; Parton et al., 2015; Chen et al., 2017) and was adopted in this study.

3.3.1 Descriptive sedimentary characteristics

Considering the general sedimentology of slope deposits in the study area, i.e. coarse gravel-sized clasts, most of the measurements and descriptions have been carried out in the field. Therefore, convenient and effective field descriptive standards were adopted in the study. The following sedimentary features have been recorded: lithological composition, roundness, sorting, grain size, fabric, and sedimentary structures (bedding, grading and texture).

1) Lithological composition

Lithological composition, i.e., the types of rocks that make up the sediment, is key to reveal sediment provenance (Briggs, 1977; Nichols, 2009). The lithological

composition in a sediment body is mainly dependent on the range of bedrocks in the source area of the sediment. Within the watershed of the GLP valley, bedrocks are dominated by limestone (distributed in areas >1700 m) and phyllite (distributed in areas between 1000–1700 m), associated with some quartz dykes intruded into the bedrock. It is expected that these three types of rock, i.e. limestone, phyllite and quartzite, would dominate the sediment lithology within the GLP valley. However, at the mouth of the GLP valley where sediments transported by the Bailong River occur, some exotic sediments are also expected. In the field, the lithological composition of sediments was determined by randomly picking 50 clasts and recording the number of observations of each different lithology. However, this method only applies to the lower sections of terrace outcrops. For terrace profiles higher than 3 m, the determination of lithology was based on visual estimation, due largely to difficulties with access. This visual estimation applies to the sediments that have one or two types of lithologies accounting for the majority of the sediments, which is the case in the GLP valley. However, this method may not be suitable to sediments with a variety of lithological types accounting for similar portions.

2) Grain size

Grain size distribution, which contains information about the processes of erosion, transport and deposition that have deposited the sediments (Briggs, 1977; Evans and Benn, 2004), is a key parameter in sedimentary analyses. Because of the variable ranges of grain sizes in natural environments, as well as the distinct objectives in different research, the measurement method and expression of grain size distributions vary (Tucker, 1988; Hoey, 2004). For coarse gravel

sediments, the grain size of a sedimentary unit is usually expressed using the maximum grain size or the modal grain size (Tucker, 1988). Because the sediments in the study area are generally poorly-sorted pebble- to cobble-sized clasts, many of which stand high in their exposure cliffs and hence are inaccessible, a qualitative descriptive method of the grain sizes was adopted. In the field, the modal grain size for a sedimentary unit was determined based on visual estimation aided by a ruler, and the unit was then described using the grain size categories proposed by Wentworth (1994) (Table. 3.1). This method may be subject to some biases regarding estimating the dominant grain sizes of a sedimentary body. Whereas considering the large ranges of each individual size category (e.g., granule, pebble, cobble and boulder), the biases may be not a problem here.

Table 3.1. Size scale after Wentworth (1922) and Friedman and Sanders (1978).

phi	mm	Wentworth (1922)	Friedman and Sanders (1978))
			Large boulders
-10	1024		
		Boulders	Medium boulders
-9	512		
			Small boulders
-8	256		
			Large cobbles
-7	128	Cobbles	
			Small cobbles
-6	64		
			Very coarse pebbles
-5	32		
		Pebbles	Coarse pebbles
-4	16		
			Medium pebbles
-3	8		
			Fine pebbles
-2	4		
		Granules	Very fine pebbles
-1	2		
		Very coarse sand	Very coarse sand
0	1		
	microns	Coarse sand	Coarse sand
1	500		
		Medium sand	Medium sand
2	250		
		Fine sand	Fine sand
3	125		
		Very fine sand	Very fine sand
4	63		
			Silt
9	2		
			Clay

Apart from the visual estimation of the modal grain sizes, some attempts (i.e., image measurement and sieving) were also carried out to obtain more detailed grain size distributions. Image analyses, which have been widely applied in clastic sediments (e.g., Francus, 1998; Buscombe, 2008; Baptista et al., 2012; Graham et al., 2012), were conducted for sections with good accessibility and clear exposures. In the study, well-exposed profiles were photographed (with referenced scales) using a Canon camera (EOS 550D). The lengths of the a-axes

of gravel-sized clasts were measured (Fig. 3.3) in the software “Nano measurer 1.2”, which was originally developed for grain size analyses of SEM（Scanning Electron Microscope）images by Jie Xu in the Department of Chemistry in Fudan University, China. The software finally produces a frequency distribution of grain size ranges.

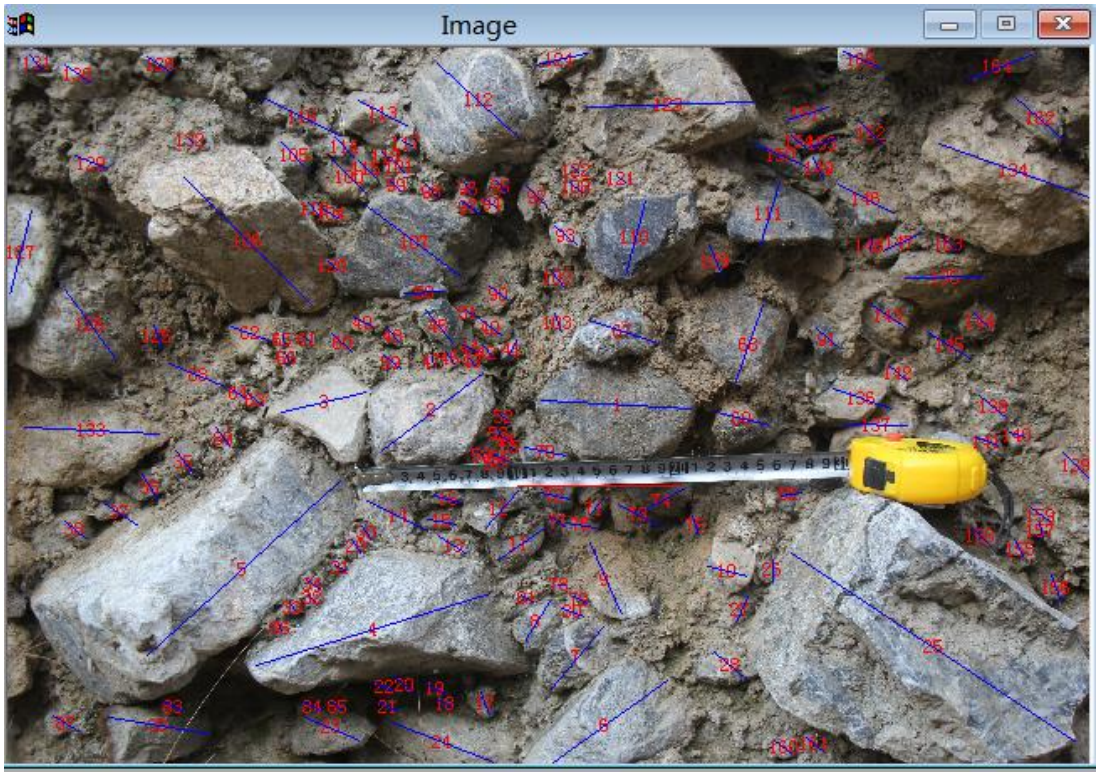

Fig. 3.3. An example of image interpretation of grain size distributions using the “Nano measurer 1.2” software. The a-axes of clasts were measured.

In some cases, the sieving method was used to obtain information on grain size distribution. The sieving equipment includes a series of sieves which have different mesh sizes (i.e., 60, 40, 20, 10, 5, 2, 1, 0.5 mm), a lid and a pan balance. Two to 10 kg of sediment from each sample was sieved through these meshes sequentially from larger meshes to smaller ones. The deposits retained on each sieve were then weighed and recorded. However, the practical setting of the

terraces in GLP (i.e., high cliff terrace outcrops and highly compact coarse sediments) makes it impossible to take enough samples to obtain reproducible and statistically meaningful grain size parameters (Hoey, 2004), and these sieving results are only provided as supplementary materials.

3) Roundness

The roundness of a particle measures the curvature of the corners and edges of clasts (Briggs, 1977; Benn, 2004). Clast roundness is affected by processes such as abrasion and wear during transportation and can partly reflect both the transport mechanism and transportation distances (Briggs, 1977; Benn, 2004; Lukas et al., 2013). In fluvial or alluvial environments, roundness has been commonly used to differentiate sediment provenance and transport distances (e.g., Mills, 1979; Lindsey et al., 2007; Roussillon et al., 2009; Tamrakar, 2009; Takahashi and Sugai, 2017). Both qualitative and quantitative methods exist in the measurement of roundness (Wadell, 1932; Krumbein, 1941; Powers, 1953; Orford and Whalley, 1991; Blott and Pye, 2008; Roussillon et al., 2009; Lukas et al., 2013). In fluvial or alluvial environments, the six categories of roundness invented by Powers (1953) have been a common way of describing roundness (Sengupta, 2007; Wilson et al., 2007; Blott and Pye, 2008; Ghazi and Mountney, 2011) and were adopted in this study. This way of clast roundness description is quick and easy in the field, though comparison between the roundness chart (Fig. 3.4) and each individual clast can be subjective.

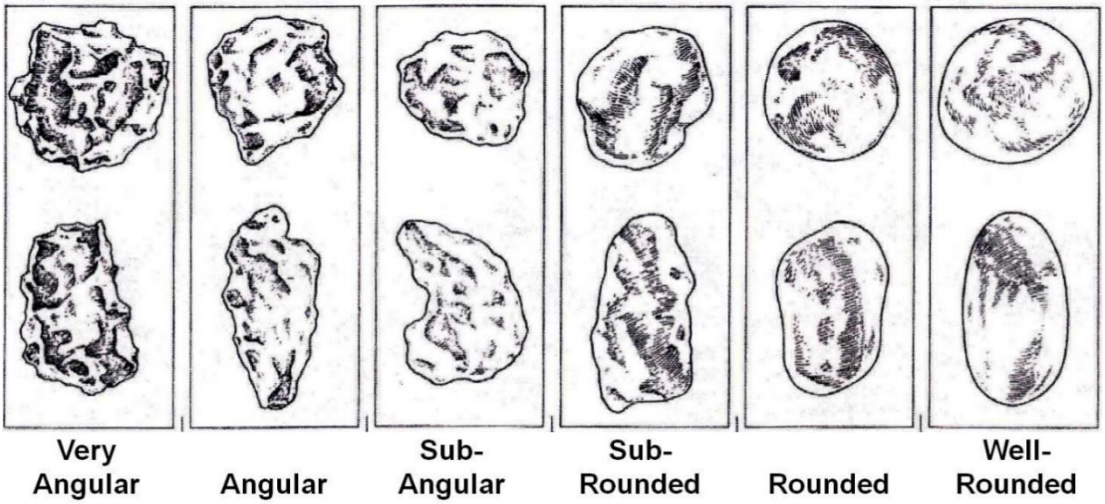

Fig. 3.4. Powers' scale of roundness. After Powers (1953).

4) Sorting

Sorting is represented by the standard deviation in grain size distribution (Briggs, 1977) and reflects the range of grain sizes that occur within a sedimentary deposit (Perry and Taylor, 2007). For gravel-sized sediments, the common method in describing sorting is to compare the sedimentary body with the standard sorting chart (Fig. 3.5) which was invented by Compton (1962) and has been used by many (e.g., Tucker, 1988; Perry and Taylor, 2007). This method was adopted in this study.

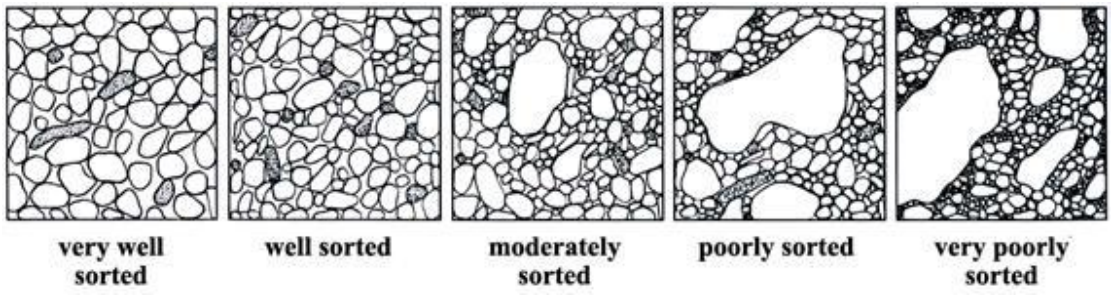

Fig. 3.5. Standard chart for sorting criteria. After Compton (1962).

5) Fabric: dip and orientation

Fabric describes the three-dimensional disposition of an individual clast (Briggs,

1977; Collinson et al., 2006). For a clast with a long axis (termed the a-axis), a short axis (termed the c–axis) and an intermediate axis (termed the b-axis), the dip and orientation of the a-b plane along either a- or b-axes are used to represent the fabric of the clast. There are two common representations of clast fabrics in fluvial environments: a (t) b (i) representing a clast with its a-axis transverse to its flow direction and its b-axis imbricated, and a (p) a (i) representing a clast with its a-axis parallel to its flow direction and its a-axis imbricated (Postma et al., 1988).

The fabric has been commonly used to distinguish the primary mode of emplacement and transport direction (Major, 1997). A strong clast fabric is suggested when the majority of the clasts are oriented similarly, a weak but detectable clast fabric is indicated by a limited number of similarly oriented particles, and an undeveloped clast fabric occurs when particles are oriented randomly. Usually, a strong, well-developed fabric suggests that particles moved freely from each other and were selectively deposited (Todd, 1996; Jo et al., 1997). In these cases, long axes are usually oriented perpendicular to flow direction due to the protracted rolling of clasts about the long axis, forming a (t) b (i) fabrics, whereas a relatively weakly developed fabric usually indicates rapid deposition from concentrated flows with frequent grain-grain collisions. Under this condition, the long axes are usually oriented parallel to the flow direction forming a (p) a (i) fabrics (Rees, 1968; Todd, 1996). To obtain a statistically valid representation of the distribution of clast fabrics, a large number of clasts should be measured. A minimum number of 25 has been suggested (Mark, 1973). In this study, clast fabrics were measured for outcrops with good exposure and accessibility. For each individual unit which was chosen for fabric measurement ,

40 measurements were conducted in this study. In some sections with a lack of measurable clasts, the numbers of clasts used for fabric measurement were reduced to 20-10.

6) Sedimentary structures

In addition to the sedimentary characteristics described above, internal bedding, grading and texture (i.e., whether a sediment is matrix-supported or clast-supported) (Collinson et al., 2006), were also recorded during field logging.

3.3.2 Lithofacies codes and lithofacies associations

To facilitate the sedimentary descriptions, sediments with similar characteristics were denoted using specific lithofacies codes (Evans and Benn, 2004; Miall, 2006). There have been two ways of coding sediments. The most commonly used one follows Miall (1978)'s method in which sediment is coded using a capital letter to indicate the dominant grain size (e.g., G=gravel, S=sand, F=fine grained sediment) and lowercase letters to denote the sedimentary structures or textures (e.g., p=planar cross-bedding, ms=matrix-supported) (Miall, 1977, 2006; Evans and Benn, 2004; Neves et al., 2005; Makhlouf et al., 2010; Colombera and Bersezio, 2011; Dutta et al., 2012; Lukas et al., 2012). A second way is to code facies using numbers or letters following sequential or alphabetical orders (Luzón, 2005; Went, 2005; Suresh et al., 2007; Shukla, 2009; Sinha et al., 2010). The code itself does not have a relationship with the physical characteristics of sediments. This method lacks a consistent nomenclature system worldwide, making comparison between different sites difficult, though the sedimentary characteristics of each facies are usually given more detailed description than the

first way of coding (Bridge, 1993). This study used Miall (2006)'s standard lithofacies codes to annotate each sedimentary unit because this version of lithofacies codes is an updated version of the old version (Miall, 1978) and has coded sediments following a more consistent rule that makes the code easier to understand. However, when annotating sediments using the existing lithofacies codes (Miall, 2006), it is found that the codes themselves cannot reflect the complex sedimentary features of the sediments in the study area. Two extra features were used to further distinguish the sediments: (1) lithology composition and (2) clast roundness. The types of clast lithologies present in the GLP valley mainly include limestones, phyllites and quartzites. For most sections examined, limestones form the majority part (> 50% volume) of the sediment body, and these sediments were coded using Miall (2006)'s standard code to refer exclusively to sedimentary units with a dominant proportion of limestone clasts. For sediments where phyllite clasts form the primary part (> 50% volume), a bracketed 'p' was added after the standard lithofacies code. For example, Gh (p) refers to phyllite dominated horizontally bedded gravels. For most sediments which consist of only limestone and phyllite with a small proportion of quartzite, the clasts are generally sub-angular to sub-rounded. However, for sediments which contain some exotic sandstone or granite clasts, the clasts are mostly rounded to well rounded. These sediments are all distributed close to the Bailong River. To differentiate these rounded clasts with those sub-angular to sub-rounded clasts, a bracketed "r" is added after the standard code. For example, the code Gh (r) refers to rounded to well rounded crudely bedded pebbly clasts with sandstones and granites.

A further distinction was also made for horizontally stratified sediments (Gh).

According to Miall (2006), the Gh sediment refers to horizontally crudely bedded gravels. However, in the GLP valley, there are some moderately sorted gravels with distinct horizontal stratifications. Therefore, a Gh' was introduced to annotate these sediments. Likewise, an Fm' code was used to denote thick (> 50 cm) fine silt which is relatively more homogeneous than the Fm sediment. Overall, new lithofacies codes including Gh', Gh (p), Gh (r) and Gh (r)' were introduced in the study. Table 3.2 presents all types of lithofacies and the corresponding features that were identified in the study.

Table 3.2. Lithofacies types identified in the GLP valley. The meaning of abbreviations: SA-SR = Sub-angular to Sub-rounded; R-WR = Rounded to Well Rounded. The meaning of lithofacies codes follows Miall (2006). Fabric a (p) means that the a-axis of a clast is parallel to the flow direction. Fabric a (t) b (i) means that the a-axis of a clast is transverse to the flow direction and the b-axis is imbricated.

Broad types		Lithofacies codes	Characteristics
Gravelly Facies	SA-SR	Gh	Poorly-sorted, clast-supported granule to cobble clasts with silty or sandy matrix. Clasts are ungraded and crudely bedded. a (p) fabrics, limestone dominated.
		Gh’	Moderately- / poorly-sorted, cobble to granule clasts with sandy matrix and distinct horizontal stratification. a(t) b(i) fabric, limestone dominated.
		Gh (p)	Moderately- / poorly- sorted, pebble to granule clasts with silty or sandy matrix and horizontal stratification. a(t) b(i) fabric, phyllite dominated.
		Gcm	Poorly-sorted, clast-supported cobble to granule clasts. Clasts are generally ungraded, but locally, especially in the mid of the bed, some larger clasts are supported by smaller clasts, weak a (p) fabric, limestone dominated.
		Gci	Poorly-sorted, clast-supported granule to cobble clasts with inverse grading, a(p) fabric, limestone dominated
		Gmm	Poorly-sorted, silty-matrix-supported granule to cobble clasts. Coarse tail normal grading or ungraded, a (p) fabric, limestone dominated.
	R-WR	Gh (r)’	Well sorted, well-bedded, granule to cobble clasts with sandy matrix. a(t) b(i) fabric. Except limestone and phyllite, sandstones and granites are also present.
		Gh (r)	Poorly sorted clast-supported pebble to cobble clasts with sandy to silty matrix. a (p) fabric, crudely bedded. Except limestone and phyllite, sandstones and granites are also present.
Fine facies		Sh	Horizontally laminated coarse to fine sand
		Fm	Silt and clay, thin (10-20 cm), intermittent, irregular base and flat top, with some gravels.
		Fm’	Relatively homogenous thick silt and clay with plant roots or voids, sometimes with some gravels.

Different lithofacies generally reveal certain types of depositional processes which may be present in a variety of depositional environments (Allen, 1983; Miall, 1985). Therefore, it is necessary to group specific types of lithofacies that have physical similarities to interpret a depositional environment (Evans and Benn,

2004). In this study, lithofacies are grouped into lithofacies associations (LFA) based on physical similarities and the nature of contact between individual lithofacies (Miall, 1985; Evans and Benn, 2004) to examine the depositional environment.

3.4 Borehole drill and core sediment description

As a key study area of a well-funded project (the Chinese national sci-tech support project aimed at hazard prevention and mitigation), four boreholes were drilled in the GLP channel in May 2013 and October 2014. An introduction of the drill equipment is presented in Appendix 3.2. Information of the positions and depths of the boreholes produces a general understanding of the depth of the incised channel. This depth information is key to understanding the history of valley aggradation and incision. Besides, the core sediments reveal invaluable information about the depositional processes occurring during the initial stages of valley filling. Sediments of two cores (i.e., D01 and D03), which were drilled during October 2014, were described in the field. However, sedimentary description of the other two cores (i.e., D02 and D04), which were drilled during 2013, was not recorded because no sediments were preserved. The features that were recorded include lithology, roundness, sorting and dominant grain size, and the description of these features followed the same methods described in Section 3.3.1. For core D03, some sediments in the core section were sieved in an attempt to obtain the grain size distribution. However, this method proved to be very time-consuming in the field and provided little extra information in interpreting the depositional processes. Consequently, this method was not applied for the sediments of core D01. Again, these sieving results were only

provided as supplementary materials. Sedimentary units with common sedimentary characteristics were annotated using lithofacies codes, and groups of lithofacies codes were integrated into lithofacies associations to interpret the depositional environment. However, as the original sedimentary structures of core materials were obscured during drilling, it is difficult to annotate a given sedimentary body using the standard lithofacies codes (Miall, 2006) which usually signify certain sedimentary structures. Here, I annotated the lithofacies mainly based on the dominant grain sizes (DGS) of a given core section. Besides, some other features such as matrix types (sandy or silty), roundness, and clast lithology are also considered to differentiate sediments comprising similar dominant grain sizes.

3.5 OSL dating of sediments

Following the geomorphic and sedimentary methods, absolute dating techniques provide the ages for borehole and terrace sediments, thus establishing the time sequence for the formation of different levels of terraces and allowing comparison between the processes and the concurrent environmental conditions. Among various dating methods, the optically stimulated luminescence (OSL) technique has been widely used in alluvial and fluvial research because of a wide availability of the datable materials in these environments (e.g., Wintle, 2008; Fuchs et al., 2010; Lauer et al., 2010; Williams et al., 2010; Zhao et al., 2015; Olszak et al., 2016; Bhattacharya et al., 2017) and has been adopted in this study.

OSL dating is a chronometric technique that is commonly used to determine the time elapsed since a sedimentary grain was last exposed to sunlight (Wintle,

2008; Madsen and Murray, 2009; Mellett, 2013; Rhodes, 2011; Roberts and Lian, 2015). Since this exposure usually occurs while the grain is being transported prior to deposition at the sample site, OSL ages are usually interpreted as depositional ages(Roberts and Lian, 2015). The technique relies on the fact that sedimentary mineral grains, such as quartz and feldspar, are exposed to ionizing radiation in the natural environment. This ionizing radiation can excite electrons in the minerals from the valence band to the conduction band, from where they migrate to defects in the crystal lattice (Aitken, 1985). These electrons are said to be trapped. Because buried mineral grains are exposed to an ongoing radiation flux, the number of trapped electrons within the crystal lattices builds up with burial time, until that the crystal lattice defects are fully occupied by electrons. The amount of ionizing radiation that caused the accumulation of trapped electrons during burial is called paleo-dose. Exposure to light will release these trapped electrons, some of which can subsequently combine with luminescence centers and emit light, termed luminescence. This light exposure may occur during transportation in nature, where it releases trapped electrons accumulated during previous burial periods (often termed “bleaching”), or during carefully controlled exposure in the laboratory (optical stimulation). The OSL dating technique employs the amount of luminescence emitted during stimulation as a proxy for the trapped electron population, and therefore for the ionizing radiation dose to which the mineral grain was exposed. For a natural sample this is the ionizing radiation dose (paleo-dose) that a sediment received during burial. In the laboratory, an equivalent dose (D_e) is obtained by comparing the luminescence signals produced by known doses of laboratory radiation to the signal measured from the natural sample. Because the rate of ionizing radiation exposure (dose

rate, D_r) in most terrestrial environments is stable (Aitken, 1985), the burial time of the sediment may be determined using Equation 3.1.

$$\text{Time} = D_e / D_r \quad (3.1)$$

In this study, the Single Aliquot Regenerative-dose (SAR) protocol (Murray and Wintle, 2000) has been used to date the burial ages of quartz. Mineral grains of quartz were employed for OSL dating in this study because they have been widely used and approved as a suitable material for OSL dating in alluvial environments (Robinson et al., 2005; Rodnight et al., 2006; Chen et al., 2008; Williams et al., 2010; Kiss et al., 2014). Besides, the OSL signals of quartz are generally easier to be bleached than those of feldspar (Godfrey-Smith et al., 1988; Buylaert et al., 2012; Murray et al., 2012; Long et al., 2018). In fluvial or alluvial environments where deposition may occur after a much shorter time of transportation than that in aeolian environments, quartz minerals may have a much larger opportunity of complete bleaching before deposition than feldspar minerals. Though there have been several successful studies using feldspar to date fluvial sediments (e.g., Colarossi et al., 2015; Smedley et al., 2016), the time required for dating feldspars is generally larger than that for quartz. The adoption of fine silt-sized quartz minerals for OSL dating was because (1) quartz grains of fine-silt are generally transported as suspension load, i.e., higher in the water-column than the bedload and take longer to settle out of suspension than sand does (Lowe, 1982), and (2) fine silt-sized materials in the study area are generally of loessic origin which provides brighter luminescence signals than the locally eroded materials. Moreover, fine silt is more common than other coarser grains (i.e., sand) in the

study area and is easier to obtain.

3.5.1 Sampling protocol and pre-preparation

1) Sampling protocol

The samples used for OSL dating are classified into two types: (1) the thin (10 – 20 cm thick), laterally discontinuous silt deposits intercalated between the gravelly deposits, denoted as lithofacies Fm, and (2) the laterally continuous paleosols or loess deposits which cap the higher terraces, denoted as Fm'. The paleosols formed in loess which was deposited after or between phases of alluvial deposition. Post-depositional alteration of these deposits will have occurred due to bioturbation and pedogenic processes. In the field, samples were collected by hammering steel tubes (4 cm in diameter, and 25 cm in length) into vertical exposures. The two ends of the tubes were immediately sealed using foil, several layers of opaque plastic bags and tape. Samples from boreholes were taken by hammering a thin steel tube into the muddy layers, and these samples were subsequently sealed using the same method as described above. At some sections, the entire thickness of the core was sampled and sealed in an opaque bag.

2) Pre-preparation

The OSL samples were shipped to Royal Holloway and prepared in the Geochronology Laboratory. Samples were opened under subdued orange or red light. For samples collected by steel tubes, the sediments from either end of the tube (the outermost 5 cm in both cases) were removed and stored for water content and dose rate assessment. For sample blocks, a scalpel was used to

carefully remove the 2-cm thick outer surface. For both tube and block samples, the inner portions (i.e., those not exposed to sunlight during sampling) were then transferred to beakers and treated in the following manner:

(1) Removal of carbonate. 10% hydrochloric (HCl) acid was decanted into the samples to react with carbonate material. The sample was periodically agitated with a glass rod, and fresh acid was added to ensure the continuation of reaction. Once no visible or audible reaction was observed upon the addition of fresh acid, the sample was rinsed three times with deionized water.
(2) Removal of organic material. Following the first step, 20 vols hydrogen peroxide (H_2O_2) was decanted into the beaker to oxidize organic materials. The sample was periodically agitated with a glass rod, and fresh H_2O_2 was added until the reaction was complete. The samples were then rinsed three times with deionized water.
(3) Separation of 4-11 μm fraction. After removal of carbonate and organic matter from the samples, the 4-11 μm fraction was separated using Stokes' settling. Briefly, the sample was transferred into a plastic bottle which was then topped up to its shoulder with deionized water and a few drops of sodium hexametaphosphate dispersant. The bottle was sealed and agitated by hand so that the sediment particles were fully dispersed, following which the contents were allowed to settle for set periods of time. The shoulder of the bottles used in this procedure is 13 cm above the base, meaning that only < 4 μm grains remain in suspension after 2 hours and 31 minutes. Consequently the > 4 μm grains were extracted by repeated settling for 2 hours and 31 minutes, after which the suspended material was discarded. The <11 μm

fraction was extracted from the remaining material by repeated settling for periods of 10 minutes. The material remaining in suspension after this second settling is the 4-11 μm fraction. The settling times quoted above are for quartz (density 2.65 g/cm^3) at 20 °C. Settling times were altered to account for slower settling rates at lower temperatures.

(4) Separation of Quartz. The 4-11 μm fraction extracted in step 3 will consist of a range of minerals. To obtain pure quartz, the sample was immersed in hydrofluorosilicic acid (H_2SiF_6) for two weeks, principally to remove feldspars. The resulting material was rinsed in deionized water and then immersed in 10% HCl overnight to remove fluorite precipitates, following which they were rinsed again in deionized water.

(5) Aliquot preparation. To prepare an aliquot of 4-11 μm quartz, a 9.7 mm diameter aluminum disc was placed in a 10 mm diameter glass vial. A 1 ml pipette was used to dispense a known volume of 4-11 μm quartz suspension into the glass vial. These vials were subsequently placed in an oven at 50 °C for 48 hours, by which time the water has evaporated leaving the 4-11 μm quartz attached to the aluminum disc.

(6) Checking of feldspar contamination. The purity of the 4-11 μm quartz separate produced was tested using the IR-depletion ratio test (Duller, 2003), which allows the detection of feldspar contamination within a sample. Samples which showed feldspar contamination were subjected to a second hydrofluorosilicic acid treatment.

3.5.2 Measurement of equivalent doses (D_e)

Equivalent doses (D_e) were measured using the Single Aliquot Regenerative

dose (SAR) procedure (Table 3.3) of Murray and Wintle (2000). All measurements were performed using a Risø TL-DA-20 TL/OSL luminescence reader (Bøtter-Jensen et al., 2003). The reader utilizes a $^{90}Sr/^{90}Y$ beta source, calibrated using the method of Armitage and Bailey (2005), to perform laboratory irradiations. Optical stimulation is achieved using an array of light emitting diodes (LEDs) illuminating the sample at either 870 nm (infrared LEDs) or 470 nm (blue LEDs). Both stimulation sources were routinely operated at 90% current, giving measured power densities of 62.5 (480 nm) and 185.4 (870 nm) mW/cm^2. The OSL signal was measured using an Electron Tubes Ltd 9235QA photomultiplier tube with 7.5 mm of Hoya U-340 filter. All the samples measured in this study yield bright and rapidly decaying OSL signals (Fig. 3.6). The OSL signal was integrated from the first 0.48 s with the averaged photon counts from the last 4 s subtracted as a background. All growth curves were fitted using a saturating exponential plus linear function. The Central Age model (Galbraith and Roberts, 2012) was used to produce the D_e value for each sample. Twelve to 24 aliquots were measured for each sample. A 160 °C 10 s preheat (PH, the preheat prior to measurement of the natural or regenerated luminescence signal) paired with a 160 °C cut-heat (the preheat prior to measurement of the test dose luminescence signal) was selected for equivalent dose measurement sequences on the basis of dose recovery tests at a variety of preheat temperatures (Appendix 3.3). Before measuring the D_e values of each individual sample, a dose recovery test was conducted for that sample to ensure that the SAR regime is able to monitor the sensitivity change of the natural sample. Results of the dose recovery tests for the measured samples are presented in Table 3.4.

Table 3.3 Generalized single-aliquot regeneration sequence. After Armitage et al. (2000).

Natural dose
1. Preheat at 160 °C for 10 s, PH
2. OSL at 125 °C for 40 s, measure natural intensity, L_n.
3. Test dose (e.g. 5 Gy), D_t
4. Cut heat to 160 °C
5. OSL at 125 °C for 40 s, measure test dose intensity, T_n
6. Regeneration dose, R_x
7. Preheat for 10 s at 160 °C as in step 1
8. OSL at 125 °C for 100 s, measure regenerated intensity, L_x
9. Test dose, D_t
10. Cut heat to 160 °C
11. OSL at 125 °C for 40 s, measure test dose intensity, T_x
12. Repeat steps 6 – 12 to build up a growth curve

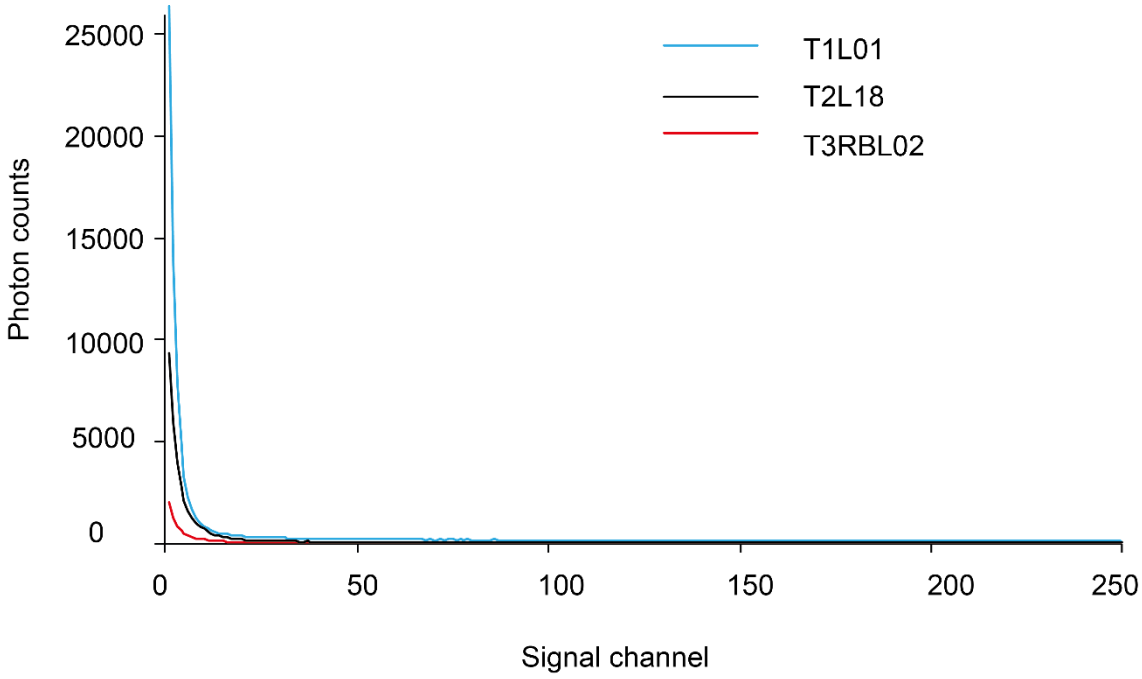

Fig. 3.6. Decaying curves of natural OSL signals for three samples. The signals were measured at the PH temperature of 160 °C. The values are averaged values of three discs.

Table 3.4. Results of dose recovery tests performed on the samples measured in the study.

Group	Sample	No. of aliquots	Administered dose (Gy)	Recovered dose (Gy)	Recovered / Administered
Core	D01-30	4	56.88	53.81 ± 1.09	0.95
	D02-4.7	8	17.07	16.55 ± 1.74	0.97
	D03-39	11	56.88	59.49 ± 0.76	1.05
T4	T4RBL01	11	14.79	15.54 ± 0.20	1.05
	T4R01	12	56.88	58.74 ± 0.60	1.03
	T4L01	7	17.07	16.18 ± 0.76	0.95
T3	T4700	3	3.98	3.61 ± 0.13	0.91
	SG-01	11	17.07	15.32 ± 0.83	0.90
	T3RBL02	4	5.69	6.02 ± 0.19	1.06
	HDG	3	2.73	2.88 ± 0.08	1.05
T2	T2RCK01	6	51.20	52.06 ± 0.83	1.02
	T2RCK02	10	56.88	59.49 ± 0.76	1.05
	T2L06	6	27.30	28.42 ± 0.36	1.04
	T2L16	5	56.88	53.94 ± 2.12	0.95
	T2L17	6	51.20	50.69 ± 0.78	0.99
	T2L18	5	62.57	68.88 ± 1.51	1.10
	T2L19	5	51.20	52.79 ± 0.85	1.03
	T2L20	6	56.88	56.29 ± 2.34	0.99
	T2L21	4	56.88	57.83 ± 1.34	1.02
	T2L22	6	54.61	56.50 ± 1.07	1.03
	T2L24	5	80.78	89.36 ± 1.96	1.11
	T2R01	6	170.65	185.56 ± 3.48	1.09
	T2R02	5	22.75	23.85 ± 0.32	1.05
	PB-T2L01	5	56.88	59.64 ± 1.06	1.05
	T2L-P	8	34.13	33.24 ± 1.96	0.97
	SG-06	4	34.13	34.18 ± 0.59	1.00
T1	T1L01	5	193.41	189.38 ± 9.35	0.98
	YD-L001	4	227.54	252.36 ± 6.53	1.11
	YD-L002	4	227.54	215.43 ± 9.51	0.95
	YD-L003	4	227.54	245.74 ± 9.51	1.08
	NS-DZ	4	284.25	264.35 ± 7.84	0.93
	NS-L27	12	164.96	184.00 ± 2.58	1.12
	NS-L70	12	238.91	264.91 ± 4.21	1.10
	NS-86	4	284.42	305.57 ± 7.22	1.07
	NS-U100	4	170.65	171.40 ± 4.08	1.0

3.5.3 Evaluation of environmental dose rates

The samples used for environmental dose rate evaluation came from the sediments removed from the two ends of the steel sample tubes. Loess or

paleosol samples (Fm') were generally taken from visually homogeneous layers with a thickness > 30 cm, and sediment taken from these tubes will have dose rates that are likely representative of the integrated ionizing radiation environment experienced by the samples. For samples of alluvial silt, which generally has a thickness of 10 – 20 cm, smaller than the maximum penetration distance of gamma rays (30 cm), the contribution from the nearby gravel layers should also be considered. Ideally this would be achieved by making in-situ gamma spectrometry measurements or by sampling adjacent gravel lenses to allow modelling of the gamma dose rate experienced by the sample. However, a field gamma spectrometer was not available for my field work, and it was not practical to take (or measure) sufficient large gravel samples to be representative. Therefore, the dose rates obtained for these alluvial silt samples were also based on analysis of sediments extracted from the light exposed outer portions of the sample, which may tend to lead to dose rate overestimates (age underestimates) since bedrock clasts are expected to be less radioactive than fine-grained silts. However, this age underestimation is expected to be low because with the exception of a small component likely derived from reworked loess, the fine and coarse grained sediments have similar provenance (within the valley) and might therefore be expected to have the same radioisotope concentrations and therefore yield similar dose rates.

The environmental dose rates were determined using a thick source alpha counter (TSAC) (i.e., a Daybreak Model 583 Intelligent Alpha Counter), and a Risø GM-25-5A low-level beta GM multicounter system ("GM beta-counter"). For each sample, the concentrations of ^{238}U and ^{232}Th were measured by the TSAC.

The beta dose rates of these two radionuclides were calculated using the conversion factors of Adamiec and Aitken (1998). The beta dose rate of ^{40}K was obtained by subtracting from the total beta dose rate (obtained by the GM beta-counter) the proportions of ^{238}U and ^{232}Th. The ^{40}K concentration was subsequently obtained using the conversion factors (Adamiec and Aitken, 1998). Finally, the alpha, beta and gamma dose rates were calculated using the radionuclide concentrations obtained above. Detailed measurement processes of the radionuclide concentrations are presented in Appendix 3.4.

The dose rates obtained above were corrected for alpha efficiency (Rees-Jones, 1995) and alpha and beta attenuation (Mejdahl, 1979; Bell, 1980). The attenuation effect of water content was also considered following Aitken (1985)'s method. For samples from above the present-day water table (which yielded 5–6% water contents), the water content was taken as 10 ± 5%, which is approximately half of the saturated water content (~20%). This value is used because terrace sediments tend to experience occasional saturation conditions prior to terrace abandonment, with dewatering occurring after terrace abandonment. For samples beneath the present-day water table it is expected that the sample has been in a saturated condition for most of the burial period, and the saturated water content was used. The cosmic dose rate was obtained following Prescott and Hutton (1994).

To determine whether the TSAC/GM beta-counter method produces accurate estimates of dose rates, a selection of the samples were also measured using inductively coupled plasma atomic emission spectroscopy (ICP-AES, for ^{40}K) and

inductive coupled plasma mass spectrometry (ICP-MS, for ^{238}U and ^{232}Th). The comparison of the dose rates produced by these two methods can also reveal whether the sediments have been in a secular equilibrium. This is because the method of ICP-AES/MS assumes that the sediment is in a secular equilibrium such that the radionuclide contents of the sediment can be used to calculate the dose rates, while the method of TSAC/GM beta-counter directly measures the dose rates without assuming an equilibrium condition. If the two methods produce consistent values of dose rates for the same sediment, it will suggest that the sediment is in a secular equilibrium, and vice versa. Comparison of the dose rates produced by these two methods is presented in Appendix 3.5. The results suggest that the two methods produce similar amounts of dose rates for same samples, consistent with Aitken (1990)'s observation. Therefore, it is deduced that the sediments have been in secular equilibrium in natural conditions and that the TSAC/GM beta-counter method used in this study provide accurate estimates of environmental dose rates.

3.6 Summary

This chapter presented a detailed description of the methods used in the study. Firstly, the methods of field mapping of alluvial terraces were presented, which was followed by a description of the processes of extracting the three key geomorphic parameters (i.e., sediment volume, and longitudinal and cross-valley profiles) from a LiDAR topographic image. Secondly, methods of depicting the terrace sedimentology were presented. These included an introduction to the parameters (e.g., lithological composition, roundness, sorting etc.) recorded in sedimentary logging, a notation on the method of lithofacies coding and the way

that was adopted in interpreting depositional environments (i.e., by analyzing lithofacies associations). Thirdly, information of four boreholes (i.e., drill equipment, drill location and the method of sedimentary description) was presented. The borehole information helped to provide a comprehensive history of the valley filling of GLP by uncovering the sediments beneath the present channel. Lastly, the chapter provided a description of the dating method used here (i.e., OSL dating), including the sampling protocol and sample pre-preparation, and the measurements of equivalent doses and environment dose rates.

Chapter 4 Results: Terrace Geomorphology

4.1 Introduction

This chapter presents the results of field mapping and geomorphic analyses of alluvial terraces in the GLP valley. The alluvial terraces were mapped and annotated following international conventions. The geomorphic analyses were conducted by comparing the sediment volumes, longitudinal profiles, and cross-valley transects of the alluvial terraces.

4.2 Classification and distribution of alluvial terraces

Four levels of alluvial terraces, denoted as T1, T2, T3 and T4 from the highest to the lowest elevation, were identified based on field investigation. These sedimentary bodies are characterized by alluvial fans at the valley mouth and valley fills upstream. All these sedimentary bodies were incised into terraces.

The T1 terraces are the highest levels of alluvial sediments in the valley, and the distribution is shown in Fig. 4.1. At the downstream end of the valley, two fan-shaped bodies of the T1 terraces are present on both sides of the channel (Fig. 4.1b). The terrace surfaces are more than 100 m above the nearby alluvial channel. In the midstream, the T1 terraces are only present on the north side of the GLP channel (Fig. 4.1c, d). The total length of these terraces at the midstream is around 1500 m, and the terraces are discontinuous and have mostly been eroded leaving few flat terrace surfaces. The T1 terrace shown in Fig. 4.1e

displays both the phyllite bedrock and the overlying alluvium. The bedrock-alluvium contact is around 70 m above the small road, which is close to the top of the T2 terraces at this site.

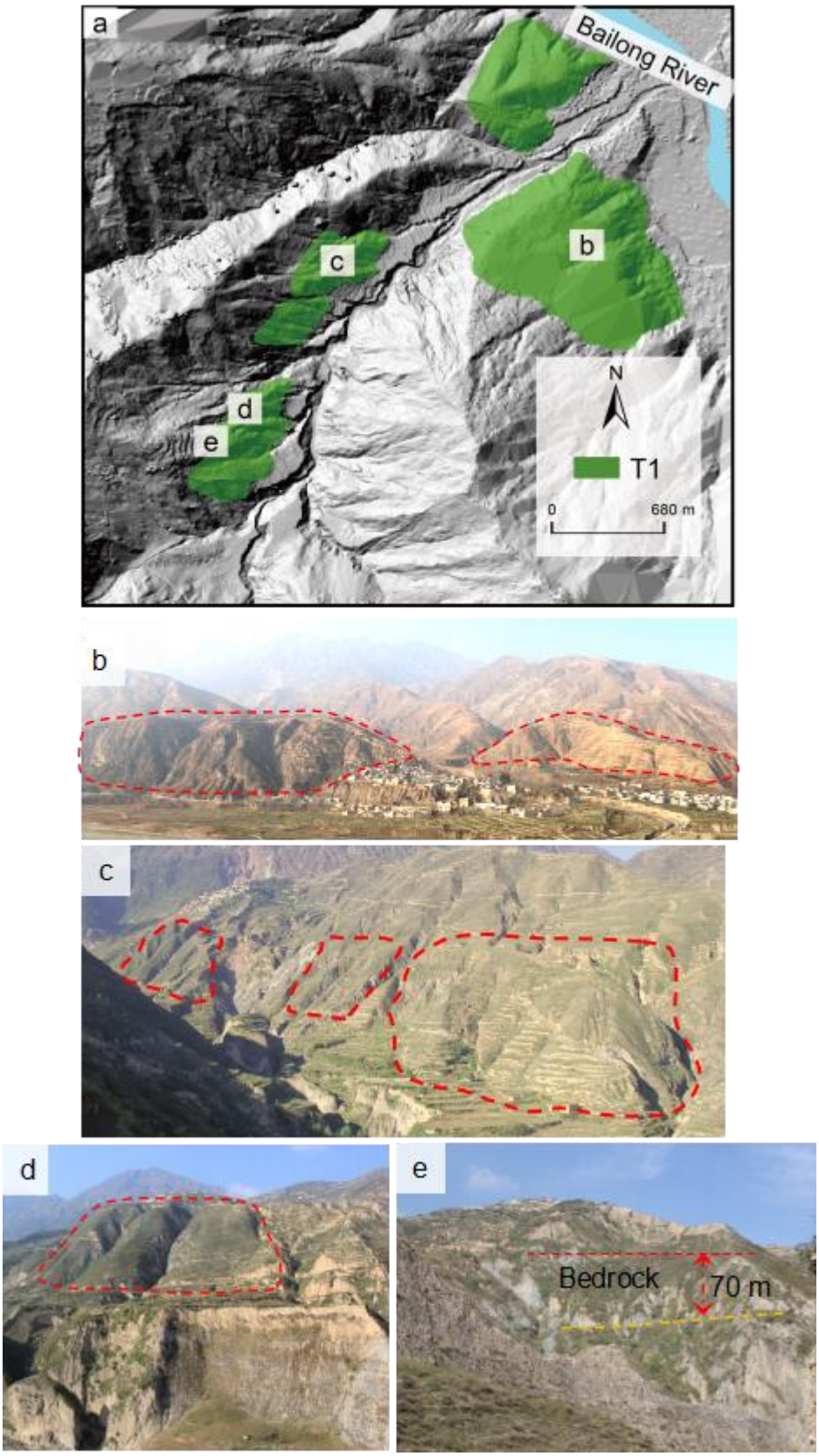

Fig. 4.1. Distribution of T1 terraces. a. General distribution of the T1 terraces in the GLP valley. Panels b, c, d and e are photographs of T1 terraces at the corresponding locations of GLP.

The T2 terraces are the first terrace surfaces below the T1 terraces, and the distribution is displayed in Fig. 4.2. These terraces generally have an exposed thickness of 20-50 m, which tends to decrease downstream. At the mouth of the valley, a fan-shaped body of T2 is located on the south side of the valley (Fig. 4.2b), which currently has a settlement built on it. The terrace surface is generally 20 m above the nearby channel. A larger T2 terrace is located on the opposite side of the channel. This terrace has been incised towards the center forming a lower surface in the middle and two higher surfaces on both sides (Fig. 4.2c). The T2 terraces are located along both sides of the major channel upstream, though the north side preserves more continuous terrace sections than the south side does (Fig. 4.2d). The exposed thickness increases upstream from around 20 m near the valley mouth to more than 50 m where T2 terminates upstream (Fig. 4.2e).

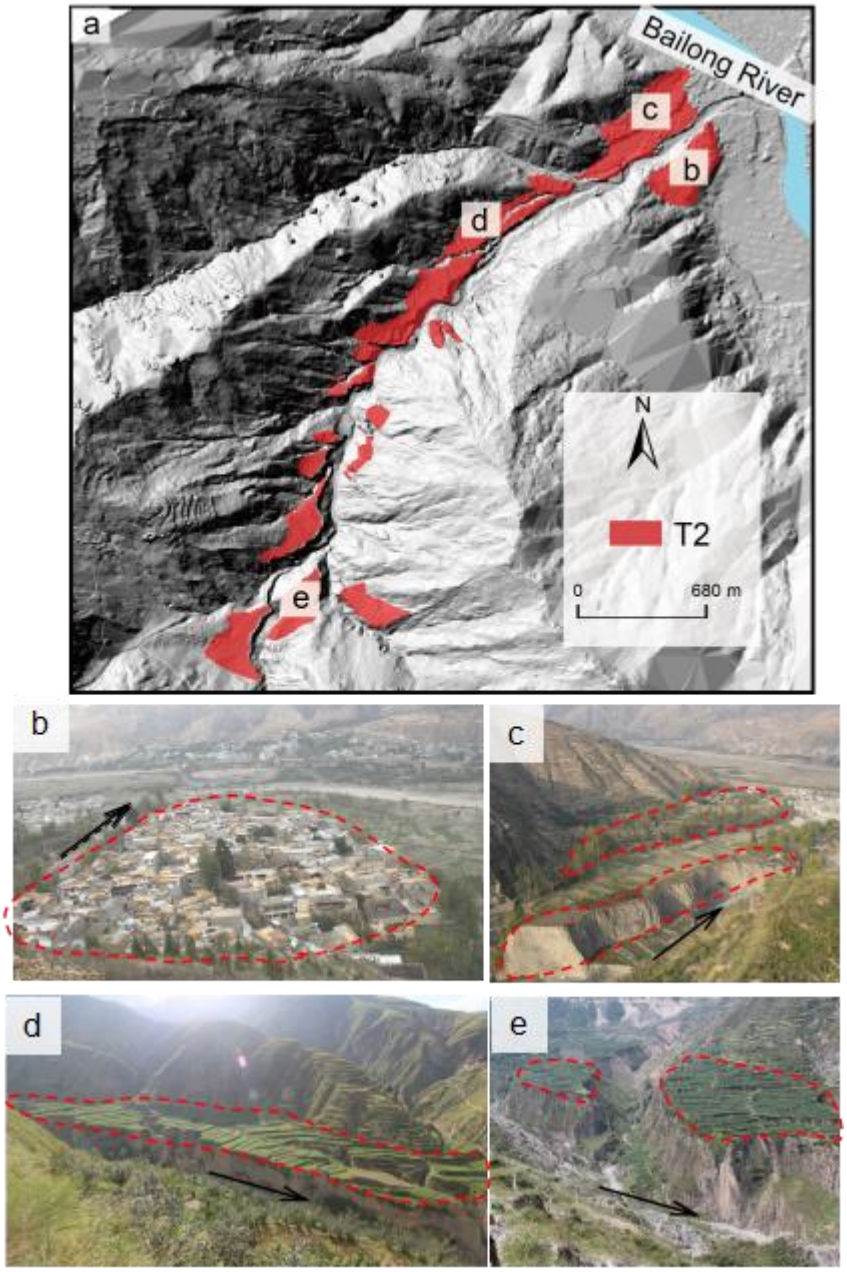

Fig. 4.2. Distribution of T2 terraces. a. General distribution of the T2 terraces in GLP. Panels b, c, d and e are photographs of T2 terraces at different part of the GLP valley. Dashed red lines delineate the boundaries of the T2 terraces. The black arrow points to the flow direction.

The distribution of the T3 and T4 terraces is displayed in Fig. 4.3. T3 terraces are below the T2 terraces, and their surface levels are ~ 5 m above the present valley floor. At the mouth of the GLP valley, they are adjacent to the T4 terraces (Fig. 4.3a, b) and are symmetrically distributed along both sides of the channel. The T3 terrace terminates 200 m from the valley mouth upstream when it meets the

higher T2 terraces. Further upstream, the T3 terraces are inset in the higher T2 terraces and are mostly on the south side of the channel (Fig. 4.3c, d). The terrace in Fig. 4.3c extends longitudinally for 200 m and has an average width of 15 m. The terrace in Fig. 4.3d extends longitudinally for around 800 m and has an average width of 50 m. The relative height between each terrace surface and the modern channel is around 5 m. These terraces are used as farmlands. In the midstream section, no well extended T3 terrace were found. In contrast, small patches (length < 20 m) were found where the channel bends (Fig. 4.3e, f).

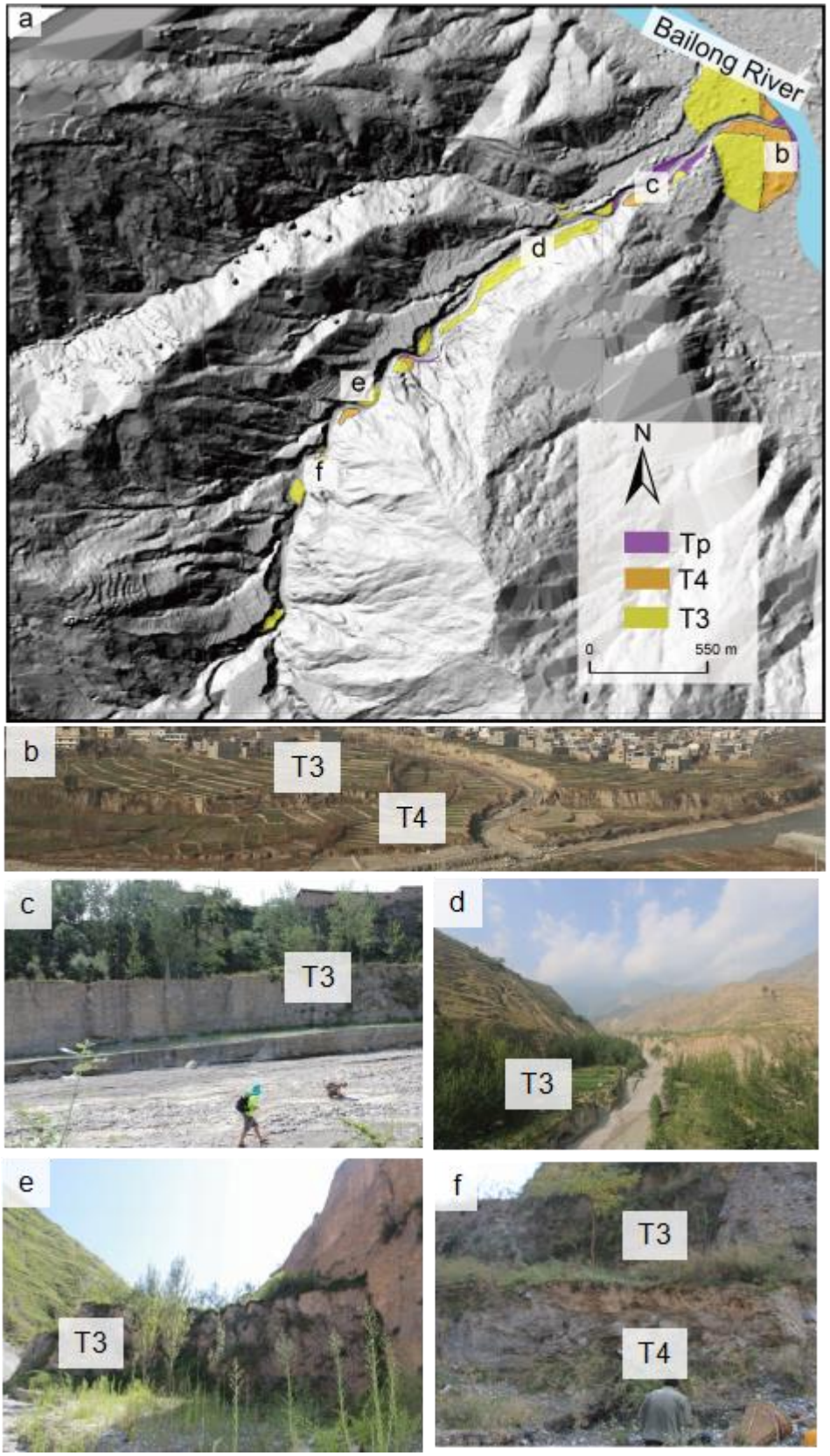

Fig. 4.3. Distribution of T4 and T3 terraces. Panels b, c, d, e and f are photographs of the terraces at the corresponding locations of panel a.

The T4 terraces are the lowest terraces that are not routinely flooded. The surfaces are generally occupied by crops and are ~3 m above the modern channel. At the mouth of the GLP valley, the T4 terraces are symmetrically distributed on both sides of the channel (Fig. 4.3b). Five more sites with terraces at a similar height relative to the nearby channel were identified throughout the valley, but these terraces are small patches (Fig. 4.3a). Except the alluvial terraces identified in the valley, some low alluvial surfaces (~ 1 to 2 m above the present channel) that have no vegetation covers are present at the valley mouth. These sediments are denoted as Tp to indicate floodplain deposits.

Overall, the distribution of the alluvial terraces in GLP is displayed in Fig. 4.4.

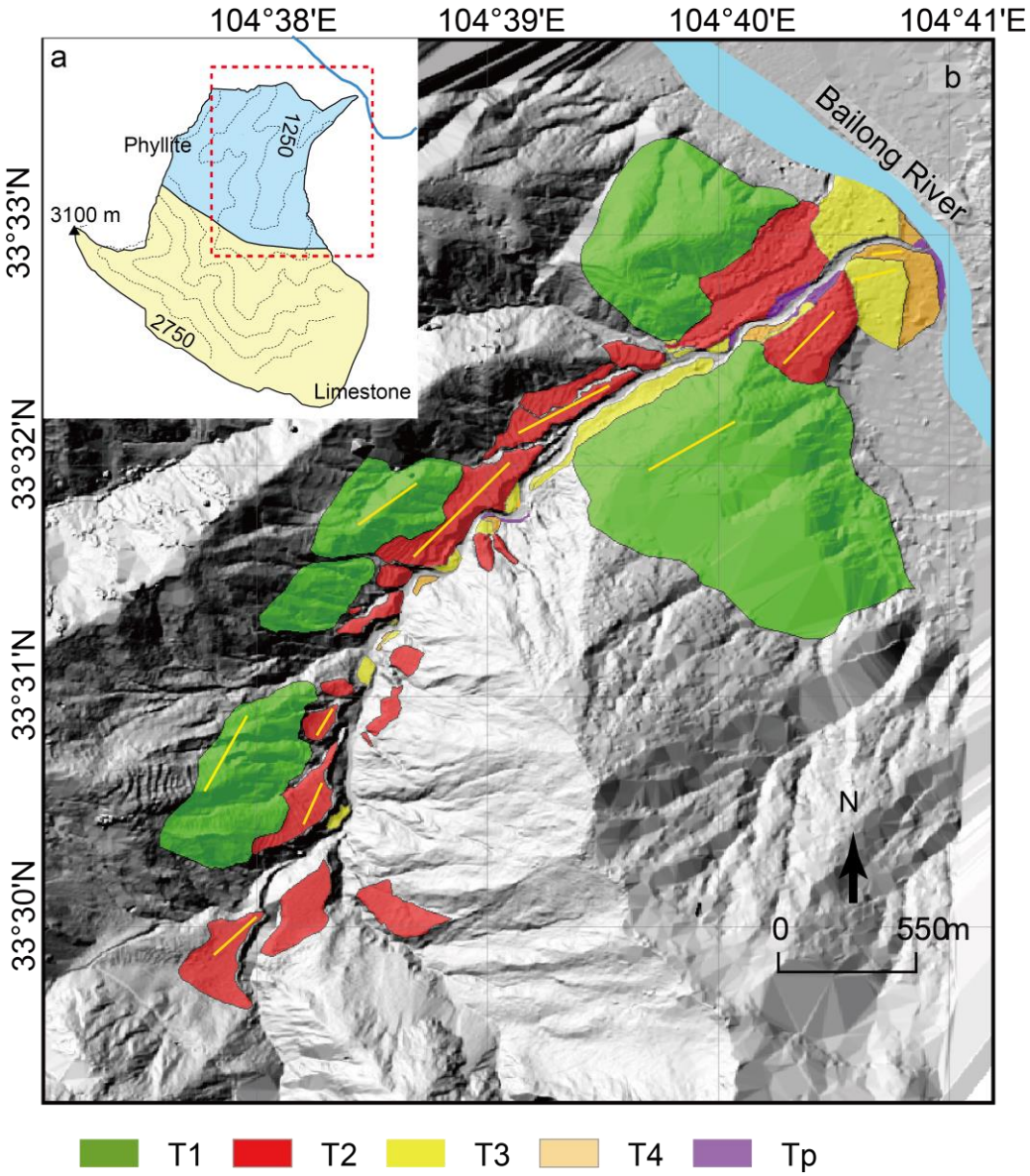

Fig. 4.4. Distribution of the alluvial terraces in the GLP valley. (a). The watershed of the GLP valley. The contour interval is 250 m with the highest point (3100 m) shown by a filled triangle. The dashed red box delineates the phyllite area, which is shown in panel b. (b). The distribution of alluvial terraces. The background image is a hill-shade image of the GLP valley. Yellow lines are the location of terrace surface profiles which are shown in Fig. 4.5. The map was produced using the software ArcGIS 10.2.

4.3 Geomorphic analyses of alluvial terraces

4.3.1 Comparison of terrace magnitudes

To compare the magnitude of each terrace level, the alluvial volume and area of the terraces were calculated and listed in Table 4.1. As has been mentioned in Section 3.2.2, the volume of each terrace was calculated using the ‘polygon volume’ tool in the 3D Analyst toolboxes in ArcGIS 10.2. It assumes that each terrace has a flat contact surface at the base, and by defining the elevation of the base surface, the volume of sediment contained within the terrace is obtained. In practice, each terrace object mapped in ArcMap was assigned a basal elevation value. The values for the T2, T3 and T4 terraces are the elevations of the channel at the nearby site, and the calculated volumes are the alluvium that is above the current channel. For the T1 terraces which have exposed bedrocks, the value of the basal elevation was taken as the elevation of the alluvium-bedrock contact. Because approximately 20 m thickness of loess has accumulated on top of the T1 terraces, the volume of the loess layer was calculated and subtracted from the terrace volume previously obtained. The surface areas of the terraces were calculated along with the calculation of the alluvium volumes using ArcGIS 10.2. Furthermore, to compare the distribution of each terrace level in the valley, the total volumes of each terrace level in the midstream and downstream sections of the valley were compared. The D/M value in Table 4.1 represents the ratio between the downstream volume and the midstream volume of the same terrace level.

Table 4.1. The total volume and area of each terrace level. V_d and V_m are the volume of the terraces at the downstream and midstream sections, respectively. D/M represents the ratio between the downstream volume and the midstream volume.

Terrace level	Volume ($\times10^4$ m^3)	V_d ($\times10^4$ m^3)	V_m ($\times10^4$ m^3)	D/M	Area ($\times10^4$ m^2)
T4	30	26	4	6.2	5
T3	298	138	110	1.3	19
T2	3257	455	2796	0.2	66
T1	5300	2868	2438	1.2	171

In Table 4.1, the alluvium volume of each terrace level decreases from the T1 to T4 terraces. The volume of T1, being 5300×10^4 m^3, is the largest, indicating a primary period of aggradation. The volume of the T1 terraces in the downstream portion of the valley is larger than those in the midstream with a D/M ratio of 1.2, indicating that the T1 terraces in the midstream have mostly been eroded. The T2 terraces have the second largest volume at 3257×10^4 m^3, which is at the same magnitude order with that of the T1 terrace, indicating an approximately equivalent period of aggradation to that of the T1 terrace. The D/M ratio for the T2 terraces is only 0.2, indicating a primary distribution of terraces at the midstream. This reflects that the majority of the T2 terraces in the midstream section have been preserved. The volume of the T3 terrace is an order of magnitude smaller than those of T1 and T2 at 298×10^4 m^3. This observation is interpreted to indicate that the T3 terrace was accumulated over a short period. The volume of the T4 terraces, being 30×10^4 m^3, is an order of magnitude smaller than that of the T3 terraces, and the terraces are mainly distributed at the downstream portion of GLP as is reflected in the D/M ratio (6.2).

4.3.2 Longitudinal profiles of terraces

To compare the surface grading of each terrace level with the modern channel, lines which are parallel to the direction of the modern channel were drawn on the terrace surfaces (Fig. 4.4b). Then, longitudinal profiles along these lines were obtained by the procedures introduced in Section 3.2.2, and the result is displayed in Fig. 4.5.

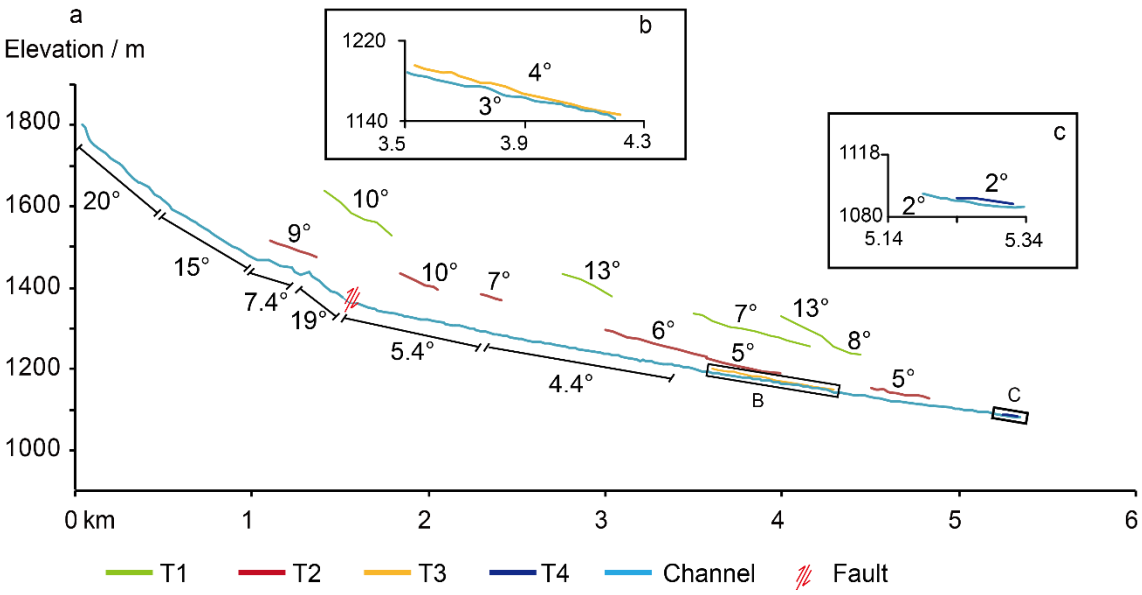

Fig. 4.5. Longitudinal profiles of terrace surfaces. The distribution of the longitudinal profiles was displayed in Fig. 4.4b. The channel was extracted using the Hydrology toolset in ArcGIS 10.2. The profiles in the black boxes (panels b and c) are close-up views of the profiles at the downstream portion of the GLP valley. The number above each line denotes the slope of the terrace surface at that profile.

In Fig. 4.5, the longitudinal profile of the modern channel shows a concave shape. The slope of the channel displays a sharp decline near the fault. The slope of the channel upstream of the fault is ~19˚, while the slope of the downstream part where the major channel develops is 5.4˚. This change in slope at the fault is interpreted as resulting from the difference of bedrock hardness, as well as the potential vertical displacement, of the limestones (upstream) and phyllites

(downstream) at the location of the fault.

The lines drawn on the T1 terraces show steep profiles with their surfaces grading at 10˚, 13˚, 7˚, and 8˚ from the upstream to the downstream (Fig. 4.5). Two of the T1 profiles, one close to the fault and the other at the mouth of the valley, show an obvious slope change in their profiles. For example, the T1 profile at the valley mouth (Fig. 4.5) displays two distinct sections: one section has a slope of 13˚ while the other section has a slope of 8˚. This occurs because the T1 terrace in this part of the valley has been incised, leaving small sections of terrace surfaces which are in the similar height with the phyllite hill-slopes capped by loess (around 20 m). Consequently, the steep part (13˚) of the slope represents phyllite hillslopes while the flat part (8˚) is the real terrace surface. In contrast, the T1 terrace on the opposite side of the valley has a relatively constant slope of 7˚, which is regarded as the T1 terrace surface.

The lines drawn on the T2 terraces have gradients between 10˚ and 5˚, and the gradients decrease from the midstream to the downstream sections. Only three and one longitudinal profiles were extracted from the T3 and T4 terraces, respectively. The T3 surface has a gradient of 5 - 2˚, while the T1 surface has a gradient of 2˚.

4.3.3 Cross-section profiles of terraces

The cross-section profiles provide a direct view of the spatial relationships between different levels of terraces. Five cross-section profiles have been obtained using the 3D analyst function in ArcGIS 10.2 (Fig. 4.6).

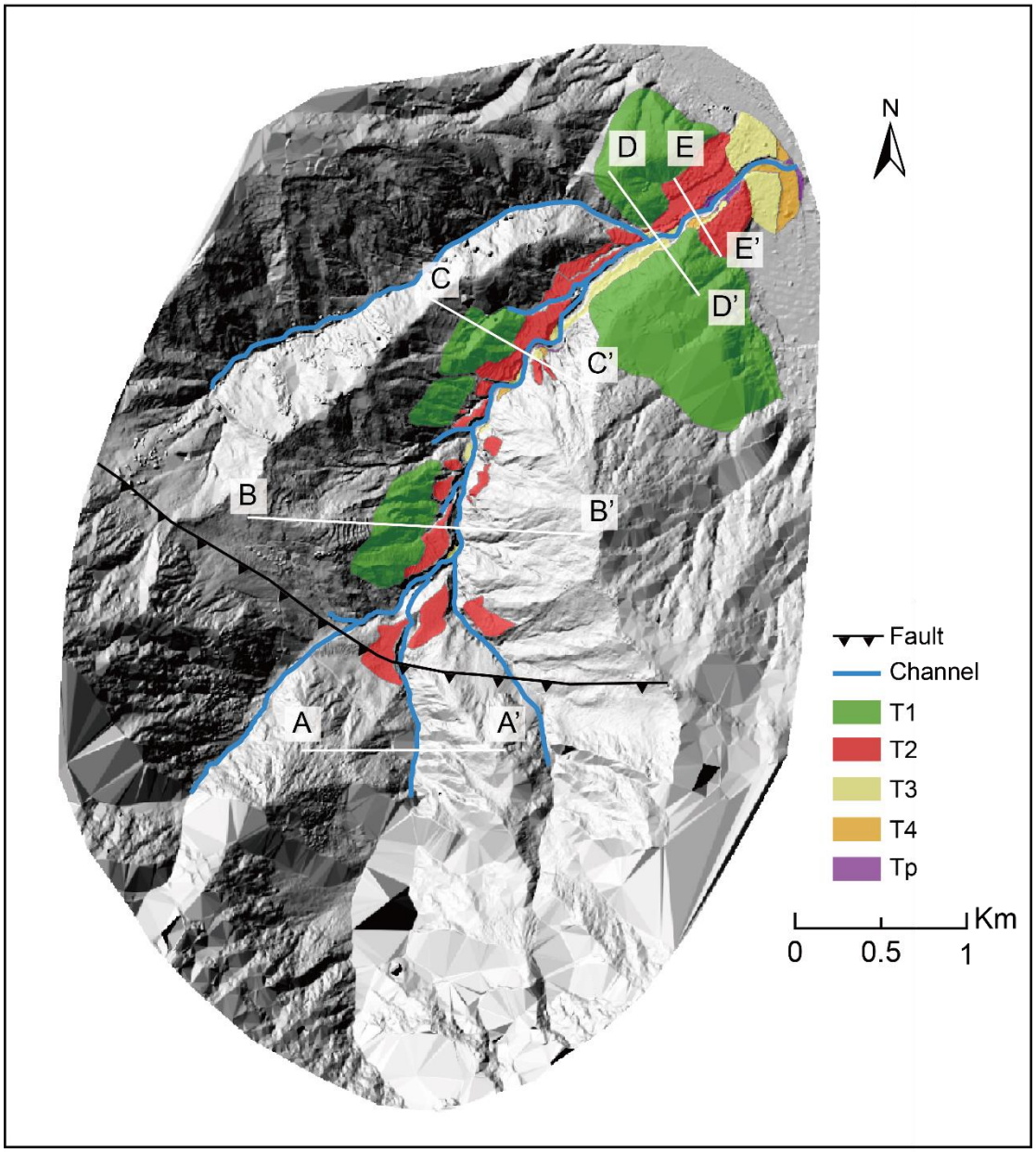

Fig. 4.6. Location of cross-section profiles drawn in the GLP valley.

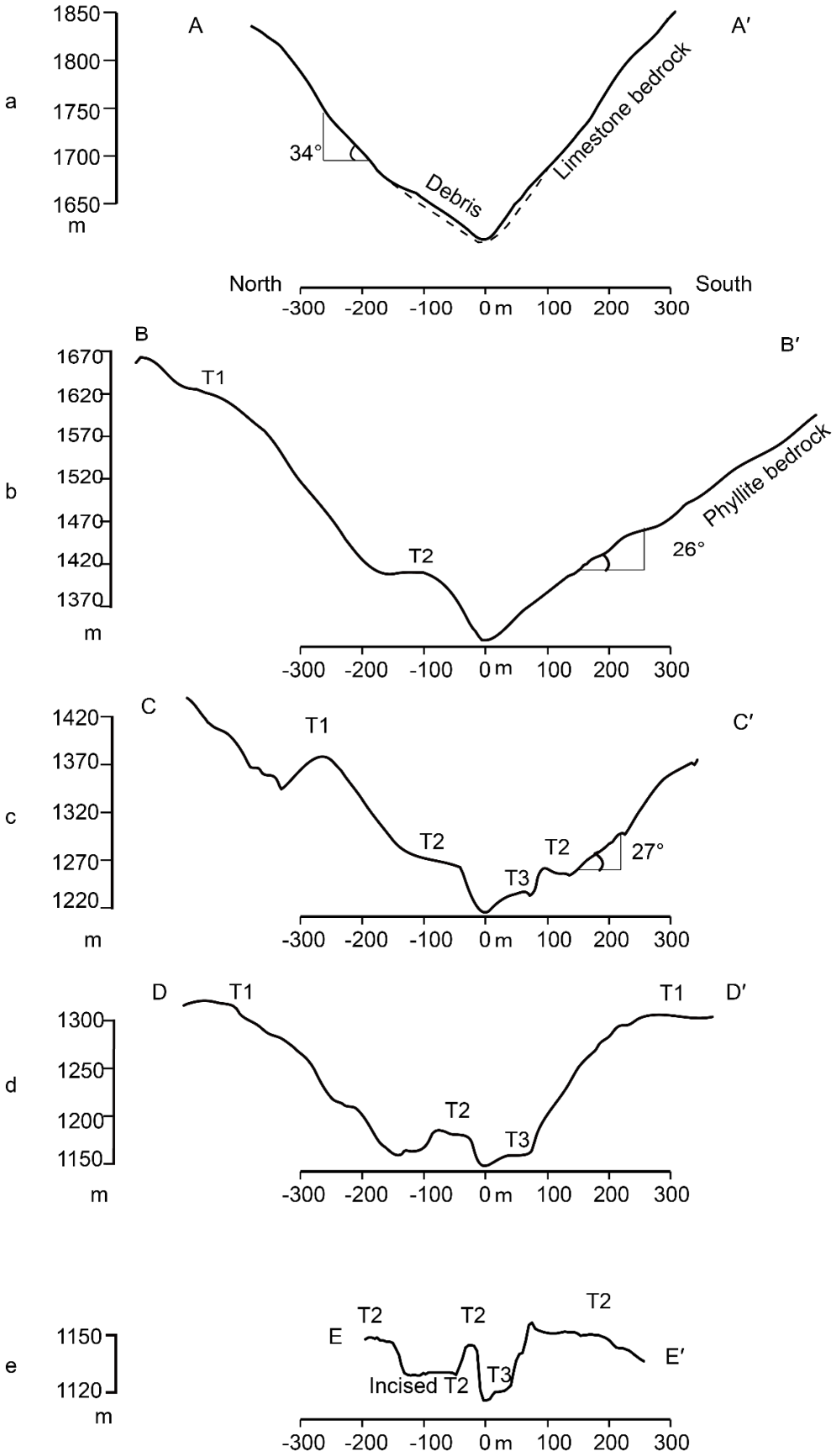

Fig. 4.7. Cross-section profiles of the GLP valley. The 0 m in the horizontal axis represents the middle of the current channel.

The AA′ profile (Fig. 4.7a) was drawn in the limestone areas near the fault. It shows a typical ‘V’ shape with steep hillslopes (34˚) and a narrow channel (5 m width). The hillslopes also contain a number of rockfall deposits.

The BB′ profile (Fig. 4.7b) was drawn in the phyllite area near the fault. It shows that (1) the valley channel is widened in this part (~20 m width), and (2) two terrace levels (T1 and T2) develop on the north side of the GLP valley with no terraces developing on the opposite side. The surface of the T1 terrace sits 180 m above the T2 surface in the profile. No T3 and T4 terraces were found in the profile.

The CC′ profile (Fig. 4.7c) is ~ 1 km away from the BB′ profile downstream the GLP valley (Fig. 4.6). The surface of the T1 terrace is about 100 m above the T2 terrace and has mostly been incised, and hence no flat surface representing the surface of the T1 terrace is observed (Fig. 4.7c). The T2 terrace is around 50 m above the channel and exists on both sides of the channel. The T3 terrace exists on the south side of the channel. The channel width is close to that at BB′. The phyllite hillslope has a gradient of 27˚.

The DD′ profile (Fig. 4.7d) was drawn at the mouth of the valley. In this section, the T1 terraces are distributed on both sides of the valley. However, on the south side a flat terrace surface is observed, whereas on the north side a steeper

surface is observed. In both cases the T1 terrace surfaces occur about 100 m above the T2 terraces.

The EE' profile (Fig. 4.7e) was drawn further downstream. The T2 terraces are distributed on both sides of the present channel, but the T2 terraces on the north side have been incised in its center, leaving a lower surface in the middle (Fig. 4.7e). This lower surface reflects the avulsion of the channel during the incision of the T2 terraces.

4.4 Conclusion

(1) Four levels of alluvial terraces (i.e., T1, T2 T3 and T4) were mapped in GLP. The surface of the T1 terraces generally sits 100 – 180 m above that of the T2 terraces, while the surfaces of the T2 terraces are generally 30 – 50 m above the present channel. The surfaces of the T3 and T4 terraces are generally ~5 m and 3 m above the present channel, respectively.

(2) The T1 and T2 terraces are distributed across the midstream and downstream sections of the valley, while the T3 and T4 terraces are mainly distributed in the downstream portion of the valley.

(3) The volumes of the four terraces decrease from the T1 to the T4 terraces. The T1 and T2 terraces are the most developed terraces in the valley and contain sediment volumes at a same order of magnitude, which is interpreted to indicate two main aggradational periods of the GLP valley.

(4) Generally, the longitudinal grades of the terraces decrease from the T1 terraces to the T4 terraces. For the T1 and T2 terraces each, the longitudinal grades decrease from the midstream to the downstream portion of the valley.

Chapter 5 Results: Terrace Sedimentology

5.1 Introduction

The previous chapter described the classification and distribution of alluvial terraces in GLP. These results suggest that the valley has been filled with considerable amounts of sediments and has experienced multiple-stages of aggradation and incision cycles. However, the genesis of the sediments (i.e., the depositional processes forming these sediments) is unknown. This section provides a detailed sedimentary analysis of the terrace sediments to reveal the primary depositional processes.

Well-exposed outcrops of alluvial terraces were selected for sedimentary logging (Fig. 5.1). Overall eighteen profiles covering the floodplain and the four levels of alluvial terraces were logged (Fig. 5.2). A detailed sedimentary description of each section is provided in Appendix 5. Based on these sedimentary analyses (Appendix 5), the characteristics of each type of lithofacies and lithofacies associations are summarized below.

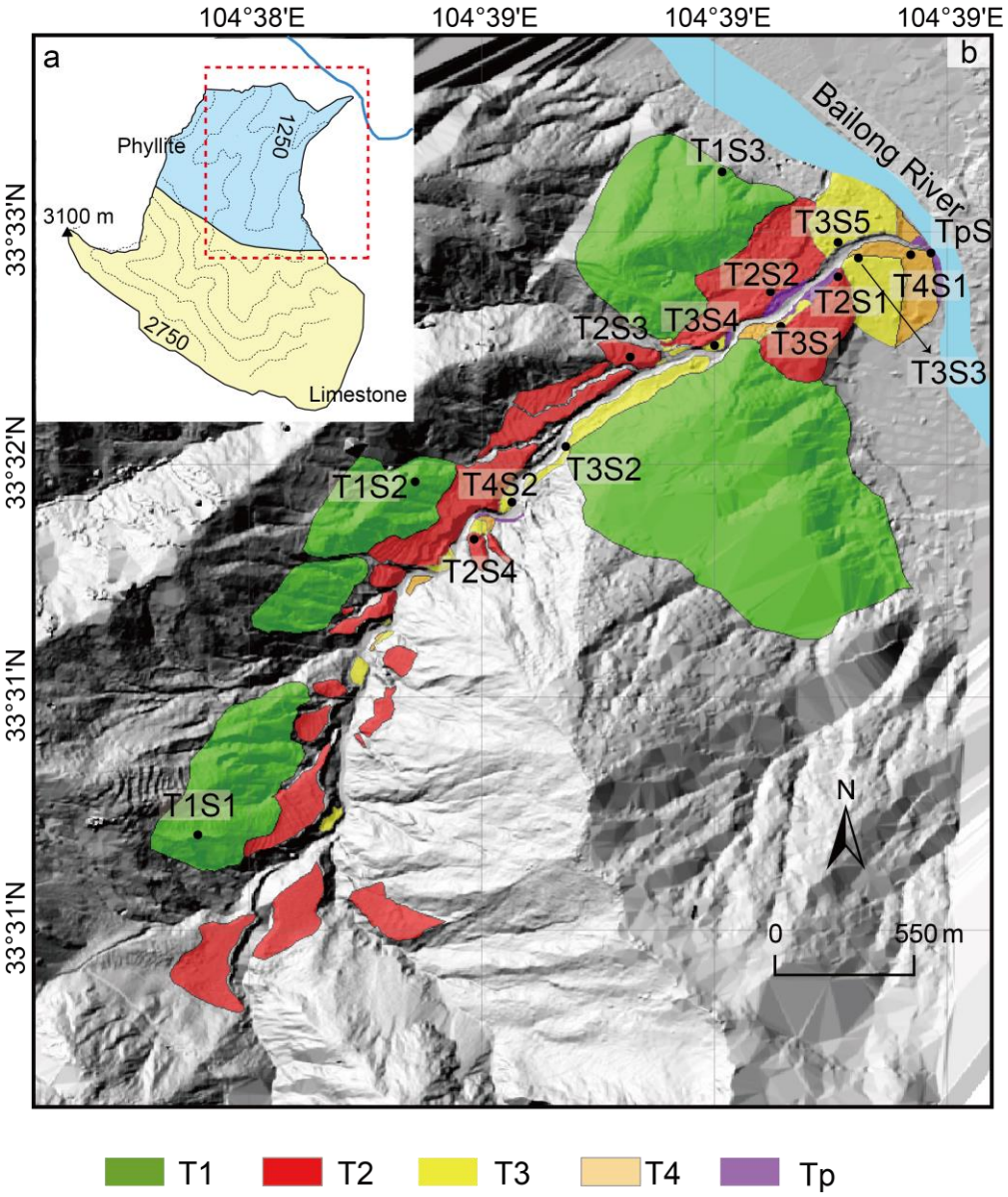

Fig. 5.1. Distribution of logged sections (filled dots) for different levels of terraces.

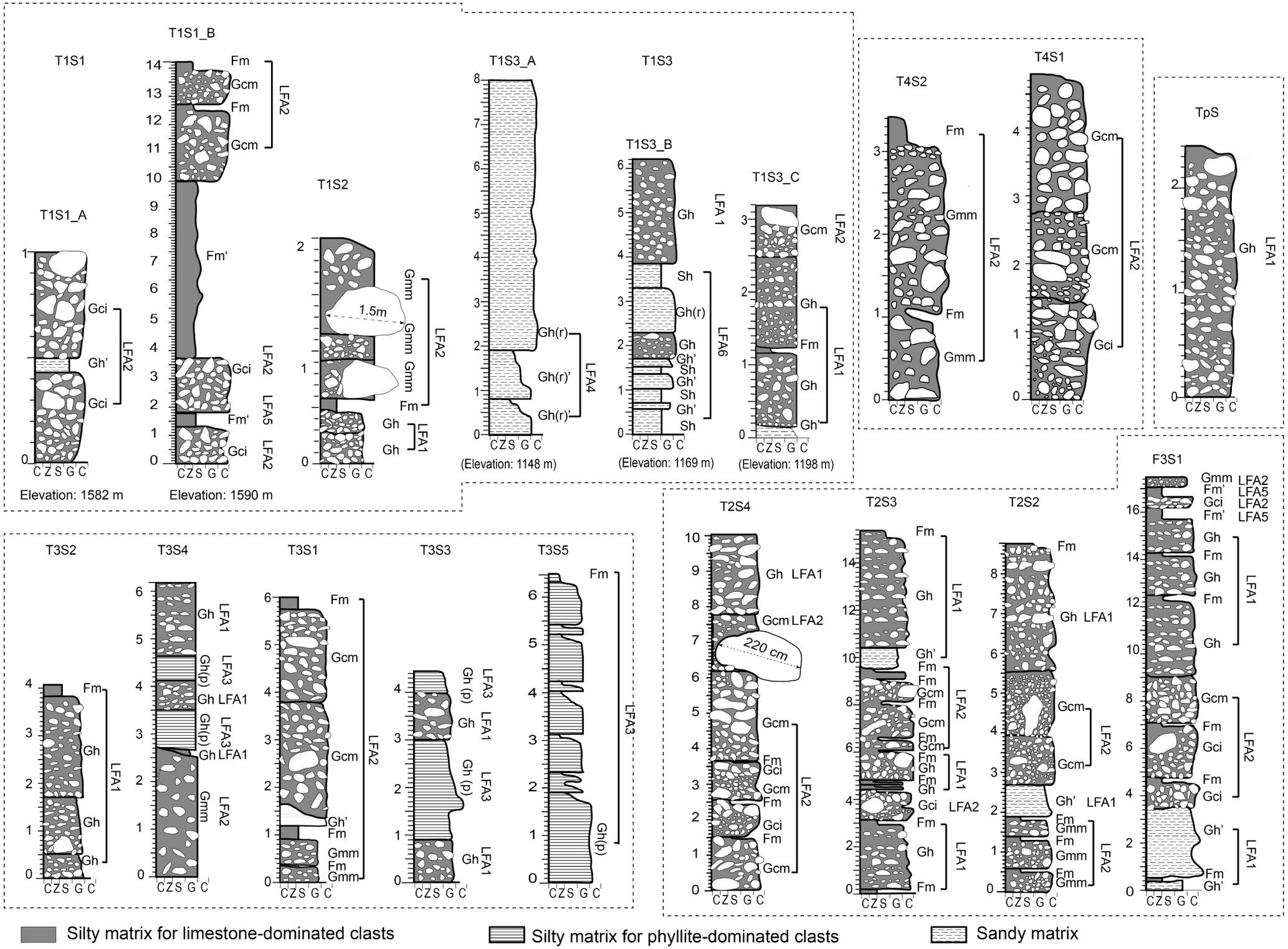

Fig. 5.2. Sedimentary logs of the alluvial terraces. The depths are in meter. Descriptions of lithofacies and Lithofacies associations (LFAs) are presented below.

5.2 Lithofacies characteristics

Lithofacies Gh refers to poorly sorted, crudely bedded clast-supported pebble to cobble clasts with silty/sandy matrix. This type of lithofacies is present in sections TpS, T3S2, T3S3, T2S1, T2S2, T2S3, T2S4, T1S1_B, T1S2, T1S3_B and T1S3_C (Fig. 5.2). Limestones form the primary lithology. Individual beds are typically a few 10–20 cm thick, with multistory beds reaching several meters in thickness (Fig. 5.3c). Generally, the beds lack internal grading (Fig. 5.3), and outsized clasts are common throughout a section (Fig. 5.3c), though in some cases well sorted cobbles or boulders are paved in the bed bases (Fig. 5.3b). Weak imbrication is present to some degree in all beds of this type of lithofacies (Fig. 5.3). The bed contacts are obscured due to the absence of well-defined bedding. Clast fabrics were measured for two units at section T3S3 (Fig. 5.4). The patterns shown on the two stereonet (Fig. 5.4) both suggest a preferential orientation of the clast a-axes along the flow direction (north-west to south-west) of the GLP valley.

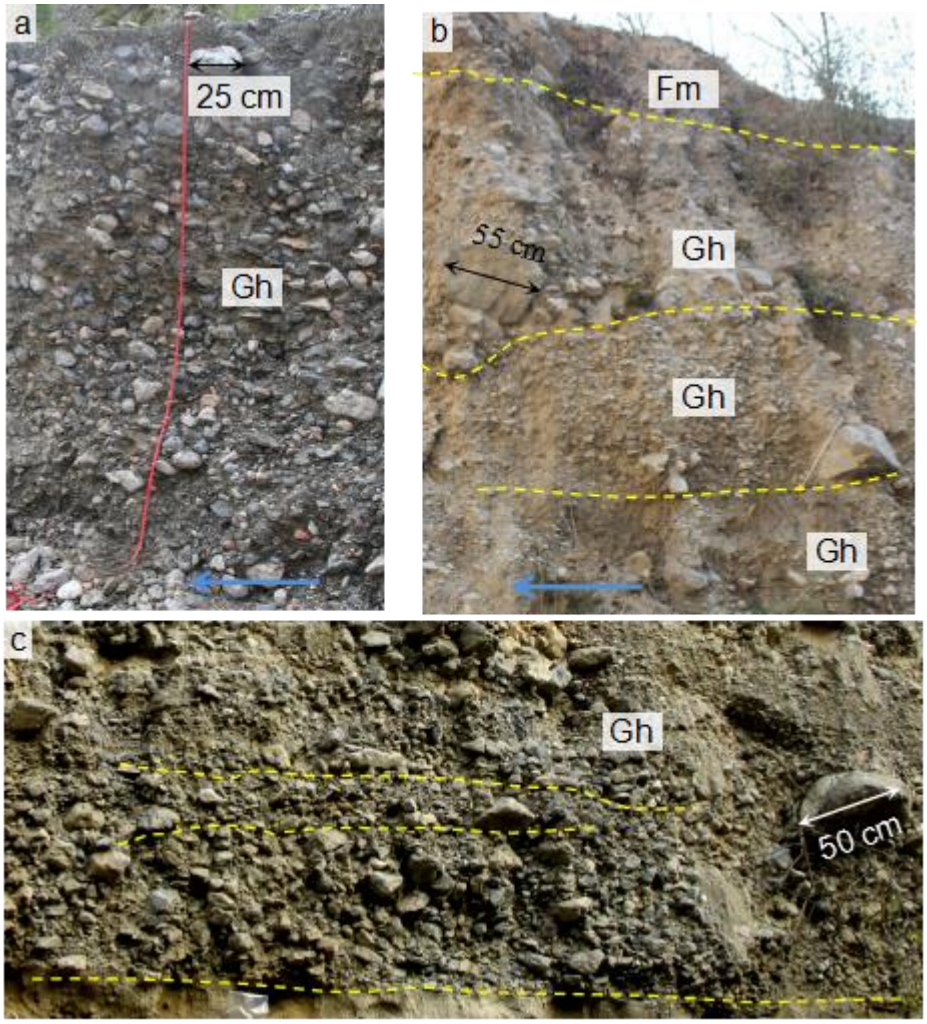

Fig. 5.3. Photographs of typical lithofacies Gh. a. Photograph of section TpS. b. Photograph of section T3S2. c. Photograph of section T2S3.

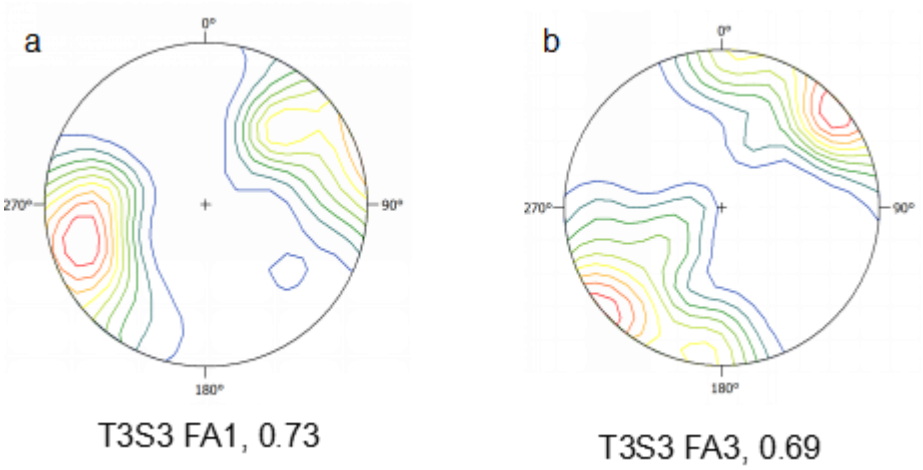

Fig. 5.4. Contoured stereonets and principal eigenvalues (the number below each stereonet) of clast fabric measurement for Gh sediments. The sampling number for T3S3 FA1 and FA2 are 30 each, and the a-axes were measured.

Lithofacies Gh' refers to moderately or poorly sorted, horizontally well-bedded, cobble- to granule-sized clasts with sandy matrix. This lithofacies is present in sections T3S1, T3S4, T2S3, T2S1, T2S2, T1S1_B, T1S2, T1S3_B and T1S3_C (Fig. 5.2), and accounts for a relatively small proportion (smaller than 10%) of the whole thickness of each section. Clast lithology is mainly composed of limestones accounting for at least 70% of the gravel-sized clasts. Phyllite clasts form ~ 20% of the sediment body and quartzite less than 10%. The sediments are usually normally graded with cobble to pebble clasts at the base and smaller clasts towards the top (Fig. 5.5a). The clasts are generally horizontally bedded. Erosive basal beds are locally developed (Fig. 5.5a). Clast fabrics were measured along the clast b-axes for these sediments at sections T3S1 and T2S2 (Fig. 5.6), and the distributions of the clast fabrics on the contoured stereonets show a preferential b-axes alignment along the flow directions of the GLP valley.

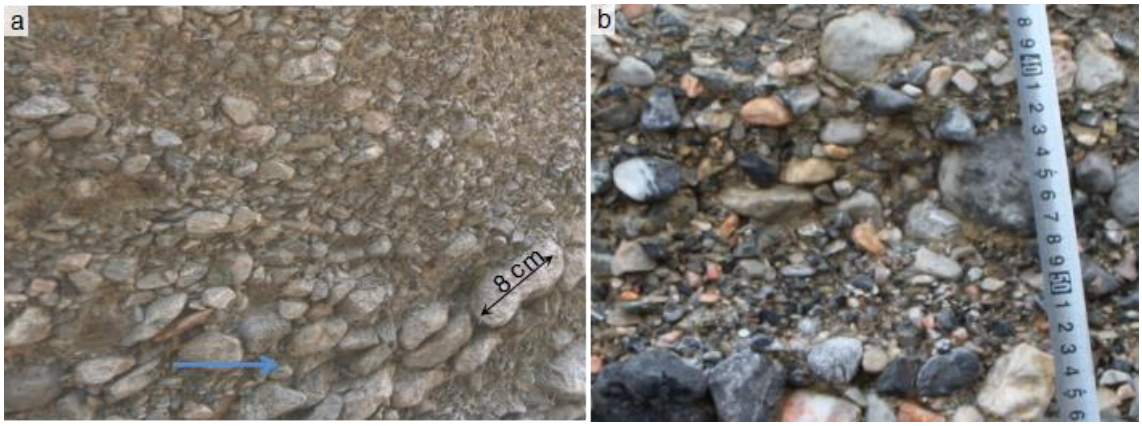

Fig. 5.5. Photographs of lithofacies Gh'. a. Gh' facies in section T2S2. The blue arrow indicates the flow direction. b. Gh' facies in section T1S3_B. The flow direction points outwards from the page.

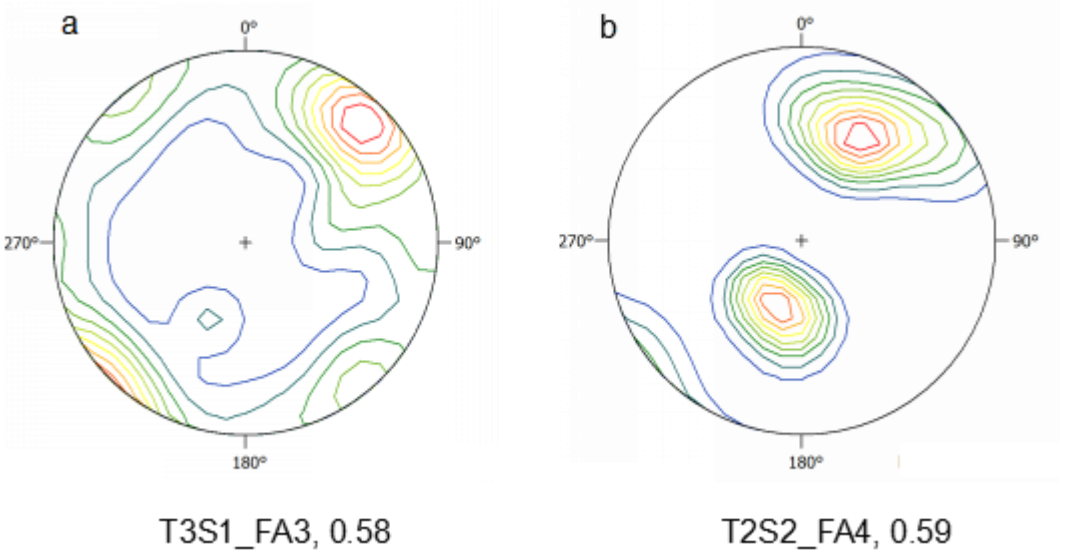

Fig. 5.6. Contoured stereonets of clast fabrics for Gh' sediments. The sampling numbers for T3S1 FA3 and T2S2 FA4 were 40 and 20 respectively. The b-axes were measured for these two units.

Lithofacies Gh (p) refers to moderately sorted, well-bedded, cobble to granule clasts with silty matrix (Fig. 5.7). Clast lithology is mainly composed of phyllites accounting for ~ 80% of the gravel-sized clasts. This type of lithofacies is mainly present in the T3 terraces (e.g., T3S3, T3S4 and T3S5), forming a significant portion of each section (>50% thickness). Clast fabrics were measured for these sediments at sections T3S3, T3S4 and T3S5. The results show a strong

preferential arrangement of clasts along their a-axes (Fig. 5.8).

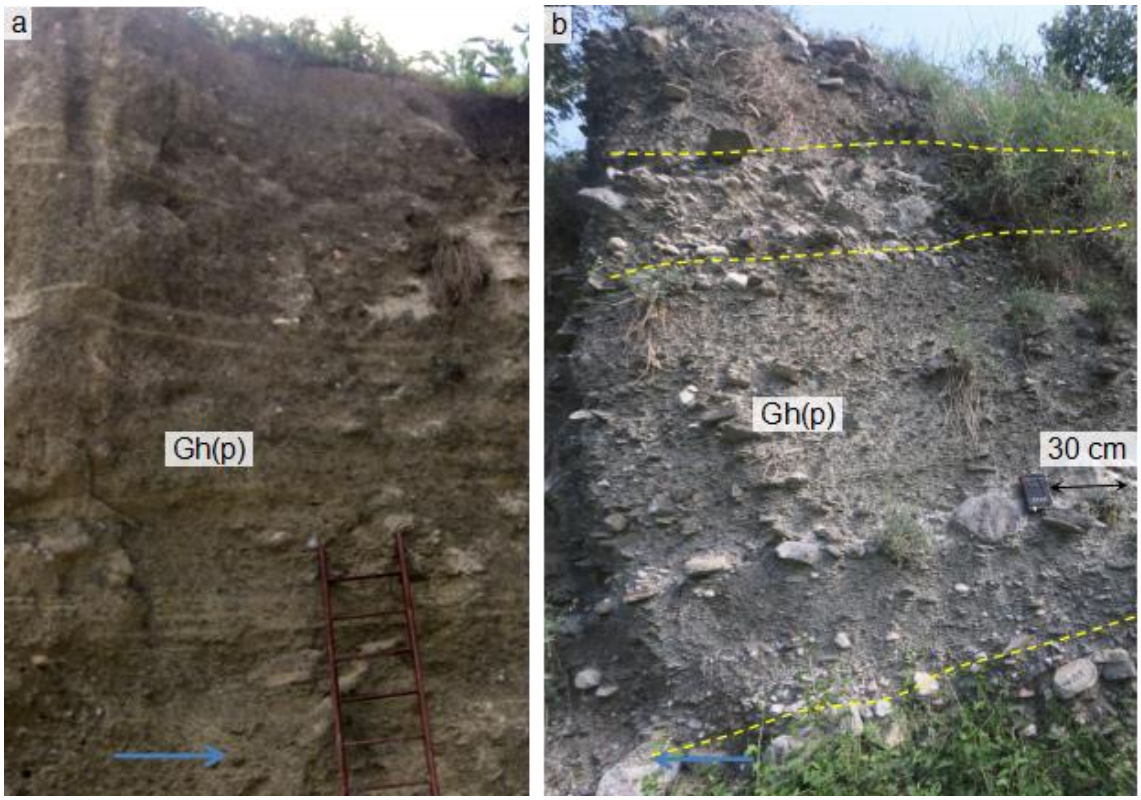

Fig. 5.7. Photographs of lithofacies Gh (p). a. Gh (p) facies in section T3S5. b. Gh (p) facies in section T3S3. Blue lines indicate the flow direction. Dashed yellow lines delineate unit boundaries.

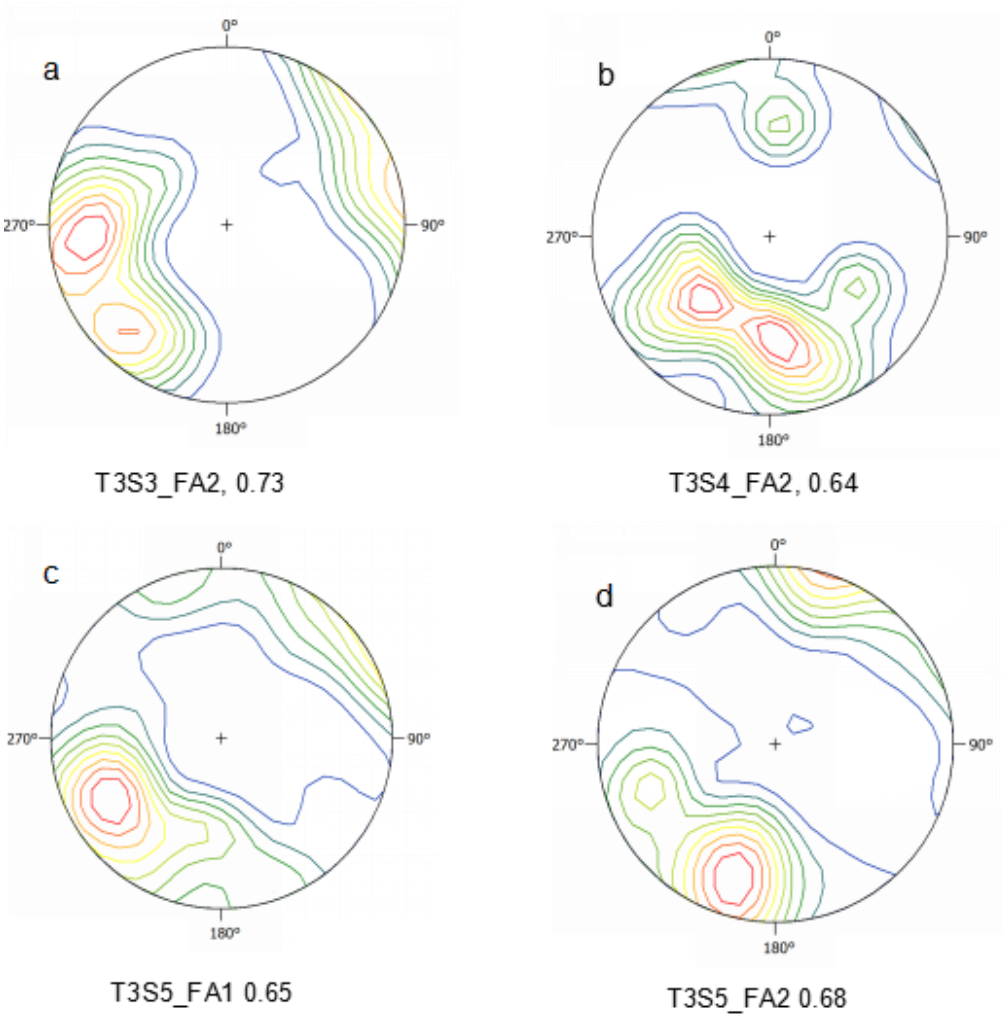

Fig. 5.8. Contoured stereonets and principal eigenvalues (the number below each stereonet) of clast fabric measurement for Gh (p) sediments. The sampling numbers for T3S3 FA2, T3S4 FA2, T3S5 FA1 and T3S5 FA2 are 20, 10, 30 and 30, respectively, and the a-axes were measured.

Lithofacies Gh (r) and Gh (r)' both refer to rounded to well rounded pebble-sized clasts with a variety of clast lithologies, including limestones, phyllites, sandstones and granites. For lithofacies Gh (r), the clasts are poorly sorted pebble- to cobble-sized clasts with sandy matrix. In some units, the bed base is formed by some imbricated cobble-sized clasts, and the clasts in the upper part of each unit dip with gentle a-b planes (Fig. 5.9a). The sedimentary structure of Gh (r)' is similar to that of Gh (r), except that in Gh (r)', clasts are dominated by pebble- to granule-sized clasts with a larger amount of sand than that in Gh (r)

(Fig. 5.9b).

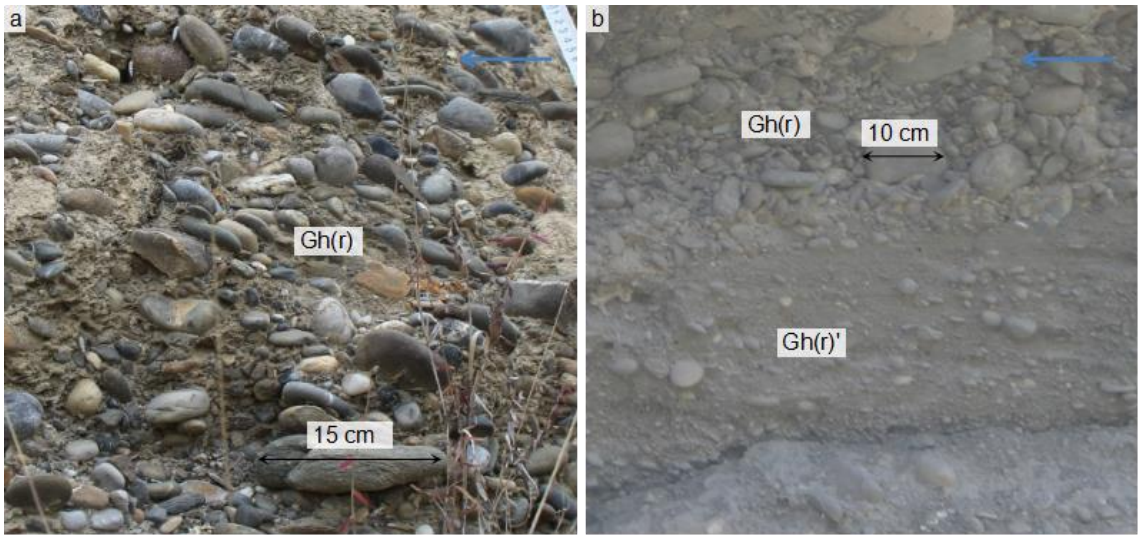

Fig. 5.9 Photographs of lithofacies Gh (r) (a) and Gh (r)' (b). Blue arrows indicate the flow direction of the Bailong River.

Lithofacies Gcm refers to clast-supported massive pebble- to boulder-sized clasts with silty matrix. This type of lithofacies is present in sections T4S1, T3S1, T2S1, T2S2, T2S3, T2S4, T1S1_B, T1S3_C. The lithology of clasts is dominated by limestones (> 50% volume). Clasts are generally weakly imbricated (Fig. 5.10). Boulder-sized clasts are distributed across the sediment unit with variable dips but similar orientations to the flow direction (Fig. 5.10). The thickness of each bed is usually larger than 1 m. The bed surface is undulatory, and the bed base can be erosive (Fig. 5.10c) or not (Fig. 5.10b). In some cases, the bed base is formed by a thin (one-grain diameter) layer of imbricated gravels (Fig. 5.10a). The sediments in each unit are massive (i.e., with no stratification), though generally the a-axes of gravels are parallel to the flow direction (Fig. 5.10). Clast fabrics measured for these sediments (Fig. 5.11) indicate variable levels of preferential arrangements, from chaotic (with a principal eigenvalue of 0.37 for section T4S2, Fig. 5.11d) to strong (with a principal eigenvalue of 0.69 for the unit in section

T2S2, Fig. 5.11c).

Fig. 5.10. Photographs of lithofacies Gcm. Panels a, b, c, and d are the photographs of Gcm at sections T4S1, T2S2, T3S1 and T2S3 respectively. Blue lines indicate the flow direction.

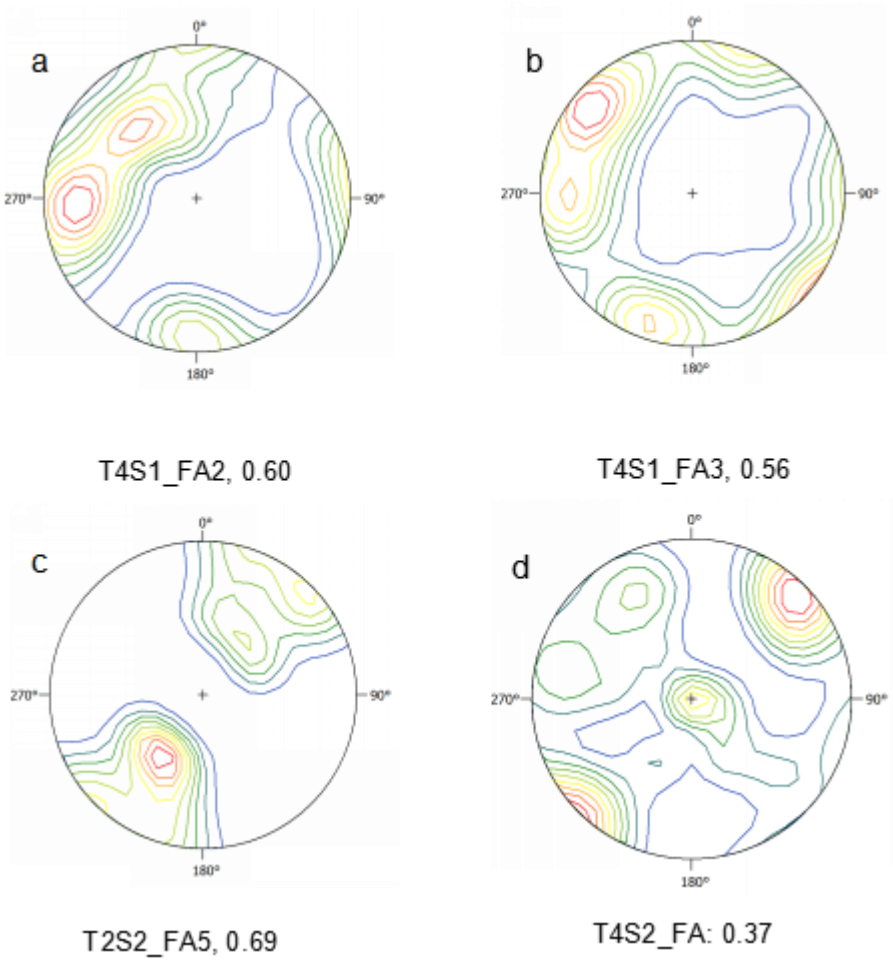

Fig. 5.11. Result of fabric measurement for facies Gcm. The sampling numbers for T4S1 FA2, T4S1 FA3, T2S2 FA5 and T4S2 FA are 40, 40, 20 and 21, respectively.

Lithofacies Gci refers to poorly sorted clast-supported cobble- to pebble-sized clasts which are inversely graded (Fig. 5.12). These sediments are present at sections T4S1, T2S1, T2S3, T2S4, and T1S1_A. Limestone forms the primary clast lithology (>50%). The bed thickness is usually larger than 50 cm (Fig. 5.12). In each unit, granule to pebble clasts are closely packed in the bed base, while cobble to boulder clasts are distributed in the bed top. The cobbles or boulders form variable dips, with their a-b planes either vertically standing (Fig. 5.12a, c) or declined gently (Fig. 5.12b, d). In contrast, the pebbles or granules in the bed base generally develop gentle dips (Fig. 5.12). No erosional base is found for

these sediments. In some cases, the bed top is covered by a thin layer (10 – 20 cm) of massive fine silt (Fig. 5.12 b, d), and this massive silt usually drapes down the clasts. Only one unit was measured for clast fabric in section T4S1. However, the b-axes were measured for this unit during early field investigations in 2013. This measurement is not discussed here.

Fig. 5.12. Photographs of lithofacies Gci. Panels a, b, c, and d are the photographs of Gci at sections T4S1, T2S3, T1S1_A and T2S1 respectively. Blue lines indicate the flow directions.

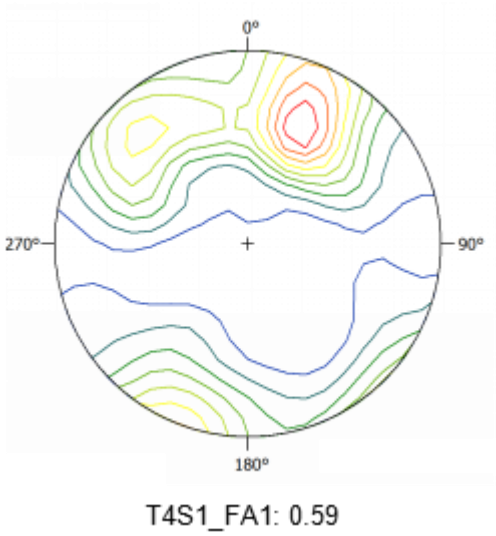

Fig. 5.13. Result of fabric measurement for facies Gci. Sampling number is 40, and the b-axes were measured.

Lithofacies Gmm refers to massive silt-matrix-supported pebble- to cobble-sized clasts. This lithofacies is present in sections T4S2, T3S1, T2S1, T2S2 and T1S2. Limestone forms the primary lithology (>50%) of the sediments. In each unit, the bed base is not erosional and usually flat. Clasts are usually of cobble size and are concentrated close to bed base. The amount of silty matrix increases upwards from the bed base, and the top of each unit is covered by a thin layer (~ 10 cm) of massive silt which drapes down the gravelly sediments. Clasts are generally chaotic with no internal grading (Fig. 5.14a), and in some cases cobble to boulder clasts are distributed close to bed base, indicating a coarse-tail grading[2] (Fig. 5.14b). The bed thickness is generally larger than 50 cm (Fig. 5.14). The principal eigenvalues of clast fabrics range between 0.42 – 0.62 (Fig. 5.15), indicating that variable levels of clast preferential alignment occur in the sediments of this type.

[2] Coarse tail grading means coarse grains become progressively smaller towards the top of the bed, and the finer grains are ungraded. This occurs in a concentrated bedload or debris flows when the flow energy drops slowly enough to allow the coarse grains settling out first while leaving the fine grains still in suspension. Bouma, A.H., Kuenen, P.H., Shepard, F.P., 1962. Sedimentology of some flysch deposits: a graphic approach to facies interpretation. Elsevier Amsterdam.

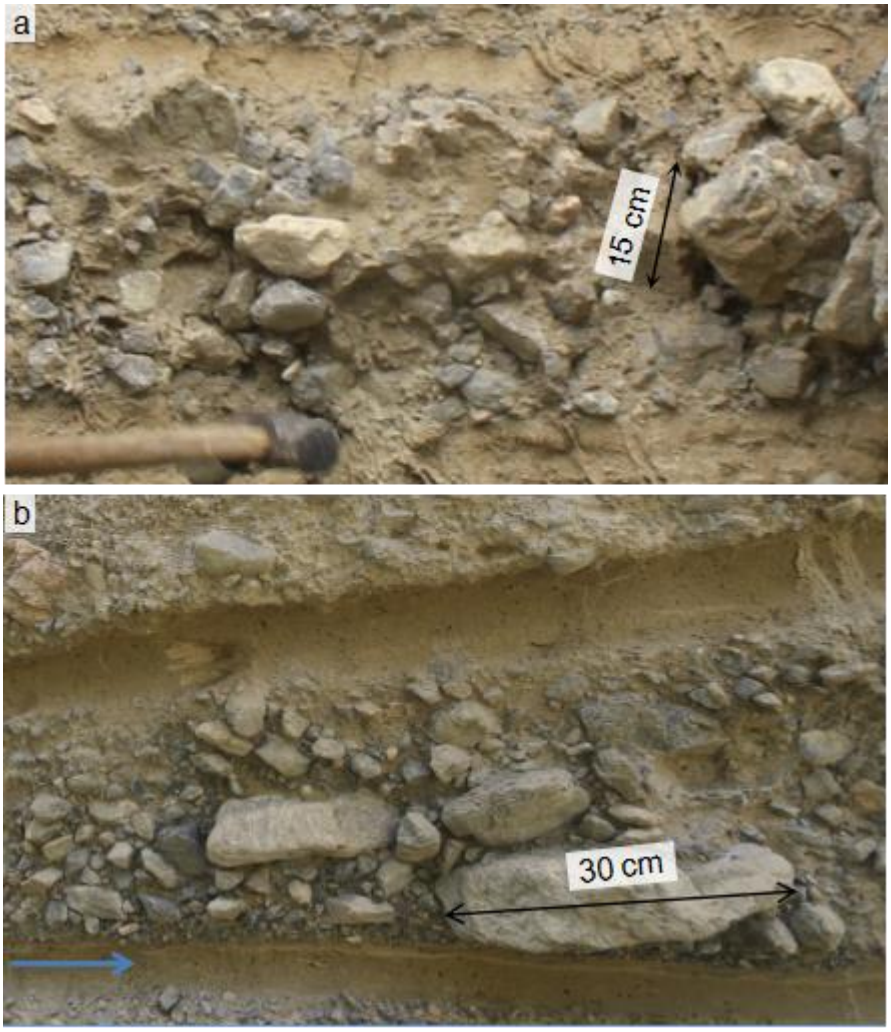

Fig. 5.14. Photographs showing the characteristics of lithofacies Gmm. a. Photograph of Gmm in section T1S2. The flow direction points into the page. b. Photograph of Gmm in section T2S2. The blue line indicates the flow direction.

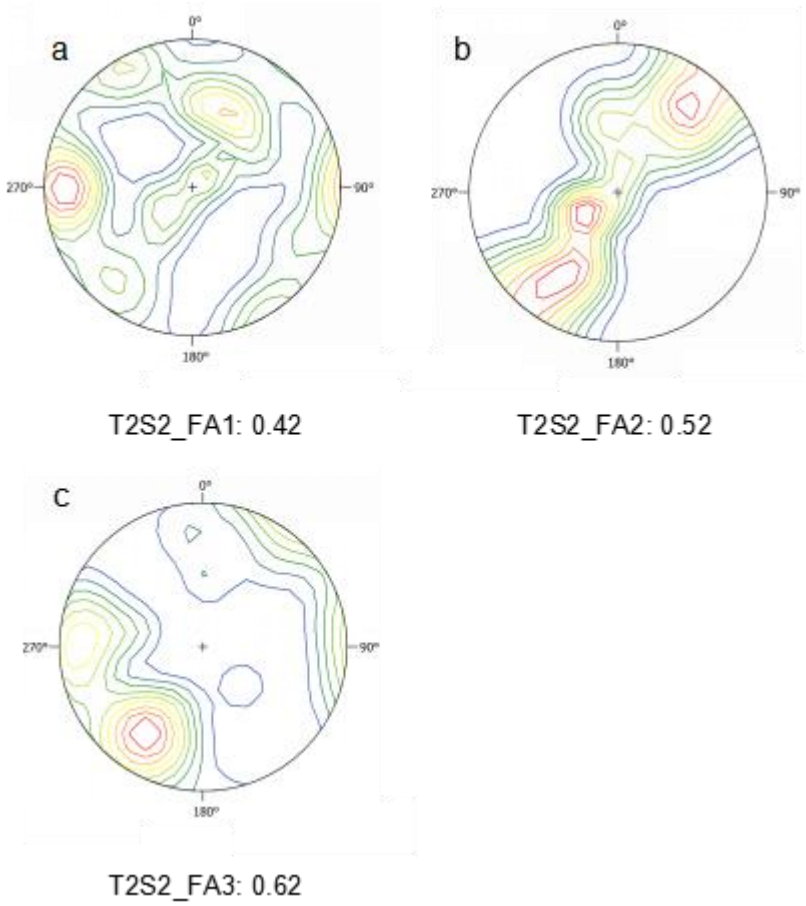

Fig. 5.15. Result of fabric measurements for lithofacies Gmm. Clast fabrics were measured along the a-axes and 20 clasts were measured for each unit.

Lithofacies Sh refers to horizontally laminated sand, which is only present in section T1S3_B. **Lithofacies Fm** refers to silt and clay with some granules. Mostly, the fine materials form thin (10 – 20 cm) flat beds and usually drape down the underlying clasts. The bed surface is flat and horizontal, but the base is irregular. The bed pinches out laterally for ~10 m. This type of beds is present in most of the sections examined in the study. Lithofacies **Fm'** refers to relatively homogeneous silt, which usually forms thick units (>50 cm). Some gravels or plant roots are present in the sediment. This type of beds is present in the upper part of the T1 and T2 terraces.

5.3 Lithofacies associations and interpretations

According to Evans and Benn (2004), certain types of lithofacies are grouped into lithofacies associations to interpret *en bloc* the depositional environments. Here six types of LFAs are summarized, and the distribution of the LFAs at each section is displayed in Table 5.1 and Fig. 5.2. A detailed description of each LFA is presented below.

Table 5.1. Types of lithofacies associations (LFAs) identified from the terrace outcrops

Section codes	Lithofacies recorded	LFA
TpS	Gh	LFA1
T4S1	Gci, Gcm	LFA2
T4S2	Gcm, Fm	LFA2
T3S1	Gmm, Gcm, Gh', Fm	LFA1, LFA2
T3S2	Gh, Fm	LFA1
T3S3	Gh, Gh (p)	LFA1, LFA3
T3S4	Gh, Gh (p)	LFA1, LFA3
T3S5	Gh (p), Fm	LFA3
T2S1	Gh, Gh', Gci, Gcm, Gmm, Fm, Fm'	LFA1, LFA2, LFA5
T2S2	Gmm, Gh, Gcm, Fm	LFA1 and LFA2
T2S3	Gh, Gci, Gcm, Gh' and Fm	LFA1 and LFA2
T2S4	Gcm, Gci, Fm, Gh'	LFA1 and LFA2
T1S1_A	Gci, Gh', Fm	LFA2
T1S1_B	Gcm, Fm, Fm'	LFA2 and LFA5
T1S2	Gmm, Gh, Fm	LFA1 and LFA2
T1S3_A	Gh (r), Gh (r)'	LFA4
T1S3_B	Gh, Sm, Gh', Gh (r)	LFA 6
T1S3_C	Gh, Fm, Gcm	LFA1 and LFA2

5.3.1 LFA1

LFA1 is mainly composed of lithofacies Gh, and sometimes Gh' and Fm are also present. LFA1 is present in most of the sections logged in this study (Table 5.1). In the Gh sediments, the poorly sorted nature of the sediments, as well as the presence of large boulders across the unit, indicates that these sediments have

been deposited by energetic processes such as floods or mass flows (Blair and McPherson, 1994). The formation of a (p) fabrics of clasts indicate some inter-particle collisions during sediment transportation (Rees, 1968, 1983), suggesting a thick bedload or traction carpet transportation (Hein and Walker, 1977; Lowe, 1982; Rust, 1984; Smith, 1986; Todd, 1989; Sohn, 1997; Suresh et al., 2007; Singh and Tandon, 2010; Hungr et al., 2014). Each sedimentation unit is comprised of many stratifications, indicating that the unit has been formed by multiple surges during a flooding event (Went, 2005). Collectively, these interpreted characteristics (i.e., traction carpet transportation in multiple surges of floods) indicate that the Gh sediments have been deposited by hyperconcentrated floods (Sohn, 1997; Hungr et al., 2014). In contrast, the sediments of lithofacies Gh' are usually better sorted than the sediments of lithofacies Gh, suggesting that they have been deposited by less energetic flooding processes. The normally graded structures within these sediments also indicate deposition in the waning stages of a flood (Whiting et al., 1988; Todd, 1989). The limestone-dominated clast lithology in both Gh and Gh' indicates that these sediments mainly came from the high-elevation limestone areas. The Fm sediments which usually overly these Gh sediments indicate deposition by relatively low-energy water flows (Blair and Mcpherson, 1994), representing slight modifications to the Gh sediments. Overall, LFA1 indicates a depositional environment dominated by hyperconcentrated floods with some waning flow or small streamflow modifications.

5.3.2 LFA2

LFA2 is mainly composed of lithofacies Gmm, Gci, and Gcm, with some

occasional Fm or Gh' sediments. For Gmm, Gci and Gcm sediments, the bed is usually larger than 50 cm thick with an absence of internal stratifications, indicating deposition from a highly concentrated body of sediments with high internal strength (Johnson, 1970; Fisher, 1971, 1983; Johnson and Rodine, 1984; Hubert and Filipov, 1989; Colombera and Bersezio, 2011). The sediments are mainly poorly sorted pebble to cobble clasts with silty matrix, and many boulder-sized clasts are present in each bed, indicating that sediments covering a large grain-size ranges (from fines to boulders) have been transported together before deposition (Lowe, 1982; Hungr, 2005). Collectively, these sediments suggest deposition by a mixture of sediments with a large range of grain sizes and high internal strength, indicating debris flow deposition (Blair and McPherson, 1994; Sohn, 2000; Dutta et al., 2012). Specifically, the three types of lithofacies (i.e., Gci, Gcm and Gmm) may indicate debris flow processes with some differences in sediment composition and transport condition. The clast-supported inversely graded sediments (Gci) indicate rapid shear among granular sediments during transportation (Bagnold, 1954; Middleton, 1970; Iverson, 1997; Kim and Lowe, 2004; Dasgupta and Manna, 2011), suggesting cohesionless debris flows (Takahashi, 1981; Pierson and Costa, 1987; Kim and Lowe, 2004). The massive clast-supported sediments (Gcm) indicate subdued rapid shears among granular sediments. This is probably caused by the increase of silty-matrix which enhance the cohesive strength of the sediment body, leading to a massive ungraded structure (Sohn et al., 1999; Miall, 2006). The massive matrix-supported sediments (Gmm) indicate deposition by cohesive debris flows (Lowe, 1982; Miall, 2006). In some cases, boulder-sized clasts are in the bed base of Gmm sediments, indicating that these clasts can settle down during flow stage and

probably suggest a flow condition with less granular sediments than those in Gci and Gcm. Smaller pebble- to cobble-sized clasts are dispersed within the matrix, indicating the existence of intergranular dispersive pressure (Lowe, 1982; Nemec, 1990; Hungr et al., 2001). The clast lithology of these three lithofacies (i.e., Gci, Gcm and Gmm) is dominated by limestones, indicating that these sediments were mainly sourced from the high-elevation limestone area of the GLP valley. The Fm sediments, which drape down the gravelly sediments, and the Gh' sediments, which are intercalated between two debris flow sediments, may indicate waning flow deposition or deposition by occasional floods on inactive segments of alluvial-fan surfaces (Sohn et al., 1999).

5.3.3 LFA3

LFA3 is mainly composed of lithofacies Gh (p) with some Fm sediments. The horizontally bedded structures of these gravelly sediments indicate deposition by stream or hyperconcentrated floods (Rust, 1984; Sohn et al, 1999). However, the sediments are dominated by phyllite clasts, indicating a different source area to the Gh sediments. Similar phyllite deposits are found in the Xiaogou valley, a tributary of the GLP valley. This valley developed exclusively in the phyllite areas. It is likely that these Gh (p) sediments have been mainly transported by channelized stream/hyperconcentrated floods from the Xiaogou valley.

5.3.4 LFA4

LFA4 is mainly composed of lithofacies Gh (r) and Gh (r)'. These sediments are mainly present at the mouth of the GLP valley. They can be easily distinguished from the sediments previously described according to clast roundness and lithology. The clasts in these sediments are generally rounded to well rounded,

indicating a longer distance of movement than that of the sub-angular clasts. The clast lithology includes some sandstones and granites which are exotic lithologies to the GLP valley. Collectively, the long distances of clast transportation and the existence of exotic clast lithology to the GLP valley indicate that these sediments were deposited by the Bailong River. The crudely bedded sediments which are dominated by gravel-sized clasts may indicate longitudinal bar deposition by some diffusive gravel sheets (Hein and Walker, 1977; Miall, 2006).

5.3.5 LFA5

LFA5 is mainly composed of lithofacies Fm'. It is present at the top part of sections T2S1 and T1S1_B. These sediments are formed by relatively homogeneous yellowish fine silt, forming thick (> 50 cm) units, indicating loess deposition by aeolian processes (Kukla, 1987; Porter, 2007). Some gravels, plant roots, and soil nodules are present in these sediments indicating that the aeolian sediments were disturbed by some alluvial and biogenic processes (Cui and Xiong, 1990; Blair and McPherson, 1994).

5.3.6 LFA6

LFA6 is composed of lithofacies Sh, Gh, Gh' and Gh (r). It is present only at section T1S3_B at the mouth of the GLP valley. The horizontally bedded sand (Sh) indicates deposition as a bedload (Lowe, 1982; Miall, 2006). This type of bedload may exist in the waning stage of a flood or in a normal streamflow (Mail, 2006). Because this type of sediment is close to the Bailong River and caps the gravelly sediments (Gh (r) and Gh (r)') which were interpreted as Bailong River deposits, it is likely that this sediment has been deposited by the Bailong River. The horizontally bedded limestone-dominated clasts (Gh' and Gh) which are

interleaved between the sandy sediments indicate occasional deposition by stream floods or hyperconcentrated floods from the GLP valley. The horizontally-bedded well rounded clasts (Gh (r)) indicate channel deposition by the Bailong River (Miall, 2006). Collectively, the alternation of the sediments of the Bailong River (lithofacies Sh and Gh (r)) and the GLP valley (lithofacies Gh and Gh') indicates that Bailong River and the GLP river alternatingly deposited sediments at this section.

5.4 Terrace sedimentology

The depositional processes/environments are revealed by the sedimentary analyses presented in Sections 5.2 and 5.3.

For the T1 terraces, three sections (i.e., T1S1, T1S2 and T1S3) from the midstream to the downstream portion of the valley were logged (Fig. 5.1). The lower section of T1S1 (i.e., section T1S1_A) is formed by debris flow sediments, specifically cohesionless debris flows (Gci). However, the upper part of the section (i.e., section T1S1_B) is formed by loess and cohesive debris flow sediments (Gcm). Section T1S2 was an outcrop representing the top part of the T1 terrace, and only has an exposed thickness of ~ 2 m. This section is mainly formed by sediments of cohesive debris flows (Gmm), accounting for the upper part of the section, with the lower part being formed by sediments of hyperconcentrated floods (LFA1). For section T1S3 (at the mouth of the GLP valley), the three sub-sections (i.e., T1S3_A, T1S3_B and T1S3_C) each indicate a distinct depositional environment. Section T1S3_A, which is formed by LFA4, indicates channel or longitudinal bar deposition of the Bailong River. Section

T1S3_B, which is composed of LFA6, indicates a depositional environment alternatingly dominated by the GLP river and the Bailong River. Section T1S3_C is mainly formed by hyperconcentrated flood sediments (LFA1) with some debris flow sediments (LFA2) that were sourced from the limestone-headwater of the GLP valley.

The T2 terraces were examined in four sections (i.e., T2S1, T2S2, T2S3 and T2S4). These sections are invariably formed by sediments of debris flows (LFA2) and hyperconcentrated floods (LFA1). However, one manifest distinction exists between section T2S4 and the other three sections. Gravels in section T2S4 are generally coated with thin (< 0.5 mm) black varnish (Appendix 5, Fig. A5.21), while gravels in the other three sections do not have such a feature, indicating that sediments of section T2S4 are older than those of sections T2S1, T2S2 and T2S3 (Bull, 1977; Dorn, 1988; McFadden et al., 1989; Bockheim, 2010). It is likely that section T2S4 represents some old terrace relics. For each of the remaining three sections (i.e. T2S1, T2S2 and T2S3), debris flow sediments generally form the lower half section while hyperconcentrated flood sediments form the upper half section (Fig. 5.2). This sequence likely indicates a decreasing trend of granular sediment supply and an increasing trend of water runoff during the construction of the T2 alluvial terraces.

The T3 alluvial terraces were examined in five sections (Fig. 5.1). Sections T3S1 and T3S2 (Fig. 5.2) both indicate deposition by sediments sourced from the limestone headwaters of the GLP valley because the sediments of these two sections are formed by limestone-dominated clasts. Section T3S1 was mainly

formed by debris flows (LFA2), and section T3S2 was formed by hyperconcentrated floods (LFA1). Sections T3S3 and T3S4, which were formed by the sediments of LFA1 and LFA3 (Fig. 5.2), indicate alternating deposition by flooding processes from the Xiaogou (with a phyllite headwater) and the Dagou valley (with a limestone headwater). Section T3S5, which was formed by LFA3 (Fig. 5.2), indicate deposition by stream/hyperconcentrated floods from the Xiaogou valley. The difference in formation processes of these five T3 terrace sections indicates that the T3 terraces have been formed by the processes from both the Xiaogou valley and the Dagou valley.

Two sections (T4S1 and T4S2) were examined for the T4 terraces and one (TpS) for the floodplain. The two sections for the T4 terraces, which were formed by LFA2, indicate debris flow deposition that was sourced from the limestone headwater of the GLP valley. The floodplain section (TpS), which was formed by LFA1, indicates deposition by hyperconcentrated flooding processes, also from the limestone headwaters of the GLP valley.

Overall, the sedimentary analyses of alluvial terraces indicate that debris flows and hyperconcentrated floods are two primary constructing processes for the terraces in GLP.

5.5 Conclusions

The eighteen sedimentary profiles logged for the alluvial terraces reveal six types of depositional processes/environments.

(1) The dominant processes forming the terrace alluvium are hyperconcentrated

floods (LFA1) and debris flows (LFA2) which were sourced from the high-elevation limestone-headwaters of the GLP valley, i.e., the Dagou valley.

(2) Some parts of the T3 terraces were formed by stream/hyperconcentrated floods (LFA3) that were sourced from the phyllite Xiaogou valley, a tributary of the GLP valley.

(3) The lower section (T1S3_A) of the T1 terraces at the mouth of the GLP valley was exclusively formed by longitudinal bar deposits of the Bailong River (LFA4), the mid-section (T1S3_B) was formed by alternating deposition from the Bailong River and the GLP valley (LFA 6), and the upper section (T1S3_C) was formed by hyperconcentrated floods (LFA1) and debris flows (LFA2) from the GLP valley.

(4) Loess deposition (LFA 5) occurred in between or after the alluvial processes that formed the T1 and T2 terraces.

Chapter 6 Results: Borehole Sedimentology

6.1 Introduction

This chapter presents the results of the boreholes drilled in the GLP valley during my PhD study. In total four boreholes were drilled in May 2013 (i.e., cores D02 and D04) and October 2014 (i.e., cores D01 and D03) (Fig. 6.1). Core D01 is positioned at the mouth of the GLP valley, and core D02 is about 800 m upstream (Fig. 6.1). Cores D03 and D04 are located at the intersections between the Xiaogou and Dagou channels. Cores D01, D02 and D03 all reached the basal bedrock. This chapter will present the results of sedimentary logging for cores D01 and D03. Sediment logs of cores D02 and D04 are not available because during the drilling of cores D02 and D04 the sediments were not preserved or well described.

During the drilling process, sediments entered the core barrel. When the core barrel was filled, or the teeth of the drill bit were worn out, the core barrel was lifted, and the core sediments were extruded under gravity with the aid of a hammer to vibrate the core barrel. The core materials were then laid on the ground in stratigraphic order for description. The core retrieval ratios are generally about 70-80%, however at some sections with sandy or no matrix, the retrieval ratio is less than 50%. These sections with low retrieval ratios usually hold underground water and are the most difficult part to drill due to the occasional collapse of the borehole wells.

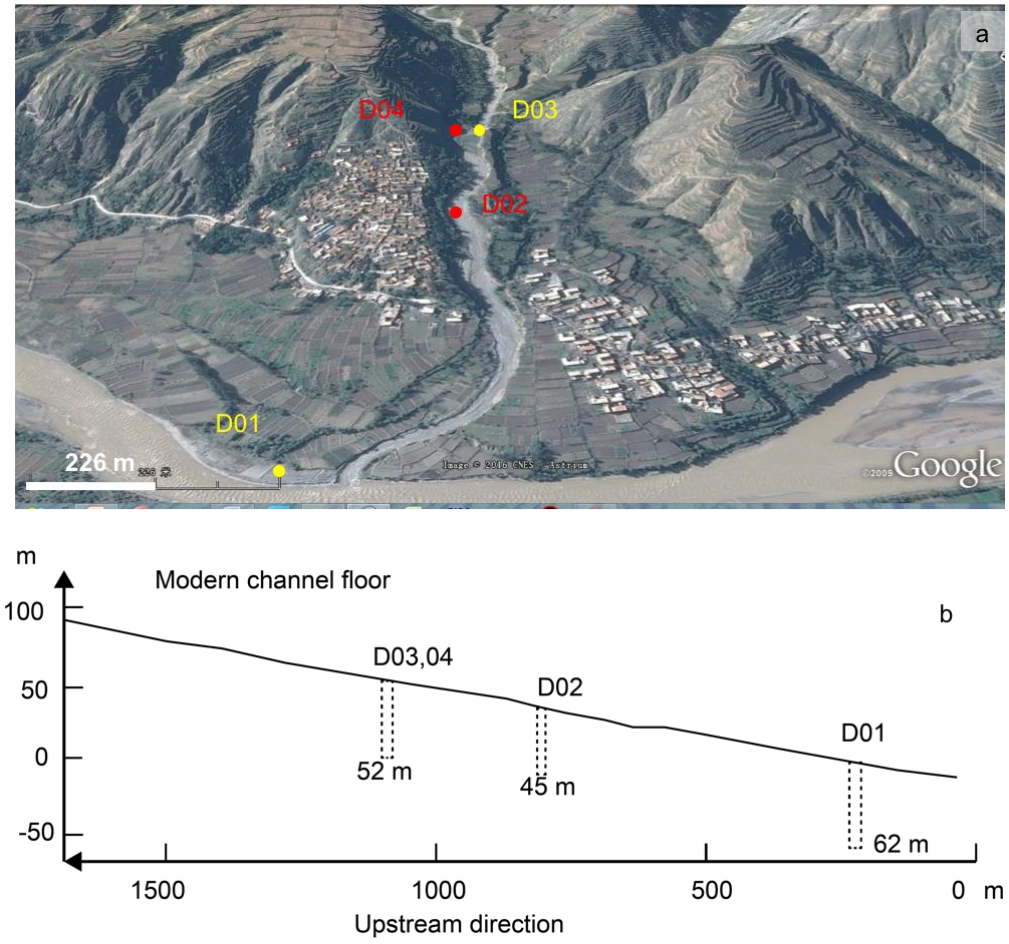

Fig. 6.1 Locations and depths of boreholes in the GLP valley. a. Locations of the boreholes in the GLP valley. Yellow points represent boreholes drilled in October 2014, and red points represent boreholes drilled in May 2013. Background image is sourced from Google Earth. b. Distribution of boreholes along the GLP channel. Drilled depth is to scale.

6.2 Lithofacies types of core materials

Detailed information of the core materials is presented in Appendix 6 and Fig. 6.2. Based on this information, the types of lithofacies were summarized (Table 6.1). The core materials were classified into cobble facies (C1 and C2), pebble facies (P1, P2 and P3), granule facies (Gr1, Gr2, Gr3 and Gr4) and fine facies (S1, S2 and S3).

Cobble lithofacies were classified into two types: the poorly/moderately sorted,

sub-angular to sub-rounded limestone-dominated clasts with no or silty matrix (C1) and the moderately sorted rounded to well rounded limestone-dominated clasts with sandy matrix and some sandstones and granites (C2). The C1 sediments were present at both D01 and D03, and the C2 sediments were only present at D01.

Pebble lithofacies were classified into three types: the poorly sorted sub-angular to sub-rounded limestone-dominated clasts with silty matrix (P1), the poorly/moderately sorted sub-angular to sub-rounded limestone-dominated clasts with no or sandy matrix (P2), and the moderately/well sorted rounded to well rounded clasts with sandy matrix and a variety of lithologies including sandstone, phyllite, limestone, granite and quartzite. The P1 and P2 sediments were present at D01 and D03, while the P3 sediments were only present at D03.

Granule lithofacies were classified into four types. The first one (Gr1) is poorly sorted, sub-angular to sub-rounded clasts with sandy matrix and a similar proportion of limestone and phyllite clasts. This type of sediment was only recovered from D01(depth 0-0.7 m). The second type (Gr2) is moderately/well sorted sub-angular to rounded limestone-dominated clasts with no or sandy matrix. This type of sediment was present in the two cores but usually accounts for a small proportion (less than 1%) of the whole section. The third type (Gr3) is moderately/well sorted rounded to well rounded clasts with sandy matrix and a variety of lithologies (limestone, phyllite, sandstone, granite and quartzite). This type of sediments was present at D01. The fourth type (Gr4) is muddy clasts with a dominant proportion of phyllite. This type of sediment was only present close to

the bottom of D01.

Fine lithofacies refer to sediments with their grain sizes smaller than 2 mm. Three distinct types of fine lithofacies were present in the two cores: the first one is sand-sized sediments (S1). This was only present at two positions in D01. Each sediment body has a thickness of ~ 20 cm. The second type (S2) is the silt-sized greyish material which is only present at the base of each core. This type of sediment is interpreted as derived from the phyllite bedrocks. During drilling, the diamond drill bits usually crushed the phyllite bedrocks into silt-sized materials. When these types of materials were drilled out, they indicate that the channel bottom had been attained. The third type (S3) comprises yellowish-brown silt-sized materials and is only present at D03.

Table 6.1 Types and characteristics of different lithofacies present in cores D01 and D02. Meaning of abbreviations: DGS=dominant grain size; LFs=lithofacies.

DGS	LFs	Characteristics
Cobble	C1	Poorly sorted, sub-angular to sub-rounded, limestone-dominated, with no or silty matrix
	C2	Moderately sorted, rounded to well rounded, limestone-dominated with sandstones and granites, with sandy matrix
Pebble	P1	Poorly sorted, sub-angular to sub-rounded, limestone-dominated, with silty matrix
	P2	Poorly sorted, sub-angular to sub-rounded, limestone-dominated, with sandy or no matrix
	P3	Moderately/well sorted, rounded to well rounded, with limestones, sandstones and granites, with sandy matrix.
Granule	Gr1	Poorly sorted, sub-angular to sub-rounded, with similar proportions of limestone and phyllite clasts, sandy matrix.
	Gr2	Moderately/well sorted, sub-angular to rounded, limestone-dominated, with no or sandy matrix,
	Gr3	Moderately/well sorted, rounded to well rounded, sandy-matrix-supported, with various lithology including limestones, sandstones, granites and phyllites
	Gr4	Muddy granule-sized phyllite clasts
Fine	S1	Sands with some granules
	S2	Silt-sized greyish phyllite materials
	S3	Silt-sized yellowish-brown materials

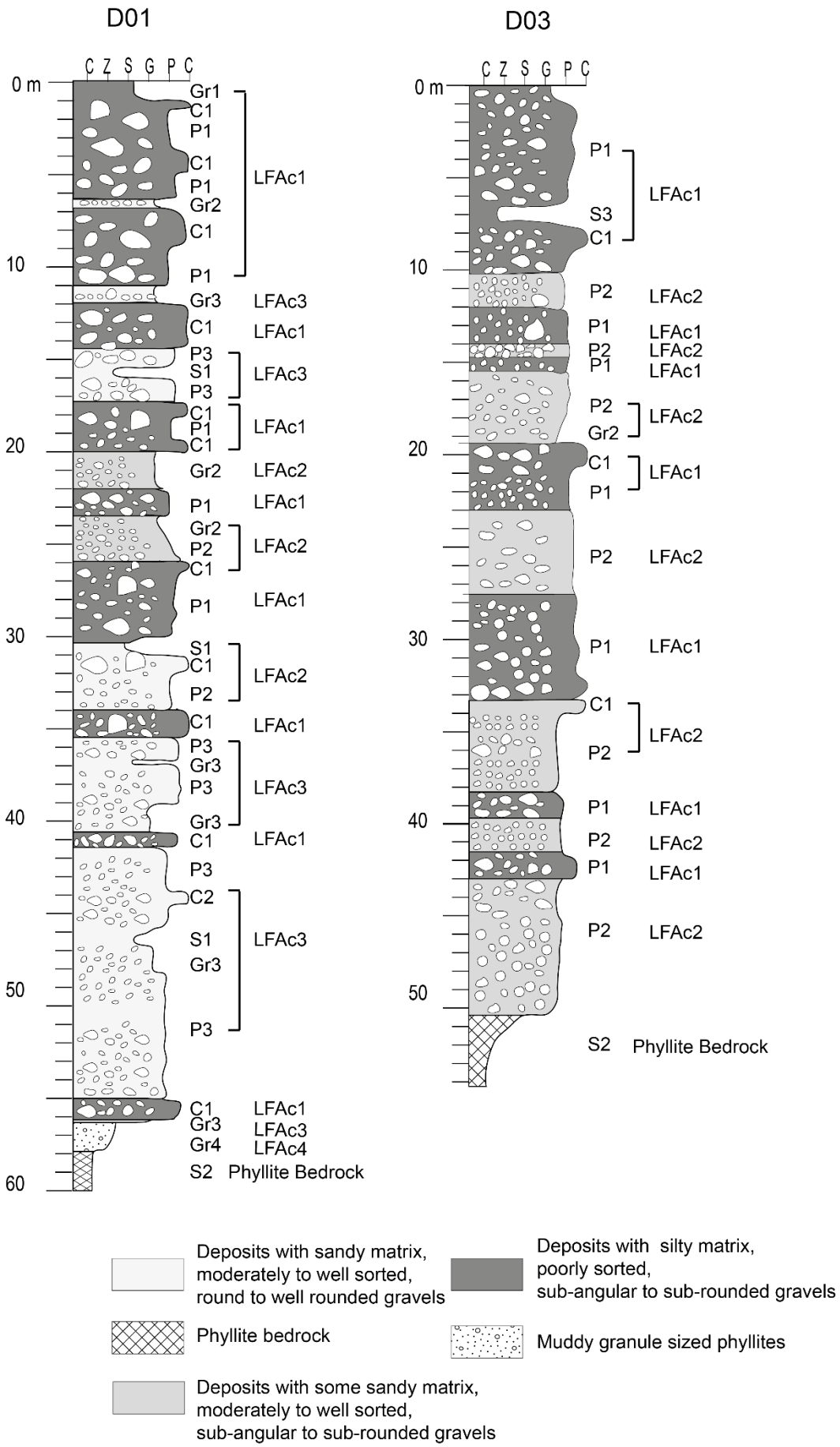

Fig. 6.2. Detailed sedimentary characteristics of cores D01 and D03.

6.3 Lithofacies associations (LFAs) and interpretations

According to the sedimentary characteristics, the sediments are classified into four types of lithofacies associations as is listed in Fig. 6.2.

LFAc1 includes lithofacies C1, P1, Gr1, Gr2 and S3. The main forming lithofacies are C1 and P1 which are characterized by poorly sorted pebble to cobble clasts with silty matrix. These sediments are limestone-dominated, indicating a source from the GLP limestone headwater. The incorporation of silty matrix in P1 makes these sediments highly cohesive, and the sediments extruded from the core barrels generally adhered to each other forming columnar shapes. Collectively, the dominance of pebble- to cobble-sized clasts and the incorporation of high cohesive strength indicate that these sediments were deposited by debris flows (Pierson and Costa, 1987; Sohn, 2000). The Gr1 and Gr2 sediments represent periods of deposition by some secondary processes such as small streamflows during the termination of debris flow deposition (Blair and McPherson, 1994),.

LFAc2 includes lithofacies C1, P2 and Gr2. The constructional facies are P2 which are characterized by poorly-sorted pebble-sized gravels with no or sandy matrix. The absence of matrix in these sediments may be due to the work of underground water as during drilling underground water was present at the depth of 7 m beneath the ground. However, it is more likely that a lack of silty-matrix within the sediment had been formed during the deposition of these sediments. The lack of silty matrix and the incorporation of a wide range of clast-sizes (from granules to cobbles) within these sediments are similar to the characteristics of the Gh sediments, and it is likely that the P2 sediments are a representation of

the Gh sediments in the boreholes. Therefore, these sediments (P2) were interpreted as deposits of hyperconcentrated floods (Sohn et al., 1999). The granule sediments (Gr2) may have been deposited during waning stages of floods or during intervals of flooding processes by some small streamflows (Blair and McPherson, 1994).

LFAc3 includes lithofacies P3, Gr3 and S1. The primary features of these sediments are clast roundness and lithological composition. The clasts are generally rounded to well-rounded indicating a longer transportation distance than that of the sub-angular to sub-rounded clasts before deposition. The incorporation of some exotic lithology such as sandstones and granites indicates that these sediments were sourced from places far away from the GLP River. The clast roundness and the incorporation of exotic lithology of these sediments (P3 and Gr3) are similar to the characteristics of Gh (r) and Gh (r)' sediments. It is likely that the P3 and Gr3 sediments are representations of the Gh (r)/Gh (r)' sediments in the boreholes. Therefore, these sediments were interpreted as deposits of the Bailong River, possibly representing longitudinal bar deposition (Mail, 2006).

LFAc4 is characterized by Gr4 which is only present at core D01. These sediments are characterized by muddy granule-sized phyllites indicating a weathering layer because these granule-sized phyllites mixed with silt-sized materials are present in many of the phyllite hillslopes in GLP forming the present weathering layer of the phyllite bedrocks. When these sediments are agitated with water, they become muddy granule-sized phyllites.

6.4 Core sedimentology

The depositional processes of the channel fills are revealed through the sedimentary analyses of the two cores.

Core D01 was filled by sediments from the GLP valley and the Bailong River. Specifically, the lower section of core D01 (core depth 55–35.4 m), was dominated by LFAc3, indicating a depositional environment dominated by the Bailong River, though at core depth 40.7–41.2 m, some LFAc1 sediments are present, representing debris flow deposition by the GLP valley. The upper section of core D01 (core depth 35.4 – 0 m) is dominated by sediments (LFAc1 and LFAc2) from the GLP valley. Specifically, LFAc1 sediments account for a total depth of ~21.5 m, while LFAc2 sediments form a total depth of ~8 m, indicating a larger portion of debris flow sediments than that of hyperconcentrated flood sediments. Some well-rounded clasts of exotic lithology are present at the core depths of 14.4 – 17.1, 11 – 11.8, 6.6 – 6.9 m, indicating that fluvial processes from the Bailong River occasionally brought sediments to this site.

Core D03 was filled by sediments (LFAc1 and LFAc2) solely from the GLP valley. The LFAc2 sediments are characterized by poorly/moderately sorted gravels with sandy/no matrix, indicating deposition by hyperconcentrated floods. These sediments lack internal strength due to the absence of silt and clay and have a very low retrieval ratio (less than 50%). These sediments were found at sections 10.4 – 12.3, 15.3 – 19.6, 23 – 27.6, 33.2 – 38.2, 39.8 – 41.8, and 43 – 50.7 m, and they have a total thickness of 25.5 m, which is 50% of the core thickness. The LFAc1 sediments are characterized by poorly sorted clasts with silty matrix,

which was interpreted as debris flows. These sediments have relatively higher cohesive strength than the sediments of LFAc2, and the majority of the sediments have been retrieved. They are present in the remaining sections and account for a total depth of 20.1 m. Collectively, core D03 was formed by sediments of debris flows and hyperconcentrated floods, and these two types of sediments account for a similar proportion of the core.

6.5 Conclusions

Four boreholes were drilled on the present channel of the GLP valley, and three of the boreholes reached the base of the channel fill at depths of 62, 45, and 52 m. Sedimentary analyses of sediments from two boreholes (D01 and D03) indicate that debris flows and hyperconcentrated floods, which were sourced from the GLP limestone headwaters, were the two primary processes forming the channel fill. At the GLP-Bailong junction, the lower portion of the borehole was dominated by fluvial deposition of the Bailong River.

Chapter 7 Results: Chronology

7.1 Introduction

This chapter presents the results of OSL dating and examines the accuracy of these OSL ages. The locations of OSL samples are presented in Fig. 7.1, and the results are provided in Fig. 7.2 and Table 7.1. The following part of this chapter assesses the accuracy of the OSL dates for samples from the four levels of terraces (T4, T3, T2 and T1) and the boreholes. The assessment mainly considers the geological settings (i.e., stratigraphic order) of the samples. The radial plot of D_e values for each OSL age is also presented, and it is used to display the D_e value overdispersion, which may provide information about the heterogeneity of each individual sample.

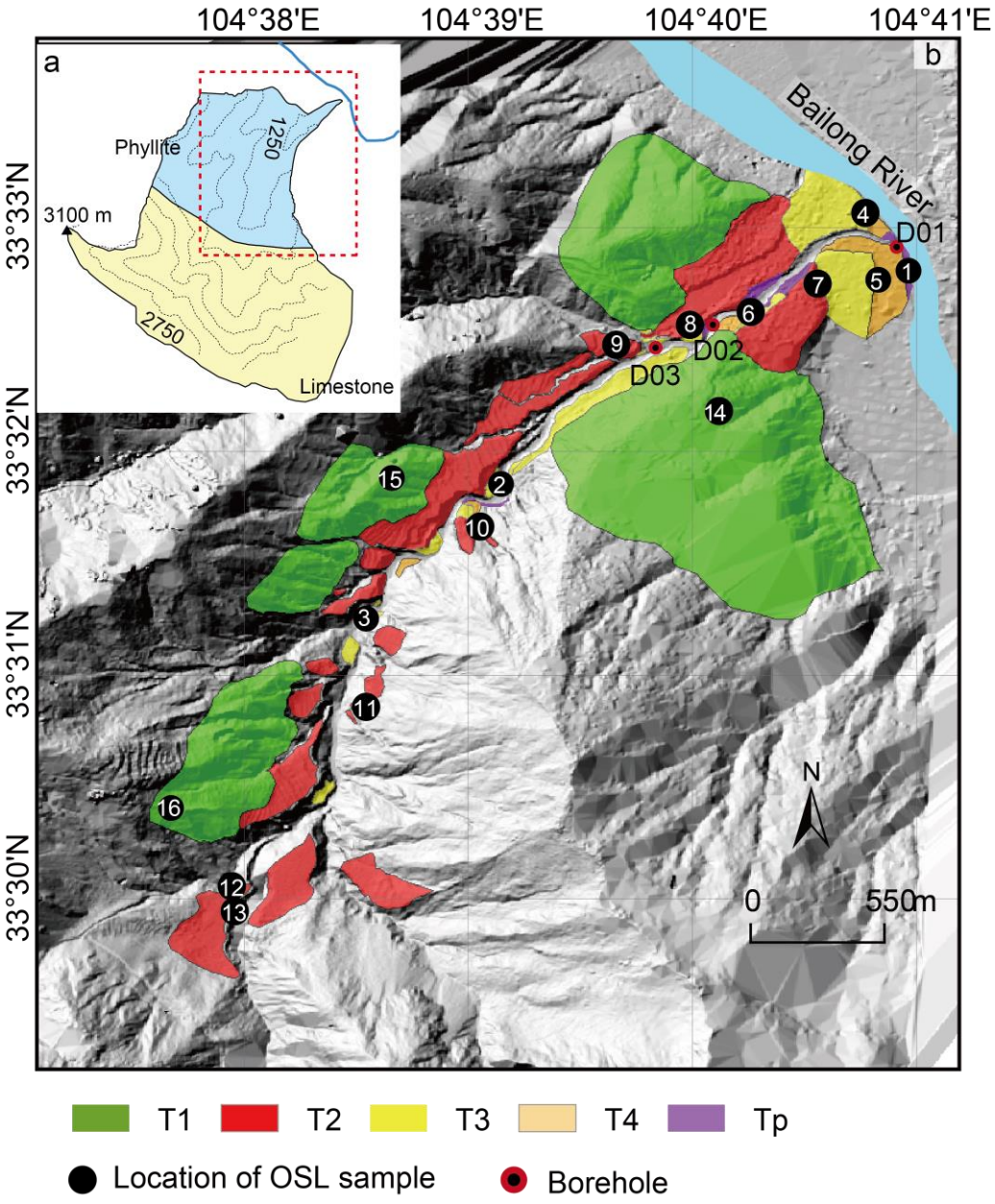

Fig. 7.1. Locations of OSL samples and boreholes. (a). The watershed of the GLP valley. The contour interval is 250 m with the highest point (3100 m) shown by a filled triangle. The dashed red box delineates the phyllite area, which is shown in panel b. (b). Locations of OSL samples in GLP. The numbered black circles indicate the locations of the OSL samples, which are shown in Fig. 7.2.

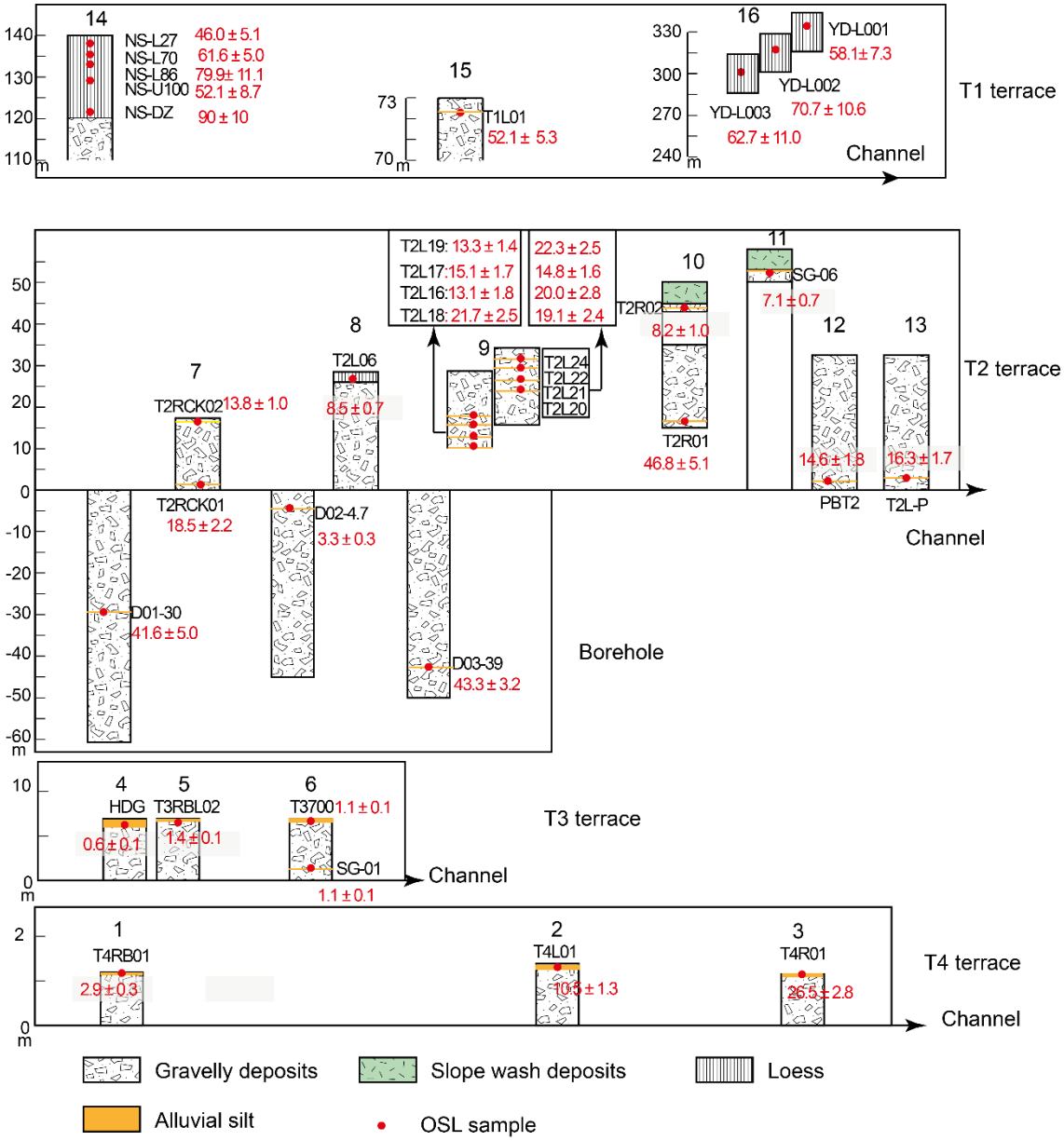

Fig. 7.2. Location and OSL ages (red numbers/ka) of the samples within each terrace profile or borehole. The vertical axis represents the elevation relative to the present channel. Upstream profiles are represented towards the right of the figure, while downstream profiles are represented towards the left. The numbers above each profile represent the locations of the profiles which were shown in Fig. 7.1.

Table 7.1 OSL dating results. W is water content. For alluvial silts above the present water table, the water content is taken as 10 ± 5% which is roughly a half of the saturated water content. For alluvial silts close to or below the present water table, their saturated water contents are measured in laboratory. For loess samples, the water content is taken as 5 ± 2%. Σ is the over-dispersion value. (n) is the number of accepted aliquots.

Sample	Origin type	Radionuclide concentrations			Sample depth	W	Cosmic dose rate	Dose rate	Equivalent Dose	(n)	σ	Age
		K (%)	U (ppm)	Th (ppm)	(m)	(%)	(Gy/ka)	(Gy/ka)	(Gy/ka)		(%)	(ka)
T4L01	Paleosol	1.54 ± 0.38	4.62 ± 0.38	4.02 ± 1.34	0.2 ± 0.2	10 ± 5	0.23 ± 0.01	3.53 ± 0.39	37.1 ± 2.1	10	18	10.5 ± 1.3
T4RBL01	Alluvial	2.83 ± 0.51	3.77 ± 0.7	13.49 ± 2.38	0.2 ± 0.2	10 ± 5	0.23 ± 0.01	5.31 ± 0.51	15.6 ± 0.2	23	6.2	2.9 ± 0.3
T4R01	Paleosol	1.74 ± 0.39	4.49 ± 0.37	4.31 ± 1.32	0.2 ± 0.2	10 ± 5	0.23 ± 0.01	3.71 ± 0.39	98.1 ± 1.3	24	5.3	26.5 ± 2.8
T3700	Paleosol	1.86 ± 0.41	3.81 ± 0.44	6.62 ± 1.52	0.5 ± 0.2	10 ± 5	0.22 ± 0.01	3.79 ± 0.39	4.1 ± 0.1	22	12	1.1 ± 0.1
SG-01	Alluvial	1.86 ± 0.41	3.81 ± 0.44	6.62 ± 1.52	5.0 ± 0.2	10 ± 5	0.12 ± 0.01	3.26 ± 0.19	2.7 ± 0.2	15	24	0.8 ± 0.1
T3RBL02	Alluvial	2.22 ± 0.45	3.19 ± 0.54	11.67 ± 1.86	1.0 ± 0.2	10 ± 5	0.2 ± 0.01	4.37 ± 0.43	6.1 ± 0.1	23	4.4	1.4 ± 0.1
HDG	Alluvial	2.37 ± 0.45	3.27 ± 0.51	10.3 ± 1.79	0.5 ± 0.2	10 ± 5	0.21 ± 0.01	4.42 ± 0.43	2.8 ± 0.1	18	7.5	0.6 ± 0.1
T2RCK01	Paleosol	1.66 ± 0.17	2.3 ± 0.23	10.84 ± 1.08	1.0 ± 0.2	10 ± 5	0.2 ± 0.01	3.49 ± 0.24	48.0 ± 0.8	20	6.8	13.8 ± 1.0
T2RCK02	Alluvial	1.39 ± 0.3	2.59 ± 0.33	7.51 ± 1.16	17.0 ± 0.2	10 ± 5	0.04 ± 0.00	2.86 ± 0.3	53 ± 2.9	18	23	18.5 ± 2.2
T2L06	Paleosol	1.74 ± 0.23	2.1 ± 0.33	9.78 ± 1.45	0.5 ± 0.2	10 ± 5	0.22 ± 0.01	3.41 ± 0.27	29.0 ± 0.4	18	4.9	8.5 ± 0.7
T2L16	Alluvial	1.52 ± 0.37	5.31 ± 0.51	5.63 ± 1.78	15.0 ± 0.2	10 ± 5	0.04 ± 0.00	3.71 ± 0.42	48.7 ± 3.8	20	35	13.1 ± 1.8
T2L17	Alluvial	1.68 ± 0.36	4.3 ± 0.4	5.64 ± 1.39	14.0 ± 0.2	10 ± 5	0.05 ± 0.00	3.53 ± 0.37	53.3 ± 1.5	21	12	15.1 ± 1.7
T2L18	Alluvial	1.18 ± 0.31	3.61 ± 0.37	6.31 ± 1.32	16.0 ± 0.2	10 ± 5	0.04 ± 0.00	2.9 ± 0.32	62.9 ± 1	23	6.4	21.7 ± 2.5
T2L19	Alluvial	1.76 ± 0.36	2.97 ± 0.44	10.4 ± 1.52	13.0 ± 0.2	10 ± 5	0.05 ± 0.00	3.61 ± 0.36	47.9 ± 1.4	24	13	13.3 ± 1.4
T2L20	Alluvial	0.66 ± 0.26	4.23 ± 0.37	4.92 ± 1.32	8 ± 0.2	10 ± 5	0.09 ± 0.00	2.53 ± 0.31	48.4 ± 0.9	20	5.9	19.1 ±2.4
T2L21	Alluvial	1.12 ± 0.45	4.32 ± 0.48	5.36 ± 1.67	7 ± 0.2	10 ± 5	0.1 ± 0.00	3.04 ± 0.42	60.9 ± 0.9	24	5.5	20.0 ±2.8
T2L22	Alluvial	1.81 ± 0.38	4.4 ± 0.45	5.8 ± 1.59	6 ± 0.2	10 ± 5	0.11 ± 0.01	3.75 ± 0.39	55.5 ± 1.8	23	15	14.8 ±1.6
T2L24	Alluvial	1.59 ± 0.38	4.68 ± 0.5	6.47 ± 1.72	3 ± 0.2	10 ± 5	0.16 ± 0.01	3.75 ± 0.41	83.7 ± 2.1	12	7	22.3 ±2.5

Table 7.2 OSL dating results. W is water content. For alluvial silts above the present water table, the water content is taken as 10 ± 5% which is roughly a half of the saturated water content. For alluvial silts close to or below the present water table, their saturated water contents are measured in laboratory. For loess samples, the water content is taken as 5 ± 2%. Σ is the over-dispersion value. (n) is the number of accepted aliquots.

Sample	Origin type	Radionuclide concentrations			Sample depth	W	Cosmic dose rate	Dose rate	Equivalent Dose	(n)	σ	Age
		K (%)	U (ppm)	Th (ppm)	(m)	(%)	(Gy/ka)	(Gy/ka)	(Gy/ka)		(%)	(ka)
T2R01	Alluvial	1.92 ± 0.41	4.53 ± 0.45	5.45 ± 1.57	8.0 ± 0.2	10 ± 5	0.09 ± 0.00	3.85 ± 0.41	180.3 ± 2.1	24	1.8	46.8 ± 5.1
T2R02	Alluvial	0.76 ± 0.29	4.43 ± 0.48	6.14 ± 1.63	5.0 ± 0.2	10 ± 5	0.12 ± 0.01	2.85 ± 0.35	23.4 ± 0.2	24	2.3	8.2 ± 1.0
PB-T2L	Alluvial	1.93 ± 0.42	4.31 ± 0.54	9.73 ± 1.89	10.0 ± 0.2	22.4 ± 2.2	0.07 ± 0.00	3.7 ± 0.38	60.2 ± 0.5	23	0.8	16.3 ± 1.7
T2L-P	Alluvial	1.46 ± 0.37	3.73 ± 0.47	9.66 ± 1.65	8.0 ± 0.2	10 ± 5	0.09 ± 0.00	3.55 ± 0.38	51.9 ± 2.8	11	16	14.6 ± 1.8
SG-06	Alluvial	2.87 ± 0.52	3.54 ± 0.5	11.7 ± 1.76	2.0 ± 0.2	10 ± 5	0.18 ± 0.01	5.06 ± 0.49	36.1 ± 0.5	10	1.3	7.1 ± 0.7
NS-L27	Loess	1.62 ± 0.4	4.6 ± 0.48	5.52 ± 1.65	2.7 ± 0.2	5 ± 2	0.17 ± 0.01	3.86 ± 0.42	177.6 ± 2.8	24	5.6	46.0 ± 5.1
NS-L70	Loess	1.93 ± 0.26	3.04 ± 0.41	10.27 ± 1.45	7.0 ± 0.2	5 ± 2	0.1 ± 0.00	4.02 ± 0.32	247.3 ± 3.2	26	3.4	61.6 ± 5.0
NS-86	Loess	1.71 ± 0.58	3.17 ± 0.39	9.31 ± 1.37	8.6 ± 0.2	5 ± 2	0.08 ± 0.00	3.74 ± 0.51	299 ± 8.5	12	8.8	79.9 ± 11.1
NS-U100	Paleosol	1.75 ± 0.61	3.60 ± 0.49	8.36 ± 1.73	10.0 ± 0.2	5 ± 2	0.08 ± 0.00	3.84 ± 0.54	200 ± 18	8	25	52.1 ± 8.7
NS-DZ	Loess	1.42 ± 0.35	3.3 ± 0.41	8.26 ± 1.41	2.0 ± 0.2	5 ± 2	0.18 ± 0.01	3.50 ± 0.36	315 ± 13	14	14	90 ± 10
YD-L001	Loess	2.13 ± 0.4	2.6 ± 0.4	9.19 ± 1.4	20 ± 0.2	5 ± 2	0.03 ± 0.00	3.89 ± 0.38	226 ± 18	17	32	58.1 ± 7.3
YD-L002	Loess	1.75 ± 0.65	3.82 ± 0.35	7.89 ± 1.31	32 ± 0.2	5 ± 2	0.03 ± 0.00	3.82 ± 0.56	267.7 ± 8.4	11	9.1	70.1 ± 10.6
YD-L003	Loess	1.78 ± 0.74	3.15 ± 0.42	8.16 ± 1.55	50 ± 0.2	5 ± 2	0.03 ± 0.00	3.64 ± 0.63	228.5 ± 8	17	13	62.7 ± 11.0
T1L01	Alluvial	2.21 ± 0.41	3.58 ± 0.41	8.63 ± 1.43	3 ± 0.2	10 ± 5	0.16 ± 0.01	4.17 ± 0.4	217.2 ± 7.3	20	14	52.1 ± 5.3
D01-30	Alluvial	1.64 ± 0.36	3.94 ± 0.34	4.03 ± 1.2	30 ± 0.2	20.2 ± 2	0.02 ± 0.00	2.90 ± 0.31	120.7 ± 6.3	23	25	41.6 ± 5.0
D02-4.7	Alluvial	2.08 ± 0.42	3.47 ± 0.45	9.31 ± 1.59	4.7 ± 0.2	20.3 ± 2	0.14 ± 0.01	3.68 ± 0.36	12.2 ± 0.4	10	9.4	3.3 ± 0.3
D03-39	Alluvial	1.72 ± 0.17	3.05 ± 0.31	9.89 ± 0.99	39 ± 0.2	22.4 ± 2	0.02 ± 0.00	3.13 ± 0.22	135.6 ± 2.6	21	8.1	43.3 ± 3.2

7.2 OSL ages for the T2, T3 and T4 terraces and boreholes

7.2.1 T4 terraces

Three samples (i.e., T4RBL01, T4R01 and T4L01) were dated for the T4 terraces (Fig. 7.2). The locations and OSL radial plots of these three samples are presented in Figs. 7.3 and 7.4, respectively. The three samples provide ages with significant differences (Fig. 7.4).

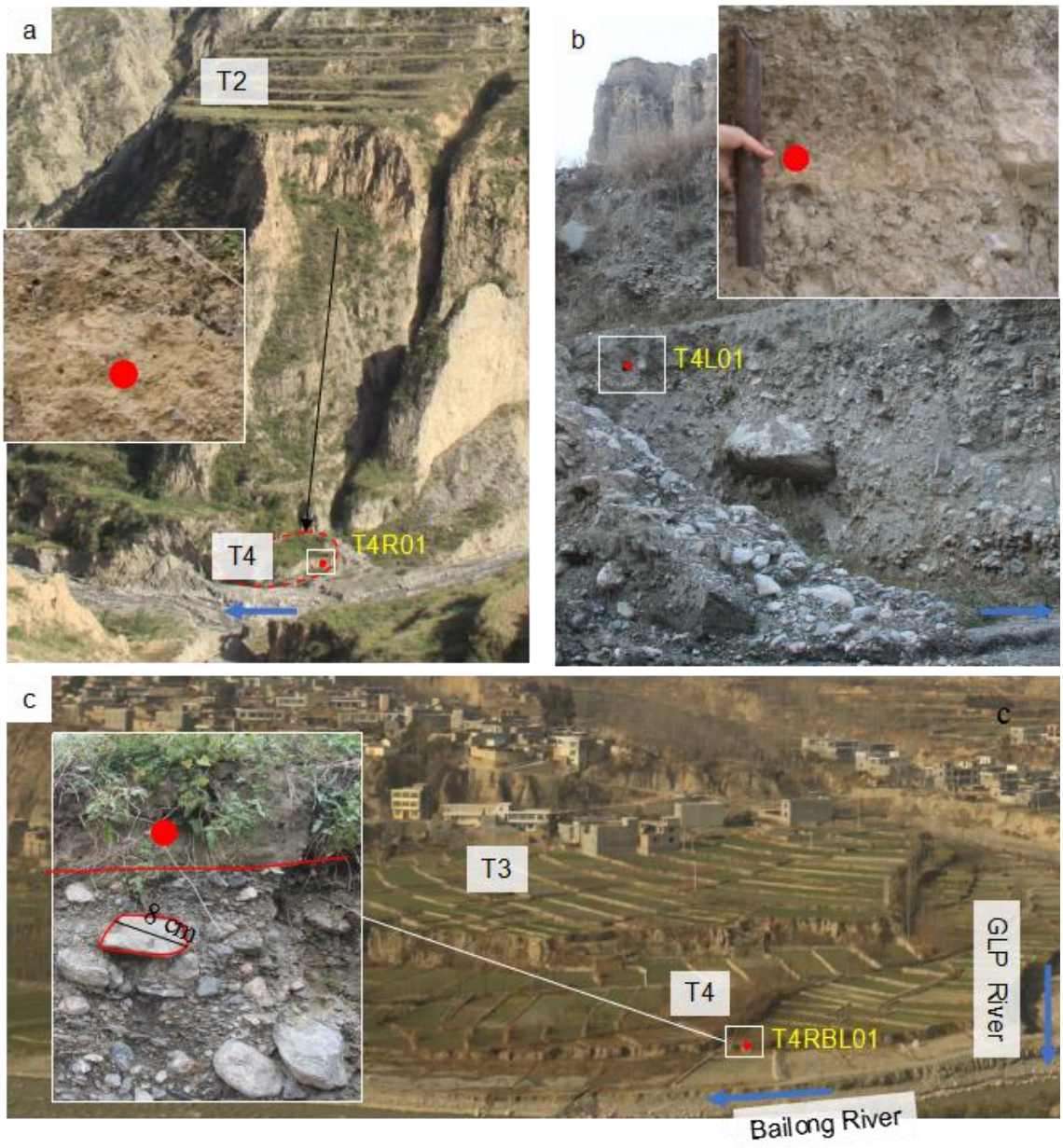

Fig. 7.3. Distribution of the OSL samples from the T4 terraces. a. Location of sample T4R01 denoted by the filled red dot. The blue arrow indicates the flow direction of the GLP river. The dashed red line circles the extent of the T4 terrace. b. Location of sample T4L01. c. Location of sample T4RBL01. Blue arrows represent the flow directions of the GLP river and Bailong River.

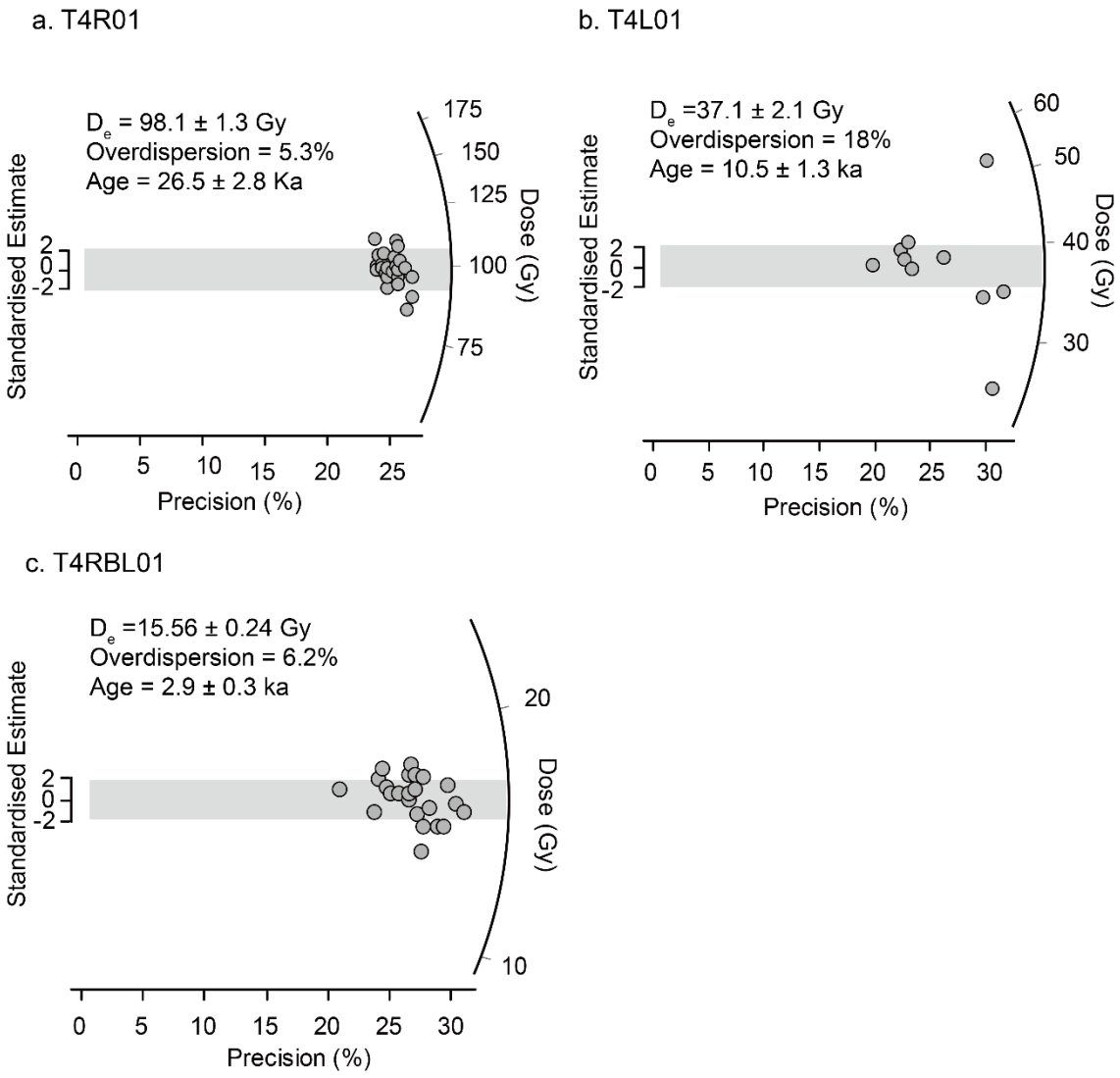

Fig. 7.4. Radial plots of equivalent doses for samples T4R01 (a), T4L01 (b) and T4RBL01 (c).

Sample T4R01 was taken from a small terrace in the midstream portion of the valley. The OSL sample was taken from a paleosol layer which is ~ 40 cm thick and caps the terrace (Fig. 7.3a). Individual aliquots of this sample (Fig. 7.4a) yield consistent equivalent doses, and the overdispersion of the dataset is relatively low (5.3%). However, the age is anomalously old at 26.5 ± 2.8 ka. The geomorphic setting of the sample suggests that it is very likely that the thick silty layer is composed of collapsed materials from the overlying T2 terrace (Fig. 7.3a). Newly collapsed materials from the T2 terraces have been found in the nearby area (Fig. 7.5). Therefore, the age for sample T4R01 is interpreted as relating to

the formation of the T2 terrace and hence is not used to provide an age for the T4 terrace.

Fig. 7.5. Photograph showing a collapsed body from the T2 terrace. The material in the foreground (beneath the dashed red line) is interpreted as a slump from the main T2 terrace seen in the background.

Sample T4L01 was taken from a T4 terrace in the midstream portion of the valley (Fig. 7.1). The sample was taken from a layer (~20 cm thick) of paleosol capping the massive silty-matrix-supported gravelly deposits (Fig. 7.3b). Plant roots and soil nodules are present in this layer, indicating a disturbance of the sedimentary layer. The D_e values shown in Fig. 7.4b have a relatively high over-dispersion value (18%), and the dataset yields an age of 10.5 ± 2.8 ka, an older age than would be expected for the (Late Holocene) T4 terrace. There are two possible ways to understanding this anomalous age: (1) the terrace from which sample T4L01 was taken may be an older terrace than the T4 terraces at the mouth of the GLP valley, and hence this age cannot represent the ages of the T4 terraces, and (2) post-depositional modification to this sample has been strong which made

this burial age anomalous. However, this study is not able to determine which one may be the reason, and therefore this age is excluded from further analysis.

Sample T4RBL01 was taken at the distal end of the T4 terrace (Fig. 7.3c). The sampled materials are interpreted as overbank deposits of the Bailong River because the sampling location is close to the Bailong River and distant from the present channel of the GLP valley (Fig. 7.3c). The D_e values cluster within the 2 standard errors of the CAM D_e (15.56 Gy), indicating relatively homogeneous OSL signals of the sample (Fig. 7.4c). However, because there are no other ages available for the T4 terraces to compare with, the accuracy of this age cannot be determined, and this age is also excluded from further analysis.

Overall, the OSL ages obtained for the T4 terraces in this study are not used to constrain the timing of the T4 terrace formation. Sample T4R01 represents collapsed loess deposits from the high T2 terraces, and hence its OSL date dose not provide information on the true age of the T4 terrace formation. The ages for samples T4R01 and T4RBL01 are subject to several uncertainties which cannot be determined in this study.

7.2.2 T3 terraces

Four samples were taken from the T3 terraces (Fig. 7.2). Samples T3700 and SG-01 were taken from the T3S1 profile (Fig. 7.6a). Sample SG-01 was taken near the base of the profile and is a layer of alluvial silt (10 cm thick) which is intercalated between gravelly deposits (Fig. 7.6a). Sample T3700 was taken from a topsoil layer which has been developed within aeolian deposits capping the

gravelly terrace sediments. The radial plots (Fig. 7.6b, c) show that the D_e values of the two samples both have some scatters around the central values. The soil layer (T3700) has a lower overdispersion value than the alluvial silt (SG-01). They both produce low CAM D_e values, with T3700 being 4.05 Gy and SG-01 being 2.66 Gy. The OSL ages for T3700 and SG-01 are 1.0.7 ± 0.11 ka and 0.8 ± 0.1 ka respectively, which are identical within 2 sigma errors. These young ages indicate that no significant residual OSL signals remained at deposition, and therefore are accepted as the ages of the T3 terraces.

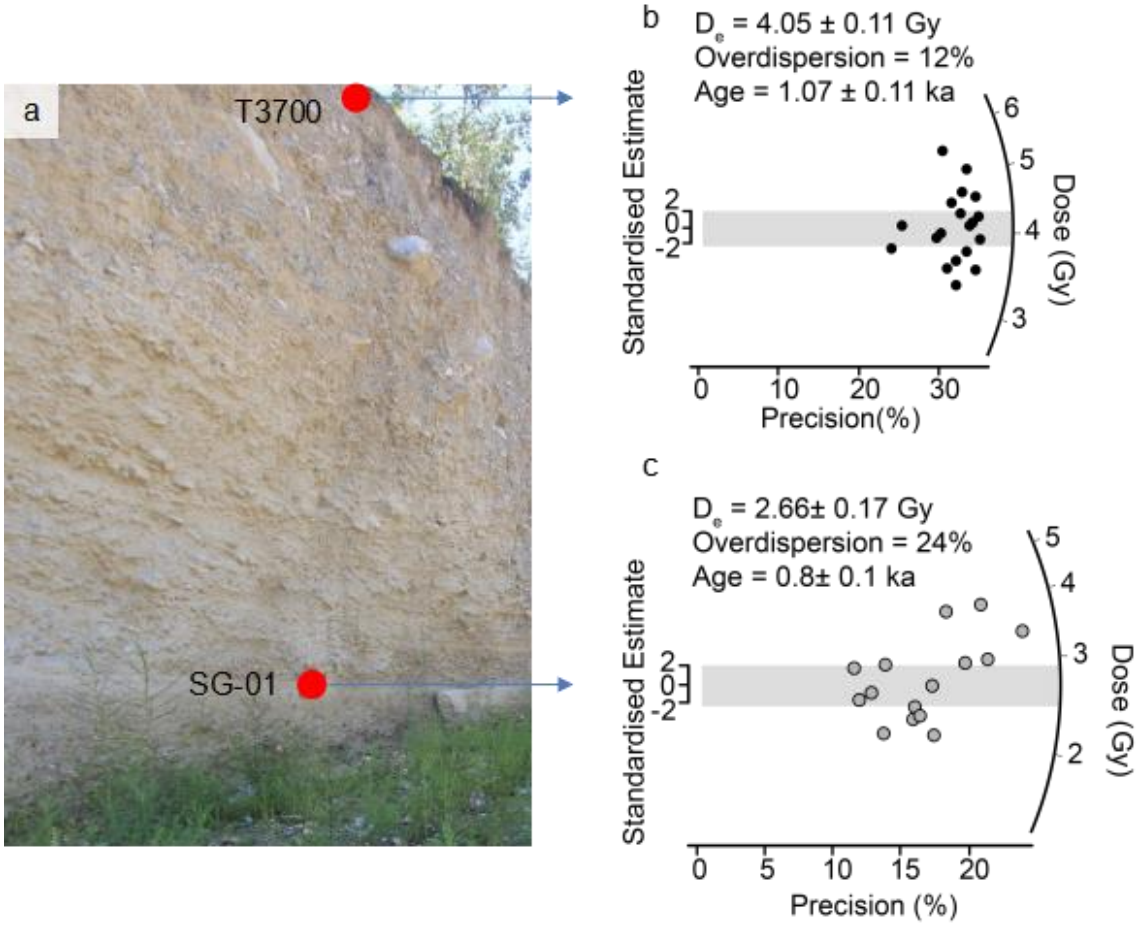

Fig. 7.6. The locations (a) and D_e radial plots (b, c) of samples T3700 and SG-01.

Samples T3RBL02 and HDG were taken from the T3 terraces that are located at the downstream portion of the GLP valley (Fig. 7.7a). Sample T3RBL02 was

taken from a layer of alluvial silt (15 cm thick) which was intercalated between massive gravelly deposits (Fig. 7.7b). It provides high-precision D_e values with only 4.4% overdispersion (Fig. 7.7d), probably indicating satisfactory OSL signal resetting upon deposition and little disturbance by post-depositional processes during burial. The OSL age of sample T3RBL02 is 1.4 ± 0.1 ka (Fig. 7.7d), indicating a consistent age with geomorphic expectations for the T3 terrace formation. Sample HDG was taken from a thick (1 m) silt layer which contains granules. This layer overlies on well-bedded pebbly limestone-dominated clasts (Fig. 7.7c). Below is a layer of rounded clasts which were deposited by a flooding process of the Bailong River. The D_e values for sample HDG show a low overdispersion (7.5 %, Fig. 7.7e). The OSL age of sample HDG is 0.6 ± 0.1 ka, indicating a consistent expectation for the age of the T3 terrace formation.

Overall, the OSL ages for the sediments of the T3 terraces indicate that they were bleached to a small level prior to deposition and are suitable for OSL dating. Moreover, these four samples produced consistent OSL ages (between 0.6 – 1.4 ka) for the T3 terraces, and therefore these ages are interpreted as broadly accurate.

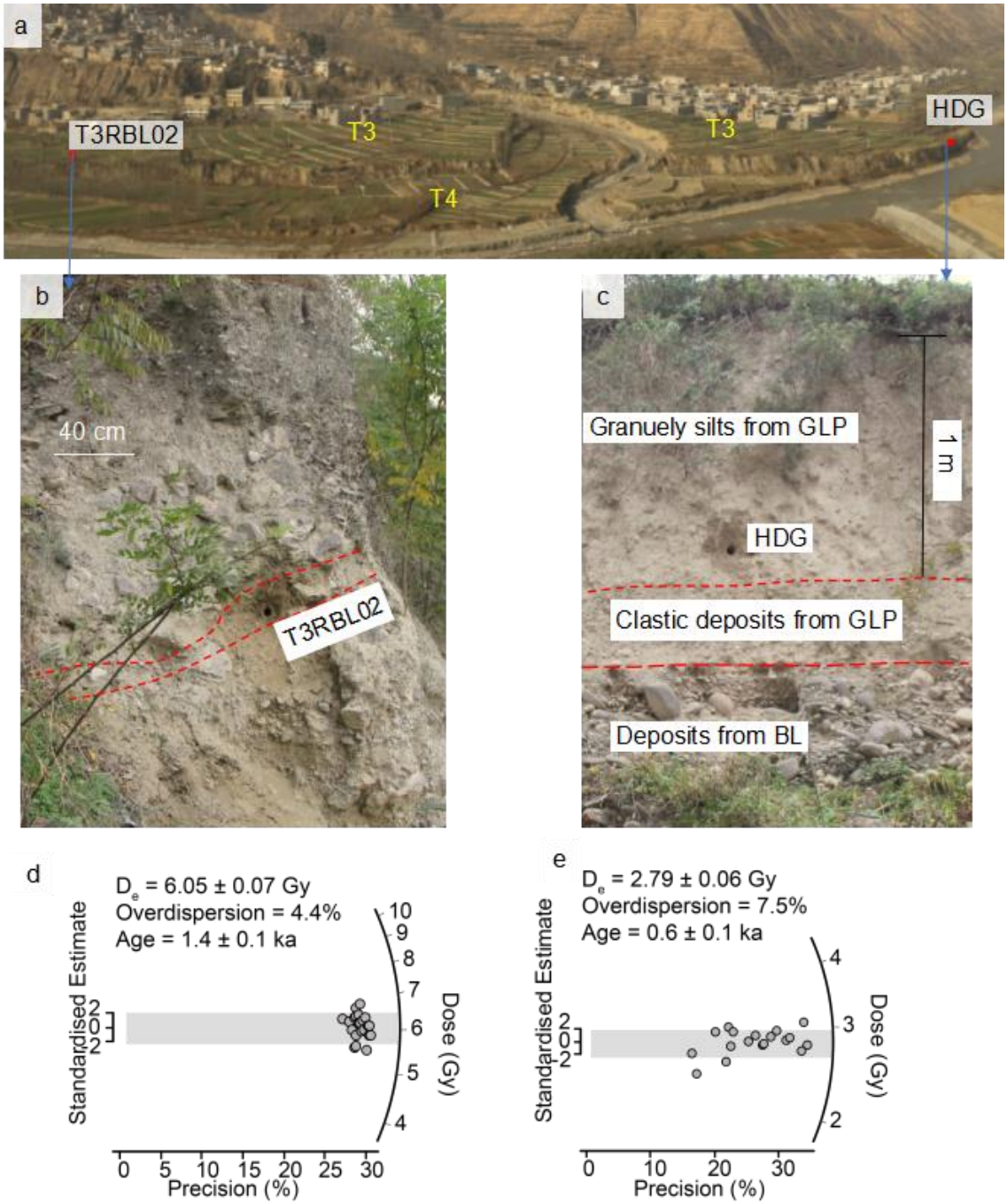

Fig. 7.7. Locations and D_e radial plots of samples T3RBL02 and HDG. a. Location of the two samples in the T3 alluvial terraces. b. Close-up view of sample T3RBL02; c. Close-up view of sample HDG. d. Radial plot of the D_e values for sample T3RBL02. e. Radial plot of the D_e values for sample HDG.

7.2.3 T2 terraces

A total of 16 samples were taken from the T2 terraces (Fig. 7.2) and dated. Samples T2L16, T2L17, T2L18, T2L19, T2L20, T2L21, T2L22 and T2L24 were taken from the T2 terrace where section T2S3 was logged**.** The relative locations of these samples are shown in Fig. 7.8, and the radial plots of D_e values are shown in Fig. 7.9. Sample T2L18 was taken at the bottom of the exposed profile, and it provides an OSL age of 21.7 ± 2.5 ka with a low overdispersion value (6.4%). Sample T2L16 was ~ 3 m above sample T2L18. It produces an age of 13.1 ± 1.8 ka but has a high overdispersion value (35%). Sample T2L17 was taken ~ 1.5 m above sample T2L16 and provides an age of 15.1 ± 1.7 ka with an overdispersion value of 12%. Sample T2L19 was 0.4 m above sample T2L17 and gives an age of 13.3 ± 1.4 ka with an over-dispersion value of 13%. Overall, samples T2L18, T2L17 and T2L19 generate OSL ages that are in stratigraphic order and have relatively low overdispersion values suggesting homogenous, probably complete bleaching prior to deposition. Conversely, sample T2L16 has a higher overdispersion value, but still yields an age within uncertainties of the age of the overlying T2L17.

Samples T2L20, T2L21, T2L22 and T2L24, which were located higher in the profile than the four samples discussed above (Fig. 7.8), yield older OSL ages. Specifically, samples T2L20, T2L21 and T2L24, which were taken from different stratigraphic horizons, provide OSL ages that are indistinguishable (Fig. 7.8). These ages are older than those of T2L19, T2L17 and T2L16, which are in stratigraphically lower positions. Therefore, the OSL ages for these three samples are not regarded as accurate. The reason for these age anomalies is

unknown from the study, and detailed sedimentological analyses of these samples are needed to uncover the reason in future studies. Sample T2L22 which is stratigraphically between T2L21 and T2L24, produces an age of 14.8 ± 1.6 ka. This age is younger than those for both T2L21 and T2L24 but is indistinguishable from the age for T2L19. Sample T2L22 is therefore considered to yield an accurate age.

Fig. 7.8. Photograph showing the locations of samples T2L16, T2L17, T2L18, T2L19, T2L20, T2L21, T2L22 and T2L24.

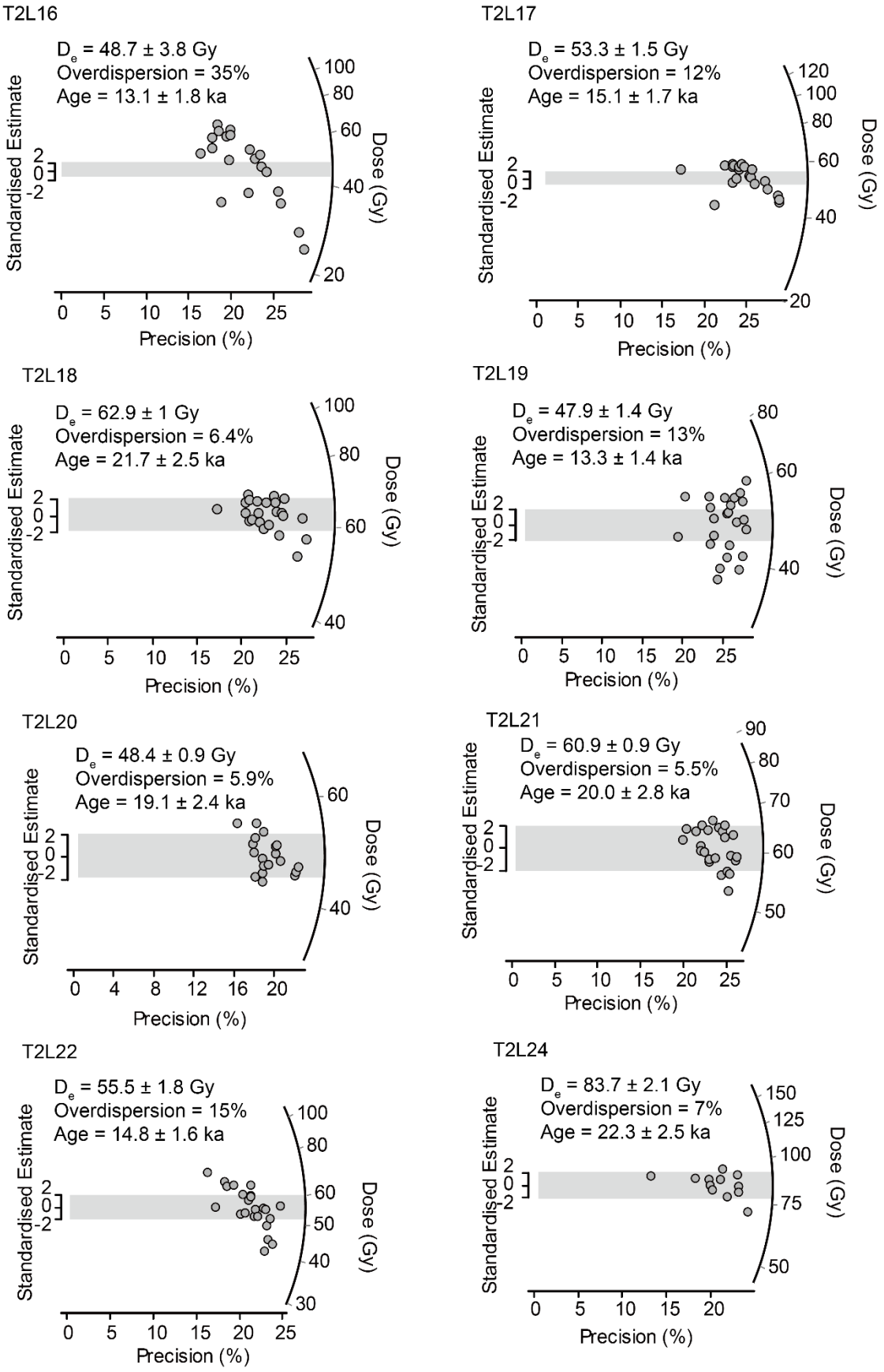

Fig. 7.9. Radial plots of D_e values for samples T2L16, T2L17, T2L18, T2L19, T2L20, T2L21, T2L22 and T2L24.

Samples T2RCK01 and T2RCK02 were taken from a T2 terrace at the mouth of the GLP valley (Fig. 7.10). Sample T2RCK02 produces an OSL age of 13.8 ± 1.0 ka with an over-dispersion value of 6.8% (Fig. 7.10). Sample T2RCK01 produces an OSL age of 18.5 ± 2.2 ka with an over-dispersion value of 23%. These two samples also result in OSL ages that are in stratigraphic order

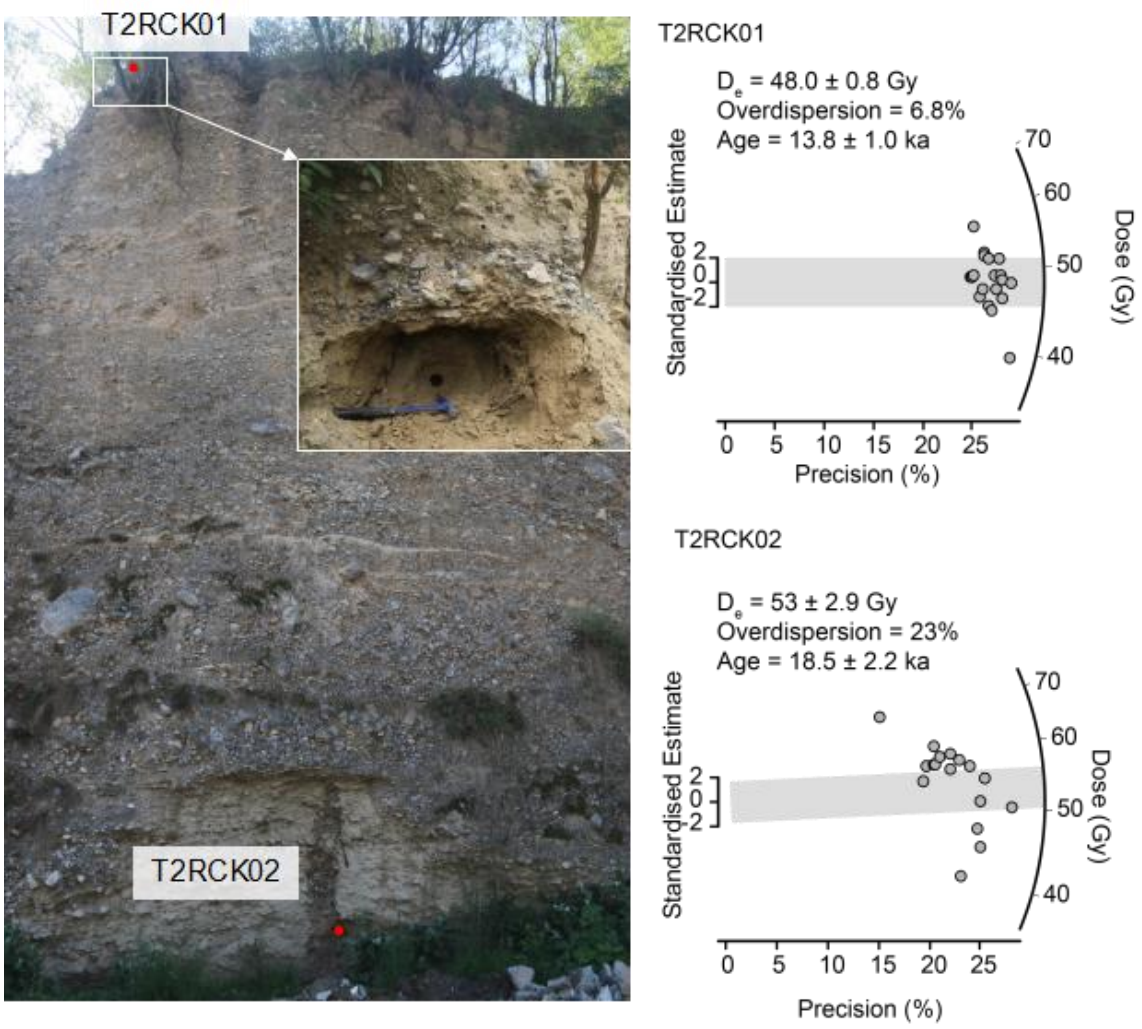

Fig. 7.10. Locations and OSL radial plots of sample T2RCK01 and T2RCK02. Inset photograph shows the sediments close to sample T2RCK01 in detail.

Samples T2R01 and T2R02 were taken from a T2 terrace at the midstream portion of GLP (Fig. 7.2). The ages of T2R01 and T2R02 are 46.8 ± 5.1 ka and 8.2 ± 1 ka respectively, and they both have low over-dispersion values, around

2% (Table 7.2 and Fig. 7.11). Noticeably, the age of T2R01 (46.8 ± 5.1 ka) is much higher than the ages of samples taken from the other T2 terraces. The gravels overlying sample T2R01 are generally coated by a layer of dark varnish (Fig. 7.12a), while the gravels at other T2 alluvial terraces do not have such a feature. I interpret this dark varnish layer as indicating a relatively old terrace which has been mostly eroded, leaving relics at this location. Besides, the age of T2R01 is also close to that of sample D03-39, which was taken from 39 m beneath the present channel, close to the bedrock valley floor (Fig. 7.2). Interestingly, the phyllite bedrock is exposed on the opposite side of the valley at the T2R01 location (Fig. 7.12). It is, therefore, likely that the position of T2R01 is also close to the phyllite bedrock. Overall all, the age of T2R01 is considered as broadly accurate.

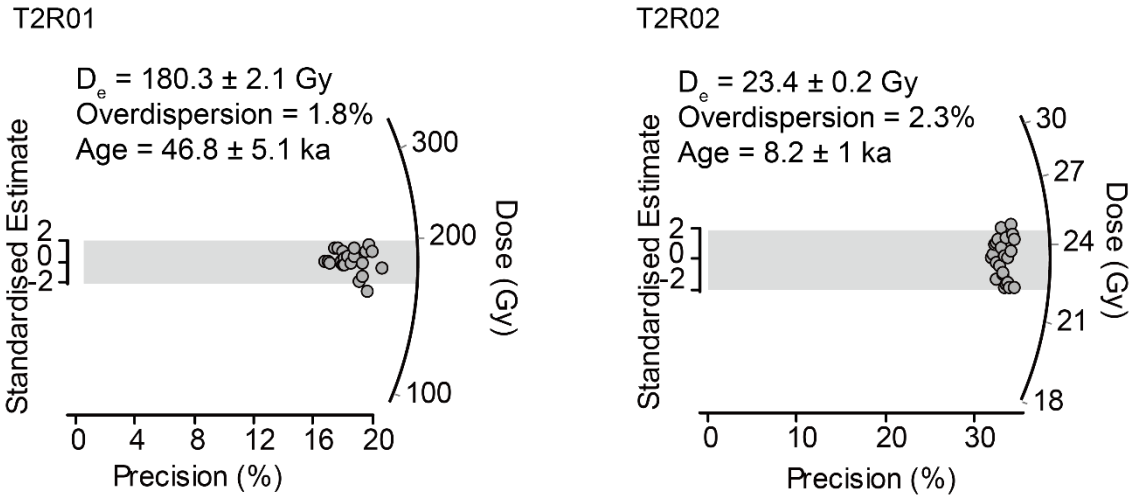

Fig. 7.11. Radial plots of D_e values for samples T2R01 and T2R02.

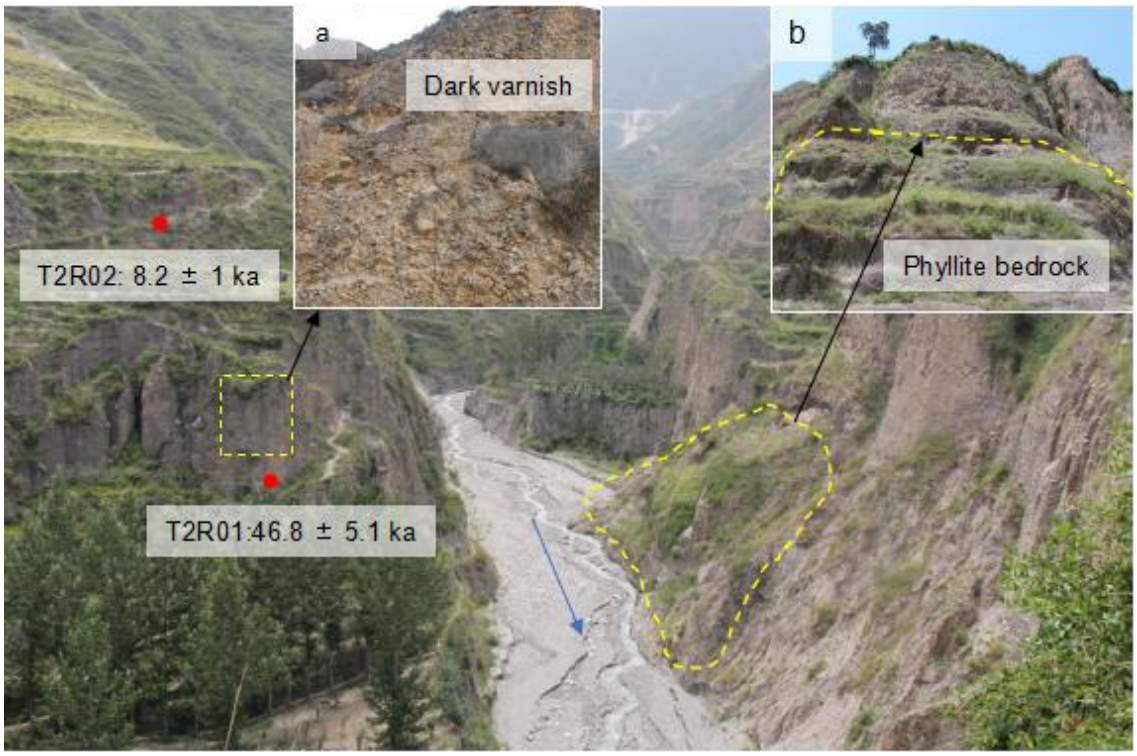

Fig. 7.12. Geological context of samples T2R01 and T2R02. The boulder and the surrounding gravels are coated with a dark varnish layer (inset photograph a). On the opposite side of the valley at the T2R01 location, the phyllite bedrock is present above the modern channel floor (inset photograph b).

Sample PB-T2L01 was taken from a layer of alluvial silt (20 cm thick) at the base of the exposed T2 terrace (Fig. 7.13a) at the midstream end of the GLP valley. Sample SG-06 was taken from a thin (10 cm thick) alluvial silty layer which caps the gravelly sediments of the T2 terrace (Fig. 7.13b) at the midstream portion of GLP. Sample T2L06 was taken from a loess layer (>50 cm thick) capping the T2 terrace at the downstream portion of the GLP valley (Fig. 7.13c). Sample T2L-P was taken from an alluvial silt layer (10 cm thick) in the middle section of a T2 terrace profile (Fig. 7.13d) in the midstream section of GLP. These four samples provide OSL ages (Fig. 7.13) that are within the age ranges provided by the T2 terrace samples described previously. Therefore, these ages are regarded as broadly accurate.

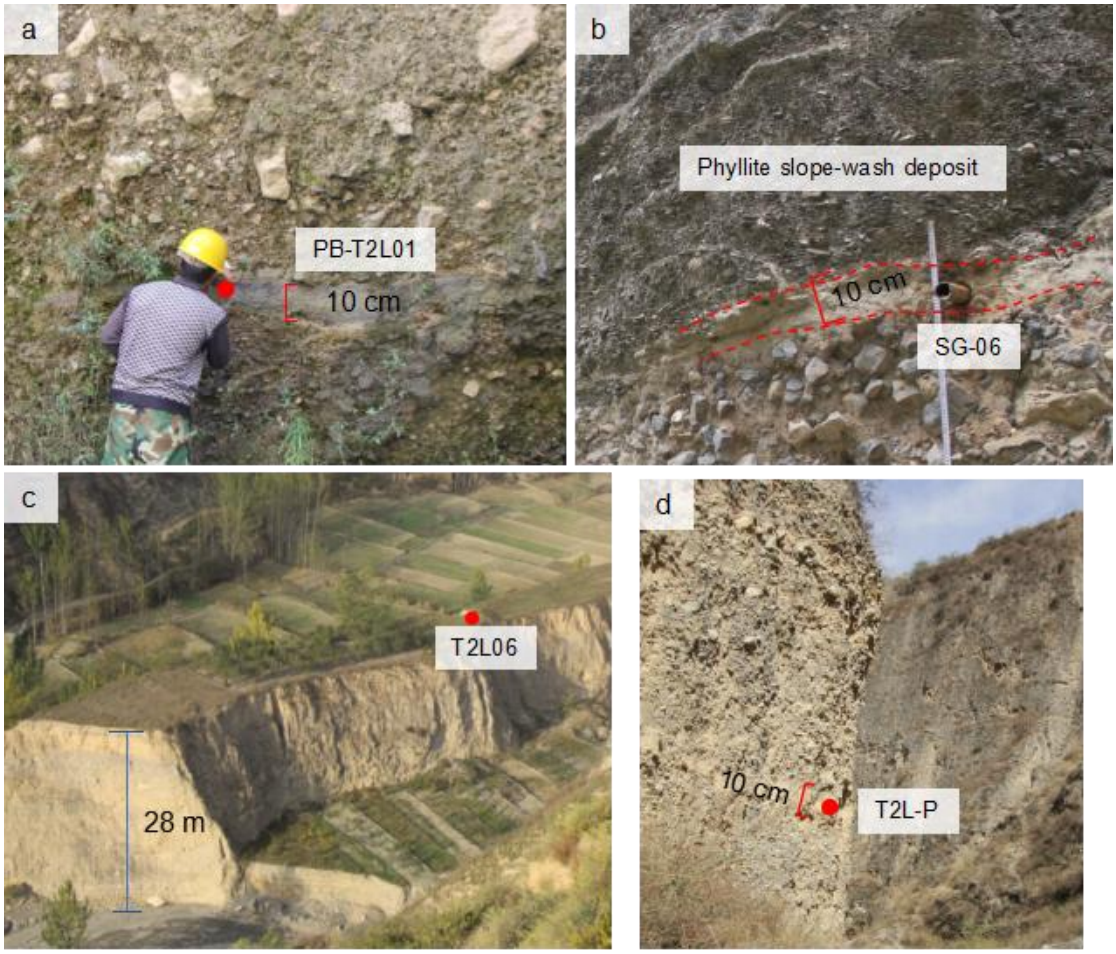

Fig. 7.13. Photographs showing the locations of sample Pb-T2L01 (a), SG-06 (b), T2L06 (c) and T2L-P (d).

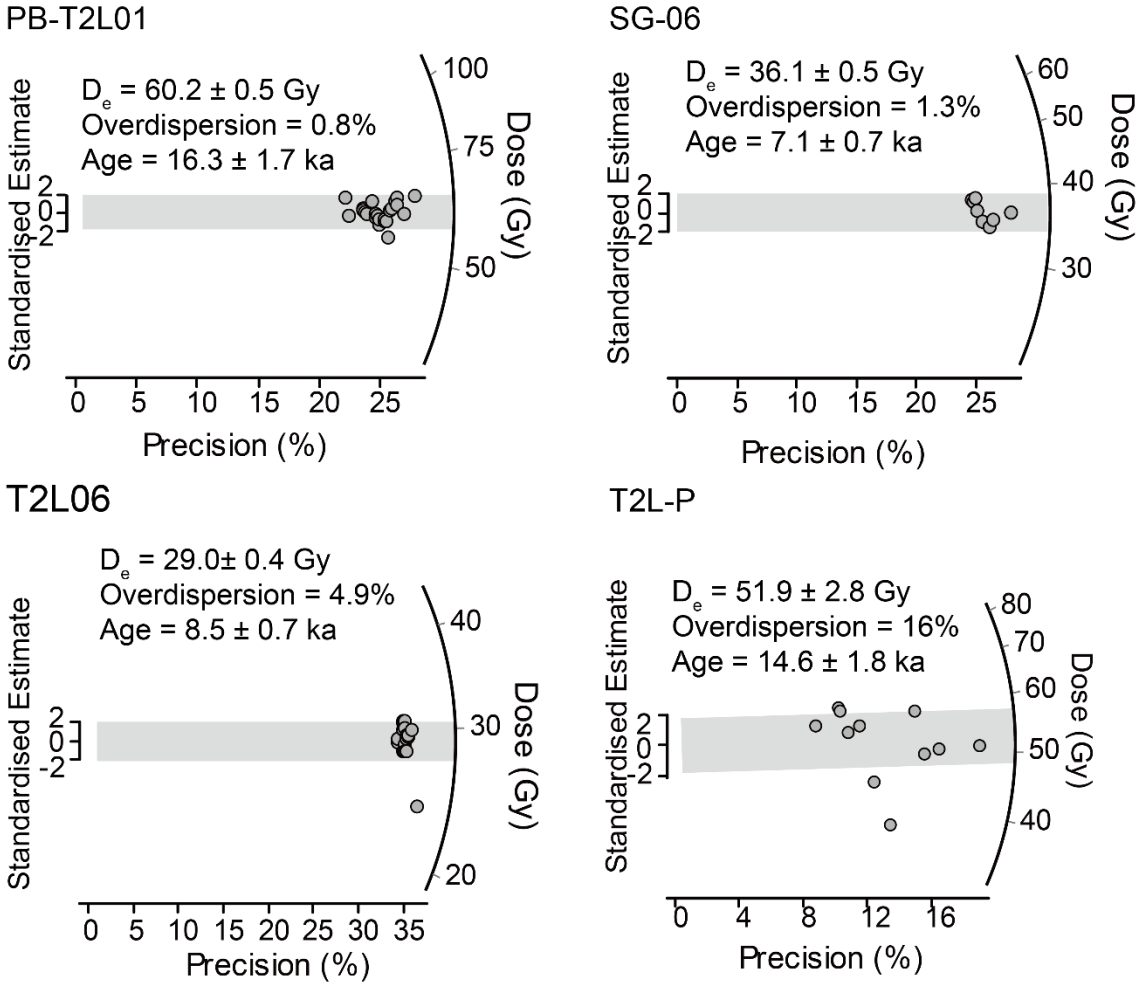

Fig. 7.14. Radial plots of D_e values for samples PB-T2L01, SG-06, T2L06 and T2L-P.

7.2.4 Borehole sediments

Three samples were taken from the boreholes (Fig. 7.2). Sample D01-30 was taken from 30 m beneath the present channel at core D01, sample D02-4.7 was from 4.7 m at D02, and sample D03-39 was from 39 m at D03. The OSL age for D01-30 is 41.6 ± 5.0 ka with a relatively high over-dispersion value of 25% (Fig. 7.15). Sample D03-39 yields an OSL age of 43.3 ± 3.2 ka with an over-dispersion value of 8.1% (Fig. 7.15). These two samples, i.e., D01-30 and D03-39, are located at similar depths beneath the present channel, and they both produce similar ages. Therefore, these ages are accepted as broadly accurate. Sample D02-4.7 produces an OSL age of 3.3 ± 0.3 ka with an over-dispersion value of

9.4% (Fig. 7.15). This OSL age is also in the stratigraphic order with those of the two other core samples and is also considered a broadly accurate estimate of the burial ages.

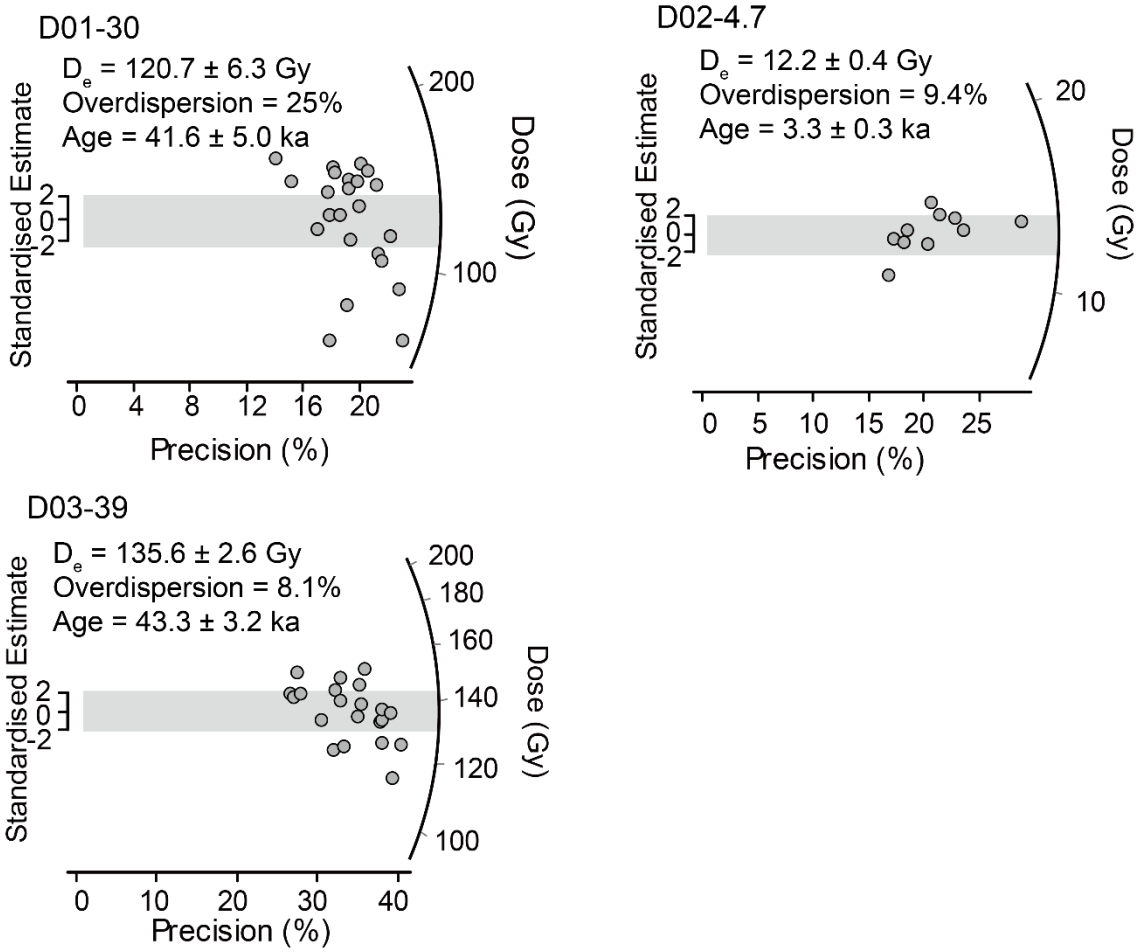

Fig. 7.15. Radial plots of D_e values for samples D01-30, D02-4.7, and D03-39.

7.3 Samples with high D_e values (T1 terraces)

Samples from two loess sections which capped the T1 terraces have been dated in an attempt to determine the ages of the T1 terraces. These samples produce D_e values which exceed 200 Gy. As high D_e values are likely to approach the saturation limits of quartz minerals (Fig. 7.16), it is likely that these ages might

not be valid ages. In this section, the accuracy of the high D_e values is examined by considering their stratigraphic orders.

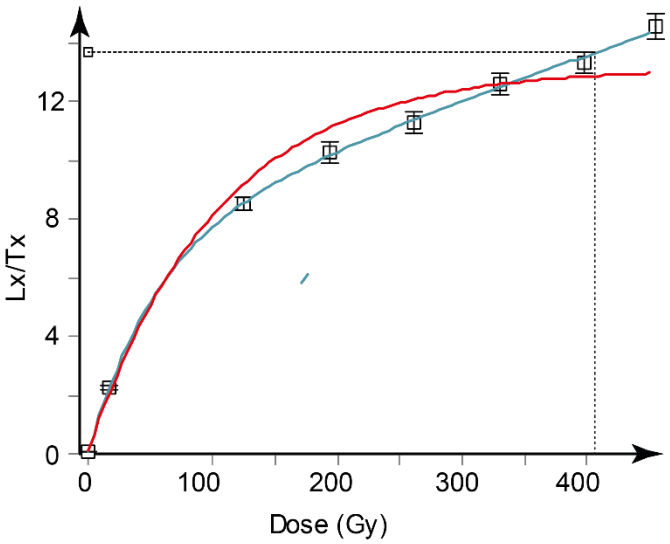

Fig. 7.16. The growth curves fitted with different functions for sample NS-DZ. The red curve is fitted using the exponential function, and the blue curve is fitted using the exponential plus linear function.

7.3.1 Loess samples in the downstream portion of GLP

Five samples, NS-L27, NS-L70, NS-L86, NS-U100 and NS-DZ, were taken from one loess profile overlying the T1 terrace at the downstream end of the GLP valley (Fig. 7.17).

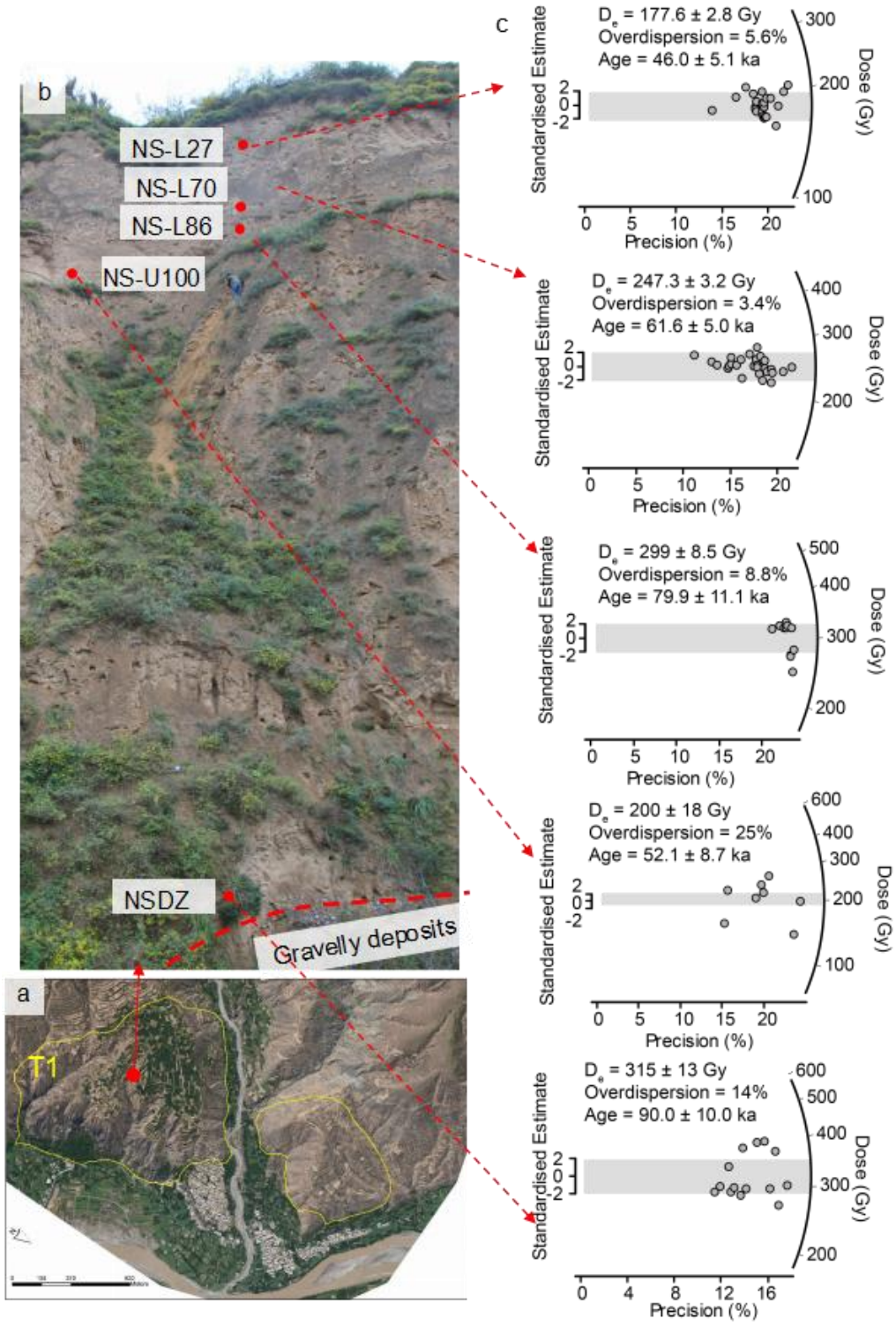

Fig. 7.17. Distribution and OSL ages for samples NS-L27, NS-L70, NS-L86, NS-U100 and NS-DZ. a. Plan view of the downstream end of the GLP valley, showing the profile location (filled red dot). The yellow lines delineate the T1 terrace boundaries. b. The loess profile where samples NS-L27, NS-L70, NS-L86, NS-U100 and NS-DZ were taken. Note that sample NS-DZ was taken from a nearby section of the profile, and the location of this sample in the figure indicates the position of NS-DZ relative to the gravelly deposits, not its actual location. c. Radial plots of the D_e values for the five samples.

These samples were taken at certain depths beneath the terrace surface, and the depth is indicated in the sample code, e.g., NS-L27 was taken from 2.7 m beneath the terrace surface. The ages for samples NS-L27, NS-L70 and NS-L86 are in the stratigraphic order (Fig. 7.17), and the D_e distributions for each sample are tightly clustered (overdispersion ranges in 3.4-8.8%), indicating satisfactory estimations of the OSL ages. These observations are consistent with aeolian deposition (Lai, 2006; Lai et al., 2007; Stevens et al., 2008), suggesting that the age estimations for these three samples are likely to be accurate. Conversely, the overdispersion for sample NS-U100 is relatively high (25%, Fig. 7.17c), and its OSL age does not fit the stratigraphic order. The cause of this discrepancy is unclear from these results alone, but it is possibly caused by post-depositional mixing. Sample NS-U100 was taken from a layer interpreted as a paleosol owing to its color and structure (dark reddish brown (5YR 3/3) silty clay with blocky structure), which in other luminescence studies of loess paleosols has resulted in inaccurate ages in some soil units (Stevens et al., 2008). Consequently, the age for sample NS-U100 is regarded as likely unreliable. Sample NS-DZ was taken from the base of the loess profile. It yields an overdispersion value of 14% (Fig. 7.17c), which is lower than that of NS-U100 but higher than those of NS-L27, NS-L70 and NS-L86. Because the D_e value is so high (315 Gy), and we know that loess tends to yield age underestimates at such high doses (Chapot et al., 2012; Lai, 2010), the OSL age, 90.0±10.0 ka, is regarded as the minimum estimate of its true burial age.

7.3.2 Loess samples in the midstream portion of GLP

Samples YD-L001, YD-L002, YD-L003 were taken from the loess deposits

capping the gravelly sediments of the T1 terrace at the midstream portion of GLP (Fig. 7.18a, b). These three samples provide D_e values higher than 200 Gy. The OSL ages of the three samples are 58.1 ± 7.3 ka (for YD-L001), 70.1 ± 10.6 ka (for YD-L002) and 62.7 ± 11.0 ka (for YD-L003) (Fig. 7.18). These three ages are not distinguishable within one standard error. Though these three samples were taken from places with different elevations (Fig. 7.18a, b), they were not in the same profile. Instead, they were taken from different loess terraces. The geomorphic settings of these loess terraces indicate that the hillslopes have experienced complex sliding, and therefore, the elevation difference among the samples might not represent their true stratigraphic orders. The ages of the three samples suggest that the gravelly sediments of the T1 terrace here have been deposited before these ages.

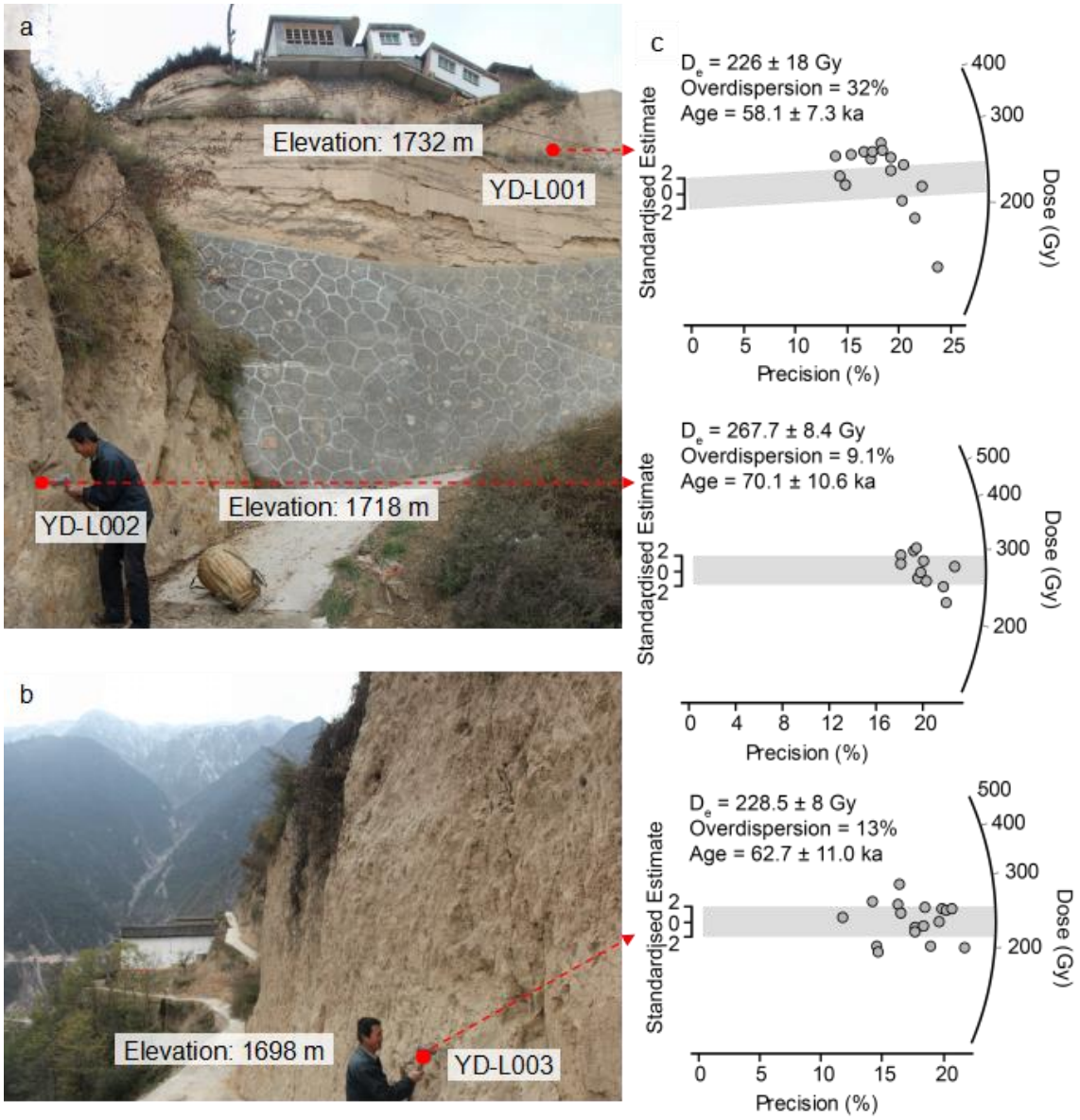

Fig. 7.18. Locations and OSL ages for samples YD-L001 and YD-L002 (a) and YD-L003 (b) and radial plots of D_e values (c).

7.3.3 Alluvial silt from a T1 terrace

One alluvial silt sample, T1L01, was taken from section T1S2 (Fig. 7.19). It provides an OSL age of 52.1 ± 5.3 ka. The D_e for this sample is 217 Gy, and it has an over-dispersion of 14% (Fig. 7.19c). This age is younger than the ages of the loess samples, i.e. NS-L27, NS-L70 etc. However, as only one alluvial sample was tested, the accuracy of the OSL age cannot be determined in this study.

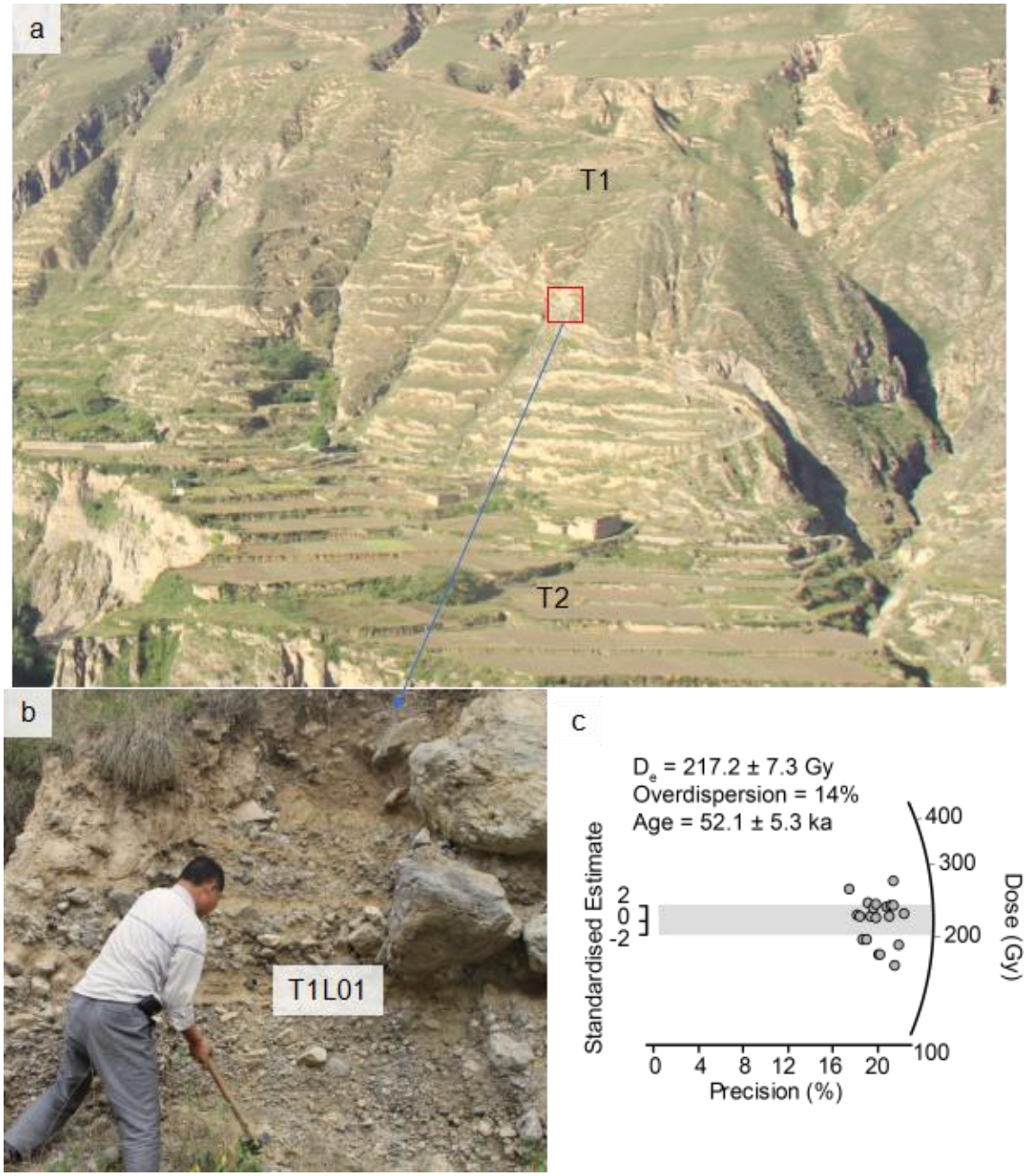

Fig. 7.19. Location and OSL age for sample T1L01. a. Location of section T1S2 from which sample T1L01 was taken. b. Photograph of sample T1L01. c. Radial plot of D_e values for T1L01.

7.4 Conclusions

This chapter examined the OSL ages of the alluvial silt, paleosol and loess samples from the four terraces and the boreholes of the GLP valley. The analyses described above allow the following conclusions to be made:

(1) The three samples, T4R01, T4L01 and T4RBL01, from the T4 terraces fail to produce OSL ages that are representative of T4 terrace formation because these three samples either came from an external source to the T4 terraces (i.e., T4R01 came from loess slumps from the nearby T2 terrace), or suffered from some uncertainties which cannot be determined by this study.

(2) The four samples, T3700, SG-01, HGD, T3RBL02, from the T3 terraces produce the youngest OSL ages among the samples measured in the study. These ages are stratigraphically consistent and also suggest satisfactory OSL bleaching of the sediments prior to deposition. Therefore, they are regarded as broadly accurate estimates for the time of the T3 terrace formation.

(3) Most of the samples taken from the T2 terraces produce stratigraphically consistent OSL ages e.g. T2R01 and T2R02, T2CK01 and T2CK02, T2L18, T2L16, T2L17, T2L19 and T2L22. These ages are regarded as accurate ages for the T2 terrace formation. Other samples taken from single outcrops of the T2 terraces (i.e. T2L-P, SG-06, PB-T2L01) produce OSL ages that are within the time range produced by the accepted T2 samples. Therefore, these ages also appear to be acceptable. However, three samples (T2L20, T2L21 and T2L24) yield ages which are significantly older than underlying samples. The reason for these anomalous ages is unknown in this study.

(4) The three samples from boreholes (D01-30, D02-4.7 and D03-39) produce stratigraphically consistent OSL ages.

(5) The ages of loess samples which were not taken from paleosol layers are in stratigraphic orders and have low overdispersion values. These characteristics are interpreted as indicating homogenous bleaching prior to deposition. The two T1 loess sequences yield apparently reliable ages up to

70-80 ka (79.9 ± 11.1 ka in the distal T1 terrace and 70.1 ± 10.6 ka in the proximal T1 terrace), providing a reliable minimum age for the underlying T1 terrace. The 90.0±10.0 ka age for sample NS-DZ is possibly an underestimate, and the deposition of T1 alluvial sediments must predate this age.

Chapter 8 Discussion: The Aggradation and Incision History of the GLP Valley and Controlling Factors

8.1 Introduction

This chapter aims to reconstruct the aggradation and incision history of the GLP valley during Late Quaternary and to discuss the impacts of climate, tectonism and base-level on this aggradation/incision history. To do this, the primary stages of aggradation/incision are identified and characterized by examining the formation of two transects of the valley (Section 8.2). The environment during each aggradation stage is briefly discussed by considering the terrace and core sedimentology. The time frame of each stage is confined by examining the OSL ages produced in Chapter 7. The chronology for each aggradation/incision period allows contemporary climatic conditions for each period to be determined by referring to proxy climatic records (i.e., speleothem and pollen). This chapter then discusses the impacts of climate, tectonism and base-level on the alternation of aggradation/incision by analyzing the geomorphological, sedimentological and chronological characteristics during each period. Lastly, the chapter attempts to apply the reconstructed aggradation/incision history to the prediction of the long-term debris flow/hyperconcentrated flood hazard based on the correlations between the evolution history and climate.

8.2 Classification of aggradation and incision stages

The evolution of the GLP valley is classified into four stages (Fig. 8.2) based on two valley-transect profiles (Fig. 8.1), BB’ towards the midstream end of the valley and DD’ towards the downstream end. The location of these two valley-transects

is shown in Fig. 4.6. Profile BB’ is close to the fault which crosses the GLP valley (Fig. 4.6). The geomorphic units crossed by profile BB’ include the T1 and T2 terraces, the present GLP channel and the phyllite hillslopes (Fig. 8.2a). Profile BB’ is used as the primary profile in defining the aggradation/incision phases of the GLP valley. Profile DD’ is at the downstream end of the GLP valley (Fig. 4.6). At this location, the alluvial sediments sourced from the GLP catchment expanded out on the flat flood-plains of the Bailong River forming fan-shaped bodies (Fig. 4.6). Profile DD’ passes through the T1, T2 and T3 terraces (Fig. 8.1b) and is used as a subordinate profile in defining the aggradation/incision phases.

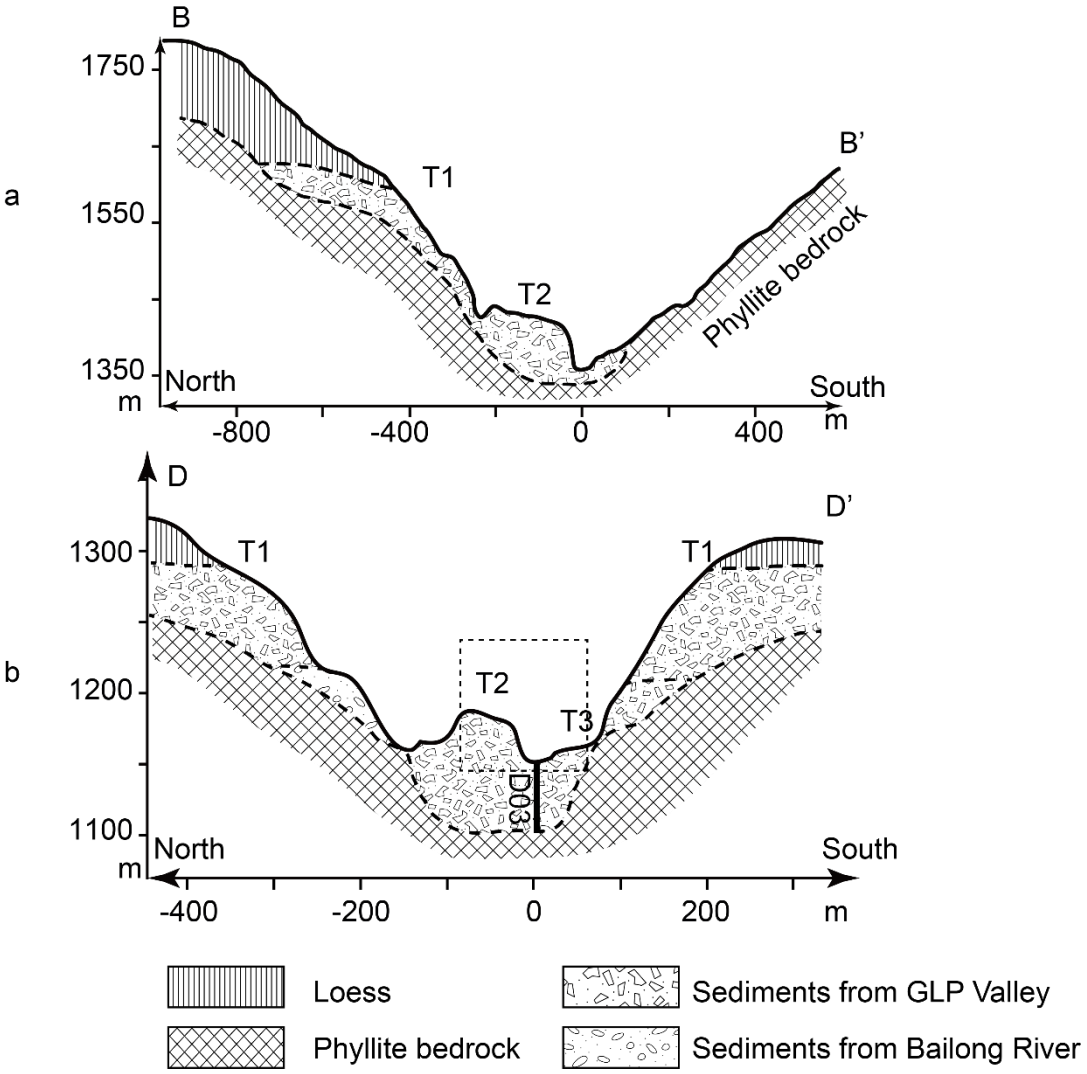

Fig. 8.1. Cross-valley profiles of BB' (a) and DD' (b). The dashed box in panel b delineates the area shown in detail in Fig. 8.2e.

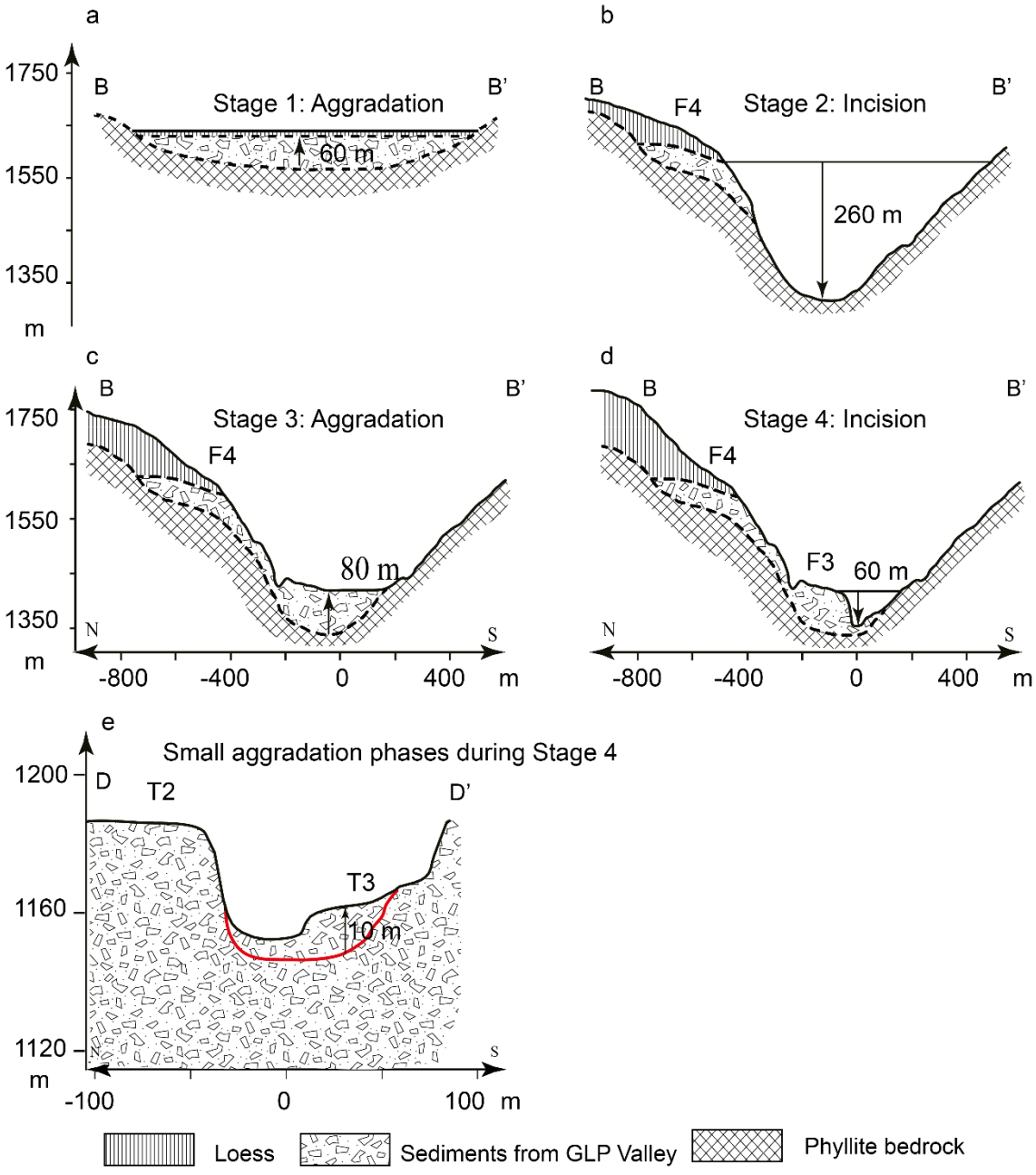

Fig. 8.2. Aggradation and incision stages of the GLP valley. The red line in panel e is the estimated boundary between the T2 and T3 sediments. A description of each stage is provided in the main text.

Stage 1 (S1) is the first GLP aggradation period which formed the T1 alluvial sediments with a thickness of ~60 m (Fig. 8.2a). The volume of the T1 alluvial sediments is 5300×10^4 m^3 (Table 4.1), which is the largest among the four terrace levels, indicating that S1 is a primary GLP aggradation period. This stage was dominated by cohesionless debris flow deposition in its initial stage (section

T1S1_A) and cohesive debris flow and loess deposition in its late stage (sections T1S1_B and T1S2) in the midstream portion of the valley. At the downstream end of the valley, the early period of this stage was dominated by the fluvial deposition of the Bailong River, which was later replaced by the hyperconcentrated flood and debris flow deposition of the GLP valley in its late stage.

Stage 2 (S2) is a period of incision which cut through the T1 terrace and the underlying phyllite bedrock (Fig. 8.2b), leading to a net incision of ~ 260 m at the location of profile BB'. At profile DD', the incision depth is ~230 m (Fig. 8.1b). This incision probably occurred during a period of efficient coupling or connectivity (Harvey, 2002b, 2012) between hillslopes, the GLP River and the Bailong River, because no sediment was preserved during this incision period. Both distally-induced (toe cutting, basal scour and marginal incision) and proximally-induced (headwater trenching) coupling mechanisms, may have occurred (Harvey, 2012; Mather et al., 2017).

Stage 3 (S3) is a period of aggradation, during which infilling of the bedrock channel and formation of the T2 alluvium occurred. The primary aggradational processes during the period were debris flows and hyperconcentrated floods, inferred from the four examined T2 sections (Fig. 5.2) and the two cores (Fig. 6.2) described earlier. Except section T2S4 which was interpreted as the relic of an older terrace, the remaining three sections (i.e., T2S1, T2S2 and T2S3) are generally formed by debris flow sediments in their lower sections and hyperconcentrated flood sediments in their upper sections (Fig. 5.2). This sequence likely indicates a decreasing trend of granular sediment supply and an

increasing trend of water runoff in the late stage of the T2 alluvium formation because debris flow deposition generally suggests more abundant supply of granular sediments and less frequent rainstorm events than hyperconcentrated flood deposition (Blair and MacPherson, 1994). This increasing trend of runoff may ultimately cause the incision of the T2 terraces.

Stage 4 (S4) is an incision period characterized by the trenching and down-cutting of the T2 terrace (Fig. 8.2d). The incision produced the ~60 m high cliffs of the T2 terraces (Fig. 8.2d). Because the T4 and T3 terraces are only present at the valley mouth, their formation was probably caused by a slight decrease in discharge, leading to the preservation of sediment at the valley mouth during this broad incision period (Fig. 8.2e).

8.3 Timing of aggradation and incision stages

The timing of phases of aggradation and incision is critical to understanding the causes of sedimentation and erosion in GLP, which is hypothesized to be representative of much of the middle portion of the Bailong valley. In this section, dates for the beginning and end of each of the aggradation/incision periods identified above are constrained using the OSL ages from Chapter 7.

The T1 terraces were deposited during the earliest aggradational phase identified in GLP, termed the S1 aggradational phase. The end of the S1 phase is defined by the OSL age for sample NS-DZ, which was a loess sample capping the alluvium of the T1 terrace (Fig. 7.2) and yields an OSL age of 90.0 ± 10.0 ka. However, the start of the S1 aggradation period has yet to be determined since it

was not possible to obtain OSL samples from the base of the T1 terraces.

Sediments from both the base and top of the T2 terraces have been dated, which allows an estimate of the duration of the S3 aggradation period. Three samples from the top of the T2 terraces (i.e., T2L06, T2R02 and SG-06) provide OSL ages between 8.5 ± 0.7 ka and 7.1 ± 0.7 ka (Fig. 7.2), which are indistinguishable, indicating a consistent date for the cessation of aggradation. However, sample T2RCK02, which was taken from the top of a T2 terrace at the valley mouth (Fig. 7.2), provides an OSL age of 13.8 ± 1.0 ka, older than the three samples located on the top of the T2 terraces upstream. This older age is similar to those of samples T2L16, T2L17 and T2L19 (Fig. 7.2), which were taken from the mid-portion of a T2 terrace upstream. From these ages it appears that when the T2 terraces in the midstream of the valley continued aggrading after 13.8 ± 1.0 ka, the T2 terrace at the valley mouth was abandoned. It is likely that the abandonment of the T2 terrace at the valley mouth was a result of channel avulsion. Therefore, the age of sample T2RCK02 does not represent the end of the S3 phase aggradation. The youngest age, 7.1 ± 0.7 ka, is taken to define the latest end of the S3 phase aggradation. The timing of the beginning of aggradation is determined using the age of sample T2R01 (46.8 ± 5.1 ka). This age is indistinguishable from that of sample D03-39 (43.3 ± 3.2 ka), which is 39 m beneath the channel in the downstream portion of GLP (Fig. 7.2). The ages of these two samples indicate that the GLP bedrock channel beneath the current alluvial channel was formed at least before 46.8 ± 5.1 ka and that the valley has experienced long-term aggradation since then forming the wide-spread T2 terraces. It is deduced, based on the varnish-coated T2 terraces at the location

of sample T2R01 (Fig. 7.2), that this aggradation had been interrupted by some short-term incision events leaving terrace relics older than the exposed T2 terraces.

Overall, the S3 aggradational phase appears to occur between 46.8 ± 5.1 ka and 7.1 ± 0.7 ka. During this phase both the exposed T2 terraces and the alluvium underlying the current channel were emplaced. The age for sample T2R01 (46.8 ka ± 5.1 ka) is a minimum estimate of the onset of aggradation because this sample was taken at an unknown distance above the phyllite bedrock, and the start of aggradation must predate this OSL age. The upper age (7.1 ± 0.7 ka) is a maximum age estimate for the termination of aggradation.

Periods of incision, termed S2 and S4, occurred between periods S1 and S3, and after S3, respectively. Therefore, the S2 incision period must have occurred between 90.0 ± 10.0 ka and 46.8± 5.1 ka, and the S4 incision period between 7.1 ± 0.7 ka and the present. Both time ranges represent the maximum duration of the incision. During the S4 incision period, the T3 and T4 terraces formed in the downstream portion of the GLP valley, representing two short-periods of aggradation during S4 period. The ages of the four samples from the T3 terraces (i.e., HDG, T3RBL02, T3700 and SG-01) constrain the aggradation time for the T3 terraces in a range of 1.4 ± 0.1 and 0.6 ± 0.1 ka (Fig. 7.2). Because these samples were taken from sediments close to the surface of the T3 terraces (Fig. 7.2), it is probably that they represent the terminal phase of T3 terrace formation, though it is possible that erosion of surficial material may have truncated the record of sediment deposition. The age of the basal sediments within the T3

terraces was not determined because no clear stratigraphic boundary was found in the exposed T3 terraces. Nevertheless, sample D02-4.7, which was taken at a depth of 4.7 m in core D02 beneath the current GLP channel (Fig. 7.2), produces an OSL age of 3.3 ± 0.3 ka. This sample was capped by some poorly sorted gravelly sediments, which were interpreted as deposits of debris flows. This age suggests that depositions of debris flows have occurred following this time. If this is the case, then deposition of the T3 terraces occurred between 3.3 ± 0.3 ka and 0.6 ± 0.1 ka. The time of the T4 alluvial terrace formation cannot be determined because no reliable OSL ages were produced for the T4 terraces in this study (Section 7.2.1).

8.4 Impact of climate

I used a composite speleothem record from Hulu Cave (Wang et al., 2001) and Sanbao Cave (Wang et al., 2008) to represent the climate covering the timeframe over which the sediments in GLP were deposited or incised (Fig. 8.3). The speleothem $\delta^{18}O$ record is interpreted as recording the strength of the East Asian Summer Monsoon (EASM) on orbital timescales (Wang et al., 2008; Wang et al., 2017). The general climatic conditions since the last interglacial period were summarized on the basis of pollen records (Li et al., 1988) into three characteristics modes of monsoon operation: the warm wet interglacial and Holocene mode (MIS 5 and 1), the cold wet transitional interstadial mode (MIS 3) and the cold dry full glacial mode (MIS 2 and 4).

The speleothem records are compared with the aggradation and incision stages observed in the GLP valley in Fig. 8.3. As the time of the S1 aggradation period

was not tightly constrained, it is difficult to discuss the climatic conditions of this period based on the speleothem based climatic records. The same applies to the S2 period because the beginning and end of the phase were not tightly constrained. In contrast, the time of the S3 and S4 phases were more tightly constrained by the OSL ages than the two previous phases, and the relationship between the S3 and S4 phases and the climatic conditions are discussed below.

The S3 aggradation phase falls into MIS 3, MIS 2 and part of MIS 1. Specifically, the borehole sediments beneath the present channel mostly formed during the MIS 3 period because two of the borehole samples (D01-30 and D03-39) provide OSL ages that are within this period. In contrast, the ages of the sediments from the exposed T2 terraces indicate that they were mostly deposited during the transition from MIS 2 to MIS 1. This period is characterized by a transitional climate from a dry-cold to a warm-wet type, which is consistent with the environment implied from the sedimentary sequences of the T2 terraces (Section 8.2). Noticeably, MIS 3, MIS 2 and the early period of Holocene represent a cold condition as is suggested from the pollen records from the nearby area (Li et al., 1988; Zhao et al., 2009). It is likely that the cold conditions were responsible for aggradation during these periods. The cold conditions, aided by the well-developed inter-crossing joints in the limestone bedrock, might enhance frost shattering (Walder and Hallet, 1985; Hales and Roering, 2007; Herman and Champagnac, 2016) in the high-elevation limestone areas (Fig. 7.1a), leading to increased rockfall activity and abundant supply of angular clasts. These angular clasts may be transported from the limestone hillslopes to the relatively low-elevation phyllite area by infrequent storms, resulting in deposition of sub-angular

clasts. The sediments making up the T2 terraces and the channel fills are mostly sub-angular limestone-dominated cobble- to pebble-sized clasts. The dominant grain size and the angularity may suggest that they have been sourced from the frost-shattering effects in the limestone headwaters (Lautridou and Ozouf, 1982; Lautridou and Seppälä, 1986; Dredge, 1992; Matsuoka, 2008).

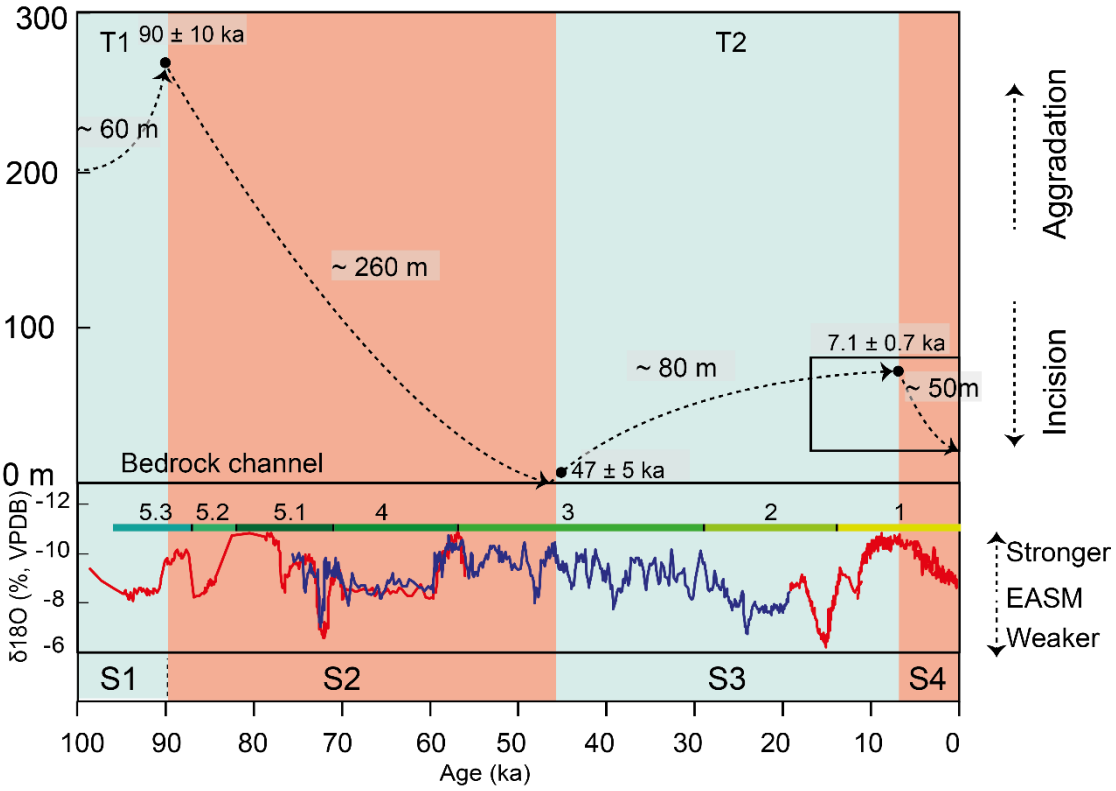

Fig. 8.3. GLP aggradation/incision stages plotted against the composite Hulu/Sanbao cave speleothem $\delta^{18}O$ records. Filled dots represent OSL ages that define the start/end of aggradation or incision periods. The red curves are the Sanbao Cave $\delta^{18}O$ speleothem records (Wang et al., 2008), and the blue curve is the Hulu Cave records (Wang et al., 2001). The numbers and colored bars above the speleothem curves are Marine Oxygen Isotopic Stages (Lisiecki and Raymo, 2005). Black dashed lines define the evolution stages in profile BB'. Black dashed lines with an upward pointing arrow represent the aggradation of the corresponding alluvial terraces, and black dashed lines with a downward pointing arrow represent the incision of the previous alluvial terraces. The blue shading represents aggradation periods, and the pink shading represents incision periods. The box on the right of the figure is enlarged in Fig. 8.4

The S4 incision occurred during the mid-Holocene period, which is after the strongest monsoon conditions indicated in the early Holocene portion of the speleothem record (Fig. 8.3). Noticeably, fossil pollen records tend to show a slow and gradual increase of effective moisture during the early Holocene and a maximum monsoon strength during the mid-Holocene, forming a contrast against the abrupt onset of the maximum monsoon indicated from the speleothem records (An et al., 2003; Lu et al., 2013; Wang et al., 2014; Chen et al., 2015). This mismatch between the pollen records and the speleothem records might be due to both the lag of vegetation response to climatic changes and the mismatch between temperature and precipitation in the early Holocene (Zhao et al., 2009). This mismatch is illustrated by plotting a pollen-based precipitation record covering the past 14 ka from Gonghai Lake, Northern China (Chen et al., 2015) against the Sanbao Cave speleothem record (Fig. 8.4). Although the pollen-based precipitation records, which was produced using transfer-functions, may subject to certain pitfalls such as spatial autocorrelation and model selection bias (Telford and Birks, 2011), the recovered precipitation record in Gonghai Lake (Chen et al., 2015) is generally consistent with other regional climatic records, such as the records of paleosol development (Wang et al., 2014), aeolian deposits (Li et al., 2014) and pollen records (Feng et al., 2006) in Northern China, indicating that it may be a suitable indicator of the regional paleoclimate.

According to Fig. 8.4, the S4 incision phase corresponds to a mid-Holocene warm and wet climate. It is likely that during the mid-Holocene the limestone hillslopes in GLP were covered by a forest vegetation similar to that which occurs in the present day. This vegetation cover may have acted to stabilize the sediments on

the hillslopes and reduce bedrock weathering rate, leading to a decrease in sediment supply. Meanwhile, annual water discharges and the frequency of flood discharges probably increased during this warm and wet period (Knox, 1993; Fowler and Hennessy, 1995), leading to exceeding of the critical stream power (Bull, 1991) and incision.

According to the Gonghai Lake pollen record, the climate started to become drier after 3.3 ka (Fig. 8.4). The vegetation in the nearby southwest Loess Plateau changed from a forest-steppe vegetation to a steppe vegetation from 4000 to 3120 years BP and further to a desert-steppe from 3120 to 2900 years BP (Feng et al., 2006). It is likely that the short aggradation of the T3 terraces was caused by increased sediment availability due to reduced vegetation cover resulting from aridity. The formation of the T3 terraces likely continued until the climate became wet again as is reflected by the sharp increase in the reconstructed precipitation around 1 ka (Fig. 8.4). Likewise, the T4 terraces probably formed in a second dry period, though here I did not obtain OSL ages for the T4 terraces.

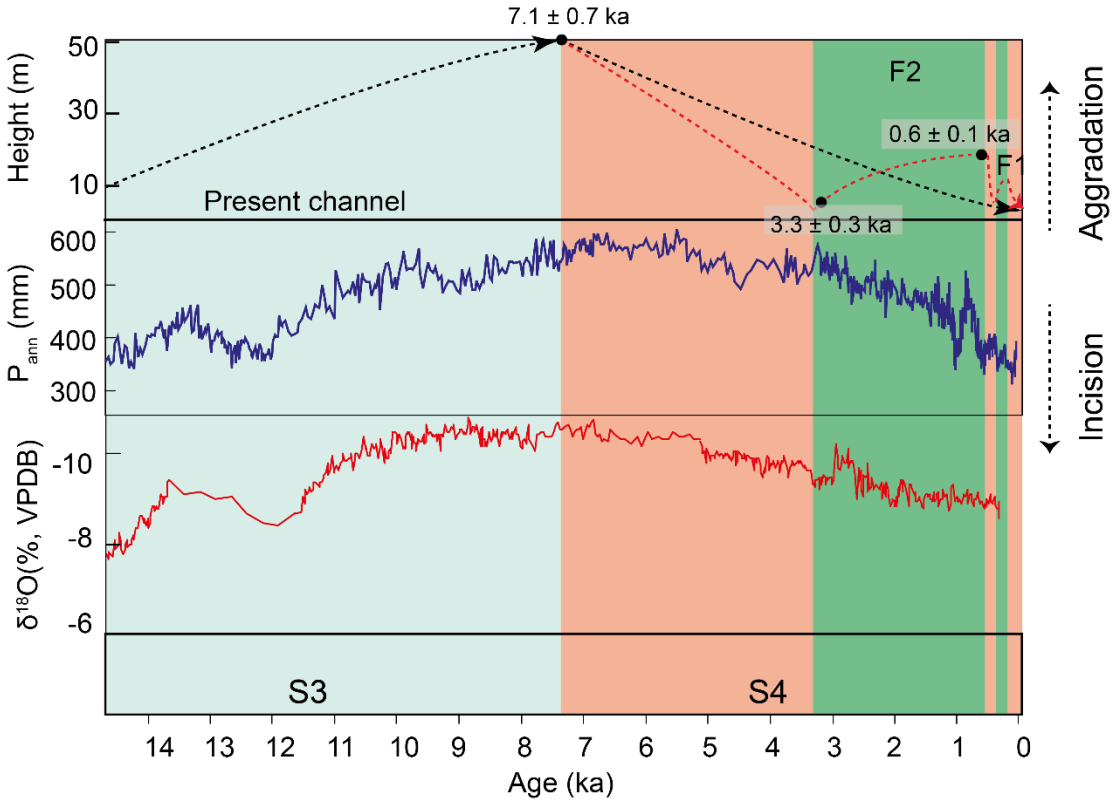

Fig. 8.4. GLP aggradation/incision stages and climatic records. Filled dots are OSL ages that define the start/end of aggradation or incision periods. The blue curve is a pollen-based precipitation record from Gonghai Lake (Chen et al., 2015), while the red curve is the Sanbao Cave $\delta^{18}O$ speleothem record (Wang et al., 2008). Black dashed lines define the evolution stages of the GLP valley at profile BB'. Black dashed lines with an upward pointing arrow represent the aggradation of the corresponding alluvial terraces. Black dashed lines with a downward pointing arrow represent the incision of the previous alluvial terraces. Dashed red lines define the evolution stages of GLP at profile DD', representing two small aggradation periods forming the T3 and T4 terraces. The blue shading represents aggradation periods, the pink shading represents incision periods, and the green shading represents the small aggradation periods.

From the discussion above, it is concluded that cold environments tend to enhance frost shattering, while dry environments generally cause reduced vegetation cover. Both effects contribute to a high sediment supply rate, leading to alluvial aggradation during infrequent flood discharge events. Conversely, warm and wet climate causes a reduction in sediment supply due to recovered vegetation and an increase in the frequency of flood discharges, leading to

incision. Similar relationships between climate and aggradation/incision pattern have been found in fluvial terraces in the marginal area of the Tibetan Plateau (Wang et al., 2009; Lu et al., 2010; Huang et al., 2014; He et al., 2015a). This similarity suggests that the GLP valley responds to climate in a similar manner to the primary rivers in the study area. Many studies argued that alluvial deposition occurred during periods of climatic transitions because great changes in flood magnitude/frequency and vegetation may occur during these periods (Bull, 1991; McDonald et al., 2003). In this study, samples of glacial ages (21-16 ka) and glacial-interglacial transition ages (13-7 ka) were obtained, indicating aggradation in both glacial and glacial-interglacial transition periods. This situation is consistent with the traditional expectations for alluvial aggradation during climatic transition periods. Besides, as the GLP valley is among the typical valleys in the mid-section of the Bailong River, representing intermediate-sized tributary valleys (10–100 km^2) with limestone drainage headwaters, the relationships between valley evolution and climate probably apply to similar valleys (in terms of watershed area, geology and relief, etc.) in the other sections of the Bailong River.

8.5 Impact of tectonism

The distribution of the T1 and T2 terraces in GLP (Fig. 4.4) indicates that the northwest part of the valley generally preserves more terraces than the southeast does. This asymmetric distribution of the alluvial sediments along the GLP valley indicates a preferential incision on the southeastern side of the valley. Analyses of the surfaces of a relatively well-extended T2 terrace (Fig. 8.5) also suggest that the terrace surfaces dip towards the southeast. This preferential incision and the preferential dipping of the terraces may be caused by the passive geological

setting of the valley or by an active southeastward dipping of the valley leading to water convergence on the southeastern side. Sedimentary analyses generally favor the passive geological setting because there is no obvious tilting or dipping of the sedimentary units. Conversely, a notable change of the deposition locus of the T1 and T2 alluvial terraces close to the fault (Fig. 8.5a) may suggest some lateral displacement of the thrust.

The deep incision which occurred during the S2 period (~260 m) may suggest large regional tectonic uplift of the eastern Tibetan Plateau because both climate and the small displacement of the local thrust fault seem unlikely to cause such a large incision. The uplift of the eastern Tibetan Plateau may have caused a fall in relative base-level at the Bailong River outlet, leading to vertical incision of the Bailong River and its tributary valleys. Considering the duration of the S2 period defined by OSL ages (90.0 ± 10.0 ka – 46.8 ± 5.1 ka), the mean incision rate during this period is ~ 6.0 mm/a. This mean incision rate is much higher than the incision rates at the foreland basins of the eastern Tibetan Plateau during this period. For example the incision rates were 0.75 mm/a in the Linxia Basin (Li et al., 1997b) and 0.32 mm/a in the Longxi Basin (Gao et al., 2008) in this period. However, the incision rate calculated for the GLP River during S2 is in agreement with the incision rates at the Gonghe Basin (4 mm/a) (Perrineau et al., 2011) and the Guide Basin (6.4 mm/a) (Pan, 1994). Both of these basins, as well as the GLP valley, represent areas where the primary rivers incised upstream into the Tibetan Plateau.

It is notable that the deformation of the local thrust fault is relatively insignificant

compared to the depth of incision. This pattern may suggest that the activity of the local thrust fault was decoupled from the regional uplift. Indeed, many thrust-faults in the Longmen Shan demonstrate small deformation, which is in striking contrast with the steep escarpment on the plateau margin (Royden et al., 1997). Royden et al. (1997) attributed the uplift in the eastern Tibet to a lower crust thickening mechanism, which is not directly related to horizontal shortening of the upper crust. Some field evidence supporting this hypothesis was identified in the Minshan region (e.g., Kirby et al., 2000), which is about 120 km south of GLP. However, no direct field evidence has been reported in the Bailong River region, further north to the Minshan region. This study suggests that it is likely that the Bailong River region, marking the northeastern to the eastern margin of the Tibetan plateau may have also been governed by this lower-crust thickening kinematics, though more field investigation is required to confirm this hypothesis.

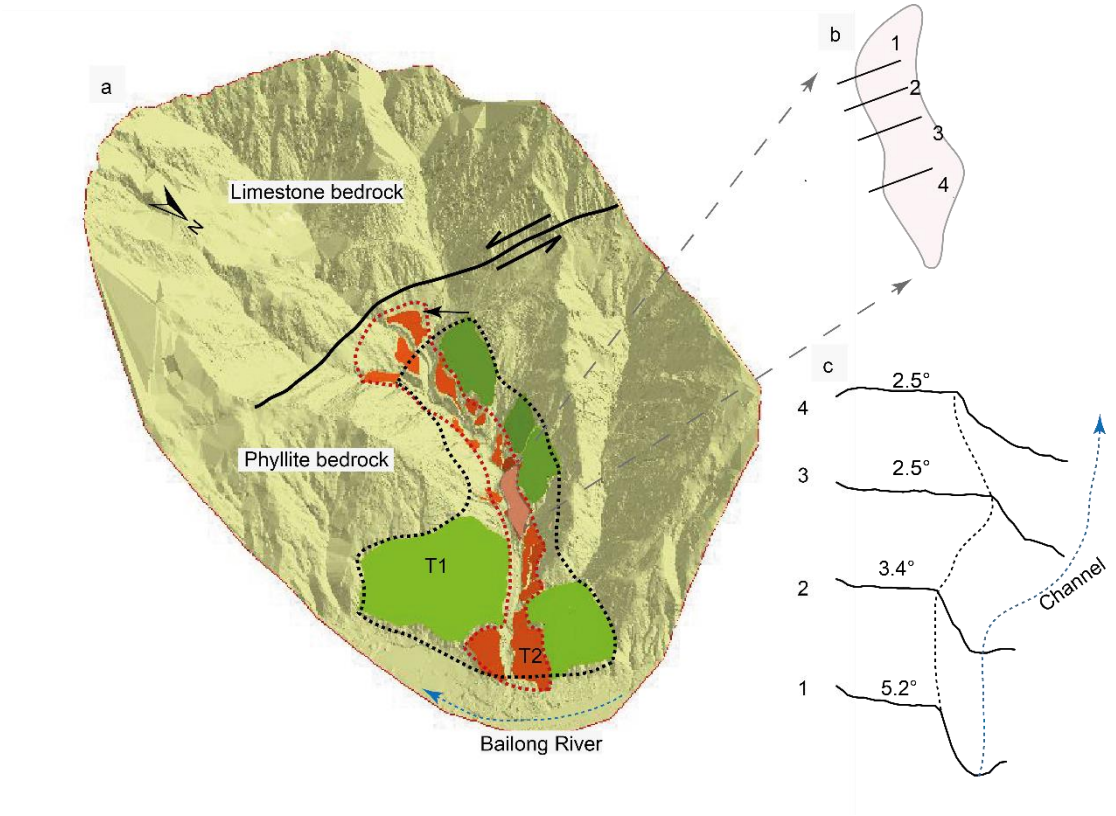

Fig. 8.5. Geomorphic analyses of the T1 and T2 terraces. a. The distribution of the T1 and T2 terraces in GLP and the reconstructed boundaries (dashed black and red lines) for the T1 and T2 terraces. The deposition loci of the T1 and T2 terraces in their proximal parts indicate a shift (the black arrow) toward the southeast of the valley. The background image is a LiDAR DEM. b. The locations of four cross-profiles on a well-extended T2 terrace which is shaded in pink in panel a. c. The four cross-profiles and their surface slopes.

8.6 Impact of base-level

As the GLP valley is connected to the Bailong River, the point at which the GLP channel intercepts the Bailong River represents the GLP base-level. Consequently the rise, fall and lateral migration of the Bailong River may have caused an impact on the development of alluvial terraces within the GLP valley.

Analyses of sediments from core D01 and section T1S3 indicate that at the mouth of the GLP valley, sediments sourced from the GLP valley overly sediments from the Bailong River. Each of the profiles consists of a lower section comprising

Bailong River sediments and an upper section comprising GLP valley sediments. Obviously, the aggradation of the alluvial terraces at the valley mouth occurred when flows in the Bailong River weakened. It is likely that the GLP aggradation periods has not been affected by the Bailong River, but only reflects the sediment-discharge balance of the GLP valley itself.

As a further deduction, the subsequent incision of the raised GLP channel must have been caused by a change in the sediment-discharge condition of the GLP valley itself. According to my observation in the valley, incision is mainly triggered by flooding events, i.e., a proximal-induced coupling regime (Mather et al., 2017). During fieldwork in May 2012, an incisional flooding event, triggered by an intense rainfall precipitating 39.5 mm within one hour, caused a 3 m vertical incision and 15 m lateral incision of the midstream portion of the GLP channel (Fig. 8.6a). During normal conditions, the channel is of a braided type (Fig. 8.6a), with limited erosive competence. These two pieces of evidence suggest that in the present day distal factors in the Bailong River are less important in driving incision than events within the GLP valley itself. However, it does appear that the GLP valley responded to climatic changes in a similar manner with the primary rivers in the eastern Tibetan Plateau. It is likely that during appropriate climatic conditions, both the Bailong River and the GLP valley experience incision, and hence both distally-induced and proximally-induced coupling (Mather et al., 2017) may occur, leading to rapid incision.

Fig. 8.6. Photographs showing the May 2012 flood event and its effects. a. The incision of the channel by the flood in the mid-stream portion of GLP. b. Photograph of the flood at the downstream portion of GLP. Dashed white lines delineate the boundary of the flow.

In contrast, during non-incising periods of the Bailong River, the lateral migration of the river channel may create or destroy the accommodation space for alluvial fans, leading to fan progradation or fan cutting respectively. The formation of the T3 and T4 terraces at the GLP valley mouth probably occurred when the Bailong River migrated laterally away from the GLP valley mouth, creating space in which gravelly sediments were deposited. These phases of terrace formation were also associated with a drying trend of the climate (Section 8.4). Moreover, the distal ends of the T3 and T4 terraces are straight (Fig. 4.4), indicating periods when the Bailong River approached the GLP valley mouth and eroded the distal ends of

the GLP alluvial fans.

8.7 Implications for debris flow/hyperconcentrated flood hazards

The GLP valley, as well as the wider Bailong River region, is affected by debris flows and hyperconcentrated floods at present. When these events deposit clastic sediments on populated alluvial terrace surfaces, they may cause significant damage or loss of life. For example, the Zhouqu debris flow, which is 37 km northwest of the GLP valley, occurred on 7 August 2010 and killed 1760 people (Tang et al., 2011; Xiong et al., 2016). These debris flows and hyperconcentrated floods are usually triggered by heavy rainfalls during summer seasons between May and September. In assessing the risk posed by these events for a specific alluvial terrace, the trend of aggradation and incision is crucial. Incision tends to deepen the channel, leading to abandonment of alluvial terraces, and hence can reduce the impact of debris flows/hyperconcentrated floods on local populations (living on alluvial terrace surfaces). Conversely, aggradation tends to elevate the channel floors, increasing the exposure of terrace surfaces to debris flows/floods, hence increasing the risk to human populations.

The evolution history of the GLP valley and its relationship to climate indicates that cold and/or dry environments tend to cause aggradation, while humid and warm environments tend to cause incision. Here, I attempt to apply this relationship to the prediction of future valley evolution with an aim of assessing debris flow/hyperconcentrated flood hazards. To do this, I analyzed the trend of precipitation and temperature anomalies over the past 62 yr (1950-2012) from a

nearby meteorological station (Fig. 8.7). During this period, annual temperatures have increased, particularly from c. 1980, while the annual precipitation remains largely unchanged. The warming, which has occurred primarily in the winter for most of China (Hu et al., 2003), would tend to decrease frost shattering, leading to a decreased rate of physical weathering. The unchanged annual precipitation may act to maintain the existing vegetation cover. Consequently, it might be expected that the valley has tended to move towards a more incision phase over the last half-century since sediment supply is reduced and discharge remains constant. Under such a scenario, the likelihood of debris flows/hyperconcentrated floods influencing the populations who live on alluvial terraces would decrease in the future. However, this trend does not exclude shorter term phases of aggradation brought about by debris flows and is contingent upon the same patterns of climate change continuing into the future. Moreover, because the T1, T2 and T3 terraces are occupied by people, human activities may influence the present incision trend of the valley. Associated activities include logging and rock mining in the limestone headwaters, which can lead to an increase of sediment supply and a more “flashy” discharge regime. Nevertheless, the general trend towards increased valley incision may be applicable to many other intermediate-sized valleys in the region because many of these valleys have also developed wide and deeply incised channels, indicating an active incision period at present. The continued incision would suggest that residents living on alluvial terraces are less likely to be impacted directly by any debris flow/hyperconcentrated flood events in the future.

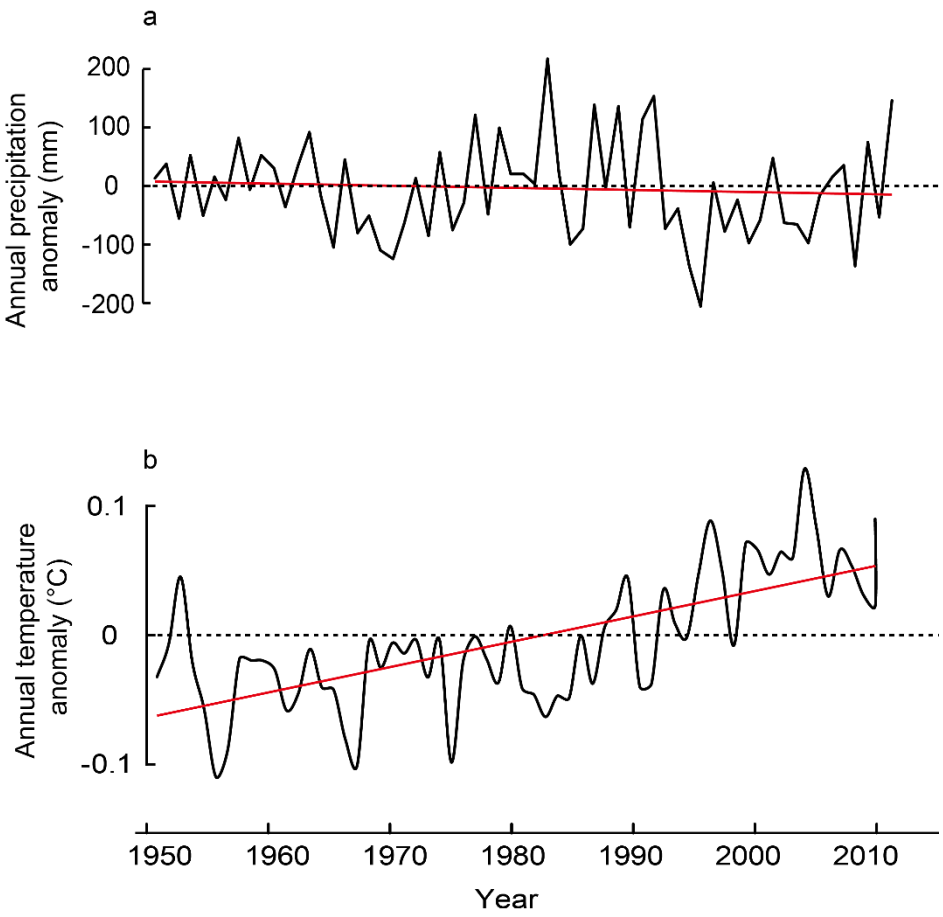

Fig. 8.7. Annual precipitation (a) and temperature anomalies (b) between 1950 and 2012, from the Wudu meteorological station, ~ 20 km from GLP. Data are provided by Mr. Yan Zhao from Lanzhou University. Red lines are the overall trend based on linear regression.

8.8 Conclusions

This chapter reconstructed the aggradation/incision history of the GLP valley by summarizing the geomorphological, sedimentological and chronological characteristics of the alluvial terraces and boreholes. The GLP aggradation/incision history is classified into two primary aggradation stages (S1 and S3) and two primary incision stages (S2 and S4). Each period is constrained by the OSL ages of samples taken from terraces/boreholes. Periods of aggradation are constrained by dating materials from the top and/or base of the terraces, and consequently, their ages are well-defined. Conversely, periods of

the incision are defined using the time intervals between two aggradation stages. Consequently, the ages for periods of incision represent the maximum length of time over which incision might have occurred. It is likely that active incision only occurred for a portion of the time periods defined above.

By examining the temporal correlations between the observed phases of aggradation and incision and the regional climate records, the study finds that the warm and wet mid-Holocene was dominated by rapid valley incision while the cold period from MIS 4 to early Holocene and the short dry periods between 3.3 and 0.6 ka were dominated by aggradation in GLP. The cold condition enhanced frost shattering effect, while the dry condition led to reduced vegetation cover. Both effects led to an increase of sediment supply in the limestone headwaters of the GLP valley. These sediments were transported by infrequent floods, forming alluvial deposits downstream. Phases of rapid incision during warm and humid periods are attributed to decreased sediment supply due to enhanced vegetation cover and an increased frequency of flood discharge.

By examining the spatial distribution of the alluvial terraces in the GLP valley, the study suggests that the asymmetric distribution of alluvial terraces along the GLP river may be determined by the passive geological setting, while the change of the deposition locus of the alluvial terraces close to the local thrust fault may suggest some lateral displacement of the thrust. The enormous incision during the S2 period is associated with the uplift of the eastern Tibetan Plateau. The contrast between the relatively small displacement of the local thrust fault and the large regional uplift suggests that the activity of the local fault was decoupled from

the regional uplift.

The effect of changes in base-level provided by the Bailong River on the alluvial terrace evolution was discussed based on: (1) the sedimentary sequences of the T1 terrace and the borehole at the mouth of the GLP valley; (2) the characteristics of the primary processes that dominate the valley evolution and (3) the plan-view shapes of the alluvial terraces which are close to the Bailong River. These analyses indicate that the base-level provided by the Bailong River may have exerted a minor control on valley aggradation and incision, whereas the lateral migration of the river channel was important in determining the accommodation space available for alluvial fans to form at the GLP valley mouth.

Lastly, this study also attempted to use insights regarding the relationship between past valley evolution and climate to make predictions about the future trend of valley evolution. The recent (past 62 years) instrumental precipitation and temperature records show a warming trend and a slight decrease in precipitation. These climatic trends are expected to have reduced sediment supply under a broadly stable discharge regime, leading to increased incision.

Chapter 9 Conclusions and Future Study

9.1 Introduction

This thesis aimed to reconstruct the Quaternary aggradation and incision history of a valley on the eastern margin of the Tibetan Plateau. To achieve this aim, detailed field-based geomorphological mapping, sedimentological analyses of alluvial terraces and cores, and optically stimulated luminescence dating were conducted. This chapter presents the general conclusions of the thesis and proposes some suggestions for future studies.

9.2 General conclusions

1) Four levels of alluvial terraces (T1, T2, T3 and T4, numbered from high-elevation to low-elevation) were mapped and characterized through field mapping and geomorphic analyses. The T1 and T2 terraces are distributed across the midstream and downstream portions of the GLP valley, whereas the T3 and T4 terraces are mainly distributed in the downstream portion of the GLP valley. The T1 and T2 terraces have the largest sediment volumes which are at least an order of magnitude larger than the T3 and T4 terraces.
2) Terrace genesis was revealed through sedimentological analyses of terrace outcrops. These analyses summarized six types of lithofacies associations, indicating six types of depositional processes/environments:
    a) hyperconcentrated floods sourced from the limestone-headwater of the GLP valley
    b) debris flows sourced from the limestone-headwater of the GLP valley,

c) stream/hyperconcentrated floods sourced from the phyllite-headwater of the GLP valley,
d) longitudinal bar deposition of the Bailong River,
e) alternating deposition of the Bailong River and GLP valley,
f) loess deposition

3) Debris flows and hyperconcentrated floods, sourced from the limestone-headwater of the GLP valley, were the primary processes causing GLP terrace aggradation. However, some T3 terraces were formed by stream/hyperconcentrated floods that were sourced from the phyllite-headwater of the GLP valley. Longitudinal bar deposition of the Bailong River and alternating deposition of the Bailong River and the GLP River occurred in the lower section of the T1 terraces at the mouth of GLP. Loess deposition occurred on the top/upper section of the T1 and T2 terraces.
4) The genesis of channel fill was revealed through sedimentological analyses of two cores (D01 and D03) on the present channel. These analyses also suggest that debris flows and hyperconcentrated floods, which were sourced from the limestone-headwater of GLP, were the primary processes causing the channel aggradation, except that at the mouth of the GLP valley some longitudinal bar deposition of the Bailong River contributed to the lower section of the channel fill.
5) Ages for loess, paleosols and alluvial silts (deposited by small streamflows or waning floods) were determined using the OSL dating of quartz using the SAR protocol. The luminescence characteristics of these samples are satisfactory (samples yield bright, rapidly decaying OSL signals and good recycling and dose-recovery ratios (Section 3.5.2)), and most samples

provided stratigraphically consistent ages. A small number of samples yielded stratigraphically anomalous ages, and these were excluded from further analysis.

6) The stages of the valley evolution during the Quaternary were determined by examining two cross-valley transects. Valley evolution was divided into two aggradation periods (S1 and S3, representing the aggradation of the T1 and T2 terraces, respectively) and two incision periods (S2 and S4, representing the incision of the T1 and T2 terraces, respectively). The formation of T3 and T4 terraces were attributed to two short aggradation stages during the longer S4 incision stage. The T3 and T4 terraces are not regarded as the result of primary aggradation stages because their sediment volumes are at least one magnitude order smaller than those of the T1 and T2 terraces.
7) The timing and duration of the aggradation/incision periods were defined using the OSL ages: the S1 period occurred before 90.0 ± 10.0 ka; the S2 period occurred between 90 ± 10.0 ka and 46.8± 5.1 ka; the S3 period occurred between 46.8 ± 5.1 ka and 7.1 ± 0.7 ka, and the S4 period occurred between 7.1 ± 0.7 ka and the present. The T3 aggradation period occurred between 3.3 ± 0.3 ka and 0.6 ± 0.1 ka. The onset time of the S1 phase is not determined because no samples could be obtained from the base of the T1 terraces. The duration of the S2 period determined above is regarded as a maximum value, since the age for the onset and termination of this event were dated based on ages from the preceding and succeeding aggradation phases respectively. The timing and duration of the S3 period is well defined because samples from the terrace top and

the valley bottom were dated. However, it is likely that some short-periods of incision may have occurred during this broad aggradation stage. The S4 incision period represents an ongoing trend in the evolution of the valley since 7.1 ± 0.7 ka. Two short aggradation periods (i.e., the formation of the T3 and T4 terraces) occurred during this incision period. The timing of the T4 terrace formation is not determined in this study because no suitable OSL samples could be obtained.

8) The effects of climatic change, tectonism and base-level change (i.e. changes in the Bailong River valley) on the evolution of the GLP valley were discussed. Climate appears to be the primary control on the alteration between valley aggradation and incision. The change of the depositional loci of the T1 and T2 terraces suggests that lateral displacement of a local thrust fault is also important. The depth of the S2 incision is regarded as a response to regional uplift of the eastern Tibetan Plateau. Lateral migration of the Bailong River channel facilitated deposition of alluvial terraces at the mouth of the GLP valley by creating accommodation space, but also eroded the distal ends of these terraces into a straight planform.

9) The above proposed relationship between climate and valley evolution was used to examine the possible future trend of valley evolution by analyzing modern climatic records, i.e. precipitation and temperature anomalies during the past 62 years. Modern climatic records indicate a warming trend with stable precipitation. This climatic trend was interpreted as likely indicating a stable valley discharge with a decreasing trend in sediment supply. Therefore the valley is anticipated to experience incision

in the future.

9.3 Recommendations for future study

This thesis provided a detailed geomorphological, sedimentological and chronological study on the alluvial landforms of a tributary valley on the eastern margin of the Tibetan Plateau. However, due to practical limitations (i.e., time and funding), a number of questions require future study. Moreover, this study also generated several important research questions which deserve further exploration.

9.3.1 Unsolved issues

1) The field mapping was carried out through investigation in the midstream portion of the valley. The upstream portion of GLP was not investigated because this portion is a sediment source area, not a depositional area. However, future investigation of the upstream portion of the valley may be required to provide a more complete understanding of sediment production, transportation and deposition in GLP.
2) Geomorphic analyses were carried out on a terrestrial LiDAR image, which provides a high-resolution DEM for the midstream and downstream portions of the valley. However, the image resolution of the upstream section of the valley is rather low due to a lack of scanner positions and vegetation shielding in the area. Airborne LiDAR systems are required to obtain a relatively high-precision image of the whole valley.
3) This study mainly used qualitative methods for sedimentary analyses. Though some quantitative measurements of sedimentary characteristics, such as clast fabric and grain size distribution, were also carried out, it was not

possible to conduct these analyses in a systematic manner through all units and consequently they did not result in a significantly deeper understanding of the relationships between process mechanics and sedimentary characteristics. In the future, it will be good practice to carry out systematic quantitative measurement of sedimentary features to establish the relationships between process mechanics and sedimentary characteristics. Specifically, two types of quantitative measurements should be refined in the future. The first one is the measurement of clast fabrics. In this study, I measured the a-axes for sediments which were interpreted as debris flows and the b-axes for sediments which were interpreted as streamflows in the field. However, this method of fabric measurement makes the comparison of clast fabrics between different sedimentary units difficult. In future, the measurement of clast fabrics should be conducted along the same axes for all sedimentary units to allow comparison between different units. The second one is the characterization of clast sizes. For most sedimentary units in this study, the dominant grain size was determined based on visual estimation. Image analyses and sieving were used to obtain the distribution of grain sizes for some sediments. However, methods for producing reproducible comparable (internally consistent) grain-size distributions using these two different methods were not explored. Comparison of different methods for grain size measurement is required to obtain rapid but consistent characterizations of grain size distributions for clastic sediments in the future.

4) Alluvial fine silts provided both satisfactory and anomalous estimates for the OSL burial ages of samples, and the reason for the success/failure of individual samples is unclear. It is likely that differences in depositional and

post-depositional processes experienced by each sample are important. Further detailed sedimentary analyses of the fine materials (e.g., grain size distribution, microstructure analyses etc.) are suggested. Also, in the present study only the fine silt fraction (4-11 μm) was dated. Other methods of OSL dating, such as single grain methods and single aliquot methods on different grain size fractions etc., and IRSL and pIR-IRSL dating of feldspar fractions, may yield further insights into the reason why some samples produced ages which appear to be erroneous. Lastly, the measurement of environmental dose rates for alluvial silt did not consider the heterogeneity of the sampled sediment, which may lead to inaccurate estimated dose rates. Future studies should also use field gamma-spectrometry to measure directly the gamma dose rate, thereby circumventing problems associated with inhomogeneous sediments.

9.3.2 Important research questions

1) The relative role of climate and tectonism in the production of coarse sediments in the Bailong River region. This study indicates that terrace aggradation occurred under cold climatic conditions. Cold periods can be regarded as responsible for the production of clastic sediments due to enhanced frost shattering. However, the broad eastern margin of the Tibetan Plateau has been subject to strong tectonic activity which has conventionally been regarded as the dominant factor in the production of coarse sediments. The question of whether these coarse sediments result from tectonic activity or from climate-induced effects, such as frost shattering and fluvial incision etc., is important to explore. Studies on the production of coarse sediments in

the high-elevation areas of the Bailong River region are recommended in the future.

2) Landform evolution pattern in the Bailong River region. This study revealed four periods of aggradation and incision during the development of the GLP valley during Quaternary. It is important to know whether Quaternary landforms have evolved in a similar manner in other valleys along the Bailong River. It is crucial to explore whether or not landform evolution is consistent between similar or different types of valleys and if differences exist, to understand why. Therefore, a regional-wide exploration of the landform evolution in the Bailong River region using the methods employed in this study is recommended in the future.

References

Adamiec, G., Aitken, M.J., 1998. Dose-rate conversion factors: update. Ancient TL 16, 37-50.

Aitken, M.J., 1990. Pairs precision required in alpha counting. Ancient TL 8, 12-14.

Aitken, M.J., 1985. Thermoluminescence dating. Academic Press, London.

Al-Farraj, A., Harvey, A.M., 2000. Desert pavement characteristics on wadi terrace and alluvial fan surfaces: Wadi Al-Bih, UAE and Oman. Geomorphology 35, 279-297.

Al-Farraj, A., Harvey, A.M., 2005. Morphometry and depositional style of Late Pleistocene alluvial fans: Wadi Al-Bih, northern UAE and Oman. Geological Society, London, Special Publications 251, 85-94.

Allen, J., 1983. Studies in fluviatile sedimentation: bars, bar-complexes and sandstone sheets (low-sinuosity braided streams) in the Brownstones (L. Devonian), Welsh Borders. Sedimentary Geology 33, 237-293.

An, C., Feng, Z., Tang, L., 2003. Evidence of a humid mid-Holocene in the western part of Chinese Loess Plateau. Chinese Science Bulletin 48, 2472-2479.

An, Z., 2000. The history and variability of the East Asian paleomonsoon climate. Quaternary Science Reviews 19, 171-187.

Antoine, P., Lautridou, J.P., Laurent, M., 2000. Long-term fluvial archives in NW France: response of the Seine and Somme rivers to tectonic movements, climatic variations and sea-level changes. Geomorphology 33, 183-207.

Armitage, S., Duller, G., Wintle, A., 2000. Quartz from southern Africa: sensitivity changes as a result of thermal pretreatment. Radiation Measurements 32, 571-577.

Armstrong, P.A., Perez, R., Owen, L.A., Finkel, R.C., 2010. Timing and controls on late Quaternary landscape development along the eastern Sierra El Mayor range front in northern Baja California, Mexico. Geomorphology 114, 415-430.

Bøtter-Jensen, L., Andersen, C., Duller, G.A., Murray, A.S., 2003. Developments in radiation, stimulation

and observation facilities in luminescence measurements. Radiation Measurements 37, 535-541.

Bagnold, R.A., 1954. Experiments on a gravity-free dispersion of large solid spheres in a Newtonian fluid under shear, Proceedings of the Royal Society of London, series A 225 , 49-63.

Bai, S., Wang, J., Thiebes, B., Cheng, C., Yang, Y., 2014. Analysis of the relationship of landslide occurrence with rainfall: a case study of Wudu County, China. Arabian Journal of Geosciences 7, 1277-1285.

Balsam, W., Ji, J., Chen, J., 2004. Climatic interpretation of the Luochuan and Lingtai loess sections, China, based on changing iron oxide mineralogy and magnetic susceptibility. Earth and Planetary Science Letters 223, 335-348.

Baptista, P., Cunha, T.R., Gama, C., Bernardes, C., 2012. A new and practical method to obtain grain size measurements in sandy shores based on digital image acquisition and processing. Sedimentary Geology 282, 294-306.

Barbour, G.B., 1936. Physiographic history of the Yangtze. The Geographical Journal 87, 17-32.

Beaty, C.B., 1963. Origin of Alluvial Fans, White Mountains, California and Nevada. Association of American Geographers 53, 516-535.

Bell, W., 1980. Alpha dose attenuation in quartz grains for thermoluminescence dating. Ancient TL 12, 8.

Benda, L., 1990. The influence of debris flows on channels and valley floors in the Oregon Coast Range, USA. Earth Surface Processes and Landforms 15, 457-466.

Benn, D. I., 2004. Clast morphology. In:Evans, D.J., Benn, D.I. (eds). A practical guide to the study of glacial sediments. Arnold, London, pp. 78-92.

Benn, D.I., Owen, L.A., Finkel, R.C., Clemmens, S., 2006. Pleistocene lake outburst floods and fan formation along the eastern Sierra Nevada, California: implications for the interpretation of intermontane lacustrine records. Quaternary Science Reviews 25, 2729-2748.

Bhattacharya, F., Shukla, A.D., Patel, R.C., Rastogi, B.K., Juyal, N., 2017. Sedimentology, geochemistry and OSL dating of the alluvial succession in the northern Gujarat alluvial plain (western India) - A record to evaluate the sensitivity of a semiarid fluvial system to the climatic and tectonic forcing since the late Marine Isotopic Stage 3. Geomorphology 297, 1-19.

Blair, T.C., 1999. Sedimentology of the debris-flow-dominated Warm Spring Canyon alluvial fan, Death Valley, California. Sedimentology 46, 941-965.

Blair, T.C., Mcpherson, J.G., 1994. Alluvial fan processes and forms. In: Parsons, A.J., Abrahams, A.D. (eds). Geomorphology of desert environments. Chapman & Hall, London, pp. 354-402.

Blasone, G., Cavalli, M., Marchi, L., Cazorzi, F., 2014. Monitoring sediment source areas in a debris-flow catchment using terrestrial laser scanning. Catena 123, 23-36.

Blott, S.J., Pye, K., 2008. Particle shape: a review and new methods of characterization and classification. Sedimentology 55, 31-63.

Blum, M.D., Törnqvist, T.E., 2000. Fluvial responses to climate and sea‐level change: a review and look forward. Sedimentology 47, 2-48.

Bockheim, J.G., 2010. Evolution of desert pavements and the vesicular layer in soils of the Transantarctic Mountains. Geomorphology 118, 433-443.

Bogaart, P.W., Balen, R.T.V., Kasse, C., Vandenberghe, J., 2003. Process-based modelling of fluvial system response to rapid climate change—I: model formulation and generic applications. Quaternary Science Reviews 22, 2077-2095.

Bollschweiler, M., Stoffel, M., Ehmisch, M., Monbaron, M., 2007. Reconstructing spatio-temporal patterns of debris-flow activity using dendrogeomorphological methods. Geomorphology 87, 337-351.

Bonneau, P.R., Scott Snow, R., 1992. Character of hearwaters adjustment to base level drop, investigated by digital modeling. Geomorphology 5, 475-487.

Bouma, A.H., Kuenen, P.H., Shepard, F.P., 1962. Sedimentology of some flysch deposits: a graphic approach to facies interpretation. Elsevier, Amsterdam.

Bowman, D., 1988. The declining but non-rejuvenating base level-The Lisan lake, the Dead Sea area, Israel. Earth Surface Processes and Landforms 13, 239-249.

Bowman, D., Shachnovich-Firtel, Y., Devora, S., 2007. Stream channel convexity induced by continuous base level lowering, the Dead Sea, Israel. Geomorphology 92, 60-75.

Bridge, J.S., 1993. Description and interpretation of fluvial deposits: a critical perspective. Sedimentology

40, 801-810.

Bridgland, D., Westaway, R., 2008. Climatically controlled river terrace staircases: a worldwide Quaternary phenomenon. Geomorphology 98, 285-315.

Bridgland, D., 2000. River terrace systems in north-west Europe: an archive of environmental change, uplift and early human occupation. Quaternary Science Reviews 19, 1293-1303.

Bridgland, D., Westaway, R., 2014. Quaternary fluvial archives and landscape evolution: a global synthesis. Proceedings of the Geologists' Association 125, 600-629.

Briggs, D., 1977. Sediments (Sources and Methods in Geography). Butterworths, Durban.

Brookfield, M., 1998. The evolution of the great river systems of southern Asia during the Cenozoic India-Asia collision: rivers draining southwards. Geomorphology 22, 285-312.

Bryant, M., Falk, P., Paola, C., 1995. Experimental study of avulsion frequency and rate of deposition. Geology 23, 365-368.

Bull, W.B., 1977. The alluvial-fan environment. Progress in Physical Geography 1, 222-270.

Bull, W.B., 1979. Threshold of critical power in streams. Geological Society of America Bulletin 90, 453-464.

Bull, W.B., 1991. Geomorphic responses to climatic change. The Blackburn Press, Caldwell

Bull, W.B., 2000. Correlation of fluvial aggradation events to times of global climate change. Quaternary Geochronology: Methods and Applications, 456-464.

Burbank, D.W., Anderson, R.S., 2011. Tectonic geomorphology. Blackwell, Oxford

Buscombe, D., 2008. Estimation of grain-size distributions and associated parameters from digital images of sediment. Sedimentary Geology 210, 1-10.

Buylaert, J.P., Jain, M., Murray, A.S., Thomsen, K.J., Thiel, C., Sohbati, R., 2012. A robust feldspar luminescence dating method for Middle and Late Pleistocene sediments. Boreas 41, 435-451.

Candy, I., Black, S., Sellwood, B., 2004. Interpreting the response of a dryland river system to Late

Quaternary climate change. Quaternary Science Reviews 23, 2513-2523.

Cavalli, M., Marchi, L., 2008. Characterisation of the surface morphology of an alpine alluvial fan using airborne LiDAR. Natural Hazards and Earth System Science 8, 323-333.

Chakrabarti Goswami, C., Mukhopadhyay, D., Poddar, B.C., 2013. Geomorphology in relation to tectonics: A case study from the eastern Himalayan foothills of West Bengal, India. Quaternary International 298, 80-92.

Chapot, M., Roberts, H., Duller, G., Lai, Z., 2012. A comparison of natural-and laboratory-generated dose response curves for quartz optically stimulated luminescence signals from Chinese Loess. Radiation Measurements 47, 1045-1052.

Chen, F., Xu, Q., Chen, J., Birks, H.J.B., Liu, J., Zhang, S., Jin, L., An, C., Telford, R.J., Cao, X., 2015. East Asian summer monsoon precipitation variability since the last deglaciation. Scientific Reports 5, 11186.

Chen, H., Chai, C., 1993. Comparison between debris flow sedimental profile and climatic change in the bordor region of eastern Qinghai-Xizang Plateau during Quaternary Journal of Chongqing Teachers college (Natural Science) 10, 461-463.

Chen, H., Li, J., 1997. General Approach on Geomorphologic Evolutino in Bailongjiang Basin since Quaternary. Journal of Chongqing Jiaotong institute 16, 18-25.

Chen, J., Dai, F., Lv, T., Cui, Z., 2013. Holocene landslide-dammed lake deposits in the Upper Jinsha River, SE Tibetan Plateau and their ages. Quaternary International 298, 107-113.

Chen, J., Dai, F., Yao, X., 2008. Holocene debris-flow deposits and their implications on the climate in the upper Jinsha River valley, China. Geomorphology 93, 493-500.

Chen, J., He, Y., Wei, F., 2005a. Debris flow erosion and deposition in Jiangjia Gully, Yunnan, China. Environmental geology 48, 771-777.

Chen, J., Wei, F., Cui, P., 2005b. Restricting conditions and their characteristics for debris flow Fans in Xiaojiang River Valley. Scientia Geographica Sinica 25, 704-708.

Chen, L., Steel, R.J., Guo, F., Olariu, C., Gong, C., 2017. Alluvial fan facies of the Yongchong Basin: Implications for tectonic and paleoclimatic changes during Late Cretaceous in SE China. Journal of Asian Earth Sciences 134, 37-54.

Clark, M., Schoenbohm, L., Royden, L., Whipple, K., Burchfiel, B., Zhang, X., Tang, W., Wang, E., Chen, L., 2004. Surface uplift, tectonics, and erosion of eastern Tibet from large-scale drainage patterns. Tectonics 23, TC1006.

Clark, M., Royden, L.H., 2000. Topographic ooze: Building the eastern margin of Tibet by lower crustal flow. Geology 28, 703-706.

Clarke, L., Quine, T.A., Nicholas, A., 2010. An experimental investigation of autogenic behaviour during alluvial fan evolution. Geomorphology 115, 278-285.

Colarossi, D., Duller, G.A.T., Roberts, H.M., Tooth, S., Lyons, R., 2015. Comparison of paired quartz OSL and feldspar post-IR IRSL dose distributions in poorly bleached fluvial sediments from South Africa. Quaternary Geochronology 30, Part B, 233-238.

Collinson, J., Mountney, N., Thompson, D., 2006. Sedimentary Structures. Dunedin Academic Press, Edinburgh.

Colombera, L., Bersezio, R., 2011. Impact of the magnitude and frequency of debris-flow events on the evolution of an alpine alluvial fan during the last two centuries: responses to natural and anthropogenic controls. Earth Surface Processes and Landforms 36, 1632-1646.

Compton, R.R., 1962. Manual of Field Geology. Wiley, London.

Coulthard, T., Lewin, J., Macklin, M., 2005. Modelling differential catchment response to environmental change. Geomorphology 69, 222-241.

Coulthard, T., Macklin, M., Kirkby, M., 2002. A cellular model of Holocene upland river basin and alluvial fan evolution. Earth Surface Processes and Landforms 27, 269-288.

Craddock, W.H., Kirby, E., Harkins, N.W., Zhang, H., Shi, X., Liu, J., 2010. Rapid fluvial incision along the Yellow River during headward basin integration. Nature Geoscience 3, 209-213.

Cui, Z., Xiong, H., 1990. A facies model of debris flow. Acta Seismologica Sinica 8, 128 - 140.

Dasgupta, P., Manna, P., 2011. Geometrical mechanism of inverse grading in grain-flow deposits: An experimental revelation. Earth-Science Reviews 104, 186-198.

De Haas, T., Densmore, A., Stoffel, M., Suwa, H., Imaizumi, F., Ballesteros-Cánovas, J., Wasklewicz, T., 2018. Avulsions and the spatio-temporal evolution of debris-flow fans. Earth Science Reviews 177, 53-75.

Demir, T., Seyrek, A., Guillou, H., Scaillet, S., Westaway, R., Bridgland, D., 2009. Preservation by basalt of a staircase of latest Pliocene terraces of the River Murat in eastern Turkey: evidence for rapid uplift of the eastern Anatolian Plateau. Global and Planetary Change 68, 254-269.

DiBiase, R.A., Whipple, K.X., Lamb, M.P., Heimsath, A.M., 2015. The role of waterfalls and knickzones in controlling the style and pace of landscape adjustment in the western San Gabriel Mountains, California. GSA Bulletin 127, 539-559.

Djuric, U., Abolmasov, B., Pavlovic, R., Trivic, B., 2011. Using ArcGIS for Landslide "Umka" 3D Visualization. In: Banjac, N., Savic, L., Maran, A., Cukavac, M., Ganic, M., Nikic, Z. (eds). The Geology in Digital Age. Proceedings of the 17th Meeting of the Association of European Geological Societies. Serbian Geological Society, Belgrade, pp. 21-25.

Dorn, R.I., 1988. A rock varnish interpretation of alluvial-fan development in Death Valley, California. National Geographic Research 4, 56-73.

Dorn, R.I., 2009. The role of climatic change in alluvial fan development. In Parsons, A.J., Abrahams, A.D. (eds). Geomorphology of Desert Environments, 2nd. Springer, Netherlands, pp. 593-615.

Dorn, R.I., DeNiro, M., Ajie, H., 1987. Isotopic evidence for climatic influence on alluvial-fan development in Death Valley, California. Geology 15, 108-110.

Dredge, L., 1992. Breakup of limestone bedrock by frost shattering and chemical weathering, eastern Canadian Arctic. Arctic and Alpine Research, 314-323.

Duller, G., 2003. Distinguishing quartz and feldspar in single grain luminescence measurements. Radiation measurements 37, 161-165.

Dutta, S., Suresh, N., Kumar, R., 2012. Climatically controlled Late Quaternary terrace staircase development in the fold-and-thrust belt of the Sub Himalaya. Palaeogeography, Palaeoclimatology, Palaeoecology 356, 16-26.

Eckis, R., 1928. Alluvial fans of the Cucamonga district, southern California. The Journal of Geology, 224-247.

Eriksson, M.G., Olley, J.M., Kilham, D.R., Pietsch, T., Wasson, R.J., 2006. Aggradation and incision since the very late Pleistocene in the Naas River, south-eastern Australia. Geomorphology 81, 66-88.

Erkens, G., Dambeck, R., Volleberg, K.P., Bouman, M.T.I.J., Bos, J.A.A., Cohen, K.M., Wallinga, J., Hoek, W.Z., 2009. Fluvial terrace formation in the northern Upper Rhine Graben during the last 20000 years as a result of allogenic controls and autogenic evolution. Geomorphology 103, 476-495.

Evans, D.J., Benn, D.I., 2004. A practical guide to the study of glacial sediments. Arnold, London.

Fang, X., Yan, M., Van der Voo, R., Rea, D.K., Song, C., Parés, J.M., Gao, J., Nie, J., Dai, S., 2005. Late Cenozoic deformation and uplift of the NE Tibetan Plateau: Evidence from high-resolution magnetostratigraphy of the Guide Basin, Qinghai Province, China. Geological Society of America Bulletin 117, 1208-1225.

Feng, Z.D., Tang, L., Wang, H., Ma, Y., Liu, K.-b., 2006. Holocene vegetation variations and the associated environmental changes in the western part of the Chinese Loess Plateau. Palaeogeography, Palaeoclimatology, Palaeoecology 241, 440-456.

Finnegan, N.J., Balco, G., 2013. Sediment supply, base level, braiding, and bedrock river terrace formation: Arroyo Seco, California, USA. Geological Society of America Bulletin 125, 1114-1124.

Fischer, A., 2009. Calculation of glacier volume from sparse ice-thickness data, applied to Schaufelferner, Austria. Journal of Glaciology 55, 453-460.

Fisher, R.V., 1971. Features of coarse-grained, high-concentration fluids and their deposits. Journal of Sedimentary Research 41, 916-927.

Fisher, R.V., 1983. Flow transformations in sediment gravity flows. Geology 11, 273-274.

Fowler, A., Hennessy, K., 1995. Potential impacts of global warming on the frequency and magnitude of heavy precipitation. Natural Hazards 11, 283-303.

Francus, P., 1998. An image-analysis technique to measure grain-size variation in thin sections of soft clastic sediments. Sedimentary Geology 121, 289-298.

Frankel, K.L., Brantley, K.S., Dolan, J.F., Finkel, R.C., Klinger, R.E., Knott, J.R., Machette, M.N., Owen, L.A., Phillips, F.M., Slate, J.L., 2007a. Cosmogenic ^{10}Be and ^{36}Cl geochronology of offset alluvial fans along the northern Death Valley fault zone: Implications for transient strain in the eastern California shear zone. Journal of Geophysical Research: Solid Earth 112, B6.

Frankel, K.L., Dolan, J.F., Finkel, R.C., Owen, L.A., Hoeft, J.S., 2007b. Spatial variations in slip rate along the Death Valley-Fish Lake Valley fault system determined from LiDAR topographic data and cosmogenic ^{10}Be geochronology. Geophysical Research Letters 34, L18303.

Friedman, G.M., Sanders, J.E., 1978. Principles of sedimentology. Wiley, New York.

Fuchs, M., Fischer, M., Reverman, R., 2010. Colluvial and alluvial sediment archives temporally resolved by OSL dating: Implications for reconstructing soil erosion. Quaternary Geochronology 5, 269-273.

Fuller, I.C., Macklin, M.G., Lewin, J., Passmore, D.G., Wintle, A.G., 1998. River response to high-frequency climate oscillations in southern Europe over the past 200 ky. Geology 26, 275-278.

Galbraith, R., Roberts, R.G., 2012. Statistical aspects of equivalent dose and error calculation and display in OSL dating: an overview and some recommendations. Quaternary Geochronology 11, 1-27.

Gao, H., Liu, X., Pan, B., Wang, Y., Yu, Y., Li, J., 2008. Stream response to Quaternary tectonic and climatic change: evidence from the upper Weihe River, central China. Quaternary International 186, 123-131.

Geach, M.R., Viveen, W., Mather, A.E., Telfer, M.W., Fletcher, W.J., Stokes, M., Peyron, O., 2015. An integrated field and numerical modelling study of controls on Late Quaternary fluvial landscape development (Tabernas, southeast Spain). Earth Surface Processes and Landforms 40, 1907-1926.

Ghazi, S., Mountney, N.P., 2011. Petrography and provenance of the Early Permian Fluvial Warchha Sandstone, Salt Range, Pakistan. Sedimentary Geology 233, 88-110.

Giano, S., 2011. Quaternary alluvial fan systems of the Agri intermontane basin (southern Italy): tectonic and climatic controls. Geologica Carpathica 62, 65-76.

Gilbert, G.K., 1877. Report on the Geology of the Henry Mountains. US Government Printing Office.

Godfrey-Smith, D.I., Huntley, D.J., Chen, W.-H., 1988. Optical dating studies of quartz and feldspar sediment extracts. Quaternary Science Reviews 7, 373-380.

Graham, D.J., Rollet, A.-J., Rice, S.P., Piégay, H., 2012. Conversions of surface grain-size samples collected and recorded using different procedures. Journal of Hydraulic Engineering 138, 839-849.

Guo, J., Han, W., Li, X., 2009. Analysis for control function of the fault framework and its active

characteristics for the geological hazards in the West Qinling. Geological Survey and Reseach 32, 241-248.

Hales, T., Roering, J.J., 2007. Climatic controls on frost cracking and implications for the evolution of bedrock landscapes. Journal of Geophysical Research: Earth Surface 112, F02033.

Hall, K., 2004. Evidence for freeze–thaw events and their implications for rock weathering in northern Canada. Earth Surface Processes and Landforms 29, 43-57.

Hallet, B., Molnar, P., 2001. Distorted drainage basins as markers of crustal strain east of the Himalaya. Journal of Geophysical Research: Solid Earth 106, 13697-13709.

Harkins, N., Kirby, E., Heimsath, A., Robinson, R., Reiser, U., 2007. Transient fluvial incision in the headwaters of the Yellow River, northeastern Tibet, China. Journal of Geophysical Research: Earth Surface 112, F03S04.

Harvey, A.M., 1978. Dissected alluvial fans in southeast Spain. Catena 5, 177-211.

Harvey, A.M., 1984. Aggradation and dissection sequences on Spanish alluvial fans: influence on morphological development. Catena 11, 289-304.

Harvey, A.M., 1996. The role of alluvial fans in the mountain fluvial systems of southeast Spain: implications of climatic change. Earth Surface Processes and Landforms 21, 543-553.

Harvey, A.M., 1997. The role of alluvial fans in arid zone fluvial systems. In:Thomas, D.S.G. (ed). Arid Zone Geomorphology: Processes, Form and Change in Drylands, 2nd. John Wiley & Sons, Chichester, pp. 231-259.

Harvey, A.M., 2002a. The role of base-level change in the dissection of alluvial fans: case studies from southeast Spain and Nevada. Geomorphology 45, 67-87.

Harvey, A.M., 2002b. Effective timescales of coupling within fluvial systems. Geomorphology 44, 175-201.

Harvey, A.M., 2005. Differential effects of base-level, tectonic setting and climatic change on Quaternary alluvial fans in the northern Great Basin, Nevada, USA. In: Harvey, A.M.,, Marther, A.E., Stokes, M. (eds). Alluvial fans, geomorphology, sedimentology, dynamics. Geological Society, London, Special Publications, 251, 117-131.

Harvey, A.M., 2011. Dryland alluvial fans. In: Thomas, D.S.G. (ed). Arid Zone Geomorphology: Processes,

Form and Change in Drylands, 3rd. John Wiley & Sons, Chichester, pp. 333-371.

Harvey, A.M., 2012. The coupling status of alluvial fans and debris cones: a review and synthesis. Earth Surface Processes and Landforms 37, 64-76.

Harvey, A.M., Mather, A.E., Stokes, M., 2005. Alluvial fans: geomorphology, sedimentology, dynamics-introduction. A review of alluvial-fan research. In: Harvey, A.M.,, Marther, A.E., Stokes, M. (eds). Alluvial fans, geomorphology, sedimentology, dynamics. Geological Society, London, Special Publications, 251, 1-7.

Harvey, A.M., Silva, P.G., Mather, A.E., Goy, J.L., Stokes, M., Zazo, C., 1999a. The impact of Quaternary sea-level and climatic change on coastal alluvial fans in the Cabo de Gata ranges, southeast Spain. Geomorphology 28, 1-22.

Harvey, A.M., Wigand, P.E., Wells, S.G., 1999b. Response of alluvial fan systems to the late Pleistocene to Holocene climatic transition: contrasts between the margins of pluvial Lakes Lahontan and Mojave, Nevada and California, USA. Catena 36, 255-281.

Harvey, A.M., Stokes, M., Mather, A., Whitfield, E., 2016. Spatial characteristics of the Pliocene to modern alluvial fan successions in the uplifted sedimentary basins of Almería, SE Spain: review and regional synthesis. Geological Society, London, Special Publications 440, 65-77.

He, Z., Zhang, X., Bao, S., Qiao, Y., Sheng, Y., Liu, X., He, X., Yang, X., Zhao, J., Liu, R., Lu, C., 2015a. Multiple climatic cycles imprinted on regional uplift-controlled fluvial terraces in the lower Yalong River and Anning River, SE Tibetan Plateau. Geomorphology 250, 95-112.

He, Z., Zhang, X., Qiao, Y., Bao, S., Lu, C., He, X., 2015b. Formation of the Yalong Downstream Terraces in the SE Tibetan Plateau and Its Implication for the Uplift of the Plateau. Acta Geologica Sinica (English Edition) 89, 542-560.

Hein, F.J., Walker, R.G., 1977. Bar evolution and development of stratification in the gravelly, braided, Kicking Horse River, British Columbia. Canadian Journal of Earth Sciences 14, 562-570.

Heller, F., Liu, T., 1982. Magnetostratigraphical dating of loess deposits in China. Nature 300, 431-433.

Heller, P.L., Paola, C., Hwang, I.G., John, B., Steel, R., 2001. Geomorphology and sequence stratigraphy due to slow and rapid base-level changes in an experimental subsiding basin (XES 96-1). AAPG bulletin 85, 0817-0838.

Herman, F., Champagnac, J.D., 2016. Plio-Pleistocene increase of erosion rates in mountain belts in response to climate change. Terra Nova 28, 2-10.

Hinderer, M., 2012. From gullies to mountain belts: a review of sediment budgets at various scales. Sedimentary Geology 280, 21-59.

Hoey, T., 2004. The size of sedimentary particles. In: Evans, D.J., Benn, D.I. (eds). A Practical Guide to the Study of Glacial Sediments. Arnold, London, pp. 52-77.

Holbrook, J., Scott, R.W., Oboh-Ikuenobe, F.E., 2006. Base-level buffers and buttresses: a model for upstream versus downstream control on fluvial geometry and architecture within sequences. Journal of Sedimentary Research 76, 162-174.

Homolová, D., Lomax, J., Špaček, P., Decker, K., 2012. Pleistocene terraces of the Vltava River in the Budějovice basin (Southern Bohemian Massif): New insights into sedimentary history constrained by luminescence data. Geomorphology 161-162, 58-72.

Hooke, R.L., 1972. Geomorphic evidence for late-Wisconsin and Holocene tectonic deformation, Death Valley, California. Geological Society of America Bulletin 83, 2073-2098.

Houben, P., 2003. Spatio-temporally variable response of fluvial systems to Late Pleistocene climate change: a case study from central Germany. Quaternary Science Reviews 22, 2125-2140.

Houben, P., Schmidt, M., Mauz, B., Stobbe, A., Lang, A., 2013. Asynchronous Holocene colluvial and alluvial aggradation: A matter of hydrosedimentary connectivity. The Holocene 23, 544-555.

Hu, Z.Z., Yang, S., Wu, R., 2003. Long-term climate variations in China and global warming signals. Journal of Geophysical Research: Atmospheres 108(D19), 4614.

Huang, W.l., Yang, X.P., Li, A., Thompson, J.A., Zhang, L., 2014. Climatically controlled formation of river terraces in a tectonically active region along the southern piedmont of the Tian Shan, NW China. Geomorphology 220, 15-29.

Hubert, J.F., Filipov, A.J., 1989. Debris-flow deposits in alluvial fans on the west flank of the White Mountains, Owens Valley, California, USA. Sedimentary geology 61, 177-205.

Huisink, M., De Moor, J.J.W., Kasse, C., Virtanen, T., 2002. Factors influencing periglacial fluvial morphology

in the northern European Russian tundra and taiga. Earth Surface Processes and Landforms 27, 1223-1235.

Hungr, O., Evans, S., Bovis, M., Hutchinson, J., 2001. A review of the classification of landslides of the flow type. Environmental & Engineering Geoscience 7, 221-238.

Hungr, O., 2005. Classification and terminology, In: Jacob, M. and Hungr, O. (eds). Debris-flow hazards and related phenomena. Springer, Berlin/ Heidelberg, pp. 9-23.

Hungr, O., Leroueil, S., Picarelli, L., 2014. The Varnes classification of landslide types, an update. Landslides 11, 167-194.

Imaizumi, F., Tsuchiya, S., Ohsaka, O., 2005. Behaviour of debris flows located in a mountainous torrent on the Ohya landslide, Japan. Canadian Geotechnical Journal 42, 919-931.

Iverson, R.M., 1997. The physics of debris flows. Reviews of geophysics 35, 245-296.

Iverson, R.M., 2014. Debris flows: behaviour and hazard assessment. Geology today 30, 15-20.

Jaboyedoff, M., Oppikofer, T., Abellán, A., Derron, M.-H., Loye, A., Metzger, R., Pedrazzini, A., 2012. Use of LIDAR in landslide investigations: a review. Natural Hazards 61, 5-28.

Jo, H., Rhee, C., Chough, S., 1997. Distinctive characteristics of a streamflow-dominated alluvial fan deposit: Sanghori area, Kyongsang Basin (Early Cretaceous), southeastern Korea. Sedimentary Geology 110, 51-79.

Johnson, A.M., Rodine, J., 1984. Debris flow. In: Brunsden, D., Piror, D.B. (eds). Slope instability. John Wiley&Sons, New York, pp. 257-361.

Johnson, A.M., 1970. Physical processes in geology: A method for interpretation of natural phenomena: intrusions in igneous rocks, fractures, and folds, flow of debris and ice. Freeman, Cooper & Co.

Johnson, K.R., Ingram, B.L., Sharp, W.D., Zhang, P., 2006. East Asian summer monsoon variability during Marine Isotope Stage 5 based on speleothem $\delta^{18}O$ records from Wanxiang Cave, central China. Palaeogeography, Palaeoclimatology, Palaeoecology 236, 5-19.

Jolivet, M., Barrier, L., Dominguez, S., Guerit, L., Heilbronn, G., Fu, B., 2014. Unbalanced sediment budgets in the catchment-alluvial fan system of the Kuitun River (northern Tian Shan, China): implications for mass-balance estimates, denudation and sedimentation rates in orogenic systems. Geomorphology 214, 168-182.

Juyal, N., Sundriyal, Y., Rana, N., Chaudhary, S., Singhvi, A.K., 2010. Late Quaternary fluvial aggradation and incision in the monsoon-dominated Alaknanda valley, Central Himalaya, Uttrakhand, India. Journal of Quaternary Science 25, 1-13.

Kar, R., Chakraborty, T., Chakraborty, C., Ghosh, P., Tyagi, A.K., Singhvi, A.K., 2014. Morpho-sedimentary characteristics of the Quaternary Matiali fan and associated river terraces, Jalpaiguri, India: Implications for climatic controls. Geomorphology 227, 137-152.

Kasse, C., Vandenberghe, J., Van Huissteden, J., Bohncke, S.J.P., Bos, J.A.A., 2003. Sensitivity of Weichselian fluvial systems to climate change (Nochten mine, eastern Germany). Quaternary Science Reviews 22, 2141-2156.

Kim, B.C., Lowe, D.R., 2004. Depositional processes of the gravelly debris flow deposits, South Dolomite alluvial fan, Owens Valley, California. Geosciences Journal 8, 153.

Kirby, E., Reiners, P.W., Krol, M.A., Whipple, K.X., Hodges, K.V., Farley, K.A., Tang, W., Chen, Z., 2002. Late Cenozoic evolution of the eastern margin of the Tibetan Plateau: Inferences from $^{40}Ar/^{39}Ar$ and (U-Th)/He thermochronology. Tectonics 21, 1-1-1-20.

Kirby, E., Whipple, K., 2001. Quantifying differential rock-uplift rates via stream profile analysis. Geology 29, 415-418.

Kirby, E., Whipple, K.X., Burchfiel, B.C., Tang, W., Berger, G., Sun, Z., Chen, Z., 2000. Neotectonics of the Min Shan, China: Implications for mechanisms driving Quaternary deformation along the eastern margin of the Tibetan Plateau. Geological Society of America Bulletin 112, 375-393.

Kiss, T., Sümeghy, B., Sipos, G., 2014. Late Quaternary paleodrainage reconstruction of the Maros River alluvial fan. Geomorphology 204, 49-60.

Klinger, Y., Avouac, J.P., Bourles, D., Tisnerat, N., 2003. Alluvial deposition and lake-level fluctuations forced by Late Quaternary climate change: the Dead Sea case example. Sedimentary Geology 162, 119-139.

Knox, J.C., 1993. Large increases in flood magnitude in response to modest changes in climate. Nature 361, 430-432.

Knox, J.C., 2001. Agricultural influence on landscape sensitivity in the Upper Mississippi River Valley. Catena 42, 193-224.

Kong, P., Zheng, Y., Caffee, M.W., 2012. Provenance and time constraints on the formation of the first bend of the Yangtze River. Geochemistry, Geophysics, Geosystems 13, Q06017.

Koons, P., 1995. Modeling the topographic evolution of collisional belts. Annual Review of Earth and Planetary Sciences 23, 375-408.

Krumbein, W.C., 1941. Measurement and geological significance of shape and roundness of sedimentary particles. Journal of Sedimentary Research 11, 64-72.

Kuang, M., Zhang, Y., Xie, S., Zeng, Y., Li, L., Feng, S., 2002. Age and stratigraphical division of diluvium-depositional sub-facies of debris-flow in Quaternary in Xiaojiang Drainage, Yunnan. Journal of Southwest China Normal University (Natural Science) 27, 974-980.

Kukla, G., 1987. Loess stratigraphy in central China. Quaternary Science Reviews 6, 191-219.

Kukla, G., Heller, F., Ming, L.X., Chun, X.T., Sheng, L.T., Sheng, A.Z., 1988. Pleistocene climates in China dated by magnetic susceptibility. Geology 16, 811-814.

Kumar Singh, A., Parkash, B., Mohindra, R., Thomas, J., Singhvi, A., 2001. Quaternary alluvial fan sedimentation in the Dehradun valley piggyback basin, NW Himalaya: tectonic and palaeoclimatic implications. Basin Research 13, 449-471.

Lai, Z.P., Brückner, H., Zöller, L., Fülling, A., 2007. Existence of a common growth curve for silt-sized quartz OSL of loess from different continents. Radiation Measurements 42, 1432-1440.

Lai, Z.P., 2006. Testing the use of an OSL standardised growth curve (SGC) for determination on quartz from the Chinese Loess Plateau. Radiation Measurements 41, 9-16.

Lai, Z.P., 2010. Chronology and the upper dating limit for loess samples from Luochuan section in the Chinese Loess Plateau using quartz OSL SAR protocol. Journal of Asian Earth Sciences 37, 176-185.

Lancaster, S.T., Hayes, S.K., Grant, G.E., 2003. Effects of wood on debris flow runout in small mountain watersheds. Water Resources Research 39(6), 1168.

Larson, P.H., Dorn, R.I., Faulkner, D.J., Friend, D.A., 2015. Toe-cut terraces: A review and proposed criteria to differentiate from traditional fluvial terraces. Progress in Physical Geography 39, 417-439.

Lauer, T., Frechen, M., Hoselmann, C., Tsukamoto, S., 2010. Fluvial aggradation phases in the Upper Rhine

Graben—new insights by quartz OSL dating. Proceedings of the Geologists' Association 121, 154-161.

Lautridou, J.-P., Seppälä, M., 1986. Experimental frost shattering of some Precambrian rocks, Finland. Geografiska Annaler: Series A, Physical Geography 68, 89-100.

Lautridou, J., Ozouf, J.-C., 1982. Experimental frost shattering: 15 years of research at the Centre de Géomorphologie du CNRS. Progress in Physical Geography 6, 215-232.

Le, K., Lee, J., Owen, L.A., Finkel, R., 2007. Late Quaternary slip rates along the Sierra Nevada frontal fault zone, California: Slip partitioning across the western margin of the Eastern California Shear Zone-Basin and Range Province. GSA Bulletin 119, 240-256.

Leeder, M., Mack, G., 2001. Lateral erosion ('toe-cutting') of alluvial fans by axial rivers: implications for basin analysis and architecture. Journal of the Geological Society 158, 885-893.

Leopold, L.B., Bull, W.B., 1979. Base level, aggradation, and grade. Proceedings of the American Philosophical Society 123, 168-202.

Leopold, L.B., Wolman, M.G., Miller, J.P., 1964. Fluvial processes in geomorphology. Courier Corporation.
Lewin, J., Macklin, M.G., 2003. Preservation potential for Late Quaternary river alluvium. Journal of Quaternary Science 18, 107-120.

Li, J.J., Fang, X.M., Van der Voo, R., Zhu, J.-J., Mac Niocaill, C., Cao, J.-X., Zhong, W., Chen, H.-L., Wang, J., Wang, J.-M., 1997a. Late Cenozoic magnetostratigraphy (11–0 Ma) of the Dongshanding and Wangjiashan sections in the Longzhong Basin, western China. Geologie en Mijnbouw 76, 121-134.

Li, J.J., Fang, X.M., Van der Voo, R., Zhu, J.J., Niocaill, C.M., Ono, Y., Pan, B.T., Zhong, W., Wang, J.L., Sasaki, T., 1997b. Magnetostratigraphic dating of river terraces: Rapid and intermittent incision by the Yellow River of the northeastern margin of the Tibetan Plateau during the Quaternary. Journal of Geophysical Research: Solid Earth (1978–2012) 102, 10121-10132.

Li, J., Feng, Z., Tang, L., 1988. Late Quaternary monsoon patterns on the Loess Plateau of China. Earth Surface Processes and Landforms 13, 125-135.

Li, Q., Wu, H., Yu, Y., Sun, A., Marković, S.B., Guo, Z., 2014. Reconstructed moisture evolution of the deserts in northern China since the Last Glacial Maximum and its implications for the East Asian Summer Monsoon. Global and Planetary Change 121, 101-112.

Li, Y., 1994. On obduction nappe structure of Bailongjinag Region. Acta Geologica Gansu 3, 41-49.

Li, Y., 2003. Influence of climatic fluctuation and human activity on debris flow movement-the case study in the east border of Tibetan Plateau and North China. Research of Soil and Water Conservation 10, 179-182.

Li, Y., Zhao, J., Cui, Z., 2002. The study of debris flow's movement regulation and reasons in late Cenozoic Era in the eastern fringe of Tibetan Plateau and the nearby regions. Geographical research 21, 561-567.

Liang, X., Chen, H., Tang, H., 2010. Studies on debris flow development properties in Quaternary on the eastern edge of Qinghai-Tibet Plateau. Journal of Chongqing Jiaotong University (Natrual Science) 29, 978-983.

Limaye, A., Lamb, M.P., 2016. Numerical model predictions of autogenic fluvial terraces and comparison to climate change expectations. Journal of Geophysical Research: Earth Surface 121, 512-544.

Lindsey, D.A., Langer, W.H., Van Gosen, B.S., 2007. Using pebble lithology and roundness to interpret gravel provenance in piedmont fluvial systems of the Rocky Mountains, USA. Sedimentary Geology 199, 223-232.

Lisiecki, L.E., Raymo, M.E., 2005. A Pliocene-Pleistocene stack of 57 globally distributed benthic $\delta^{18}O$ records. Paleoceanography 20, PA1003.

Liu, G., Cui, Z., 1999. Sedimentary macro-structures and forming mechanism of debris flow. Chinese Geographical Science 9, 33-39.

Liu, J., Chen, S., Chen, J., Zhang, Z., Chen, F., 2017. Chinese cave $\delta^{18}O$ records do not represent northern East Asian summer monsoon rainfall. Proceedings of the National Academy of Sciences, 201703471.

Liu, X., Tang, L., Zhang, S., Chen, M., 1992. The geomorphological characteristics of debris fans and their model experiments. The Chinese Journal of Geological Hazard and Control 3, 34-42.

Long, H., Tsukamoto, S., Buylaert, J.-P., Murray, A.S., Jain, M., Frechen, M., 2018. Late Quaternary OSL chronologies from the Qinghai Lake (NE Tibetan Plateau): Inter-comparison of quartz and K-feldspar ages to assess the pre-depositional bleaching. Quaternary Geochronology, https://doi.org/10.1016/j.quageo.2018.05.003.

Lowe, D.R., 1982. Sediment gravity flows: II Depositional models with special reference to the deposits of high-density turbidity currents. Journal of Sedimentary Research 52, 279-297.

Lu, H., Burbank, D.W., Li, Y., 2010. Alluvial sequence in the north piedmont of the Chinese Tian Shan over the past 550kyr and its relationship to climate change. Palaeogeography, Palaeoclimatology, Palaeoecology 285, 343-353.

Lu, H., Wang, X., An, Z., Miao, X., Zhu, R., Ma, H., Zhen, L., Tan, H., Wang, X., 2004. Geomorphologic evidence of phased uplift of the northeastern Qinghai-Tibet Plateau since 14 million years ago. Science in China Series D-Earth Sciences 47, 822-833.

Lu, H., Yi, S., Liu, Z., Mason, J.A., Jiang, D., Cheng, J., Stevens, T., Xu, Z., Zhang, E., Jin, L., 2013. Variation of East Asian monsoon precipitation during the past 21 ky and potential CO^2 forcing. Geology 41, 1023-1026.

Lukas, S., Benn, D.I., Boston, C.M., Brook, M., Coray, S., Evans, D.J., Graf, A., Kellerer-Pirklbauer, A., Kirkbride, M.P., Krabbendam, M., 2013. Clast shape analysis and clast transport paths in glacial environments: A critical review of methods and the role of lithology. Earth-Science Reviews 121, 96-116.

Lukas, S., Graf, A., Coray, S., Schlüchter, C., 2012. Genesis, stability and preservation potential of large lateral moraines of Alpine valley glaciers–towards a unifying theory based on Findelengletscher, Switzerland. Quaternary Science Reviews 38, 27-48.

Luzón, A., 2005. Oligocene–Miocene alluvial sedimentation in the northern Ebro Basin, NE Spain: Tectonic control and palaeogeographical evolution. Sedimentary Geology 177, 19-39.

Macklin, M.G., Fuller, I.C., Lewin, J., Maas, G.S., Passmore, D.G., Rose, J., Woodward, J.C., Black, S., Hamlin, R.H.B., Rowan, J.S., 2002. Correlation of fluvial sequences in the Mediterranean basin over the last 200ka and their relationship to climate change. Quaternary Science Reviews 21, 1633-1641.

Maddy, D., 1997. Uplift-driven valley incision and river terrace formation in southern England. Journal of Quaternary Science 12, 539-545.

Maddy, D., Bridgland, D., Westaway, R., 2001. Uplift-driven valley incision and climate-controlled river terrace development in the Thames Valley, UK. Quaternary International 79, 23-36.

Madsen, A.T., Murray, A.S., 2009. Optically stimulated luminescence dating of young sediments: A review. Geomorphology 109, 3-16.

Major, J.J., 1997. Depositional processes in large-scale debris-flow experiments. The Journal of Geology 105, 345-366.

Major, J.J., Iverson, R.M., 1999. Debris-flow deposition: Effects of pore-fluid pressure and friction concentrated at flow margins. Geological Society of America Bulletin 111, 1424-1434.

Makhlouf, I.M., Amireh, B.S., Abed, A.M., 2010. Sedimentology and morphology of Quaternary alluvial fans in Wadi Araba, Southwest Jordan. Jordan Journal of Earth and Environmental Sciences3, 79-98.
Marchi, L., Arattano, M., Deganutti, A.M., 2002. Ten years of debris-flow monitoring in the Moscardo Torrent (Italian Alps). Geomorphology 46, 1-17.

Mark, D.M., 1973. Analysis of axial orientation data, including till fabrics. Geological Society of America Bulletin 84, 1369-1374.

Marston, R.A., Weihs, B.J., Butler, W.D., 2011. Slope failures and cross-valley profiles, Grand Teton National Park, Wyoming. University of Wyoming National Park Service Research Center Annual Report 33, 51-64.

Mather, A., Stokes, M., Whitfield, E., 2017. River terraces and alluvial fans: The case for an integrated Quaternary fluvial archive. Quaternary Science Reviews 166, 74-90.

Matmon, A., Schwartz, D., Finkel, R., Clemmens, S., Hanks, T., 2005. Dating offset fans along the Mojave section of the San Andreas fault using cosmogenic 26Al and 10Be. Geological Society of America Bulletin 117, 795-807.

Matsuoka, N., 2001. Direct observation of frost wedging in alpine bedrock. Earth Surface Processes and Landforms 26, 601-614.

Matsuoka, N., 2008. Frost weathering and rockwall erosion in the southeastern Swiss Alps: Long-term (1994–2006) observations. Geomorphology 99, 353-368.

May, C.L., Gresswell, R.E., 2004. Spatial and temporal patterns of debris-flow deposition in the Oregon Coast Range, USA. Geomorphology 57, 135-149.

McDonald, E.V., McFadden, L.D., Wells, S.G., 2003. Regional response of alluvial fans to the Pleistocene-Holocene climatic transition, Mojave Desert, California. Special Papers-Geological Society of America, 189-206.

McFadden, L.D., Ritter, J.B., Wells, S.G., 1989. Use of multiparameter relative-age methods for age estimation and correlation of alluvial fan surfaces on a desert piedmont, eastern Mojave Desert, California. Quaternary Research 32, 276-290.

Meetei, L.I., Pattanayak, S.K., Bhaskar, A., Pandit, M.K., Tandon, S.K., 2007. Climatic imprints in Quaternary valley fill deposits of the middle Teesta valley, Sikkim Himalaya. Quaternary International 159, 32-46.

Mejdahl, V., 1979. Thermoluminescence dating: Beta-dose attenuation in quartz grains. Archaeometry 21, 61-72.

Mellett, C.L., 2013. Luminescence Dating. Geomorphological Techniques. British Society for Geomorphology.

Miall, A.D., 1977. A review of the braided-river depositional environment. Earth-Science Reviews 13, 1-62.

Miall, A.D., 1978. Lithofacies types and vertical profile models in braided river deposits: a summary. In: Miall, A.D. (ed). Fluvial Sedimentology. Canadian Society of Petroleum Geologists, Calgary, pp. 597-604.

Miall, A.D., 1985. Architectural-element analysis: a new method of facies analysis applied to fluvial deposits. Earth-Science Reviews 22, 261-308.

Miall, A.D., 2006. The geology of fluvial deposits: sedimentary facies, basin analysis, and petroleum geology, 4th. Springer, Berlin.

Middleton, G.V., 1970. Experimental studies related to problems of flysch sedimentation, In: Lajoie, J. (ed). Flysch Sedimentatology in North America. Geol. Assoc. Canada Special Paper 7, pp. 253-272.

Miller, D.M., Schmidt, K.M., Mahan, S.A., McGeehin, J.P., Owen, L.A., Barron, J.A., Lehmkuhl, F., Löhrer, R., 2010. Holocene landscape response to seasonality of storms in the Mojave Desert. Quaternary International 215, 45-61.

Mills, H.H., 1979. Downstream rounding of pebbles-a quantitative review. Journal of Sedimentary Research 49, 295-302.

Mol, J., Vandenberghe, J., Kasse, C., 2000. River response to variations of periglacial climate in mid-latitude Europe. Geomorphology 33, 131-148.

Montgomery, D.R., 2002. Valley formation by fluvial and glacial erosion. Geology 30, 1047-1050.

Murray, A.S., Thomsen, K.J., Masuda, N., Buylaert, J.P., Jain, M., 2012. Identifying well-bleached quartz using the different bleaching rates of quartz and feldspar luminescence signals. Radiation Measurements

47, 688-695.

Murray, A.S., Wintle, A.G., 2000. Luminescence dating of quartz using an improved single-aliquot regenerative-dose protocol. Radiation measurements 32, 57-73.

Nemec, W., 1990. Aspects of sediment movement on steep delta slopes. Coarse-grained deltas 10, 29-73.

Neves, M., Morales, N., Saad, A., 2005. Facies analysis of Tertiary alluvial fan deposits in the Jundiaí region, São Paulo, southeastern Brazil. Journal of South American Earth Sciences 19, 513-524.

Nicholes, G., 2009. Sedimentology and Stratigraphy, 2nd. Wiley-Blackwell, Chichester.

Nicholas, A., Clarke, L., Quine, T., 2009. A numerical modelling and experimental study of flow width dynamics on alluvial fans. Earth Surface Processes and Landforms 34, 1985-1993.

Nicholas, A.P., Quine, T.A., 2007. Modeling alluvial landform change in the absence of external environmental forcing. Geology 35, 527-530.

Notebaert, B., Verstraeten, G., 2010. Sensitivity of West and Central European river systems to environmental changes during the Holocene: A review. Earth-Science Reviews 103, 163-182.

Oguchi, T., 1997. Late quaternary sediment budget in alluvial-fan-source-basin systems in Japan. Journal of Quaternary Science 12, 381-390.

Okuda, S., Suwa, H., 1981. Topographical change caused by debris flow in Kamikamihori Valley, northern Japanese Alps. Transactions-Japanese Geomorphological Union 2, 343-352.

Olszak, J., 2017. Climatically controlled terrace staircases in uplifting mountainous areas. Global and Planetary Change 156, 13-23.

Olszak, J., Kukulak, J., Alexanderson, H., 2016. Revision of river terrace geochronology in the Orawa-Nowy Targ Depression, south Poland: insights from OSL dating. Proceedings of the Geologists' Association 127, 595-605.

Orford, J., Whalley, W., 1991. Quantitative grain form analysis. In: James, P.M. Syvitski (ed). Principles, Methods, and Application of Particle Size Analysis. Cambridge University Press, New York, pp. 88-108.

Ouimet, W.B., Whipple, K.X., Royden, L.H., Sun, Z., Chen, Z., 2007. The influence of large landslides on river

incision in a transient landscape: Eastern margin of the Tibetan Plateau (Sichuan, China). Geological Society of America Bulletin 119, 1462-1476.

Owen, L.A., Windley, B., Cunningham, W., Badamgarov, J., Dorjnamjaa, D., 1997. Quaternary alluvial fans in the Gobi of southern Mongolia: evidence for neotectonics and climate change. Journal of Quaternary Science 12, 239-252.

Owen, L.A., Clemmens, S.J., Finkel, R.C., Gray, H., 2014. Late Quaternary alluvial fans at the eastern end of the San Bernardino Mountains, Southern California. Quaternary Science Reviews 87, 114-134.

Owen, L.A., Finkel, R.C., Haizhou, M., Barnard, P.L., 2006. Late Quaternary landscape evolution in the Kunlun Mountains and Qaidam Basin, Northern Tibet: A framework for examining the links between glaciation, lake level changes and alluvial fan formation. Quaternary International 154–155, 73-86.

Pan, B., 1994. Research upon the geomorphologic evolution of the Guide Basin and the development of the Yellow River. Arid Land Geography 7, 43-50.

Pan, B., Hu, X., Gao, H., Hu, Z., Cao, B., Geng, H., Li, Q., 2013. Late Quaternary river incision rates and rock uplift pattern of the eastern Qilian Shan Mountain, China. Geomorphology 184, 84-97.

Pan, B., Su, H., Hu, Z., Hu, X., Gao, H., Li, J., Kirby, E., 2009. Evaluating the role of climate and tectonics during non-steady incision of the Yellow River: evidence from a 1.24Ma terrace record near Lanzhou, China. Quaternary Science Reviews 28, 3281-3290.

Parton, A., Farrant, A.R., Leng, M.J., Telfer, M.W., Groucutt, H.S., Petraglia, M.D., Parker, A.G., 2015. Alluvial fan records from southeast Arabia reveal multiple windows for human dispersal. Geology 43, 295-298.

Pastre, J.-F., Limondin-Lozouet, N., Leroyer, C., Ponel, P., Fontugne, M., 2003. River system evolution and environmental changes during the Lateglacial in the Paris Basin (France). Quaternary Science Reviews 22, 2177-2188.

Pazzaglia, F.J., 2013. Fluvial terraces. In: John, F.S. (ed). Treatise on geomorphology. Academic Press, San Diego: pp. 379-412.

Pazzaglia, F.J., Gardner, T.W., Merritts, D.J., 1998. Bedrock fluvial incision and longitudinal profile development over geologic time scales determined by fluvial terraces. Geophysical Monograph Series 107, 207-235.

Pederson, C.A., Santi, P.M., Pyles, D.R., 2015. Relating the compensational stacking of debris-flow fans to characteristics of their underlying stratigraphy: Implications for geologic hazard assessment and mitigation. Geomorphology 248, 47-56.

Perrineau, A., Van Der Woerd, J., Gaudemer, Y., Liu-Zeng, J., Pik, R., Tapponnier, P., Thuizat, R., Rongzhang, Z., 2011. Incision rate of the Yellow River in Northeastern Tibet constrained by ^{10}Be and ^{26}Al cosmogenic isotope dating of fluvial terraces: implications for catchment evolution and plateau building. Geological Society, London, Special Publications 353, 189-219.

Perry, C., Taylor, K., 2007. Environmental sedimentology. Blackwell Publishing, Oxford.

Petter, A.L., Muto, T., 2008. Sustained alluvial aggradation and autogenic detachment of the alluvial river from the shoreline in response to steady fall of relative sea level. Journal of Sedimentary Research 78, 98-111.

Pierson, T.C., 1980. Erosion and deposition by debris flows at Mt Thomas, north Canterbury, New Zealand. Earth Surface Processes 5, 227-247.

Pierson, T.C., Costa, J.E., 1987. A rheologic classification of subaerial sediment-water flows. Reviews in engineering geology 7, 1-12.

Pope, R., Wilkinson, K., Skourtsos, E., Triantaphyllou, M., Ferrier, G., 2008. Clarifying stages of alluvial fan evolution along the Sfakian piedmont, southern Crete: new evidence from analysis of post-incisive soils and OSL dating. Geomorphology 94, 206-225.

Pope, R.J., Candy, I., Skourtsos, E., 2016. A chronology of alluvial fan response to Late Quaternary sea level and climate change, Crete. Quaternary Research 86, 170-183.

Pope, R.J., Wilkinson, K.N., 2005. Reconciling the roles of climate and tectonics in Late Quaternary fan development on the Spartan piedmont, Greece. Geological Society, London, Special Publications 251, 133-152.

Posamentier, H., Vail, P., 1988. Eustatic controls on clastic deposition II—sequence and systems tract models. In: Wilgus, C.K., Hastings, B.S., C.G.St.C. Kendall, H.W. Posamentier, C.A. Ross, J.C. Van Wagoner (eds), Sea-Level Changes: An Integrated Approach, SEPM Special Publication 42, pp. 125-154

Postma, G., Nemec, W., Kleinspehn, K.L., 1988. Large floating clasts in turbidites: a mechanism for their emplacement. Sedimentary geology 58, 47-61.

Porter, S.C., 2007. Loess records, China. in: Elias, S.A. (Ed.), Encyclopedia of Quaternary Science. Elsevier, Oxford, pp. 1429-1440.

Powers, M.C., 1953. A new roundness scale for sedimentary particles. Journal of Sedimentary Petrology 23, 117-119.

Prescott, J.R., Hutton, J.T., 1994. Cosmic ray contributions to dose rates for luminescence and ESR dating: large depths and long-term time variations. Radiation measurements 23, 497-500.

Qiao, L., Meng, X.-m., Chen, G., Zhang, Y., Guo, P., Zeng, R.-q., Li, Y.-j., 2017. Effect of rainfall on a colluvial landslide in a debris flow valley. Journal of Mountain Science 14, 1113-1123.

Railsback, L.B., Xiao, H., Liang, F., Akers, P.D., Brook, G.A., Dennis, W.M., Lanier, T.E., Tan, M., Cheng, H., Edwards, R.L., 2014. A stalagmite record of abrupt climate change and possible Westerlies-derived atmospheric precipitation during the Penultimate Glacial Maximum in northern China. Palaeogeography, Palaeoclimatology, Palaeoecology 393, 30-44.

Rees-Jones, J., 1995. Optical dating of young sediments using fine-grain quartz. Ancient TL 13, 9-14.

Rees, A., 1968. The production of preferred orientation in a concentrated dispersion of elongated and flattened grains. The Journal of Geology, 457-465.

Rees, A., 1983. Experiments on the production of transverse grain alignment in a sheared dispersion. Sedimentology 30, 437-448.

Rhodes, E.J., 2011. Optically stimulated luminescence dating of sediments over the past 200,000 years. Annual Review of Earth and Planetary Sciences 39, 461-488.

Ritter, J.B., Miller, J.R., Enzel, Y., Wells, S.G., 1995. Reconciling the roles of tectonism and climate in Quaternary alluvial fan evolution. Geology 23, 245-248.

Roberts, R.G., Lian, O.B., 2015. Illuminating the past. Nature 520, 438.

Robinson, R., Spencer, J., Strecker, M., Richter, A., Alonso, R., 2005. Luminescence dating of alluvial fans in intramontane basins of NW Argentina. Special Publication, Geological Society of London 251, 153-168.

Rodnight, H., Duller, G., Wintle, A., Tooth, S., 2006. Assessing the reproducibility and accuracy of optical

dating of fluvial deposits. Quaternary Geochronology 1, 109-120.

Rosgen, D.L., 1994. A classification of natural rivers. Catena 22, 169-199.

Roussillon, T., Piégay, H., Sivignon, I., Tougne, L., Lavigne, F., 2009. Automatic computation of pebble roundness using digital imagery and discrete geometry. Computers & Geosciences 35, 1992-2000.

Roy, P., Caballero, M., Lozano, R., Ortega, B., Lozano, S., Pi, T., Israde, I., Morton, O., 2010. Geochemical record of Late Quaternary paleoclimate from lacustrine sediments of paleo-lake San Felipe, western Sonora Desert, Mexico. Journal of South American Earth Sciences 29, 586-596.

Royden, L.H., Burchfiel, B.C., King, R.W., Wang, E., Chen, Z., Shen, F., Liu, Y., 1997. Surface deformation and lower crustal flow in eastern Tibet. Science 276, 788-790.

Rust, B.R., 1984. Proximal braidplain deposits in the Middle Devonian Malbaie Formation of Eastern Gaspé, Quebec, Canada. Sedimentology 31, 675-695.

Schürch, P., Densmore, A.L., Rosser, N.J., McArdell, B.W., 2011. Dynamic controls on erosion and deposition on debris-flow fans. Geology 39, 827-830.

Schanz, S.A., Montgomery, D.R., Collins, B.D., Duvall, A.R., 2018. Multiple paths to straths: A review and reassessment of terrace genesis. Geomorphology 312, 12-23.

Schumm, S.A., 1977. The fluvial system. Wiley, New York.

Schumm, S.A., 1979. Geomorphic thresholds: the concept and its applications. Transactions of the Institute of British Geographers 4, 485-515.

Schumm, S.A., Mosley, M.P., Weaver, W., 1987. Experimental fluvial geomorphology. Wiley, New York.

Schumm, S.A., Parker, R.S., 1973. Implications of complex response of drainage systems for Quaternary alluvial stratigraphy. Nature Physical Science 243, 99-100.

Sengupta, S., 2007. Introduction to sedimentology. CBS Publisher & Distributor, New Delhi

Shukla, U., 2009. Sedimentation model of gravel-dominated alluvial piedmont fan, Ganga Plain, India. International Journal of Earth Sciences 98, 443-459.

Silva, P., Harvey, A., Zazo, C., Goy, J., 1992. Geomorphology, depositional style and morphometric relationships of Quaternary alluvial fans in the Guadalentin Depression (Murcia, Southeast Spain). Zeitschrift für Geomorphologie 36, 325-341.

Singh, A.K., Jaiswal, M.K., Pattanaik, J.K., Dev, M., 2016. Luminescence chronology of alluvial fan in North Bengal, India: Implications to tectonics and climate. Geochronometria 43, 102-112.

Singh, V., Tandon, S., 2010. Integrated analysis of structures and landforms of an intermontane longitudinal valley (Pinjaur dun) and its associated mountain fronts in the NW Himalaya. Geomorphology 114, 573-589.

Sinha, S., Suresh, N., Kumar, R., Dutta, S., Arora, B., 2010. Sedimentologic and geomorphic studies on the Quaternary alluvial fan and terrace deposits along the Ganga exit. Quaternary International 227, 87-103.

Sinha, S.K., Parker, G., 1996. Causes of concavity in longitudinal profiles of rivers. Water Resources Research 32, 1417-1428.

Slingerland, R., Smith, N.D., 2004. River avulsions and their deposits. Annu. Rev. Earth Planet. Sci. 32, 257-285.

Smedley, R., Glasser, N., Duller, G., 2016. Luminescence dating of glacial advances at Lago Buenos Aires (~ 46° S), Patagonia. Quaternary Science Reviews 134, 59-73.

Smith, G.A., 1986. Coarse-grained nonmarine volcaniclastic sediment: Terminology and depositional process. Geological Society of America Bulletin 97, 1-10.

Sohn, Y.K., 1997. On traction-carpet sedimentation. Journal of Sedimentary Research 67, 502-509.

Sohn, Y.K., 2000. Coarse-grained debris-flow deposits in the Miocene fan deltas, SE Korea: a scaling analysis. Sedimentary Geology 130, 45-64.

Sohn, Y.K., Rhee, C.W., Kim, B.C., 1999. Debris flow and hyperconcentrated flood‐flow deposits in an alluvial fan, northwestern part of the Cretaceous Yongdong basin, central Korea. The Journal of geology 107, 111-132.

Soria-Jáuregui, Á., González-Amuchástegui, M.J., Mauz, B., Lang, A., 2016. Dynamics of Mediterranean late Quaternary fluvial activity: An example from the River Ebro (north Iberian Peninsula). Geomorphology 268, 110-122.

Sowers, J.M., Amundson, R.G., Chadwick, O.A., Harden, J.W., Jull, A.J.T., Ku, T.L., McFadden, L.D., Reheis, M.C., Taylor, E.M., Szabo, B.J., 1989. Geomorphology and pedology on the Kyle Canyon alluvial fan, southern Nevada. In: Rice Jr.(ed). Soil Geomorphology Relationships in the Mojave Desert, California, Neveda: Field Tour Guidebook for the 1989, Soil Science Society of America Annual Meeting Pre-Meeting Tour, pp. 93-112.

Spelz, R.M., Fletcher, J.M., Owen, L.A., Caffee, M.W., 2008. Quaternary alluvial-fan development, climate and morphologic dating of fault scarps in Laguna Salada, Baja California, Mexico. Geomorphology 102, 578-594.

Staley, D.M., Wasklewicz, T.A., Blaszczynski, J.S., 2006. Surficial patterns of debris flow deposition on alluvial fans in Death Valley, CA using airborne laser swath mapping data. Geomorphology 74, 152-163.

Starkel, L., 2003. Climatically controlled terraces in uplifting mountain areas. Quaternary Science Reviews 22, 2189-2198.

Stefanini, M.C.R., A, 2003. Dendrogeomorphological investigations of debris flow in the Maritime Alps (Northwestern Italy). In: Rickenmann, D.C., Chen, L. (eds), 3th International Conference on" Debris-Flow Hazards Mitigation: Mechanics, Prediction, and Assessment. Millpress, Rotterdam, pp. 231-242.

Stevens, T., Lu, H., Thomas, D.S., Armitage, S.J., 2008. Optical dating of abrupt shifts in the late Pleistocene East Asian monsoon. Geology 36, 415-418.

Stock, J., Dietrich, W.E., 2003. Valley incision by debris flows: Evidence of a topographic signature. Water Resources Research 39(4), 1089.

Stock, J.D., Dietrich, W.E., 2006. Erosion of steepland valleys by debris flows. Geological Society of America Bulletin 118, 1125-1148.

Stoffel, M., 2010. Magnitude–frequency relationships of debris flows — A case study based on field surveys and tree-ring records. Geomorphology 116, 67-76.

Stoffel, M., Beniston, M., 2006. On the incidence of debris flows from the early Little Ice Age to a future greenhouse climate: a case study from the Swiss Alps. Geophysical Research Letters 33, L16404.

Stoffel, M., Conus, D., Grichting, M.A., Lièvre, I., Maître, G., 2008. Unraveling the patterns of late Holocene debris-flow activity on a cone in the Swiss Alps: chronology, environment and implications for the future. Global and Planetary Change 60, 222-234.

Stoffel, M., Lièvre, I., Conus, D., Grichting, M.A., Raetzo, H., Gärtner, H.W., Monbaron, M., 2005. 400 years of debris-flow activity and triggering weather conditions: Ritigraben, Valais, Switzerland. Arctic, Antarctic, and Alpine Research 37, 387-395.

Stokes, M., 2008. Plio-Pleistocene drainage development in an inverted sedimentary basin: Vera basin, Betic Cordillera, SE Spain. Geomorphology 100, 193-211.

Stokes, M., Cunha, P.P., Martins, A.A., 2012. Techniques for analysing Late Cenozoic river terrace sequences. Geomorphology 165-166, 1-6.

Stokes, M., Mather, A., Harvey, A., 2002. Quantification of river-capture-induced base-level changes and landscape development, Sorbas Basin, SE Spain. Geological Society, London, Special Publications 191, 23-35.

Suresh, N., Bagati, T.N., Thakur, V.C., Kumar, R., Sangode, S., 2002. Optically stimulated luminescence dating of alluvial fan deposits of Pinjaur Dun, NW Sub Himalaya. Current Science 82, 1267-1274.

Suresh, N., Bagati, T.N., Kumar, R., Thakur, V.C., 2007. Evolution of Quaternary alluvial fans and terraces in the intramontane Pinjaur Dun, Sub‐Himalaya, NW India: Interaction between tectonics and climate change. Sedimentology 54, 809-833.

Suwa, H., 1983. Deposition of debris flows on a fan surface, Mt. Yakedake, Japan. Zeitschrift fur Geomorphologie 46, 79-101.

Takahashi, T., 1981. Debris flow. Annual review of fluid mechanics 13, 57-77.

Takahashi, T., Sugai, T., 2017. Tributary effects on fluvial terrace development since the last interglacial in the upper Tama River valley, central Japan. Quaternary International 471, Part B, 318-331.

Tamrakar, N.K., 2009. Riverbed-material texture and composition of Bishnumati River, Kathmandu, Nepal; implications in provenance analysis. Bulletin of the Department of Geology 12, 55-62.

Tan, X., Chen, W., Yang, J., Cao, J., 2011. Laboratory investigations on the mechanical properties degradation of granite under freeze–thaw cycles. Cold Regions Science and Technology 68, 130-138.
Tang, C., 1990. Study on the geomorphology of debris flow formed fans. Yunnan Geology, 239-246.

Tang, C., Rengers, N., van Asch, T.W., Yang, Y., Wang, G., Luino, F., 2011. Triggering conditions and depositional characteristics of a disastrous debris flow event in Zhouqu city, Gansu Province, northwestern

China. Natural Hazards & Earth System Sciences 11, 2903-2912.

Tang, C., Zhu, J., Duan, J., Du, R., 1991. Study on debris flow fans in the Xiaojiang River, Yunnan. Journal of Mountain Science 9, 179-184.

Telford, R., Birks, H., 2011. A novel method for assessing the statistical significance of quantitative reconstructions inferred from biotic assemblages. Quaternary Science Reviews 30, 1272-1278.

Todd, S.P., 1989. Stream-driven, high-density gravelly traction carpets: possible deposits in the Trabeg Conglomerate Formation, SW Ireland and some theoretical considerations of their origin. Sedimentology 36, 513-530.

Todd, S.P., 1996. Process deduction from fluvial sedimentary structures. In: Carling, P. A. and Dawson, M. R. (eds). Advances in fluvial dynamics and stratigraphy, pp. 299-350.

Trimble, S.W., 1983. A sediment budget for Coon Creek basin in the Driftless Area, Wisconsin, 1853-1977. American Journal of Science 283, 454-474.

Tucker, M.E., 1988. Techniques in Sedimentology, in: Tucker, M.E. (ed.). Blackwell Science, Oxford.

Tudhope, A.W., Chilcott, C.P., McCulloch, M.T., Cook, E.R., Chappell, J., Ellam, R.M., Lea, D.W., Lough, J.M., Shimmield, G.B., 2001. Variability in the El Niño-Southern Oscillation through a glacial-interglacial cycle. Science 291, 1511-1517.

Tzedakis, P., 1994. Vegetation change through glacial-interglacial cycles: a long pollen sequence perspective. Philosophical Transactions of the Royal Society of London B: Biological Sciences 345, 403-432.

Van Balen, R., Houtgast, R., Van der Wateren, F., Vandenberghe, J., Bogaart, P., 2000. Sediment budget and tectonic evolution of the Meuse catchment in the Ardennes and the Roer Valley Rift System. Global and Planetary Change 27, 113-129.

van Huissteden, J., Gibbard, P.L., Briant, R.M., 2001. Periglacial fluvial systems in northwest Europe during marine isotope stages 4 and 3. Quaternary International 79, 75-88.

Vandenberghe, J., 1995. Timescales, climate and river development. Quaternary Science Reviews 14, 631-638.

Vandenberghe, J., 2003. Climate forcing of fluvial system development: an evolution of ideas. Quaternary

Science Reviews 22, 2053-2060.

Vandenberghe, J., 2015. River terraces as a response to climatic forcing: Formation processes, sedimentary characteristics and sites for human occupation. Quaternary International 370, 3-11.

Vandenberghe, J., Wang, X., Lu, H., 2011. Differential impact of small-scaled tectonic movements on fluvial morphology and sedimentology (the Huang Shui catchment, NE Tibet Plateau). Geomorphology 134, 171-185.

Veldkamp, A., Tebbens, L.A., 2001. Registration of abrupt climate changes within fluvial systems: insights from numerical modelling experiments. Global and Planetary Change 28, 129-144.

Veldkamp, A., van Dijke, J.J., 2000. Simulating internal and external controls on fluvial terrace stratigraphy: a qualitative comparison with the Maas record. Geomorphology 33, 225-236.

Viseras, C., Calvache, M.a.L., Soria, J.M., Fernández, J., 2003. Differential features of alluvial fans controlled by tectonic or eustatic accommodation space. Examples from the Betic Cordillera, Spain. Geomorphology 50, 181-202.

Wadell, H., 1932. Volume, shape, and roundness of rock particles. The Journal of Geology 40, 443-451.

Walder, J., Hallet, B., 1985. A theoretical model of the fracture of rock during freezing. Geological Society of America Bulletin 96, 336-346.

Wang, A., Smith, J.A., Wang, G., Zhang, K., Xiang, S., Liu, D., 2009. Late Quaternary river terrace sequences in the eastern Kunlun Range, northern Tibet: A combined record of climatic change and surface uplift. Journal of Asian Earth Sciences 34, 532-543.

Wang, H., Chen, J., Zhang, X., Chen, F., 2014. Palaeosol development in the Chinese Loess Plateau as an indicator of the strength of the East Asian summer monsoon: Evidence for a mid-Holocene maximum. Quaternary International 334, 155-164.

Wang, J., Chen, Z., Zhou, X., Ren, X., Luo, L., 2002. A breif review of the debris flow occurrence and deposition at the Northeastern fringe of Qinghai-Xizang Plateau. Journal of Southwest China Normal University (Natural Science) 27, 766-770.

Wang, J., Wang, Y., Shi, Y., 2000. A preliminary study on debris flow and environmental evolution in Holocene at the Bailongjiang River Valley. Journal of Southwest China Normal University (Natural Science)

25, 452-456.

Wang, P., Jiang, H., Yuan, D., Liu, X., Zhang, B., 2010. Optically stimulated luminescence dating of sediments from the Yellow River terraces in Lanzhou: Tectonic and climatic implications. Quaternary Geochronology 5, 181-186.

Wang, P.X., Wang, B., Cheng, H., Fasullo, J., Guo, Z., Kiefer, T., Liu, Z., 2017. The global monsoon across time scales: Mechanisms and outstanding issues. Earth-Science Reviews 174, 84-121.

Wang, Y.J., Cheng, H., Edwards, R.L., An, Z., Wu, J., Shen, C.-C., Dorale, J.A., 2001. A high-resolution absolute-dated late Pleistocene monsoon record from Hulu Cave, China. Science 294, 2345-2348.

Wang, Y.J., Cheng, H., Edwards, R.L., Kong, X., Shao, X., Chen, S., Wu, J., Jiang, X., Wang, X., An, Z., 2008. Millennial-and orbital-scale changes in the East Asian monsoon over the past 224,000 years. Nature 451, 1090-1093.

Wells, S.G., Harvey, A.M., 1987. Sedimentologic and geomorphic variations in storm-generated alluvial fans, Howgill Fells, northwest England. Geological Society of America Bulletin 98, 182-198.

Wells, S.G., McFadden, L.D., Dohrenwend, J.C., 1987. Influence of late Quaternary climatic changes on geomorphic and pedogenic processes on a desert piedmont, eastern Mojave Desert, California. Quaternary Research 27, 130-146.

Went, D.J., 2005. Pre-vegetation alluvial fan facies and processes: an example from the Cambro-Ordovician Rozel Conglomerate Formation, Jersey, Channel Islands. Sedimentology 52, 693-713.

Wentworth, C.K., 1922. A scale of grade and class terms for clastic sediments. The Journal of Geology 30, 377-392.

Westaway, R., 2006. Investigation of coupling between surface processes and induced flow in the lower continental crust as a cause of intraplate seismicity. Earth Surface Processes and Landforms 31, 1480-1509.

Westaway, R., Bridgland, D.R., Sinha, R., Demir, T., 2009. Fluvial sequences as evidence for landscape and climatic evolution in the Late Cenozoic: A synthesis of data from IGCP 518. Global and Planetary Change 68, 237-253.

Whipple, K.X., Dunne, T., 1992. The influence of debris-flow rheology on fan morphology, Owens Valley, California. Geological Society of America Bulletin 104, 887-900.

Whipple, K.X., Parker, G., Paola, C., Mohrig, D., 1998. Channel dynamics, sediment transport, and the slope of alluvial fans: experimental study. The Journal of Geology 106, 677-694.

Whiting, P.J., Dietrich, W.E., Leopold, L.B., Drake, T.G., Shreve, R.L., 1988. Bedload sheets in heterogeneous sediment. Geology 16, 105-108.

Williams, J.W., Post*, D.M., Cwynar, L.C., Lotter, A.F., Levesque, A.J., 2002. Rapid and widespread vegetation responses to past climate change in the North Atlantic region. Geology 30, 971-974.

Williams, M., Williams, F., Duller, G., Munro, R., El Tom, O., Barrows, T., Macklin, M., Woodward, J., Talbot, M., Haberlah, D., 2010. Late Quaternary floods and droughts in the Nile valley, Sudan: new evidence from optically stimulated luminescence and AMS radiocarbon dating. Quaternary Science Reviews 29, 1116-1137.

Wilson, K., Berryman, K., Cochran, U., Little, T., 2007. A Holocene incised valley infill sequence developed on a tectonically active coast: Pakarae River, New Zealand. Sedimentary Geology 197, 333-354.

Wintle, A.G., 2008. Luminescence dating of Quaternary sediments – Introduction. Boreas 37, 469–470.

Wu, C., Zheng, W., Zhang, Z., Jia, Q., Yu, J., Zhang, H., Han, G., Yao, Y., 2018. Terrace sequence along the Yushanguxi River in the southern piedmont of Tian Shan and its relationship to climate and tectonics in northwestern China. Geomorphology 313, 48-57.

Xiong, M., Meng, X., Wang, S., Guo, P., Li, Y., Chen, G., Qing, F., Cui, Z., Zhao, Y., 2016. Effectiveness of debris flow mitigation strategies in mountainous regions. Progress in Physical Geography 40, 1-26.

Yang, S., Ding, Z., 2008. Advance-retreat history of the East-Asian summer monsoon rainfall belt over northern China during the last two glacial–interglacial cycles. Earth and Planetary Science Letters 274, 499-510.

Yang, X., Liang, S., 2007. Analyses of debris flow deposits in Longnan. West-china Exploration Engineering 19, 19-21.

Yanites, B.J., Tucker, G.E., Mueller, K.J., Chen, Y.-G., 2010. How rivers react to large earthquakes: Evidence from central Taiwan. Geology 38, 639-642.

Ye, Y.G., Diao, S.-B., He, J., Gao, J.-C., Lei, X.-Y., 1998. ESR dating studies of palaeo-debris-flow deposits in

Dongchuan, Yunnan Province, China. Quaternary Science Reviews 17, 1073-1076.

Yu, J., Cheng, W., Yuan, D., Pang, J., Liu, X., Liu, B., 2012. late quaternary active characteristics and slip-rate of pinding-huama fault, the eastern segment of Guangaishan-Dieshan fault zone (west Qinling mountian). Quaternary Science 32, 957-967.

Yuan, D., Lei, Z., He, W., Xiong, Z., Ge, W., Liu, X., Liu, B., 2007. Textual research of Wudu earthquake in 186 BC in Gansu Province, China and discussion on its causative structure. Acta Seismologica Sinica 20, 696-707.

Yuan, D., Lei, Z., Yang, Q., Wang, A., Su, Q., 2014. Seismic disaster features of the 1879 southern Wudu M8 earthquake in Gansu Province. Journal of Lanzhou University (Natural Science) 50, 611-621.

Zhang, M., Li, Z., Wang, G., 2011. The geological hazard characteristics and exploration ideas of the Bailong River Basin. Northeastern Geology 44, 1-9.

Zhang, P., Cheng, H., Edwards, R.L., Chen, F., Wang, Y., Yang, X., Liu, J., Tan, M., Wang, X., Liu, J., 2008. A test of climate, sun, and culture relationships from an 1810-year Chinese cave record. Science 322, 940-942.

Zhao, Q., Thomsen, K.J., Murray, A.S., Wei, M., Pan, B., Song, B., Zhou, R., Chen, S., Zhao, X., Chen, H., 2015. Testing the use of OSL from quartz grains for dating debris flows in Miyun, Northeast Beijing, China. Quaternary Geochronology 30: 320-327.

Zhao, Y., Yu, Z., Chen, F., Zhang, J., Yang, B., 2009. Vegetation response to Holocene climate change in monsoon-influenced region of China. Earth-Science Reviews 97, 242-256.

Appendix 3 Methodology

A3.1 Remotely sensed images used in the study

Fig. A3.1. The China Source Satellite image obtained in 2013.

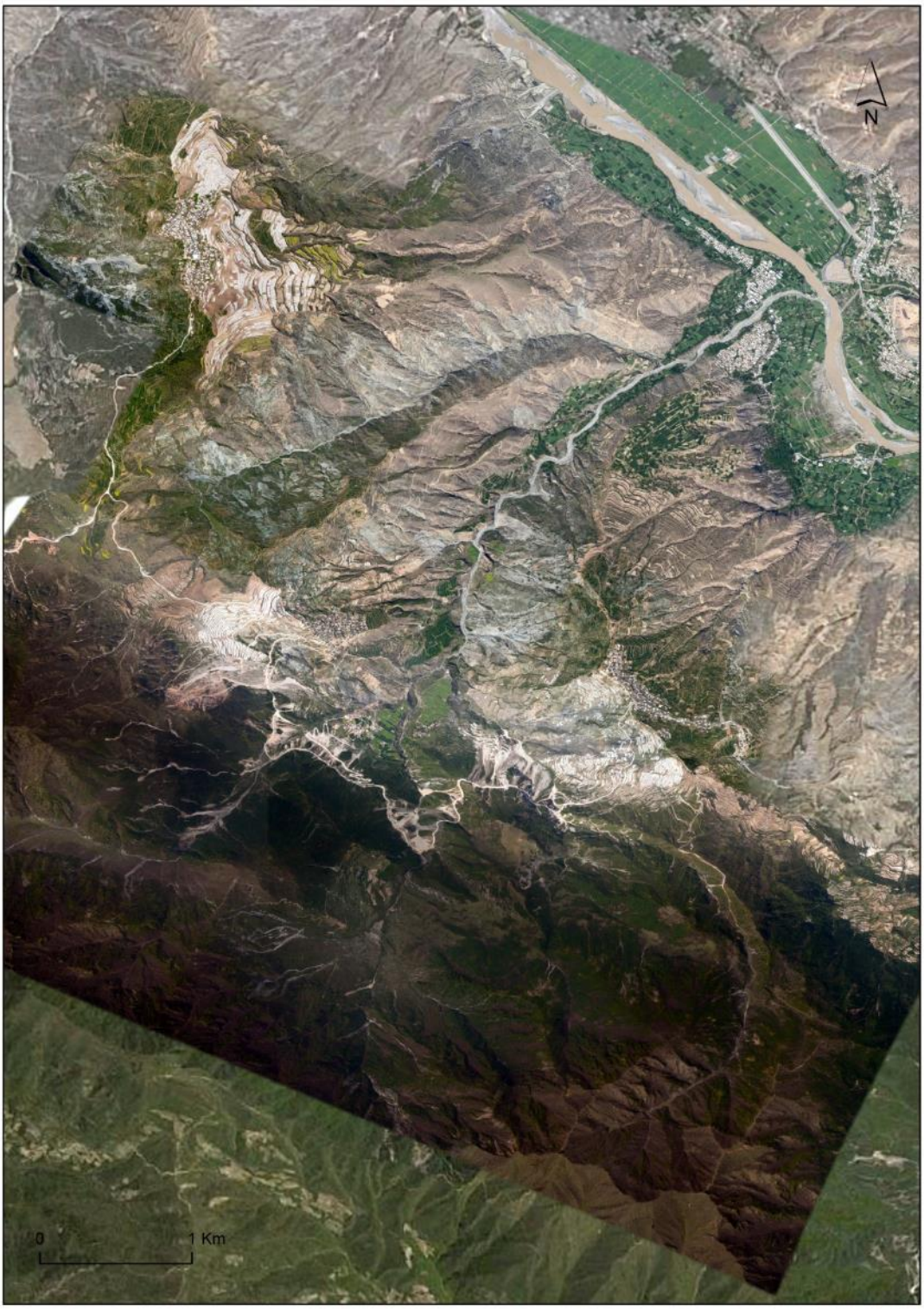

Fig. A3.2. The UAV (unmanned aerial vehicle) image of GLP obtained in 2013.

A3.2 Introduction to drill equipment

The machine used for drilling is a rotary drilling machine. It employs sharp, rotating drill bits to dig down through sediments. It is composed of four functional parts: (1) the power source, (2) the hoisting system, (3) the rotating system and (4) the stablizing system (Fig. A3.3).

(1) The power source is provided by a diesel engine (Fig. A3.3a).

(2) The hoisting system is composed of a derrick and a tall tower-like structure which lifts or lowers the drill pipes and bits from the borehole (Fig. A3.3a).

(3) The rotating system is comprised of drill bits, drill pipes, and a core barrel which connect to each other, dig the ground and take samples (Fig. A3.3b). Each drill pipe is 6 m in length, and several drill pipes were interlocked to allow the drill bit to penetrate to a maximum 100 m depth. The core barrel is used to retain the sediment core during drilling. The upper end of the core barrel is connected to the drill pipe, and the base end is connected to the drill bit. The drill bit is responsible for making direct contact with the subsurface layers and drilling through them. Two types of drill bits were used: one type was the Tungsten carbide tooth bits which were used to drill the relatively soft sediment layers, and the other one was diamond teeth rotary bits used for relatively rigid sediment layers. Drill bits with diameters being 146 mm, 127 mm, and 89 mm are available for the two types.

(4) Because the sediments in the channel are mostly structureless gravelly clasts, the walls of the borehole are prone to collapse, which might cause the whole drill project to fail. Therefore, to ascertain the stability of the well is a key step. In this study, casing pipes and stabilising liquids (made by a mixture of water

and bentonite) were used to sustain the stability of the borehole wall. Practically, the 146 mm drill bits were used for the upper 10-15 m of drilling, and the casing pipes (with the diameter being around 140 mm) were placed in the borehole for stabilization. Below this depth, the 127 mm drill bits were used, and smaller casing pipes were placed in the subsequent boreholes until the supply of casing pipes ran out. Below this depth, the 87 mm drill bits were used for drilling, and the mixed water and bentonite were used for stabilizing the walls of the borehole.

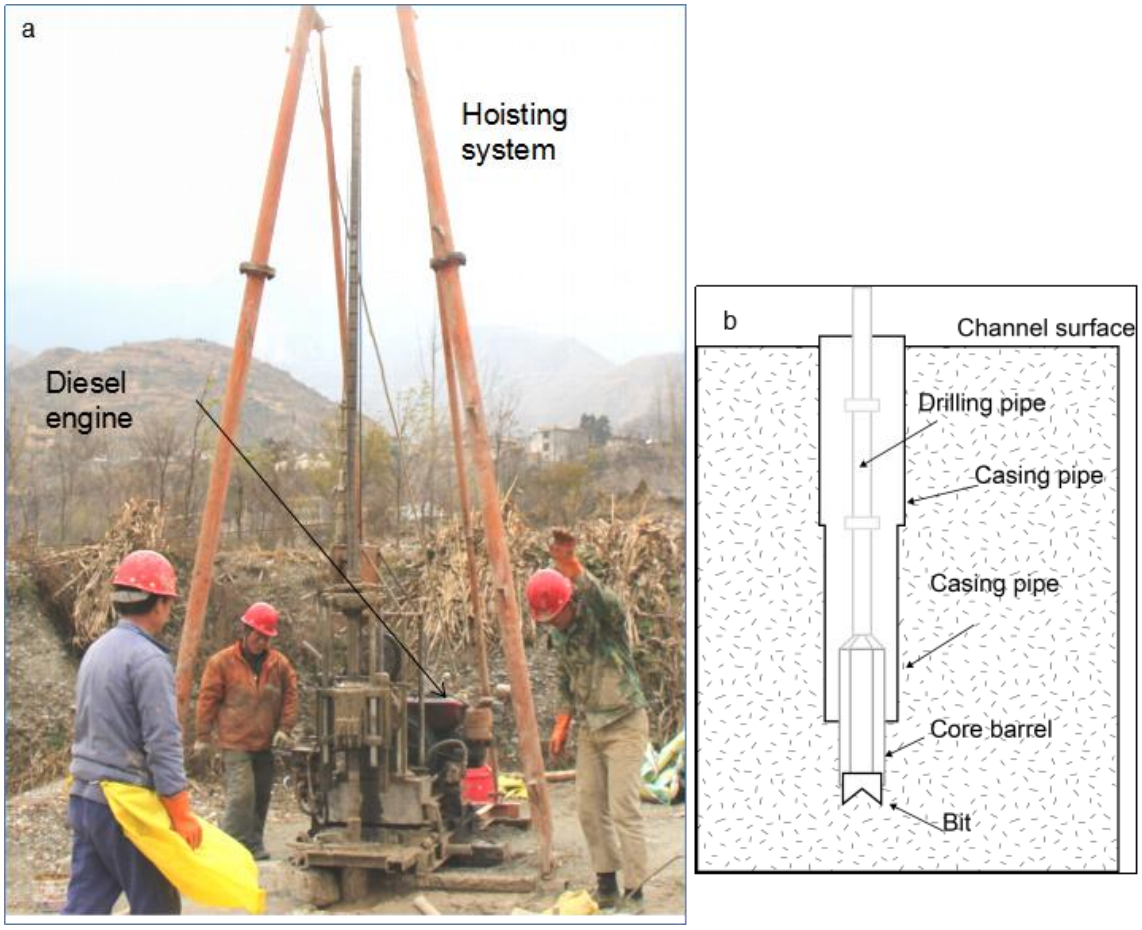

Fig. A3.3 Configuration of the drilling system. a. Diesel engine and Hoisting system; b. Underground rotating system and stabilizing system (Casing pipe).

During the drilling process, sediments enter the core barrel. When the core barrel was filled, or the teeth of the bit were worn out, the core barrel was lifted by the

derrick to the surface, and the cored sediments were extruded under gravity with the aid of a hammer to vibrate the core barrel. The core materials were then laid on the ground in stratigraphic order (Fig. A3.4) for field analyses.

Fig. A3.4 Core material extraction and emplacement. a. Photograph showing how the core materials were retrieved from the core barrel. b. Emplacement of samples on the ground.

A3.3 Dose recovery tests at a variety of preheat temperatures

The optimal preheating conditions are known to vary between samples and particularly between sites (e.g., Armitage et al., 2000; Tribolo et al., 2013). Consequently, it is good practice to perform dose recovery experiments at a range of preheat temperatures before which preheating regime to use in routine equivalent dose estimation. To determine the most appropriate preheat temperatures for samples used in this study, dose recovery experiments were performed on two samples using PH temperatures ranging from 160 ˚C up to 280 ˚C. The dose-recovery ratios (recovered dose/administered dose), as well as the recycling ratios at different PH temperatures, were compared, and the optimal PH temperature was selected accordingly. As the samples measured in the study come from a relatively small basin, the quartz minerals are thought to come from the same sources within the catchment. Consequently, the most appropriate preheating regime for the two samples tested (D01-30 and T2L18) is assumed to

be applicable to all other samples in the study. Data from these dose recovery experiments are discussed below.

A3.3.1 Changes of recycling ratios with PH temperatures

The recycling ratio monitors the effectiveness of sensitivity change corrections within the SAR measurement protocol. Fig. A3.5 shows the recycling ratio of each aliquot measured at different PH temperature for sample D01-30 and T2L18. The recycling ratios are mostly within 10% of unity at PH temperatures between 160 – 220 °C, while larger variance is shown at PH temperatures between 240 - 260 °C, indicating that sensitivity correction at these higher temperatures is not effective.

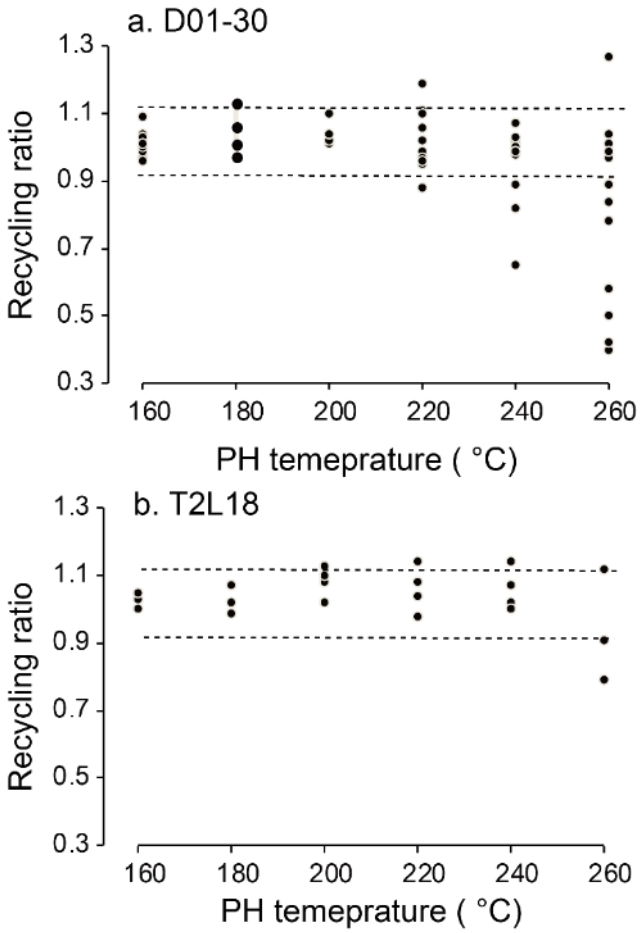

Fig. A3.5 Recycling ratio versus PH temperature for sample D01-30 (a) and T2L18 (b). Filled dots represent individual aliquots. Dashed lines define the area within 10% of 1.

A3.3.2 Changes of dose recovery ratios with PH temperatures

The ratio of dose recovery (i.e., the ratio between recovered dose and administered doses) measures the effectiveness of sensitivity correction for natural samples. Fig. A3.6 shows the dose recovery ratios versus PH temperature for the both samples. The best dose recovery results are at the PH temperature of 160 °C for both D01-30 and T2L18. At this PH temperature, the dose recovery ratios cluster within the 10% of unity. Aliquots measured using a PH temperature of 180, 200 and 220 °C generally produced underestimated doses (dose recovery ratios lower than 0.9). At high PH temperatures (i.e., 240 °C and 260 °C), large variance in the dose recovery ratio among aliquots occurs. This is particularly true for D01-30 at a PH temperature of 260 °C, and it is notable that the recycling ratios for this sample at this temperature are also poor.

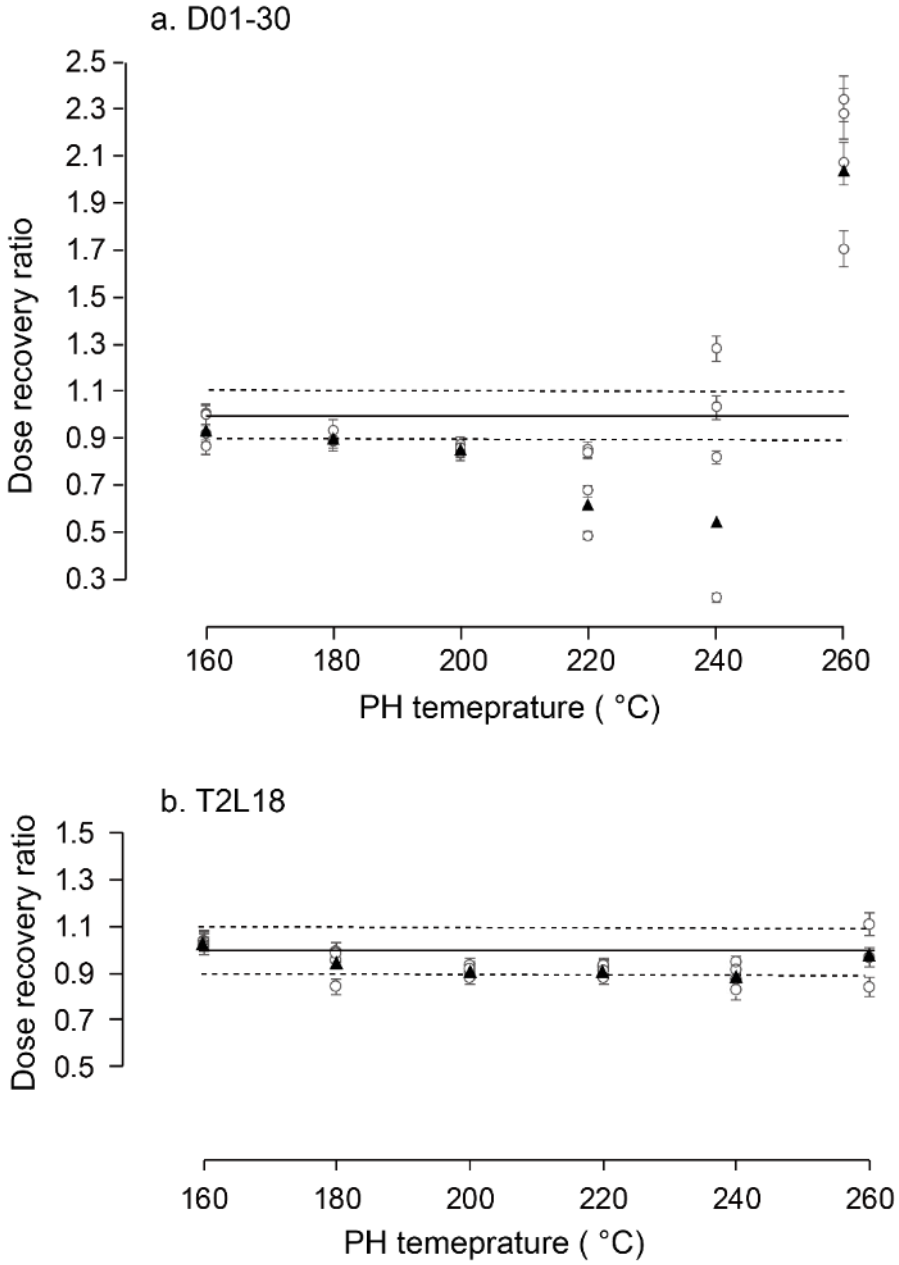

Fig. A3.6. Dose recovery ratios versus PH temperatures for sample D01-30 (a) and T2L18 (b). Open circles represent individual recovery ratios, and filled triangles represent the averaged recovery ratios. Dashed lines define the area within 10% of 1 (straight line).

A3.4 Determination of radionuclide concentrations

A3.4.1 Thick source alpha counting

Thick-source alpha counting (TSAC) was carried out using a Daybreak Model 583 Intelligent Alpha Counter. This technique records the rate of alpha particle emission from an alpha-thick source, as indicated by scintillations from a silver

doped zinc sulphide (ZnS) screen in contact with the sample. Both count rate and "slow pairs" rate are recorded by the Daybreak Model 583, allowing determination of the concentration of both ^{238}U and ^{232}Th in a sample.

Slow pairs (a second scintillation detected within a time window open 0.02-0.4 s after the first scintillation) occur where two alpha counts are observed in quick succession due to the decay of ^{220}Rn (radon) and ^{216}Po (polonium) in the ^{232}Th decay series. Because ^{216}Po (with a half-life of 0.15 s) is the daughter isotope of ^{220}Rn, and because both radioisotopes are alpha emitters, the slow pair count rate can be used to determine the count rate for this sample due to the entire ^{232}Th decay series (Aitken, 1985, Appendix J). By subtracting this value from the total sample count rate, the count rate due to the uranium decay series is obtained. The count rates of ^{232}Th and ^{238}U can be used to determine the concentrations of ^{232}Th and ^{238}U using the conversion factors of Adamiec and Aitken (1998). In this study, samples were dried at 50 ˚C in an oven and then homogenized using a ball mill before alpha counting. To obtain good precision on the alpha count rates, TSAC measurements were continued until a minimum number of 5,000 counts had been recorded. Background count rates for ZnS scintillation screens were measured for at least 24 hours prior to sample counting, and the background count rate was subtracted before calculating sample count rates.

A3.4.2 GM beta-counting

The dried and homogenized samples which had been used for alpha counting were subsequently prepared for measurement in a Risø GM-25-5A low-level beta

GM multicounter system ("GM beta-counter" hereafter). Three sub-samples were prepared for each sample. Each sub-sample was prepared by packing homogenised sediment into a nylon pot with an internal diameter of 21 mm and an internal depth of 7 mm. The sample was packed to the top of the pot, levelled with a spatula and sealed with cling film to avoid contamination to the measurement chamber. The Risø GM-25-5A beta counter has five measurement positions. In routine operation at Royal Holloway, two of these positions are occupied by standards, while the remaining three are used to measure samples with unknown dose rates. The standards used for this study are a stainless steel blank provided by Risø and the Volkagem loess standard (De Corte et al., 2007), with known beta dose rates of 0.00 and 1.98 Gy/ka, respectively. All samples were measured for 48 hours, with data being recorded in 1 hour bins.

The beta dose rate for each sub-sample was calculated according to equation A3.1:

$$D_{\beta sample} = D_{\beta Volk}[(Sample\ C - SS\ C)/(Volk\ C - SS\ C)] \qquad \text{(A3.1)}$$

Where $D_{\beta sample}$ is the beta dose rate of the measured sample, $D_{\beta Volk}$ is the beta dose rate of the Volkagem loess sample and C is the recorded count rate. SS is stainless steel blank. The beta count of each sample was calculated as the mean of the three sub-samples.

A3.4.3 Calculation of the concentration of K

The contents of ^{238}U and ^{232}Th were determined using TSAC, and their

contribution to the beta dose rates was calculated by using the conversion factors of Adamiec and Aitken (1998) (Table A3.1).

Table. A3.1. Conversion factors from Adamiec and Aitken (1998).

	Nat U 1 ppm	Th 1 ppm	K 1%
Alpha (Gy/ka)	2.78 ± 0.0834	0.732 ± 0.02196	0
Beta (Gy/ka)	0.146 ± 0.00438	0.0273 ± 0.000819	0.782 ± 0.02346
Gamma (Gy/ka)	0.113 ± 0.00339	0.0476 ± 0.001428	0.243 ± 0.00729

From the GM beta-counter, the infinite beta dose rate of a sample was obtained. By subtracting the beta dose contribution from ^{238}U and ^{232}Th from the infinite beta dose rate, the remaining beta dose rate was produced by K, and the content of K was then obtained using the conversion factor (Table. A3.1). The dose rate of gamma was calculated based on the determined concentrations of ^{238}U, ^{232}Th and K for the sample.

A3.5 Comparison between TSAC/GM beta-counting and ICP-MS/AES

A3.5.1 Comparison of radionuclide concentrations (^{238}U, ^{232}Th, and ^{40}K)

The radionuclide concentrations of the selected samples were obtained using the TSAC/GM beta-counting methods and the ICP-MS/AES methods separately, and the results are compared in Fig. A3.7 and Table. A3.2.

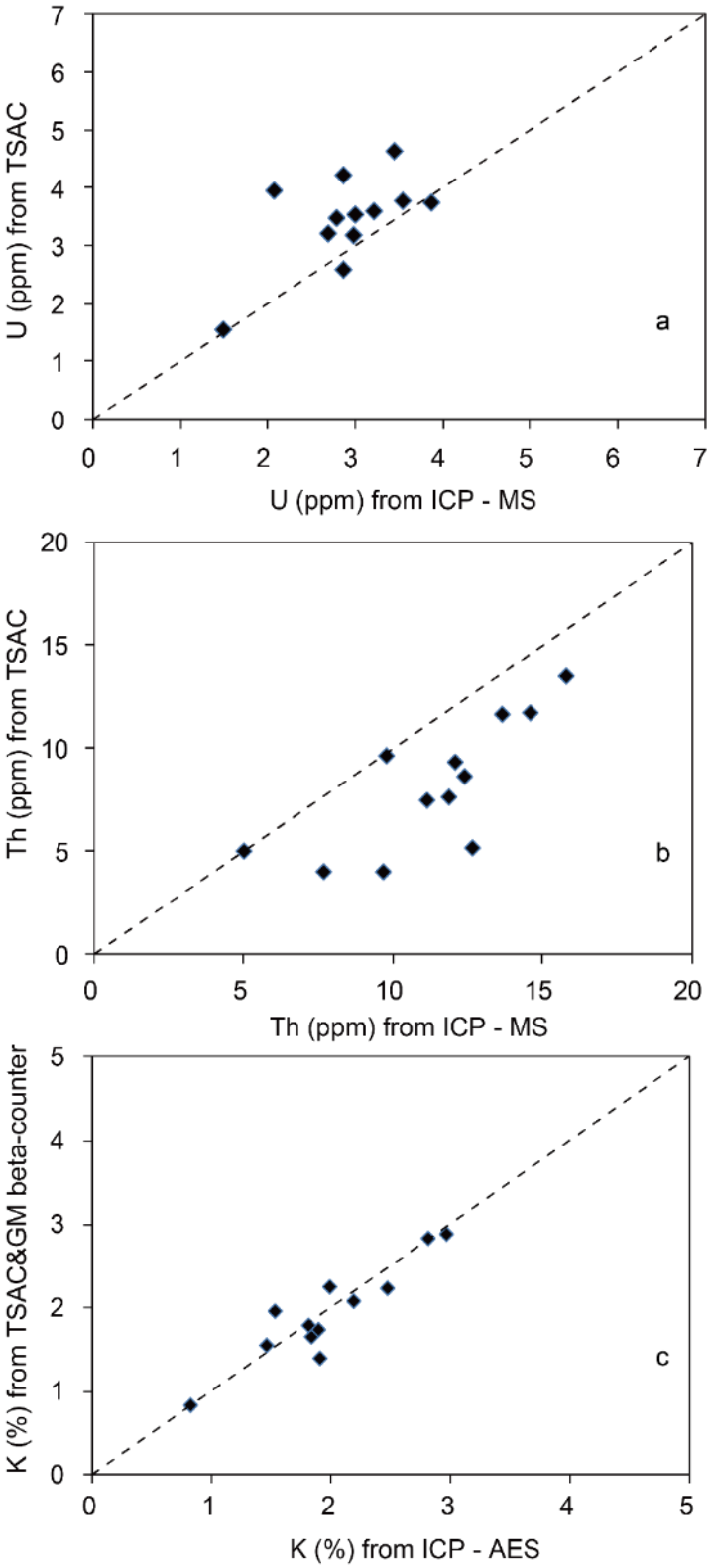

Fig. A3.7. Comparison of the concentrations of ^{238}U (a), ^{232}Th (b) and ^{40}K (c) that were obtained using TSAC/GM beta-counting and ICP-MS/AES. The dashed line is y=x representing equal concentrations calculated by each method.

Table A3.2 Comparison of radionuclide concentrations obtained from TSAC/GM beta-counter and ICP-MS/AES.

Sample	K (%)			Th (ppm)			U (ppm)		
	ICP-AES	TSAC/ GM beta-count	ICP-AES/ TSAC/GM beta-counter	ICP-MS	TSAC	ICP-MS/TSAC	ICP-MS	TSAC	ICP-MS/TSAC
D01-30	1.84 ± 0.18	1.64 ± 0.36	1.12 ± 0.27	9.70 ± 0.97	4.03 ± 1.20	2.41 ± 0.76	2.06 ± 0.21	3.94 ± 0.34	0.52 ± 0.07
T3RBL02	2.48 ± 0.25	2.22 ± 0.45	1.12 ± 0.25	13.66 ± 1.37	11.67 ± 1.86	1.17 ± 0.22	2.99 ± 0.30	3.19 ± 0.54	0.94 ± 0.18
XZ-T201	1.82 ± 0.18	1.79 ± 0.38	1.02 ± 0.24	11.91 ± 1.19	7.64 ± 1.37	1.56 ± 0.32	2.69 ± 0.27	3.21 ± 0.39	0.84 ± 0.13
D02-4.7	2.19 ± 0.22	2.08 ± 0.42	1.05 ± 0.24	12.10 ± 1.21	9.31 ± 1.59	1.30 ± 0.26	2.78 ± 0.28	3.47 ± 0.45	0.80 ± 0.13
T4L01	1.46 ± 0.15	1.54 ± 0.38	0.95 ± 0.25	7.71 ± 0.77	4.02 ± 1.34	1.92 ± 0.67	3.44 ± 0.34	4.62 ± 0.38	0.74 ± 0.10
SG-T401	1.53 ± 0.15	1.95 ± 0.27	0.78 ± 0.13	9.81 ± 0.98	9.66 ± 1.65	1.02 ± 0.20	3.86 ± 0.39	3.73 ± 0.47	1.03 ± 0.17
SG-06	2.97 ± 0.30	2.87 ± 0.52	1.03 ± 0.21	14.64 ± 1.46	11.7 ± 1.76	1.25 ± 0.23	3.00 ± 0.30	3.54 ± 0.5	0.85 ± 0.15
T2RCK02	1.91 ± 0.19	1.39 ± 0.30	1.37 ± 0.33	11.16 ± 1.11	7.51 ± 1.16	1.49 ± 0.27	2.86 ± 0.29	2.59 ± 0.33	1.10 ± 0.18
2013.9.1-02	0.82 ± 0.08	0.83 ± 0.21	0.99 ± 0.27	5.01 ± 0.50	5.07 ± 0.90	0.99 ± 0.20	1.49 ± 0.15	1.53 ± 0.25	0.97 ± 0.19
T4RBL01	2.82 ± 0.28	2.83 ± 0.51	1.00 ± 0.21	15.80 ± 1.58	13.49 ± 2.38	1.17 ± 0.24	3.55 ± 0.36	3.77 ± 0.7	0.94 ± 0.20
XZ-T102	1.90 ± 0.19	1.72 ± 0.27	1.10 ± 0.21	12.65 ± 1.27	5.21 ± 1.17	2.43 ± 0.60	2.86 ± 0.29	4.21 ± 0.33	0.68 ± 0.09
T1L01	1.99 ± 0.20	2.25 ± 0.42	0.88 ± 0.19	12.40 ± 1.24	8.63 ± 1.43	1.44 ± 0.28	3.20 ± 0.32	3.58 ± 0.41	0.89 ± 0.14
Mean ratio			1.04 ± 0.07			1.51 ± 0.12			0.86 ± 0.04

In Fig. A3.7a, the concentrations of ^{238}U obtained from TSAC are plotted against those derived from ICP-MS. The data points generally plot above the 1:1 line (y=x), indicating that the ^{238}U concentrations calculated using TSAC are generally larger than those obtained from ICP-MS. In contrast, the distribution of the concentrations of ^{232}Th (Fig. A3.7b) shows a reversed pattern where the data points plot below the 1:1 line, indicating lower estimation of ^{232}Th concentrations measured by TSAC than that by ICP-MS. These patterns may be explained via reference to the method by which ^{238}U and ^{232}Th concentrations are determined in the TSAC method. The ^{232}Th concentration is calculated from the "slow pairs" count rate, from which the total alpha count rate due to the ^{232}Th decay series is calculated. The ^{238}U concentration is calculated by subtracting this ^{232}Th decay series count rate from the total count rate and assuming that the remaining counts are due to ^{238}U. Consequently, an underestimate of the true ^{232}Th concentration will lead to an overestimation of the ^{238}U concentration, and *vice versa*.

The data points of ^{40}K concentrations are generally distributed along the 1:1 line (y=x) with small deviations (Fig. A3.7c) indicating that the concentrations of ^{40}K derived from the TSAC/GM beta-counter are comparable to those derived from ICP-AES.

A3.5.2 Comparison of dose rates

To assess the difference between dose rates determined by TSAC/GM beta-counting and those calculated using ICP-MS/AES, the alpha, beta and gamma

dose rates were calculated using the two methods. For purposes of comparison the corrected dose rates (i.e. after water, grain size and alpha attenuation corrections had been made) were compared (Fig. A3.8).

In Fig. A3.8, the data points for the four dose rates are distributed along the 1:1 line (y=x) indicating that the dose rates calculated by the TSAC/GM beta-counting and ICP-MS/AES are similar. There is a tendency for the data points of alpha, gamma and the total dose rate to plot below the line, indicating that slightly higher dose rates are calculated from the ICP-MS/AES data. This observation might be explained by the release of radon during alpha counting, which will cause slight underestimations of the uranium concentration.

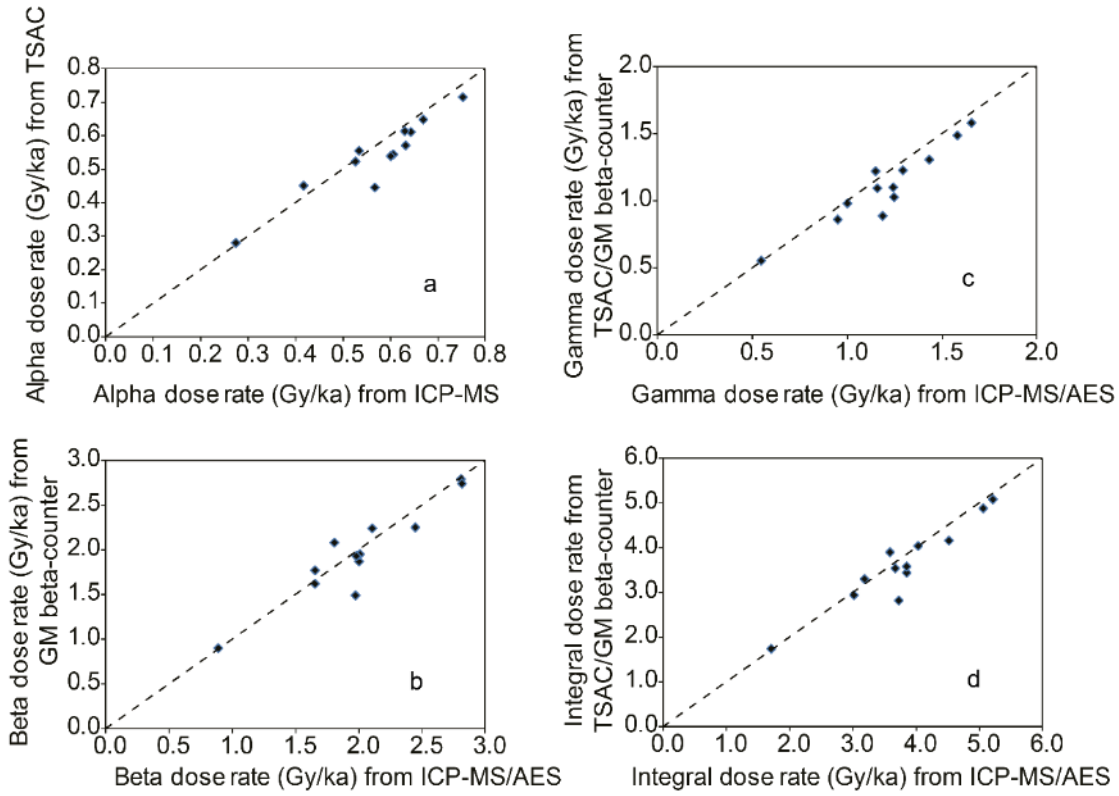

Fig. A3.8 Comparison of the dose rates obtained from TSAC/GM beta-counting and ICP-MS/AES respectively. a. Alpha dose rates obtained from emission counter plotted against those from ICP-MS. The calculated dose rates have included the grain size attenuation factor, alpha efficiency and water content. b. Beta dose rate from emission counter plotted against those from ICP-MS./AES. The beta dose rate has included the grain-size (4-11 μm) attenuation factor and water content. c. Gamma dose rates from emission counter plotted against those from ICP-MS/AES. d. Integral dose rates from emission counter plotted against those from ICP-MS/AES. The integral dose rates are the sum of the alpha, beta and gamma dose rates and the cosmic contribution has not been included. Dashed lines represent y = x i.e. identical results from the two techniques used.

Table. A3.3. Comparison of dose rates derived from the two methods. The alpha dose rates were calculated by considering the attenuation factors of grain-size, alpha efficiency and water content; The beta dose rates were calculated by considering the grain-size attenuation factor and water content. The total dose rates were calculated as the sum of the three dose rates without considering the cosmic contribution.

Sample name	alpha dose rate (Gy/ka)			Beta dose rate (Gy/ka)			Gamma dose rate (Gy/ka)			Total dose rate (Gy/ka)		
	ICP-MS	Counter	ICP/ Counter	ICP-MS/AES	Counter	ICP/ Counter	ICP-MS/AES	Counter	ICP/ Counter	ICP-MS /AES	Counter	ICP/ Counter
D01-30	0.42 ± 0.15	0.45 ± 0.19	0.93 ± 0.51	1.65 ± 0.13	1.62 ± 0.24	1.02 ± 0.17	0.95 ± 0.06	0.86 ± 0.09	1.10 ± 0.14	3.02 ± 0.21	2.94 ± 0.32	1.03 ± 0.13
T3RBL02	0.64 ± 0.23	0.61 ± 0.23	1.05 ± 0.55	2.45 ± 0.19	2.25 ± 0.33	1.03 ± 0.17	1.43 ± 0.09	1.31 ± 0.14	1.09 ± 0.14	4.52 ± 0.32	4.17 ± 0.43	1.08 ± 0.13
XZ-T201	0.6 ± 0.22	0.54 ± 0.2	1.11 ± 0.58	2.01 ± 0.15	1.95 ± 0.29	1.01 ± 0.17	1.24 ± 0.08	1.1 ± 0.12	1.13 ± 0.14	3.85 ± 0.28	3.58 ± 0.38	1.07 ± 0.14
D02-4.7	0.53 ± 0.19	0.52 ± 0.2	1.02 ± 0.53	1.98 ± 0.15	1.93 ± 0.28	1.01 ± 0.17	1.16 ± 0.07	1.09 ± 0.11	1.06 ± 0.13	3.67 ± 0.26	3.54 ± 0.36	1.04 ± 0.13
T4L01	0.53 ± 0.2	0.55 ± 0.24	0.96 ± 0.55	1.65 ± 0.13	1.77 ± 0.28	0.93 ± 0.17	1 ± 0.07	0.98 ± 0.11	1.05 ± 0.12	3.19 ± 0.25	3.3 ± 0.39	0.97 ± 0.14
SG-T401	0.63 ± 0.23	0.61 ± 0.23	1.03 ± 0.54	1.81 ± 0.13	2.08 ± 0.21	0.87 ± 0.11	1.15 ± 0.07	1.22 ± 0.11	0.94 ± 0.10	3.58 ± 0.27	3.91 ± 0.33	0.92 ± 0.10
SG-06	0.67 ± 0.24	0.65 ± 0.24	1.03 ± 0.54	2.82 ± 0.23	2.75 ± 0.38	1.03 ± 0.16	1.58 ± 0.1	1.49 ± 0.15	1.06 ± 0.13	5.07 ± 0.35	4.88 ± 0.47	1.04 ± 0.12
T2RCK02	0.57 ± 0.2	0.45 ± 0.17	1.27 ± 0.66	1.97 ± 0.15	1.49 ± 0.22	1.32 ± 0.22	1.19 ± 0.07	0.89 ± 0.09	1.33 ± 0.16	3.73 ± 0.26	2.83 ± 0.29	1.32 ± 0.16
SG-9.1-02	0.27 ± 0.1	0.28 ± 0.11	0.98 ± 0.51	0.89 ± 0.07	0.9 ± 0.16	0.98 ± 0.19	0.55 ± 0.04	0.55 ± 0.07	0.98 ± 0.14	1.71 ± 0.13	1.74 ± 0.2	0.98 ± 0.14
T4RBL01	0.75 ± 0.27	0.72 ± 0.27	1.05 ± 0.55	2.81 ± 0.24	2.79 ± 0.39	1.01 ± 0.17	1.65 ± 0.11	1.58 ± 0.18	1.05 ± 0.14	5.21 ± 0.38	5.09 ± 0.51	1.02 ± 0.13
XZ-T102	0.61 ± 0.22	0.55 ± 0.22	1.11 ± 0.58	2 ± 0.16	1.87 ± 0.21	1.07 ± 0.15	1.25 ± 0.09	1.03 ± 0.09	1.22 ± 0.14	3.86 ± 0.29	3.45 ± 0.32	1.12 ± 0.13
T1L01	0.63 ± 0.23	0.57 ± 0.21	1.11 ± 0.58	2.11 ± 0.16	2.25 ± 0.31	0.94 ± 0.15	1.29 ± 0.08	1.23 ± 0.12	1.05 ± 0.12	4.03 ± 0.29	4.04 ± 0.39	1.00 ± 0.12
Mean			1.05 ± 0.16			1.03 ± 0.05			1.09 ± 0.04			1.05 ± 0.04

References

Adamiec, G., Aitken, M.J., 1998. Dose-rate conversion factors: update. Ancient TL 16, 37-50.

Aitken, M.J., 1985. Thermoluminescence dating. Academic press, London.

Armitage, S., Duller, G., Wintle, A., 2000. Quartz from southern Africa: sensitivity changes as a result of thermal pretreatment. Radiation Measurements 32, 571-577.

De Corte, F., Vandenberghe, D., Hossain, S., De Wispelaere, A., Buylaert, J.-P., Van den Haute, P., 2007. Preparation and characterization of loess sediment for use as a reference material in the annual radiation dose determination for luminescence dating. Journal of radioanalytical and nuclear chemistry 272, 311-319.

Tribolo, C., Mercier, N., Douville, E., Joron, J.-L., Reyss, J.-L., Rufer, D., Cantin, N., Lefrais, Y., Miller, C.E., Porraz, G., 2013. OSL and TL dating of the Middle Stone Age sequence at Diepkloof Rock Shelter (South Africa): a clarification. Journal of Archaeological Science 40, 3401-3411.

Appendix 5 Terrace Sedimentology

Section TpS

Section TpS is at the mouth of the GLP valley (Fig. A5.1). The exposed thickness of the section is 2.4 m. The section (with an exposed thickness of 2.4 m) is formed by poorly sorted clast-supported pebble clasts with silty to sandy matrix (Gh)**.** The largest clast in the whole exposed profile is 80 cm long in it's a-axis and is present on left side of the logged section (Fig. A5.1a). Limestone, phyllite and quartzes constitute the lithology and account for 51%, 31% and 18% respectively. Clast fabrics and grain size were measured at the lower and upper part of the section (Fig. A5.1c), and the results are presented in Fig. A5.2. The principal eigenvalues for the lower and upper section are 0.58 and 0.55 respectively (Table A5.1). Visually, clasts are mostly aligned with their a-axes parallel to the flow direction.

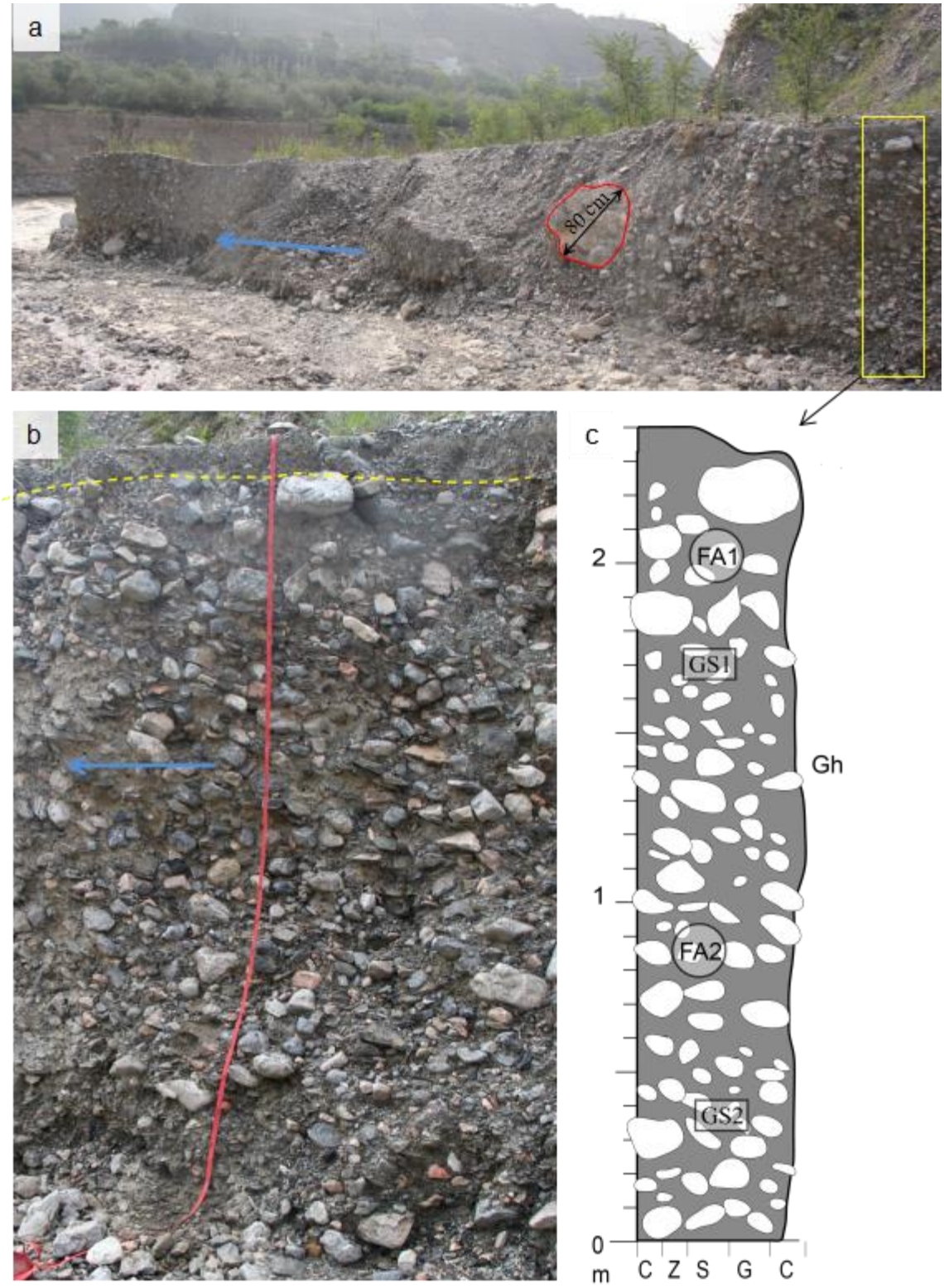

Fig. A5.1. Location and sedimentary characteristics of section TpS. a. Tp terrace and the location of section TpS (delineated by the yellow box). The blue arrow indicates the flow direction of the GLP river; The red line circles the largest clast with an a-axis length of 80 cm. b. Close-up photograph of section TpS. c. Sedimentary log of section TpS. FA1 and FA2 are the locations of fabric measurement. GS1 and GS2 are the locations of grain size measurement.

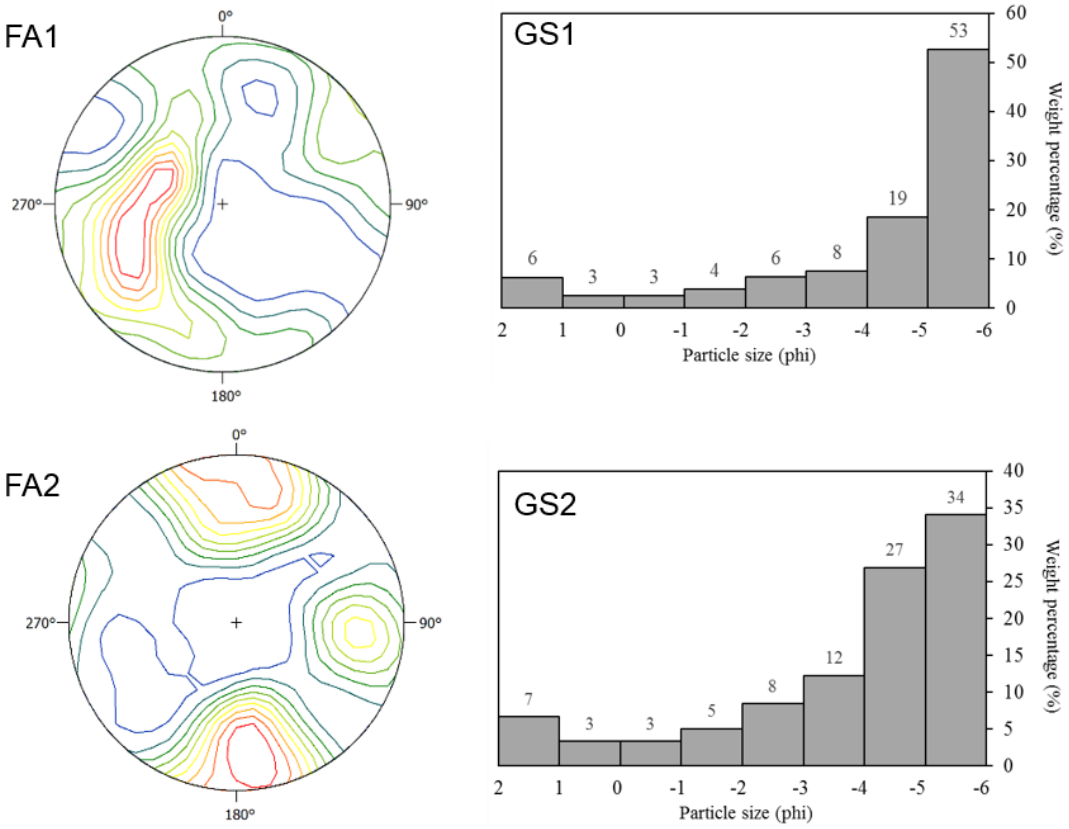

Fig. A5.2. Results of clast fabric measurement and grain size distribution (sieved result).

Table A5.1. Characteristics of clast fabrics of section TpS. S refers to the normalized eigenvalue, and K is a shape index. Sampling number for each is 40 and the b-axes were measured.

	Eigenvector	Orientation (°)	Dip (°)	S	K
FA1	1	254.6	30.5	0.55	0.47
	2	358.2	21.8	0.33	
	3	117.9	51.1	0.12	
FA2	1	354	0.2	0.58	1.01
	2	84.1	19.7	0.28	
	3	263.4	70.3	0.14	

Section T4S1

The sedimentary characteristics of section T4S1 is displayed in Fig. A5.3. Grain size and clast fabrics were measured, and the results are displayed in Fig. A5.4. Broadly, the section is divided into three sub-sections. The lower part of the section (0-1.5 m) is composed of very poorly sorted, clast-supported pebbly

inversely graded clasts with silty to sandy matrix (Gci). No stratification or bedding is present in this unit, but vertical variation in clast size and arrangement can be visually identified (Fig. A5.3c). Clasts at the upper part are moderately sorted cobbly clasts with little matrix, while clasts at the lower part are poorly sorted pebbly clasts with abundant matrix (Fig. A5.3c). This grain size variation indicates an inversely graded structure. The majority of the clasts are oriented with their b-axes at 6.4˚ (Table A5.2). This orientation forms an acute angle with the flow direction of GLP (45˚). The principal eigenvalues for the clast fabric is 0.59, indicating a weak but identifiable preferential arrangement of clasts. The surface of the unit bed is undulatory. The middle (1.5-2.7 m) and upper part (2.7–4.8 m) of the section is similar to the lower part except that clasts are not inversely graded. Locally, cobble to boulder-sized clasts (larger than 50 cm in diameter) lie on relatively smaller pebble-sized clasts with their long axes aligned parallel to the flow direction (Fig. A5.3d). The bed base has some imbricated cobble sized clasts (Fig. A5.3e). On left of the upper section, a boulder (Fig. A5.3a) with an a-axis length of 1 m is present. This boulder and the surrounding cobble-sized clasts form a bouldery snout of which the thickness and grain size decrease to the upstream direction (Boulder snout in Fig. A5.3a). The eigenvalues of fabric measurement for the middle and upper parts are 0.60 and 0.56, respectively, indicating weak but identifiable preferential arrangement of clasts.

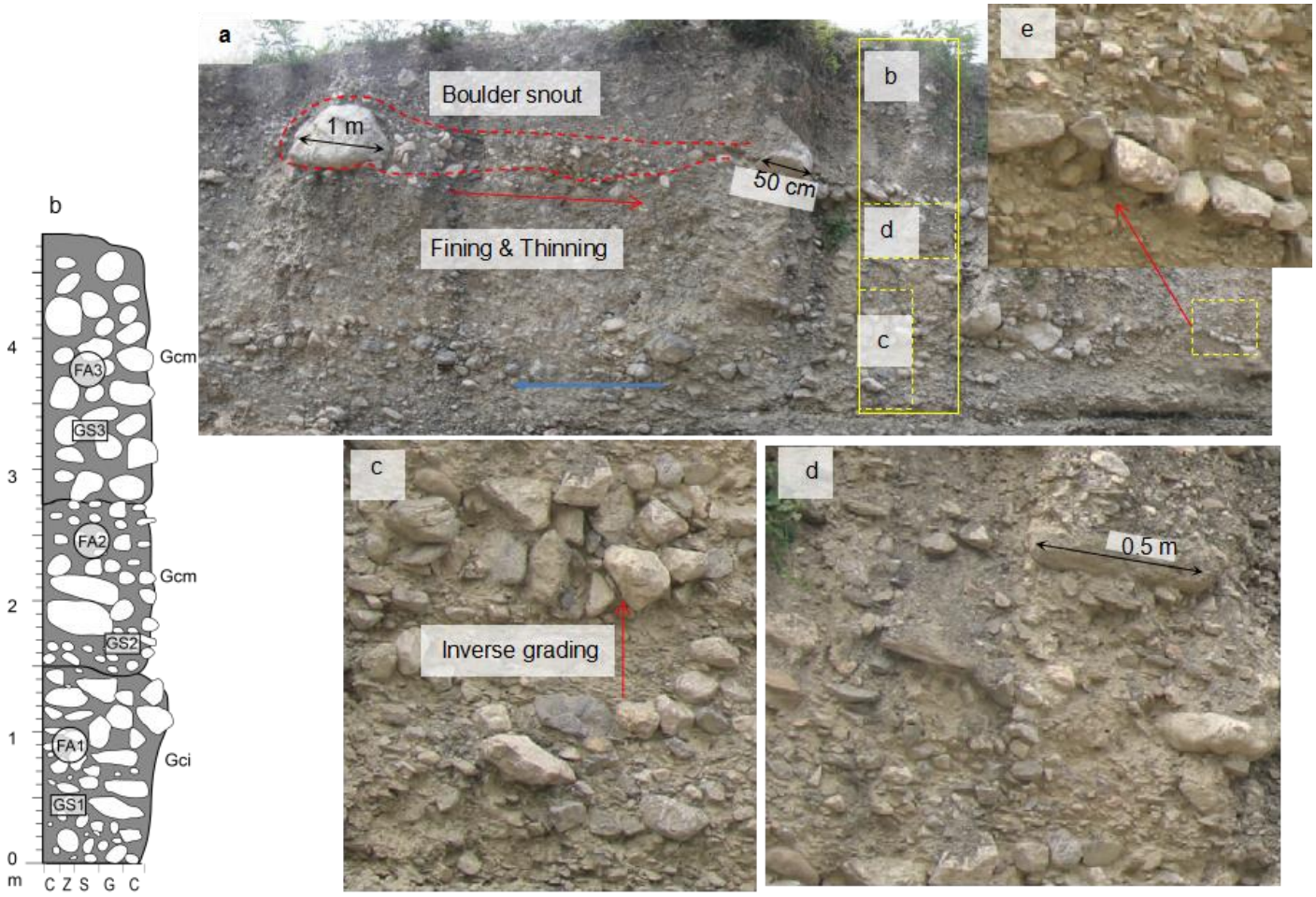

Fig. A5.3. Sedimentary structures of section T4S1. a. Exposed outcrop of section T4S1. Yellow box denotes the location of section T4S1. The blue line is the flow direction. The dashed red line circles the bouldery snout structure, in which cobbles and boulders cluster at the front forming a thick sediment body and finer clasts form thinner beds in behind. b. Sedimentary log for section T4S1. c and d. Close-up photographs of the lower and middle part of section T4S1. e. Close-up photograph showing clast imbrication at the bed base.

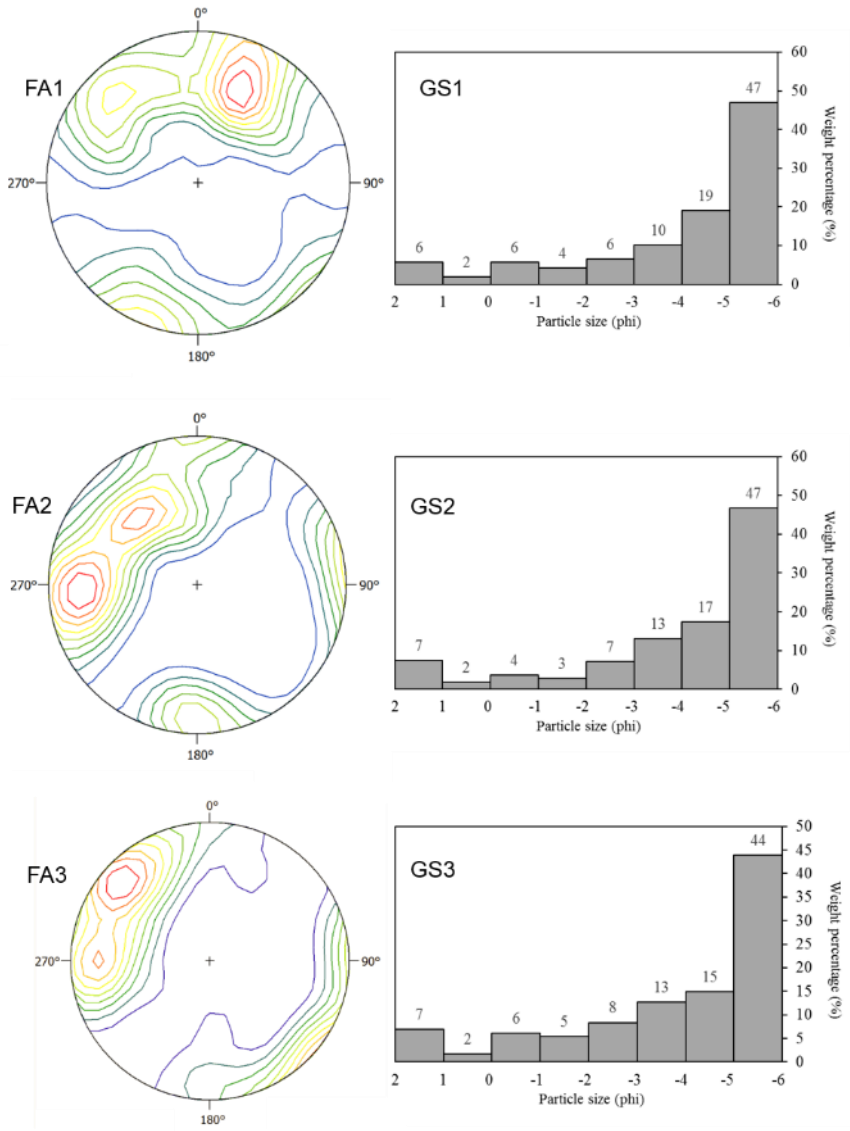

Fig. A5.4. Results of fabric and grain size (sieved) measurements for section T4S1. The b-axes were measured for 40 clasts for each unit.

Table A5.2. Results of clast fabrics of section T4S1. Sampling number is 40, and the b-axes were measured.

	Eigenvector	Orientation	Dip	S	K
FA1	1	6.4	19.0	0.59	0.68
	2	273.5	8.2	0.30	
	3	161.1	69.2	0.11	
FA2	1	304.2	25.6	0.60	0.31
	2	35.1	2.0	0.34	
	3	129.3	64.4	0.06	
FA3	1	304.9	10.3	0.56	0.18
	2	213.0	10.3	0.39	
	3	79.0	75.3	0.05	

Section T4S2

The sedimentary characteristics of section T4S2 is displayed in Fig. A5.5. It is mainly composed of poorly sorted silty-matrix-supported pebbly clasts (Gmm). In the sediment body, fines and coarse gravels form a highly compact body (Fig. A5.5c). The largest clast present in the exposed section has an a-axis length of 1.2 m (Fig. A5.5a). The lithology is composed of 85% limestone, 10% phyllite and 5% quartz. The matrix color is moderate yellowish (Munsell number: 5Y 7/6). Clasts with their a-b planes standing vertically or nearly horizontally are distributed across the section (Fig. A5.5c). No predominant orientation is present in the contoured stereonet (Fig. A5.5e), and this is also reflected from the low principal eigenvalue (0.37, Table A5.3). Near the top of the section, the sediments change into crudely bedded medium to coarse gravels. The a-axes of the clasts are aligned parallel to the direction of GLP. On top of the section is a layer of moderately yellowish brown (Munsell number: 10YR 5/4), massive silt with some granules (Fm). Many plants are rooted in this layer.

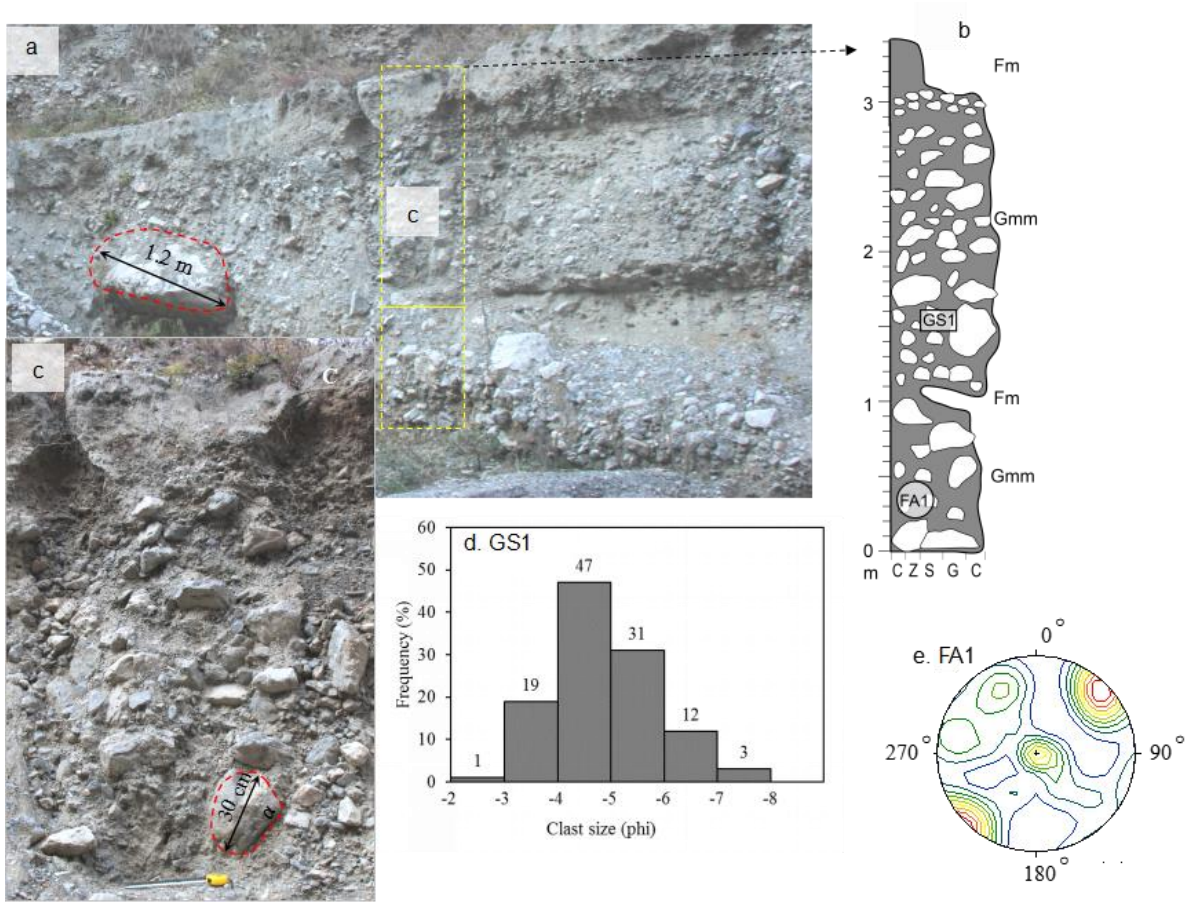

Fig. A5.5. Sedimentary characteristics of section T4S2. a. Outcrop of section T4S2 (delineated by a dashed yellow box). The length of a boulder is for scale. b. Sedimentary log of section T4S2. c. Close-up photograph of T4S2. d. Grain size distribution based on “Nano measurer 1.2”. e. Fabric measurement of clast a-axes. The sampling number is 21.

Table A5.3. Results of fabric measurement for section T4S2. 21 clasts were measured along their a-axes

	Eigenvector	Orientation	Dip	S	K
FA1	1	251°	10.2°	0.37	0.47
	2	14.8°	72.0°	0.34	
	3	158.3°	14.6°	0.28	

Section T3S1

The sedimentary characteristics of this section is displayed in Fig. A5.6. The section is 6 m thick. Four types of lithofacies are present in the section: (1) silty-matrix-supported pebbly gravels (Gmm), (2) clast-supported massive gravels (Gcm), (3) well-bedded pebbly gravels (Gh') and (4) fine silt (Fm).

In the lower part of the section (Fig. A5.6a, b), Gmm sediments form two sedimentary beds with each a thickness of ~0.4 m. In each of the bed, the lithological composition is formed by ~70% of limestone, ~ 20% of phyllite and ~ 10% of quartzite. The a-axes of clasts are generally parallel to the flow direction of the GLP valley, with relatively shallow dips. The normalized eigenvalues for these two beds are 0.58 (lower) and 0.57 (upper) (Table A5.4), suggesting weak but discernable preferential fabrics. The bed base is flat without erosion to the underlying sediments, and the bed top gradually changes from gravels to a silty layer (Fm).

The Gh' sediments overly the silty layer, forming a thickness of 30 cm (Fig. A5.6b). The lithology is composed of 90% limestones and 10% phyllites. The principal eigenvalue (Table A5.4) is 0.58, still indicating weak but discernable preferential fabrics. The base of this unit is characteristic by a sharp contact in which clasts are imbricated with their b-axes parallel to the flow direction (Fig. A5.6a). The bed

top of this unit is an erosional plane (Fig. A5.6a).

Two thick layers (> 2 m each) of clast-supported massive gravels (Gcm) overly the Gh' unit (Fig. A5.6a). Several boulders with their a-axes larger than 30 cm are present in the sediment body (Fig. A5.6a). In each of the Gcm layers, limestone forms the primary proportion (> 75%), with phyllite and quartzite accounting for ~15% and ~10% respectively. The principal eigenvalues for fabric measurements of the two units are 0.44 (lower) and 0.49 (upper) respectively (Table A5.4), indicating weak preferential arrangement of clasts. The fabric stereonets of the two units each display three clusters (Fig. A5.6c). The clusters generally center to the plane origin, indicating that clasts generally dip with large angles. For each unit, the bed surface is undulatory, and the bed base is erosional. On the top of the section is a layer of massive silt (Fm) with some granules. Root pores and soil cement are present.

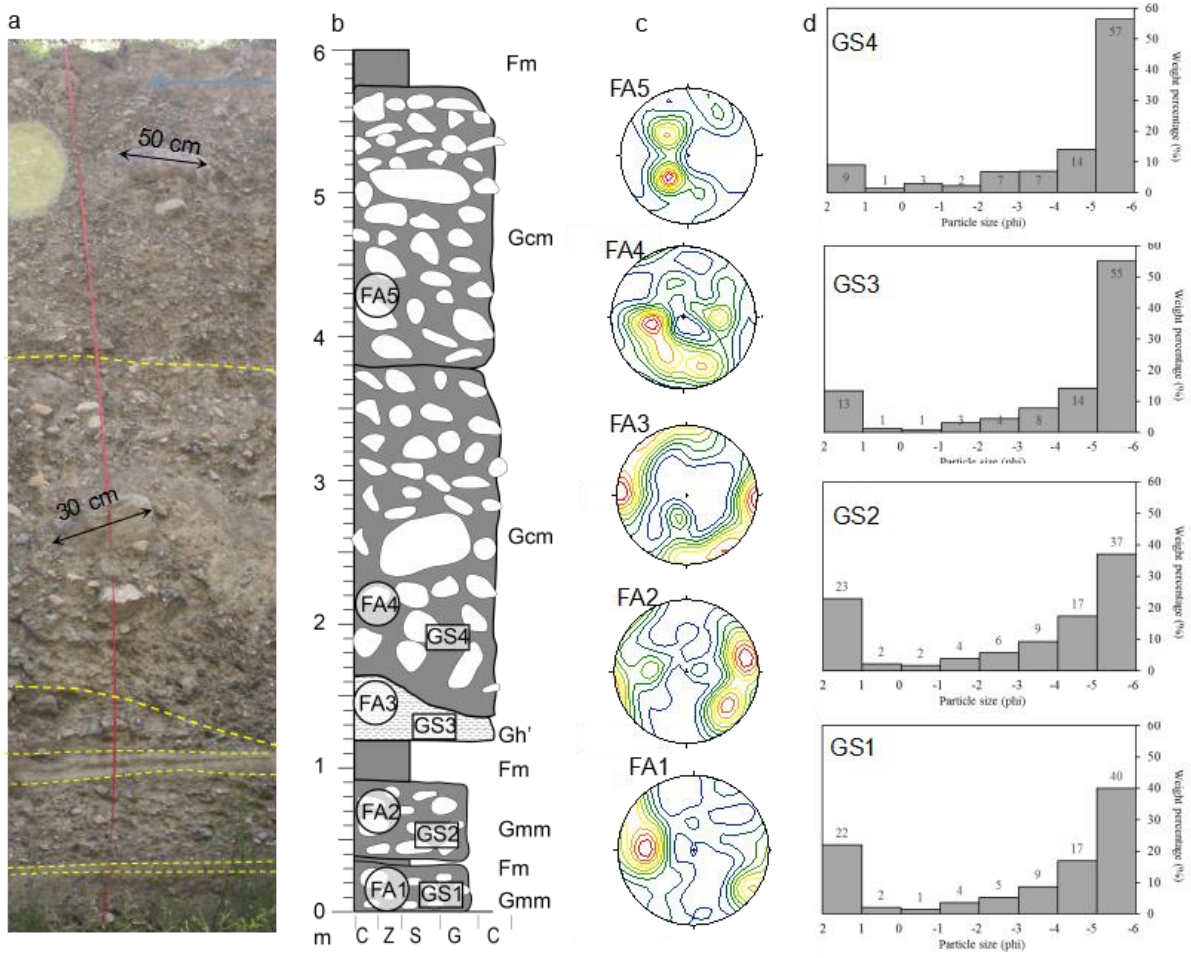

Fig. A5.6. Sedimentary characteristics of section T3S1. A. Photograph of section T3S1. Dashed yellow lines delineate different sedimentary units. B. Sedimentary log of T3S1. c. Contoured stereonets of fabric measurements. The b-axes were measured, and the sampling number is 40 for each unit. d. Grain size distribution (sieved results).

Table A5.4. Results of fabric measurement of section T3S1. The b-axes were measured, and the sampling number is 40 for each sedimentary unit.

	Eigenvector	Orientation (°)	Dip (°)	S	K
FA1	1	276.3	18.3	0.58	6.47
	2	186.2	0.5	0.22	
	3	94.8	71.7	0.19	
FA2	1	96.3	8.3	0.57	11.70
	2	187.0	4.6	0.22	
	3	305.9	80.5	0.20	
FA3	1	49.1	10.0	0.58	0.42
	2	140.3	7.1	0.33	
	3	265.2	77.7	0.09	
FA4	1	218.4	38.5	0.44	2.13
	2	116.7	14.2	0.30	
	3	10.39	48.0	0.25	
FA5	1	238.8	52.5	0.49	0.17
	2	349.6	14.6	0.40	
	3	89.6	33.7	0.11	

Section T3S2

Section T3S2 has a thickness of 4.1 m (Fig. A5.7). It is mainly formed by three layers of poorly sorted crudely-stratified clast-supported pebbly clasts (Gh). The base of each layer is paved with cobble to boulder sized clasts with their a-b planes imbricated (Fig. A5.7a). Clasts in the primary body of each layer are crudely bedded, with their a-b planes aligned horizontally and parallel to the flow direction. The top of each layer is undulatory. On the top of the section is a layer (0.3 m) of massive silt with some granules (Fm). Plant roots and voids are present in this unit.

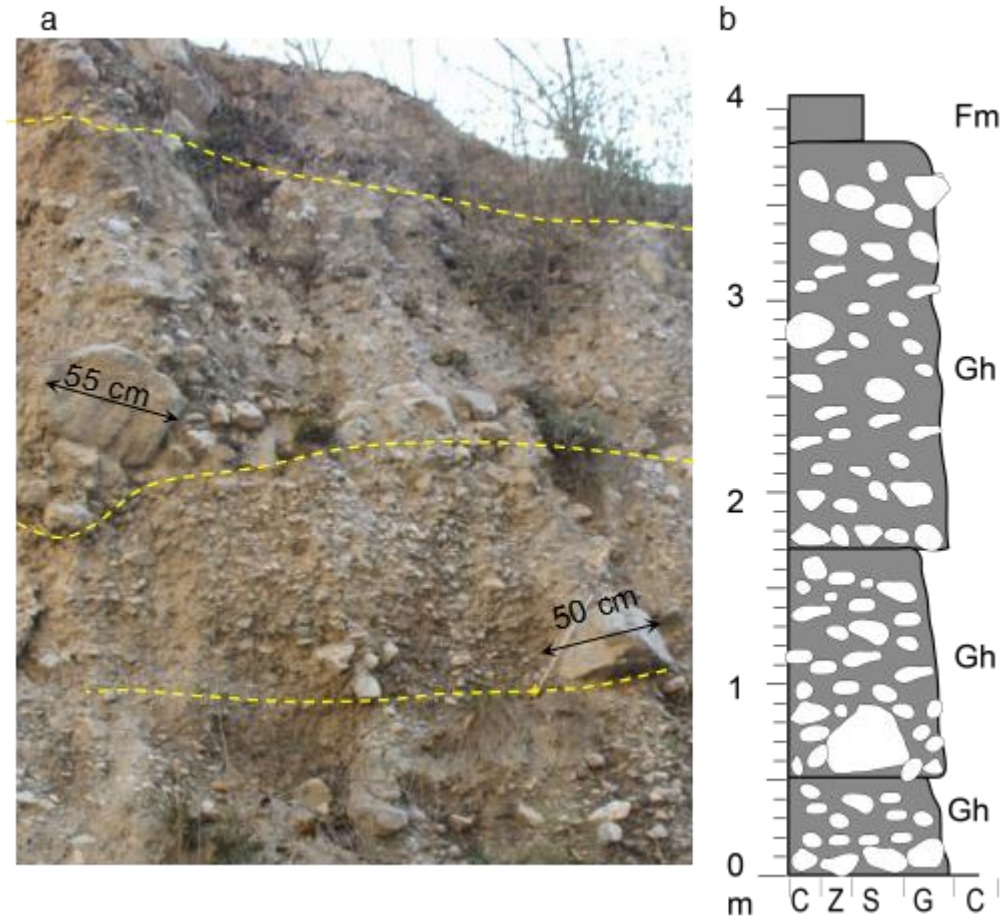

Fig. A5.7. Sedimentary characteristics of section T3S2. a. Photograph of section T3S2. b. Sedimentary log of section T3S2.

Section T3S3

The relative location and detailed sedimentary characteristics of section T3S3 are displayed in Fig. A5.8. The result of clast fabric measurement is displayed in Table A5.5. Broadly, this section is 4.4 m thick and is composed of two types of lithofacies: the poorly sorted crudely bedded pebbly limestone-dominated clasts with silty and sandy matrix (Gh) and the moderately sorted well-bedded phyllite-dominated pebbly clasts with silty and sandy matrix (Gh (p)). Clasts in the sedimentary unit of Gh contain 95% of limestone and 5% of phyllite, while clasts in the sedimentary unit of Gh (p) contain 80% of phyllite and 10% of limestone. The locations of grain size and clast fabric measurement are displayed in Fig.

A5.8c, and the associated results are presented in Fig. A5.9. The results of fabric measurement (Fig. A5.9 and Table A5.5) indicate a strong preferential arrangement of clasts, with their principal eigenvalues being 0.69 – 0.73.

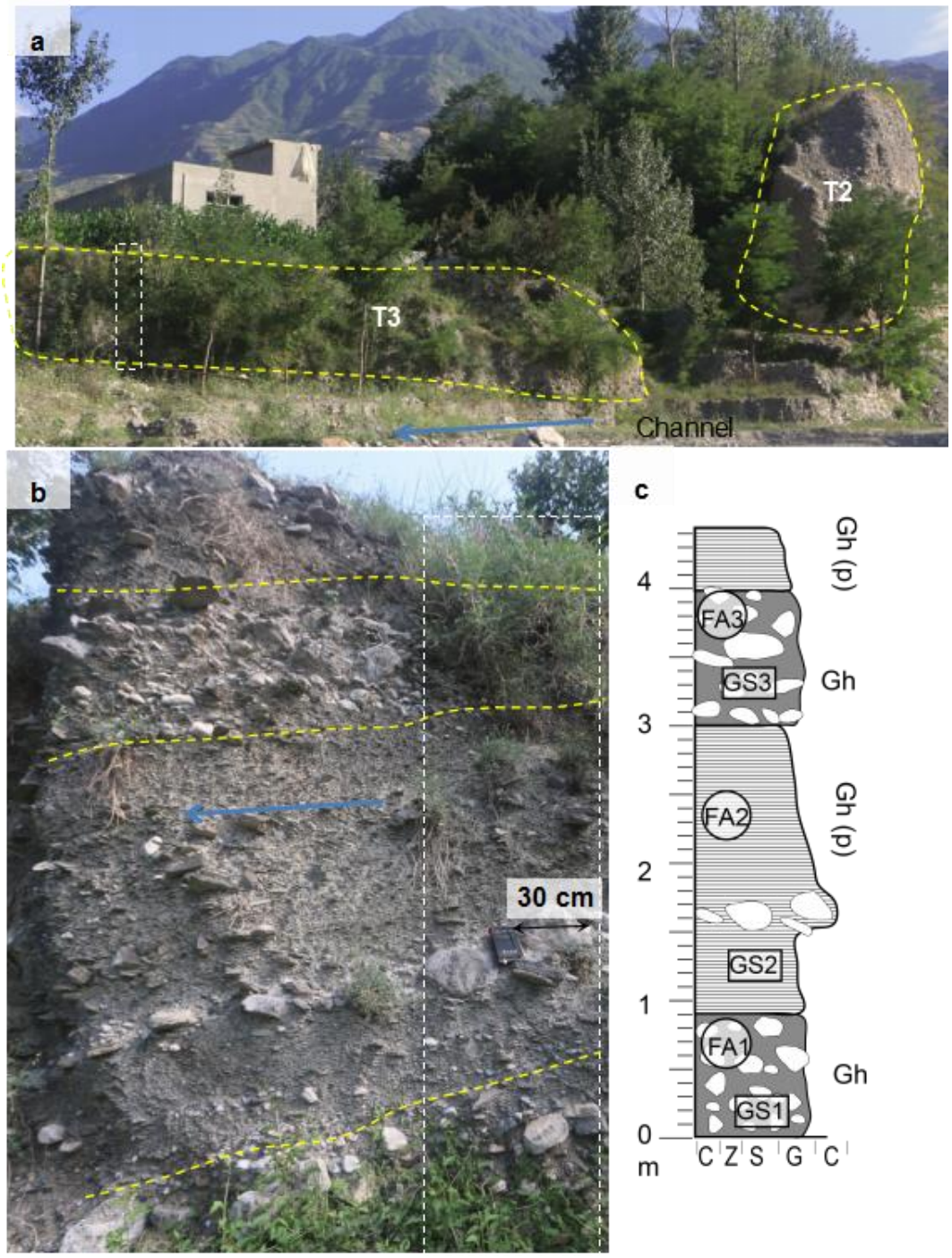

Fig. A5.8. Sedimentary features of section T3S3. a. Location of T3S3 (dashed white box). The dashed yellow lines show the relative positions of the T2 and T3 terrace. The blue arrow represents the flow direction of GLP. b. Photograph of T3S3. c. Sedimentary log of T3S3.

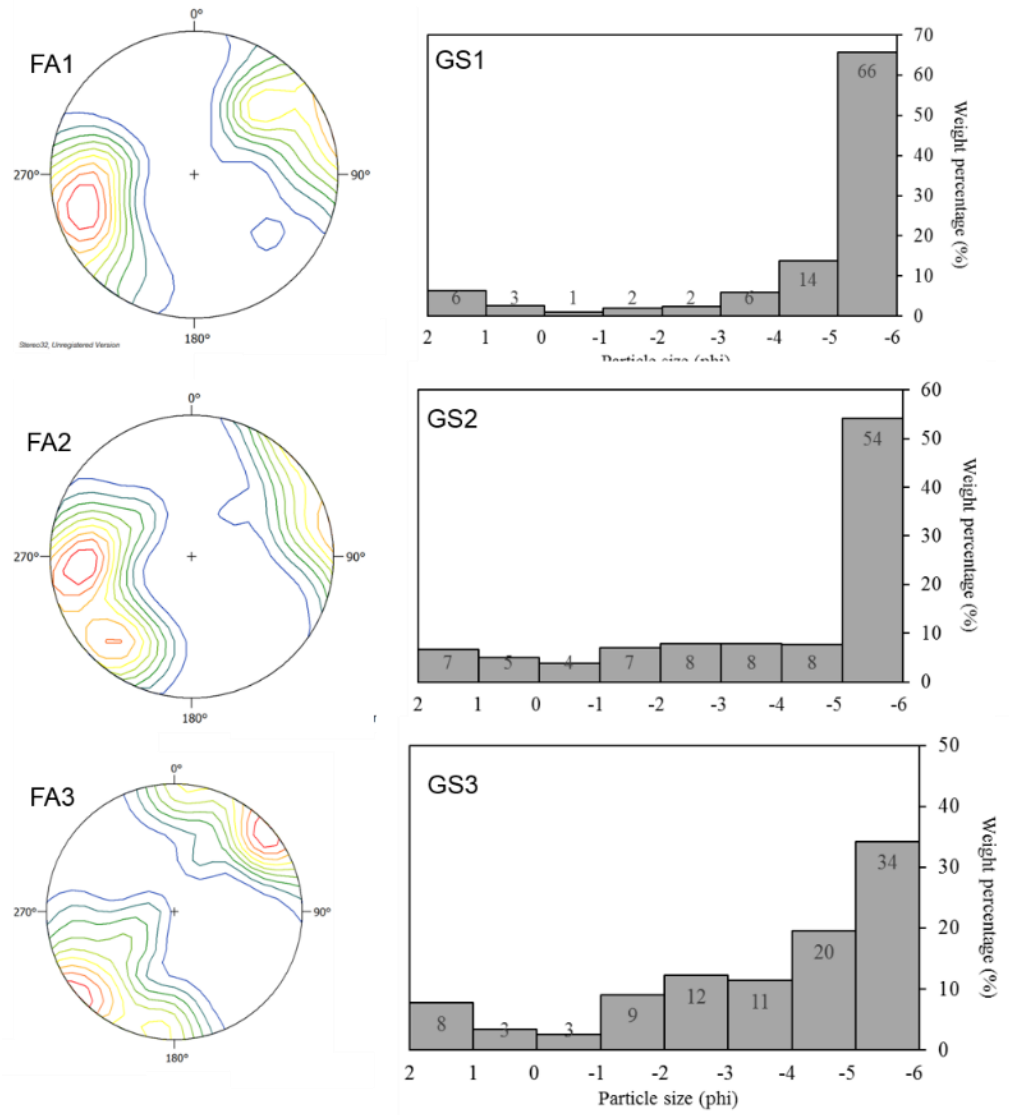

Fig. A5.9. Results of fabric and grain size (sieved) measurements for section T3S3. The a-axes were measured, and the sampling number is 20 for each fabric measurement.

Table A5.5. Results of fabric measurement for section T3S3.

	Eigenvector	Orientation	Dip	S	K
FA1	1	247.8	2.1	0.73	2.02
	2	340.1	47.1	0.18	
	3	155.9	42.8	0.09	
FA2	1	251.1	13.3	0.73	1.55
	2	346.5	21.8	0.19	
	3	131.9	64.1	0.08	
FA3	1	220.3	9.3	0.69	1.93
	2	321.1	48.8	0.20	
	3	122.5	39.7	0.11	

Section T3S4

The section is displayed as a small patch in the place where the GLP channel bends (Fig. A5.10). Broadly, three types of lithofacies are present in this section: (1) massive silty-matrix supported pebbly to cobbly limestone-dominated clasts (Gmm), (2) moderately sorted crudely bedded pebbly limestone-dominated clasts (Gh), and (3) moderately sorted well-bedded phyllite-dominated clasts (Gh (p)).

The base of the section is formed by a thick layer (0-2.6 m) of Gmm sediments (Fig. A5.11 a). Clasts of this unit are composed of 80% limestone and 20% phyllite. Clasts are randomly emplaced without preferential orientation. Fabric data show many clusters (Fig. A5.12, FA1) indicating that no preferential fabric has been developed. This is also reflected in the principal eigenvalues 0.44 (Table A5.6). The bed top is an inclined surface overlain by Gh sediments. The Gh unit is distributed at the section depth 2.6 - 2.7 m, 3.5 - 4.1, and 4.7 - 6.2 m. The sediments are mainly pebbly to cobbly limestones with sandy matrix, and clasts are generally aligned with their a-b planes parallel to the flow direction. The Gh (p) units are interleaved between the Gh units, forming a total thickness of 1.4 m. The lithology is mainly composed of phyllites which account for 85% with the other 15% being limestones. The principal eigenvalue of fabric measurements is 0.64 (Table A5.6).

Fig. A5.10. Location of section T3S4, delineated by the dashed yellow box. Dashed yellow arrow points to the flow direction.

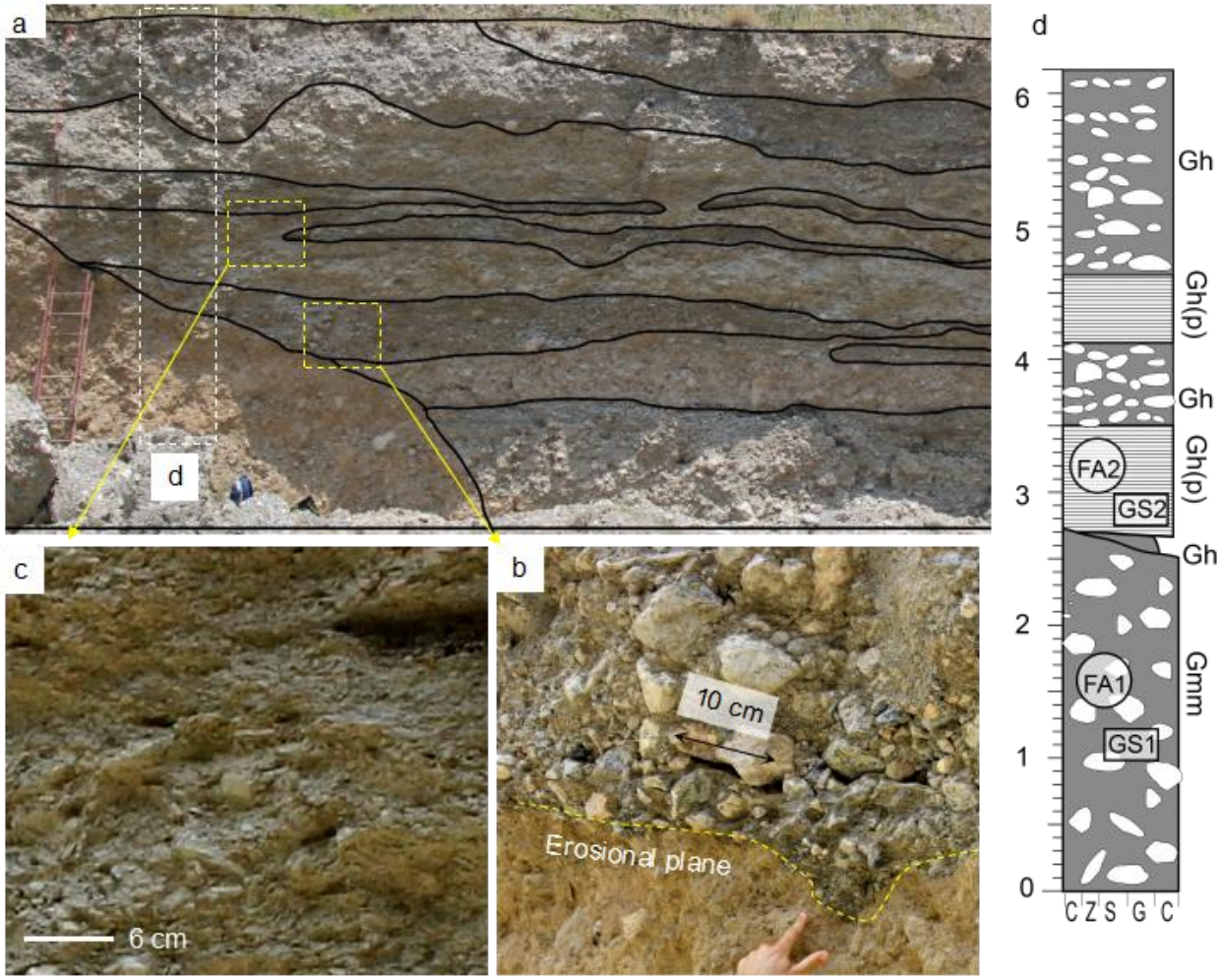

Fig. A5.11. Sedimentary characteristics of section T3S4. a. Exposed face of section T3S4 (dashed white box). Black lines delineate the sedimentary boundaries. b. Close-up photograph of the contact between Gmm and Gh. c. Close-up photograph of Gh(p). d. Sedimentary log of section T3S4.

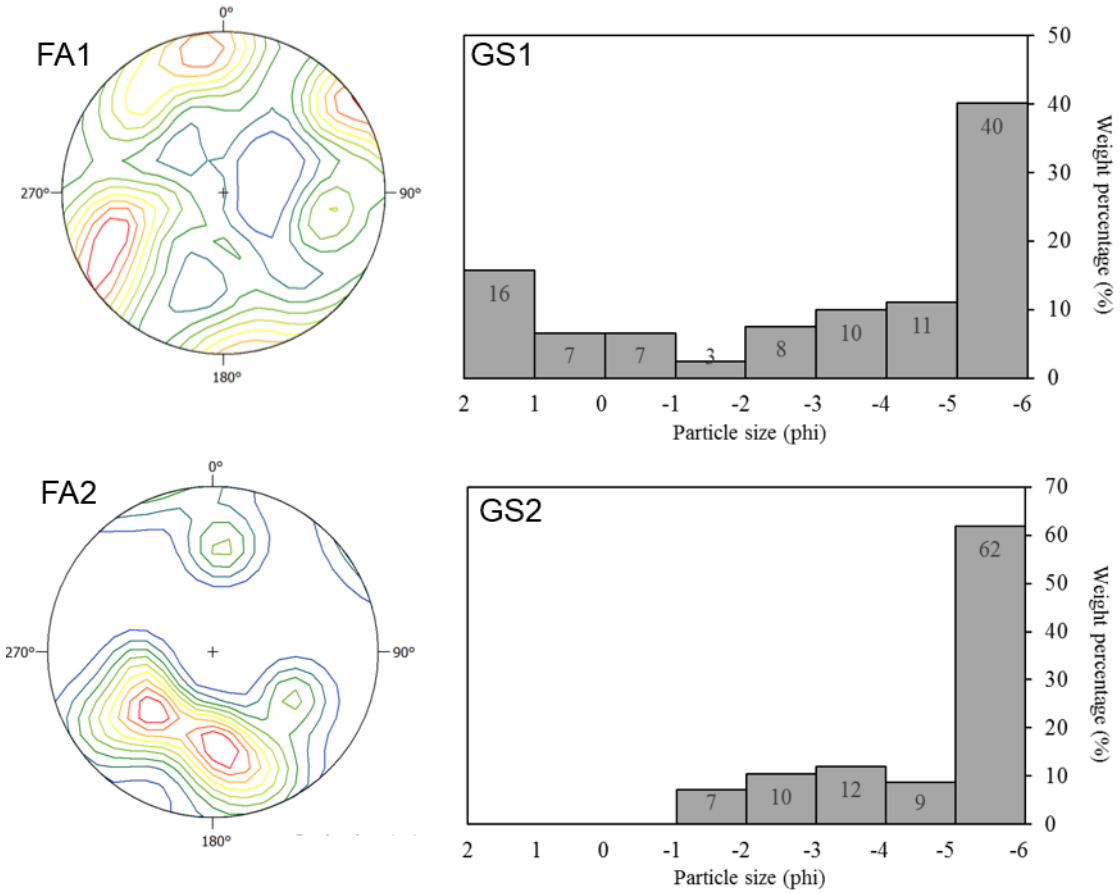

Fig. A5.12. Results of fabric and grain size (sieved) measurements for section T3S4. The a-axes were measured with the sampling number being 30 and 10 respectively for FA1 and FA2. The sampling number for FA2 measurement is relatively small due to the lack of available clasts during field measurement.

Table A5.6. Results of the fabric measurement for section T3S4.

	Eigenvector	Orientation	Dip	S	K
FA2	1	194.9	31.3	0.64	1.424
	2	290.6	9.2	0.25	
	3	35.01	57.05	0.11	
FA1	1	250.1	17.6	0.44	0.2271
	2	342.4	7.2	0.37	
	3	93.7	70.9	0.19	

Section T3S5

Section T3S5, with an exposed thickness of 6.4 m is located near the mouth of the GLP valley (Fig. A5.13). The section is essentially formed by the alteration of two types of sediments: the poorly to moderately sorted well-bedded pebbly

phyllite dominated clasts (Gh(p)) and the thin silt layer (Fm). Each layer of Gh (p) sediments has a thickness of at least 20 cm, while the Fm sediments are relatively thinly (less than 10 cm thick) developed in the section (Fig. A5.13). For the Gh(p) sediments, phyllites account for 90%, and limestones for 10% of the clast present. The clast fabrics and grain sizes were measured in this section (Fig. A5.13 b), and the results are displayed in Fig. A5.14 and Table A5.7. The fabrics for two of the units in the section (Fig. A5.14) indicate strong clast alignment, with their principal eigenvalues being 0.65 and 0.68 (Table A5.7). The clast orientation is roughly parallel to the flow direction of the GLP valley.

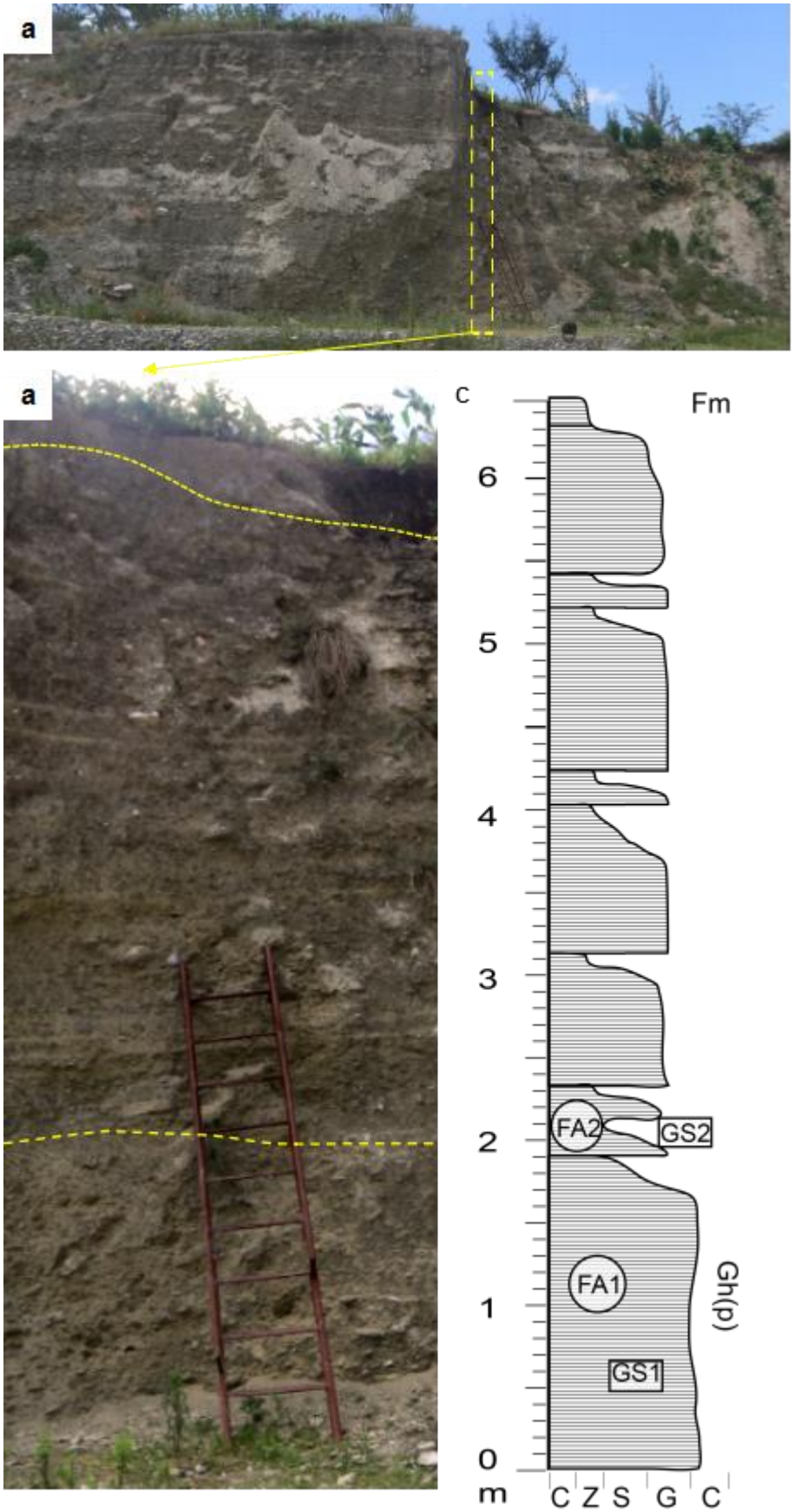

Fig. A5.13. Sedimentary characteristics of section T3S5. a. Photograph of the outcrop of a T2 terrace from which section T3S5 (dashed box) was logged. b. Photograph of section T3S5. c. Sedimentary log

of section T3S5.

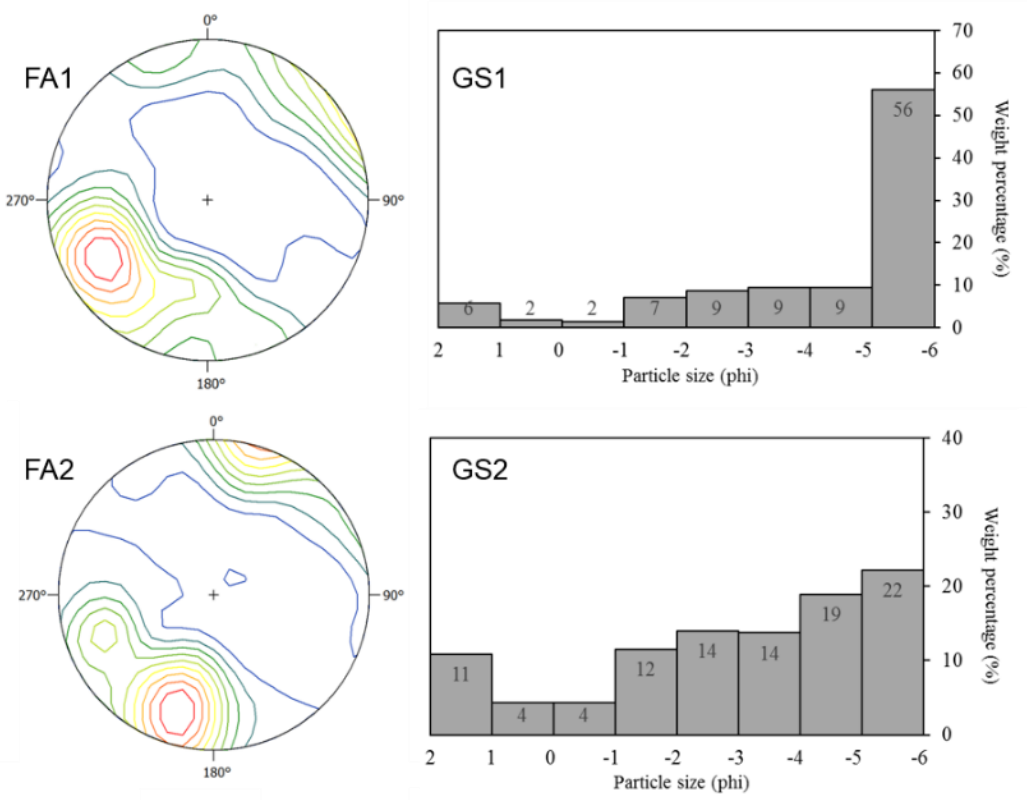

Fig. A5.14. Results of fabric and grain size (sieved) measurements for section T3S4. The a-axes were measured, and the sampling number is 30 for each fabric measurement.

Table A5.7. Results of the fabric measurement for section T3S5.

	Eigenvector	Orientation	Dip	S	K
FA2	1	208.6	16.8	0.68	1.50
	2	303.6	16.3	0.22	
	3	74.9	66.4	0.10	
FA1	1	224.5	18	0.65	0.62
	2	315.1	1.7	0.28	
	3	50.4	71.9	0.07	

Section T2S1

Section T2S1, with an exposed thickness of 17 m, is positioned at the mouth of the GLP valley. The lithofacies present in this section include Gh', Gci, Gcm, Gh, Gmm, Fm and Fm' (Fig. A5.15). For some parts with good exposures in the section, grain size distribution was measured using the software "Nano measurer 1.2", and the result is shown in Fig. A5.16.

The Gh’ sediments form the section 0 - 0.4 m and 0.6 - 3.4 m (Fig. A5.15 a). Clasts in these units are moderately sorted and horizontally bedded granule- to pebble-sized clasts. Limestone forms the primary portion of clast lithology. Mostly, the b-axes of the clasts are aligned parallel to the direction of GLP channel (Fig. A5.15c). Generally, the grain size shows an upward-fining trend with the base paved with very coarse gravels and cobbles while the upper section with medium to coarse gravels (Fig. A5.15 d)

The Gci sediments form the sections 3.4 - 4.6 m, 4.8 - 7.0 m and 16.2 - 16.7 m (Fig. A5.15 e & f). In each of the unit, limestone forms the primary clast lithology. Clasts in each unit base are generally pebbly clasts with their mean diameter being around 3 cm. In the upper part of each unit, clasts become cobbles and boulders. The clasts near each unit base are generally aligned with their a-axes parallel to the flow direction with small dip angles (below 10˚), while clasts in the upper part of each unit dip with various angles ranging from nearly vertical to horizontal (Fig. A5.15e). The amount of matrix increases from the unit base towards the top of the unit, and the top is covered by a thin layer (20cm) of silt (Fm).

The Gcm sediments form the section 7.2 - 9.2 m. In the unit, a boulder with an a-axis length of 150 cm is supported by smaller cobble-sized clasts (Fig. A5.15g). The a-axis of the boulder is oriented at 60˚ and dips at 5˚. Clasts at the unit base are imbricated along their b-axes. The boulder together with its underlying supporting clasts form a snout shape (Fig. A5.15g). The thickness of the snout is

1.5 m at the front and decreases in the upstream direction of the GLP channel.

The Gh sediments form the section 9.2 - 15.6 m which is composed of several layers of Gh sediments. For each layer, the sediments are composed of moderately to poorly sorted clast-supported pebbly clasts. Most of the clasts are aligned with their a-axes parallel to the flow direction, though some imbricated cobbly clasts also exist (Fig. A5.15h).

The Gmm sediments form the section 17.1 - 17.5 m (Fig. A5.15h). The lower part of the unit is composed of very poorly sorted matrix-supported pebbly clasts. No preferential orientation of the clasts is present. In the upper part, massive fine silt constitutes the major proportion of the sediment with some granule-sized clasts interspersed in the fine matrix. The clasts are generally aligned horizontally with their a-b planes.

The Fm sediments is interleaved between the gravelly sediments forming thin planar layers which pinch out laterally (Fig. A5.15b). The Fm' sediments are present in sections 15.6 – 16.2 m and 16.7 – 17.1 m, forming thick (40 – 60 cm) units (Fig. A5.15h).

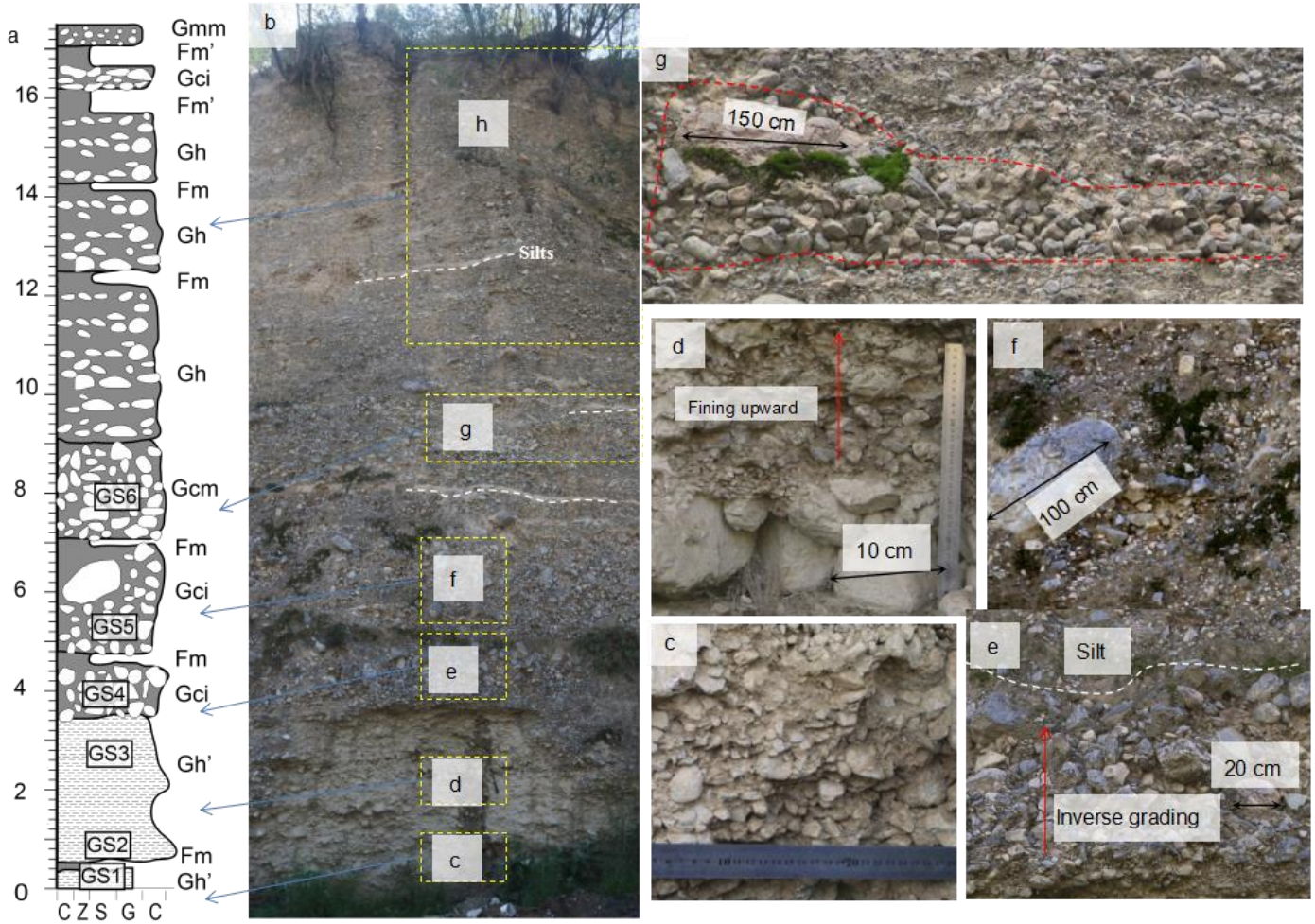

Fig. A5.15. Sedimentary characteristics of section T2S1. a. sedimentary log of section T2S1. b. Photograph of section T2S1. Sediments delineated by dashed yellow boxes (c, d, e, f, g) are shown in detail in the corresponding photographs. Dashed red lines on photograph g delineates a bouldery snout in which the front is a thick layer of boulders and cobbles, and the tail is a thinner layer of smaller clasts. The length of the a-axis of the largest clast is 150 cm (Continued overleaf).

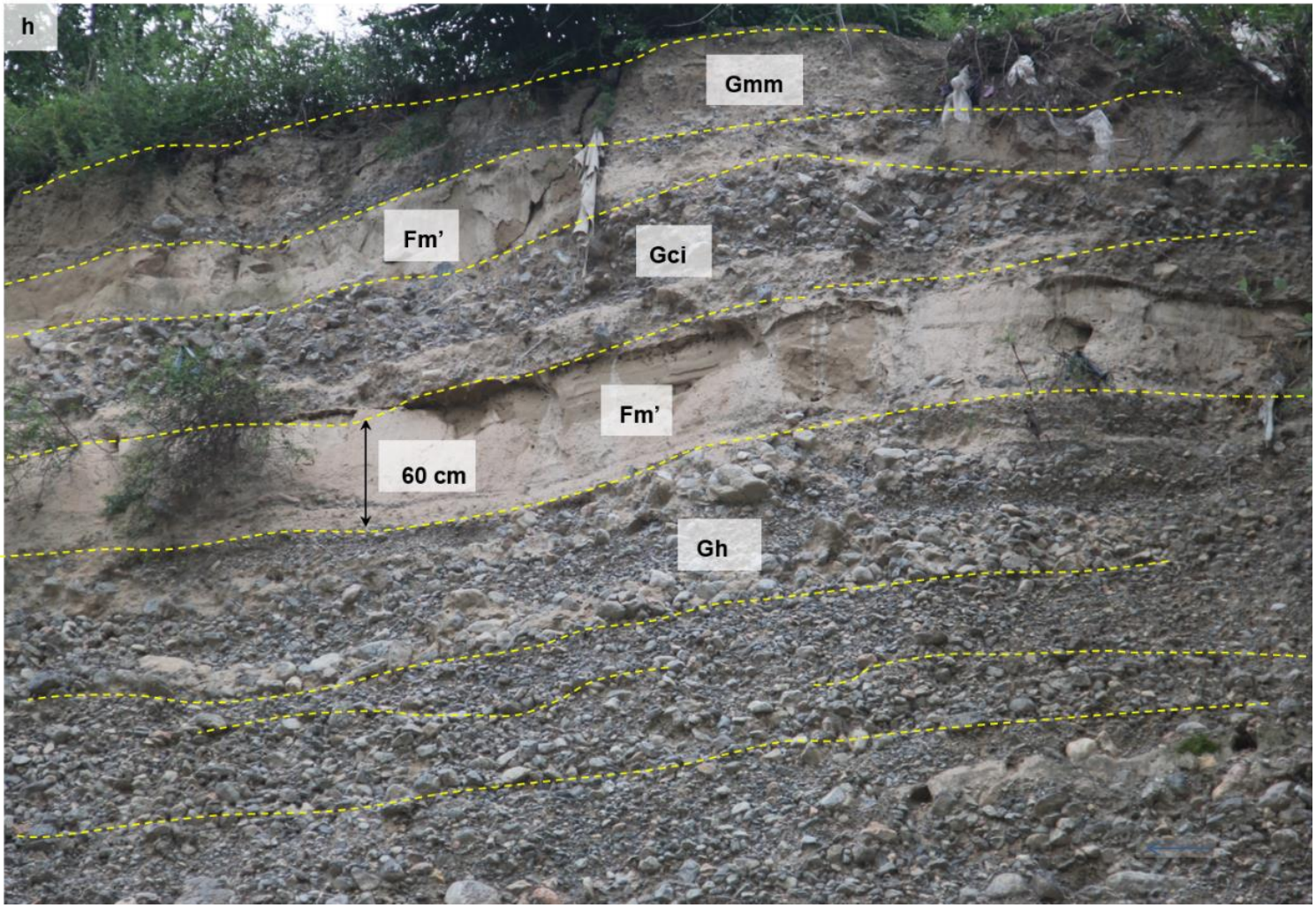

Fig. A5.15. Sedimentary characteristics of section T2S1.

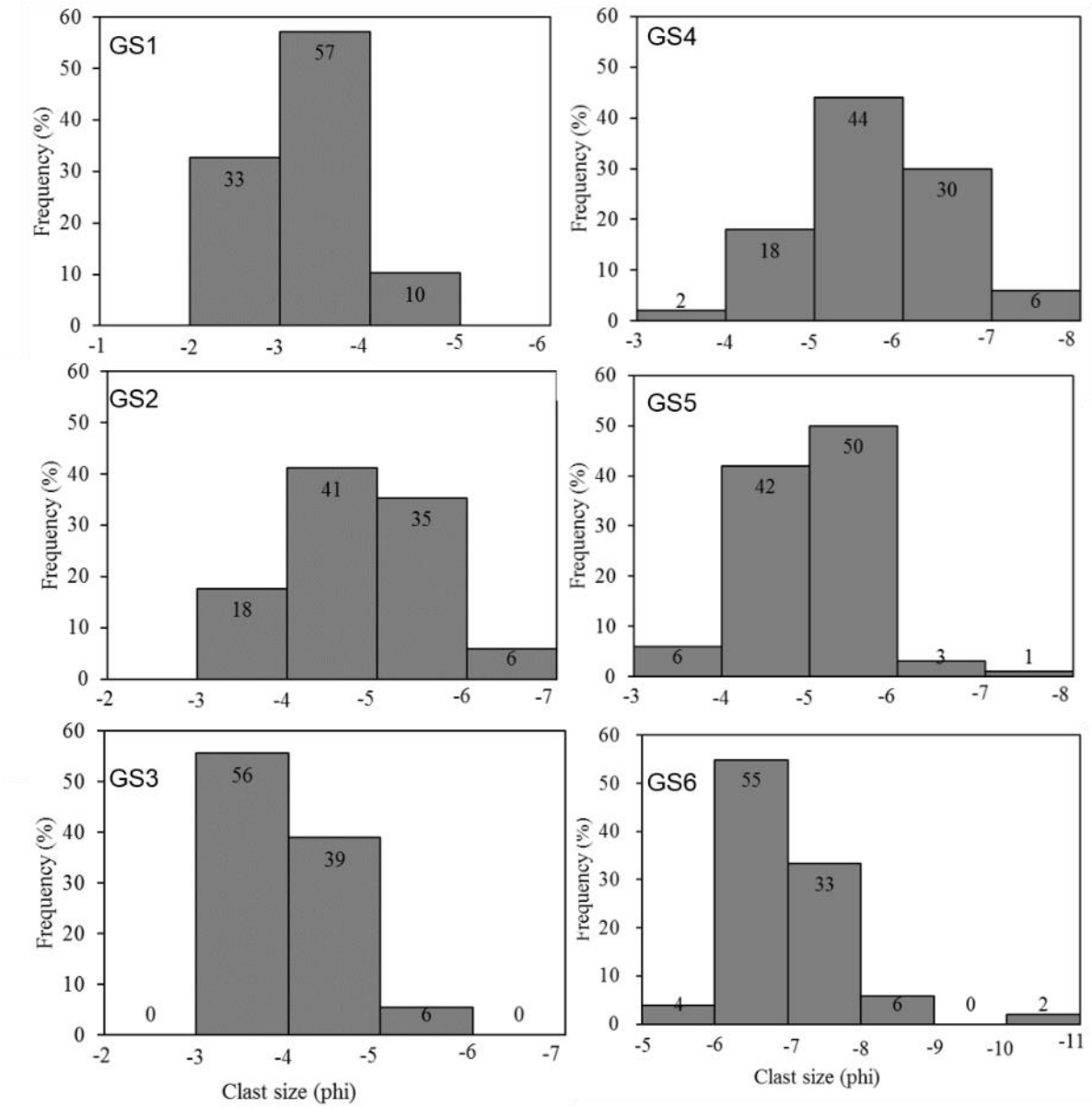

Fig. A5.16. Grain size distribution of sediments in section T2S1. The result is produced using the software Nano measurer 1.2.

Section T2S2

The exposed outcrop where section T2S2 was logged, as well as the sedimentary characteristics of section T2S2, is shown in Fig. A5.17. For some parts of the section (Fig. A5.17b), clast fabrics and gain size distributions were measured, and the results are displayed in Fig. A5.18.

The T2S2 section, with a thickness of 8.75 m, is composed of five types of

lithofacies: (1) silty-matrix-supported limestone-dominated pebbly to cobbly clasts (Gmm), (2) well--bedded limestone-dominated pebbly clasts (Gh'), (3) massive clast-supported limestone-dominated pebbly to cobbly clasts (Gcm), (4) crudely-bedded limestone-dominated pebbly to cobbly clasts (Gh), and 5) silt with some granules (Fm).

The Gmm sediments are in the lower part of the section and form three units (sections 0 - 0.5 m, 0.6 - 1.3 m and 1.4 - 1.8 m) that are separated by thin layers of Fm sediment (Fig. A5.17b, c). In each of the unit, limestone form the primary lithology with no visible phyllite clasts present. The amount of fine matrix is relatively small in the lower part of each unit and gradually increases upwards. At the top of each unit, gravelly sediments gradually change to a thin layer (10 cm) of silt (Fig. A5.17c). The clasts are massive without any grading and bedding. Clast orientations are variable as is shown by several low-density clusters in the contoured stereonet (Fig. A5.18, FA1, FA2 and FA3). The a-b planes of clasts are generally parallel to the flow direction (Fig. A5.17c). The principal eigenvalue (S1) for the three units are 0.42 (for FA1), 0.52 (for FA2) and 0.62 (for FA3), showing an upward stronger trend of clast arrangement (Table A5.8).

The Gh' sediments are present in section 1.9 - 2.7 m (Fig. A5.17b, d). Limestones are the dominant lithology with some phyllites present. The clasts near the bed base are imbricated pebbly to cobbly gravels (Fig. A5.17d). The clasts fine upwards showing a normal grading trend and are well-bedded (Fig. A5.17d). The bed base is erosional (Fig. A5.17d). The principal orientation and dip for clasts are 207.2˚ and 4.3˚ respectively, and the principal eigenvalue is 0.59 (Table A5.8).

The Gcm sediments form two units at sections 2.7 - 3.9 m and 3.9 - 5.6 m (Fig. A5.17b). The contact of the two units is not clear. The clasts are mainly sub-angular limestones without phyllites. Pebble- and cobble-sized clasts are distributed in the base forming an imbrication structure with their b-axes parallel to the direction of the GLP channel (Fig. A5.17e). The clasts at the upper part of each unit are massive and ungraded.

The Gh sediments are distributed in the upper part of the section (Fig. A5.17b, 5.6 - 8.75 m). They form a stack of similar units. In each unit, the base is paved by imbricated cobble- to boulder-sized clasts with their b-axes preferentially aligned parallel to the direction of the GLP channel (Fig. A5.17g). The upper part of each unit is composed of poorly sorted massive cobble-sized clasts with little matrix.

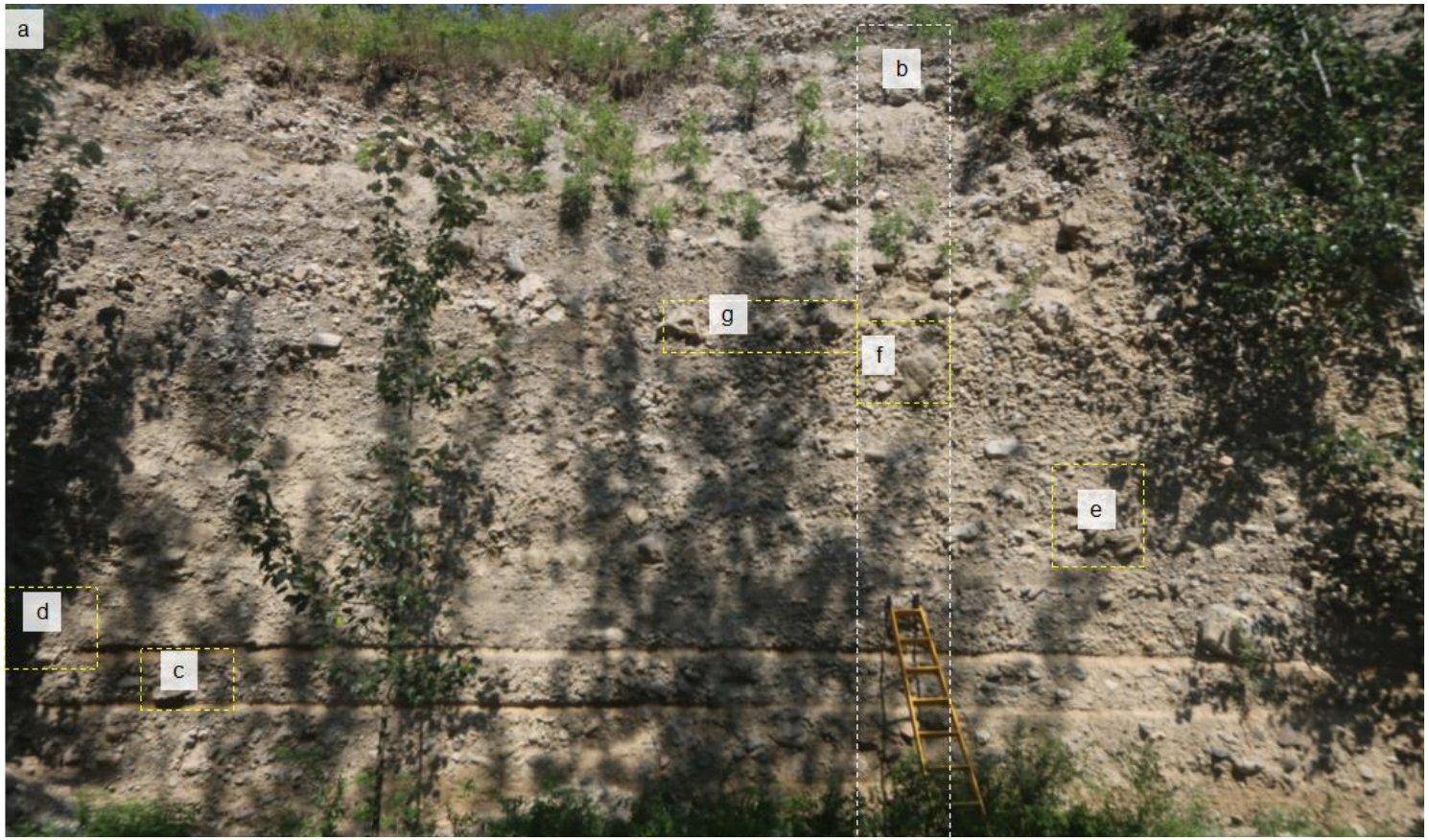

Fig. A5.17. Sedimentary characteristics of section T2S2. a. Photograph of a T2 outcrop where section T2S2 (dashed white box) was logged. Dashed yellow boxes delineate the areas which will be shown in enlarged photographs.

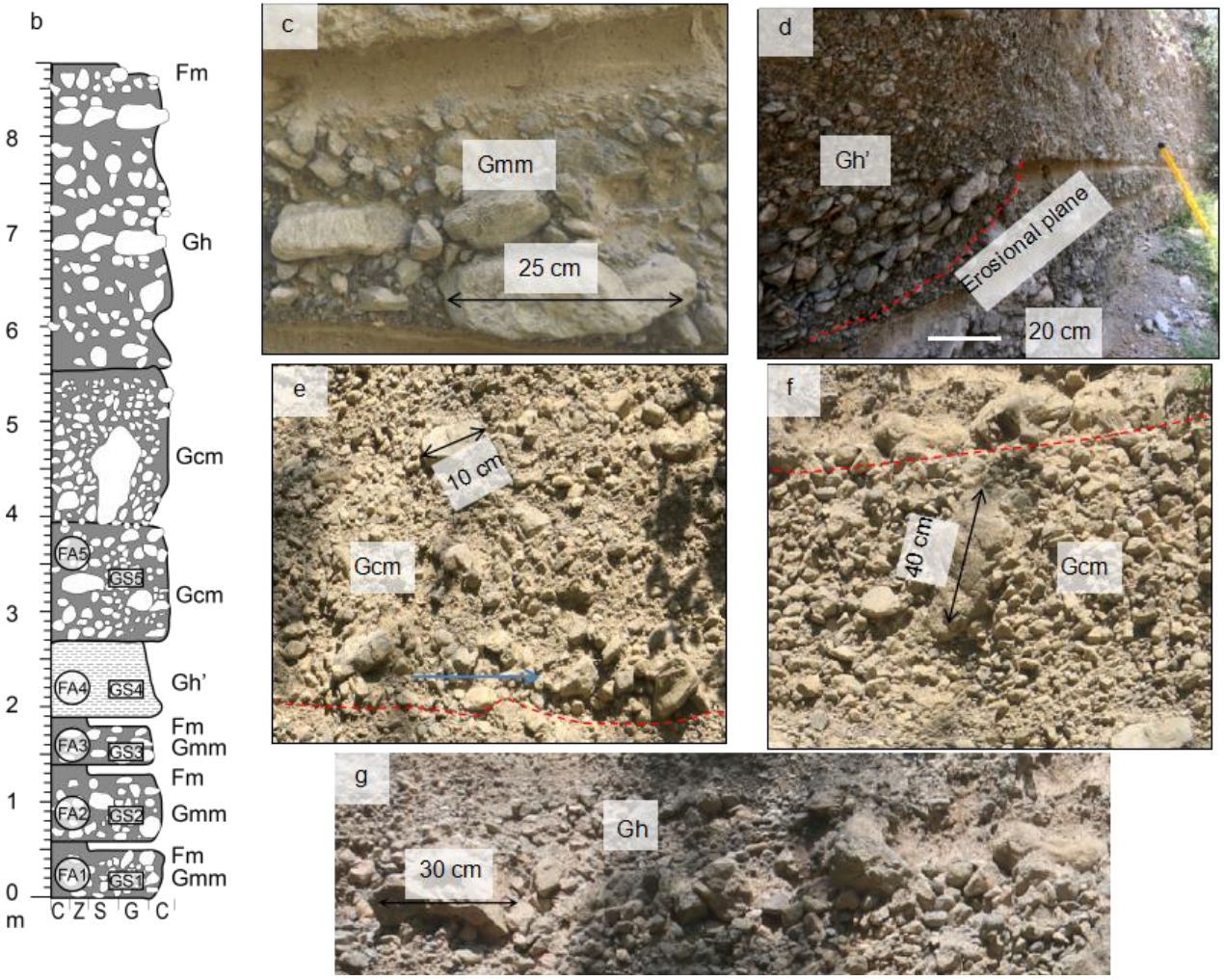

Fig. A5.17. Sedimentary characteristics of section T2S2 b. Sedimentary log of section T2S2. c, d, e, f and g are detailed photographs showing the characteristics of different units.

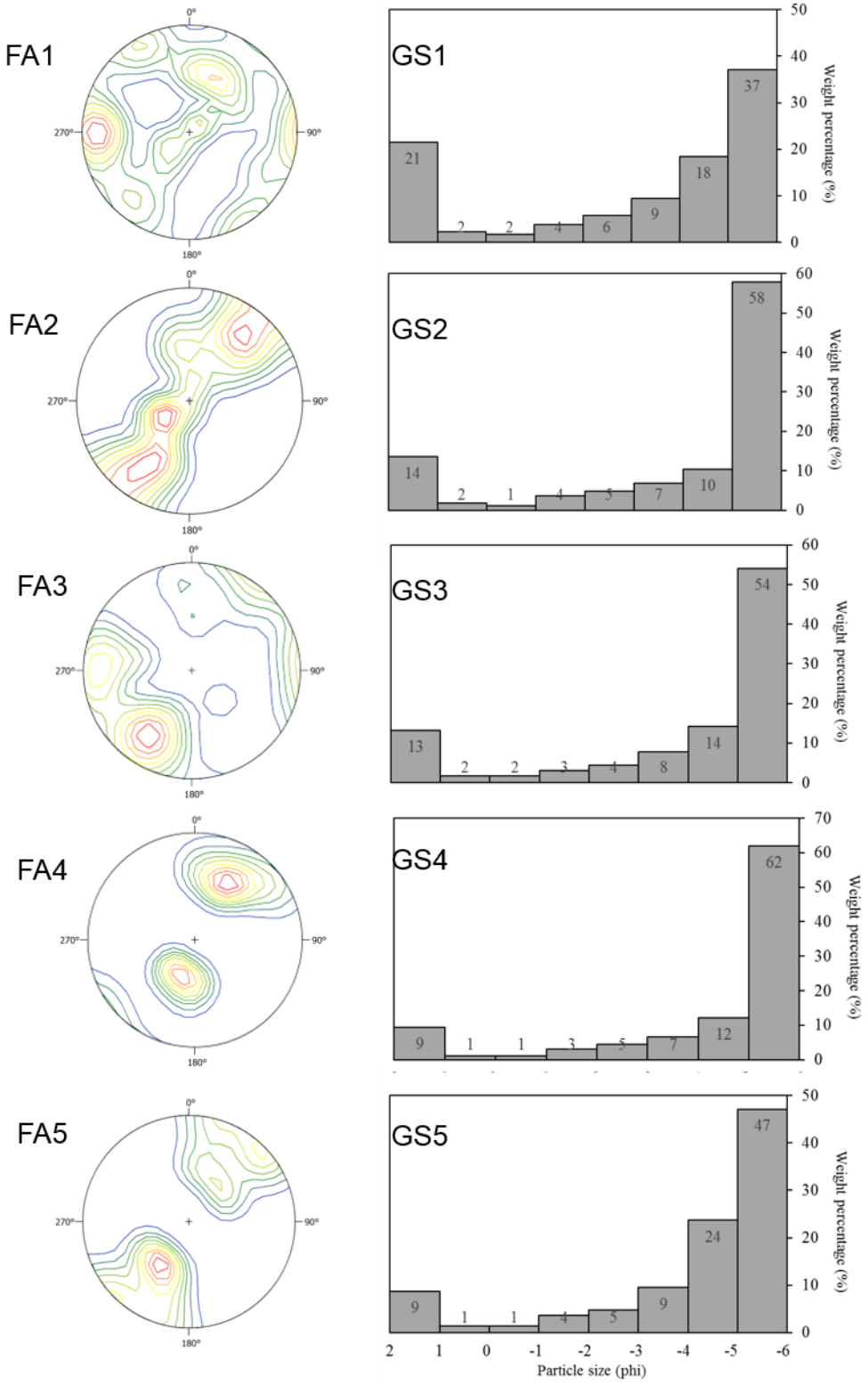

Fig. A5.18. Results of fabric and grain size (sieved) measurements for section T2S2. The sampling number for each measurement is 20, and the a-axes of the clasts were measured except for FA4 where the clast b-axes were measured.

Table A5.8. Results of fabric measurement for section T2S2.

	Eigenvector	Orientation	Dip	S	K
FA1	1	57.9	8.5	0.42	0.59
	2	317.4	50.7	0.34	
	3	154.6	38.1	0.24	
FA2	1	215.9	9.2	0.52	0.10
	2	348.2	76.5	0.42	
	3	124.3	9.8	0.06	
FA3	1	229.8	17.3	0.62	1.09
	2	321.3	4.9	0.26	
	3	66.4	72.0	0.1161	
FA4	1	207.2	4.3	0.59	0.29
	2	77.7	83.3	0.35	
	3	297.6	5.1	0.06	
FA5	1	213.0	7.0	0.69	0.69
	2	29.8	83.0	0.25	
	3	123.0	0.4	0.06	

Section T2S3

This section has an exposed thickness of ~ 15 m. A composite sedimentary log was constructed from different parts of the exposure outcrop to represent the section (Fig. A5.19a,k). Detailed features of the sedimentary units are shown in Fig. A5.19b–j. Broadly, this section is composed of lithofacies Fm, Gci, Gmm, Gh and Gh'.

The Fm units are shown as thin planar units (10 cm) which are intercalated between gravelly sediments and usually pinch out laterally (Fig. A5.19a). It occurs at the sections 0 - 0.2 m, 2.9 - 3.2 m, 4.2 - 4.4 m, 4.5 - 4.6 m, 4.7 - 4.8 m, 5.9 - 6.0 m, 6.5 - 6.6 m, 8 - 8.1 m, 9.4 - 9.6 m, and 15-15.3 m (Fig. A5.19k). The unit base is usually gradational, and sediment drapes the underlying gravely sediments. The unit surface is flat. Usually, some granules are present in the unit.

The Gh units are present at sections 0.2 - 2.8 m, 4.4-4.5, 4.6-4.7, 4.8-5.9 and 10.4 - 15.3 m (Fig. A5.19a). These sediments usually formed thick units with

crude stratifications (Fig. A5.19b, e, f and j).

The Gci units are present at section 3.2 - 4.2 m (Fig. A5.19k). It has two sub-units (Fig. A5.19c, d), each with a thickness of 0.5 m. In each sub-unit, granule- or pebble-sized clasts are in the unit base, and the clast size increases gradually upwards forming an inverse grading (Fig. A5.19c). Clasts at the upper part of each unit have variable dipping angles from 0˚ to 70˚; while clasts at the base of each unit have shallow dips. More silts are present in the upper than in the lower part of the unit, and on the top of the unit gravelly sediments are gradually changed into silt (Fig. A5.19c). The bed base is usually flat, while the bed surface is undulatory.

The Gcm units are present at section 6 - 9.6 m (Fig. A5.13k). They form ~ 5 sub-units which are separated by thin layers (5 - 10 cm) of silt (Fig. A5.19g, h). The sediments are poorly sorted pebble- to cobble-sized clasts. Usually large clasts (cobbles to boulders) develop variable dips and orientations with a weak a (p) fabric (Fig. A5.19g, h). The base of each unit is paved with imbricated gravels, and the top is draped by massive fine silt.

The Gh' unit is present at the section 9.6 - 10.4 m (Fig. A5.19k, i). The unit is formed by well sorted well-bedded granule-sized clasts with some sandy matrix. These sediments overly an erosional surface (Fig. A5.19i).

Fig. A5.19. Sedimentary characteristics of section T2S3. a. The outcrop face where section T2S3 was logged. b, c, d, e, f, g, h, i, and j are the places which are shown in close-up photographs. k. Sedimentary log of section T2S3. (Continued overleaf).

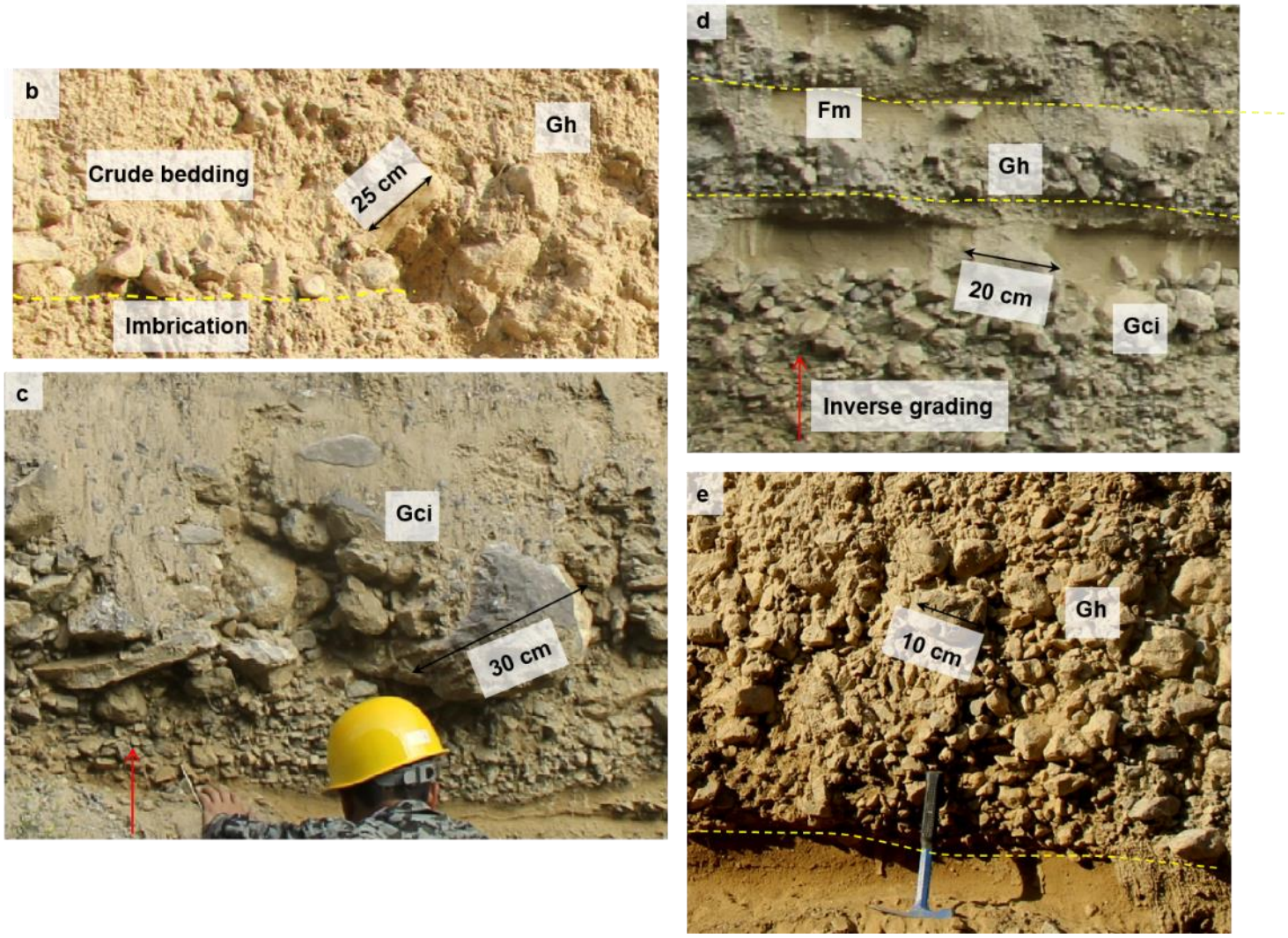

Fig. A5.19. Sedimentary characteristics of section T2S3 (continued overleaf).

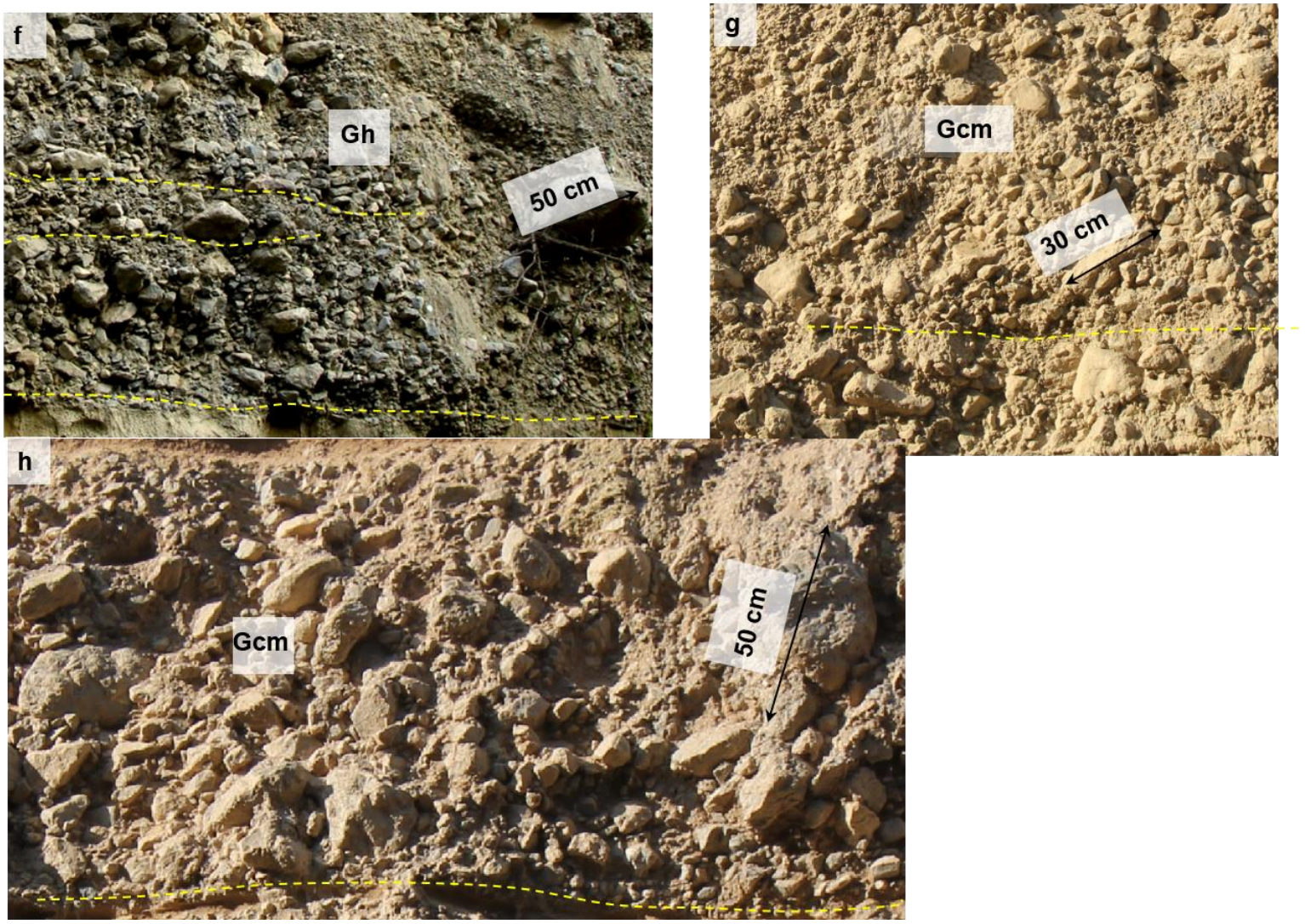

Fig. A5.19. Sedimentary characteristics of section T2S3 (continued overleaf).

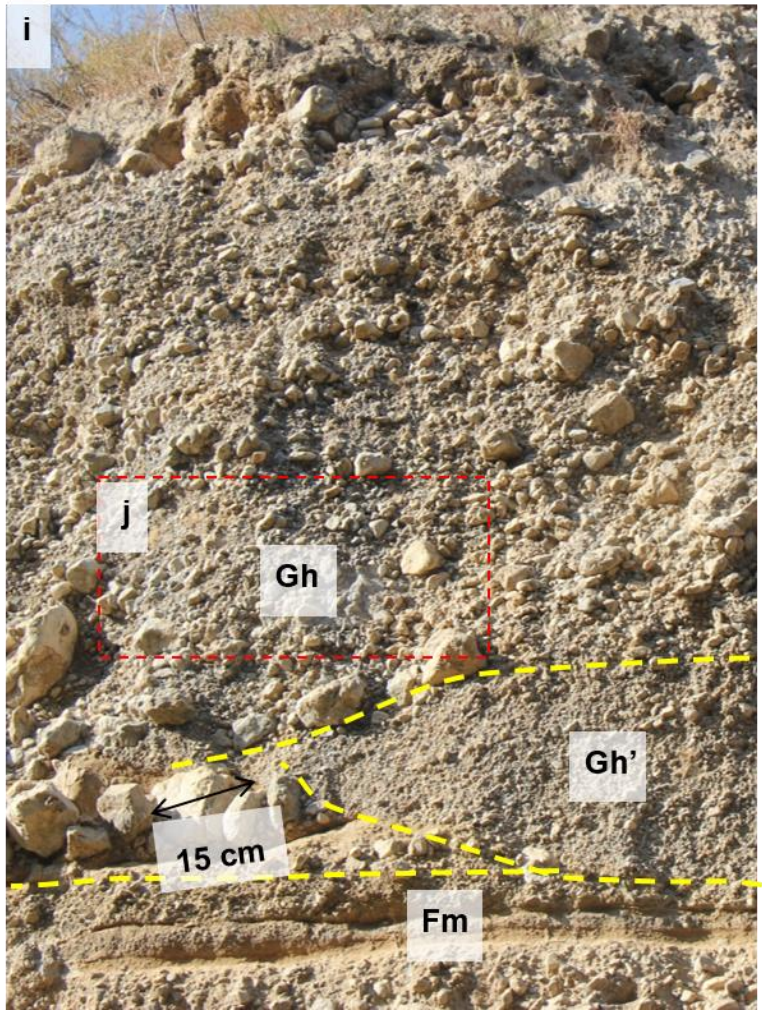

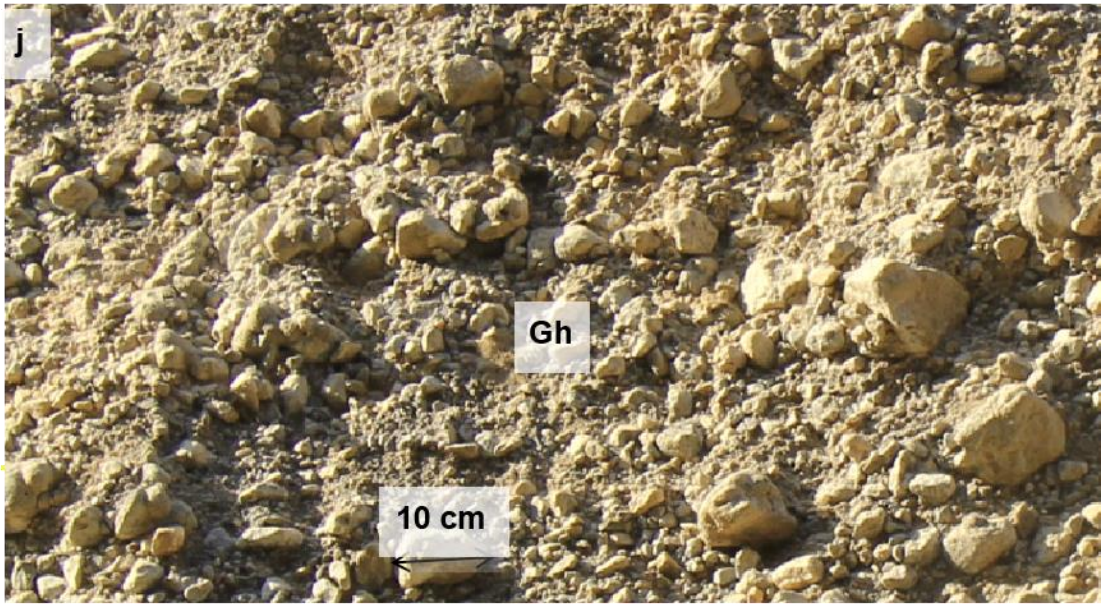

Fig. A5.19. Sedimentary characteristics of section T2S3.

.

Section T2S4

Section T2S4 is located at an incised T2 terrace (Fig. A5.20). The terrace here has been incised into two planes, and section T2S4 is located at the edge of the lower plane (Plane 2 in Fig. A5.20), and the exposure is 10 m thick.

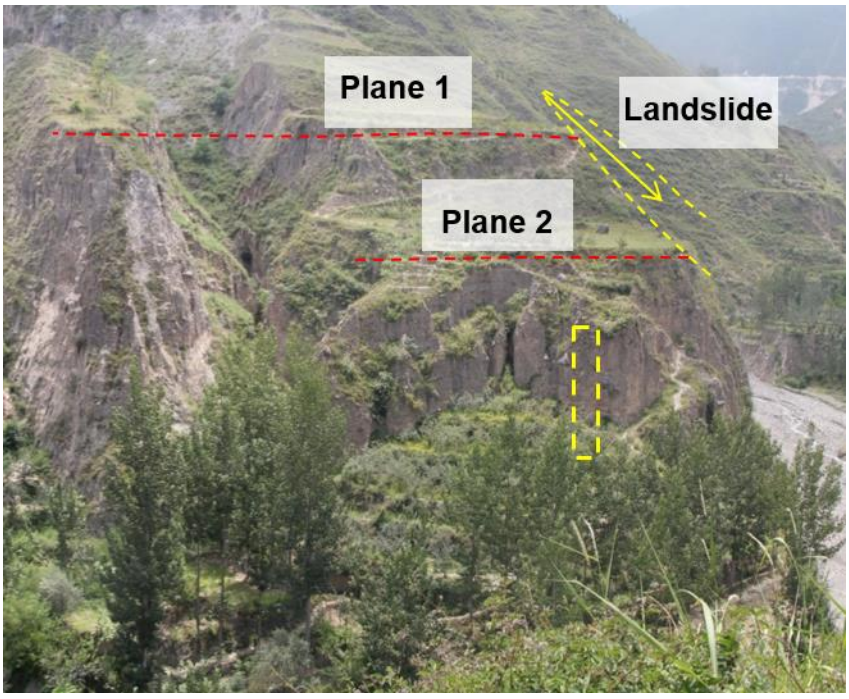

Fig. A5.20. Relative location of section T2S4

The sedimentary characteristics of section T2S4 is displayed in Fig. A5.21. The grain sizes of some exposures (Fig. A5.21 b) were measured using the software Nano measurer 1.2, and the results are displayed in Fig. A5.22.

The section has an exposed thickness of 10 m. The clasts that form the section are mainly angular to sub-angular limestones. Clasts surfaces in this section are generally coated by a dark varnish (Fig. A5.21a). The lithofacies present in this section include Gcm, Gci, Gh and Fm.

The Gcm sediment are present at sections 0 - 1.4 m, 2.5 - 3.6 m, and 3.7 - 7.8 m

(Fig. A5.21b). The clasts are mainly pebble- to cobble-sized clasts, and some large boulders are present in these units (Fig. A5.21a). The clasts usually formed weak a (p) fabrics (Fig. A5.21c, e and f). The base of each unit is usually flat without clear imbrications, and the unit surface is undulatory (Fig. A5.21c, e and f).

The Gci sediments are present at sections 1.5 - 1.9 m and 3.1 - 3.6 m (Fig. A5.21b). A variety of dips and orientations exist in the upper part of each unit (Fig. A5.21d, e). The clasts in the upper part of each section are mainly cobbles, while the clasts in the lower part are mainly pebbles. This vertical variation of clast size indicates an inversely graded structure. The bed base is flat (Fig. A5.21d, e). The bed surface is undulatory, which is covered by a thin layer (~ 10 cm) of silt (Fm).

The Gh sediments are present at section 7.8 - 10 m (Fig. A5.21b, g). Several horizontal beddings are present in the sediments (Fig. A5.21g).

The Fm sediments are present at sections 0.9 - 1.0 m, 1.8 - 2.0 m, and 3.6 - 3.7 m (Fig. A5.21a, b), which are displayed as thin layers of fine silts. These fine silts are compact and are harder than the massive silt present in the other T2 terraces.

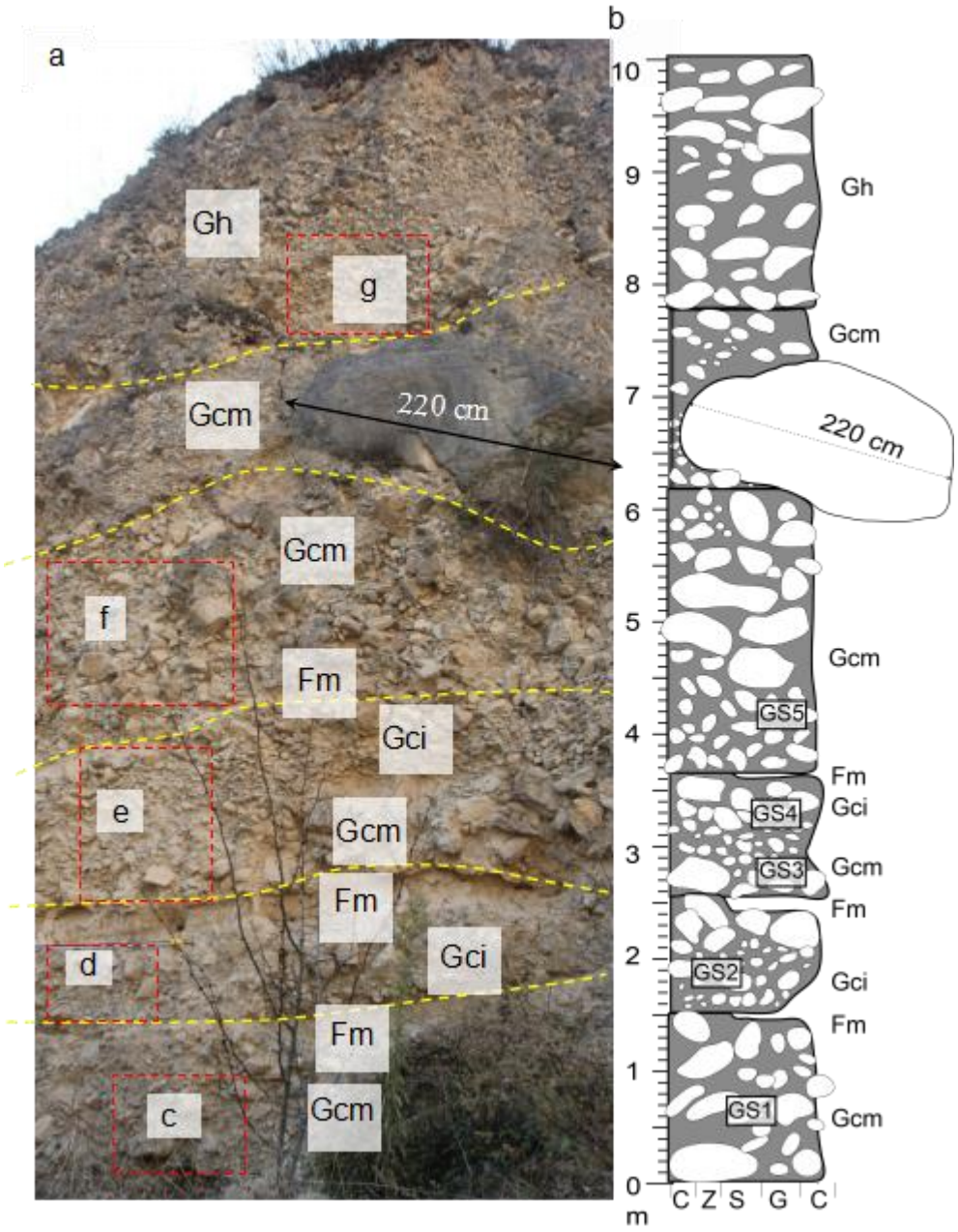

Fig. A5.21. Sedimentary characteristics of section T2S4. a. Photograph of section T2S4. b. Sedimentary log of section T2S4. c, d, e, f and g are places which will be shown in close-up photographs. Dashed yellow lines delineate different sedimentary units. (Continued overleaf)

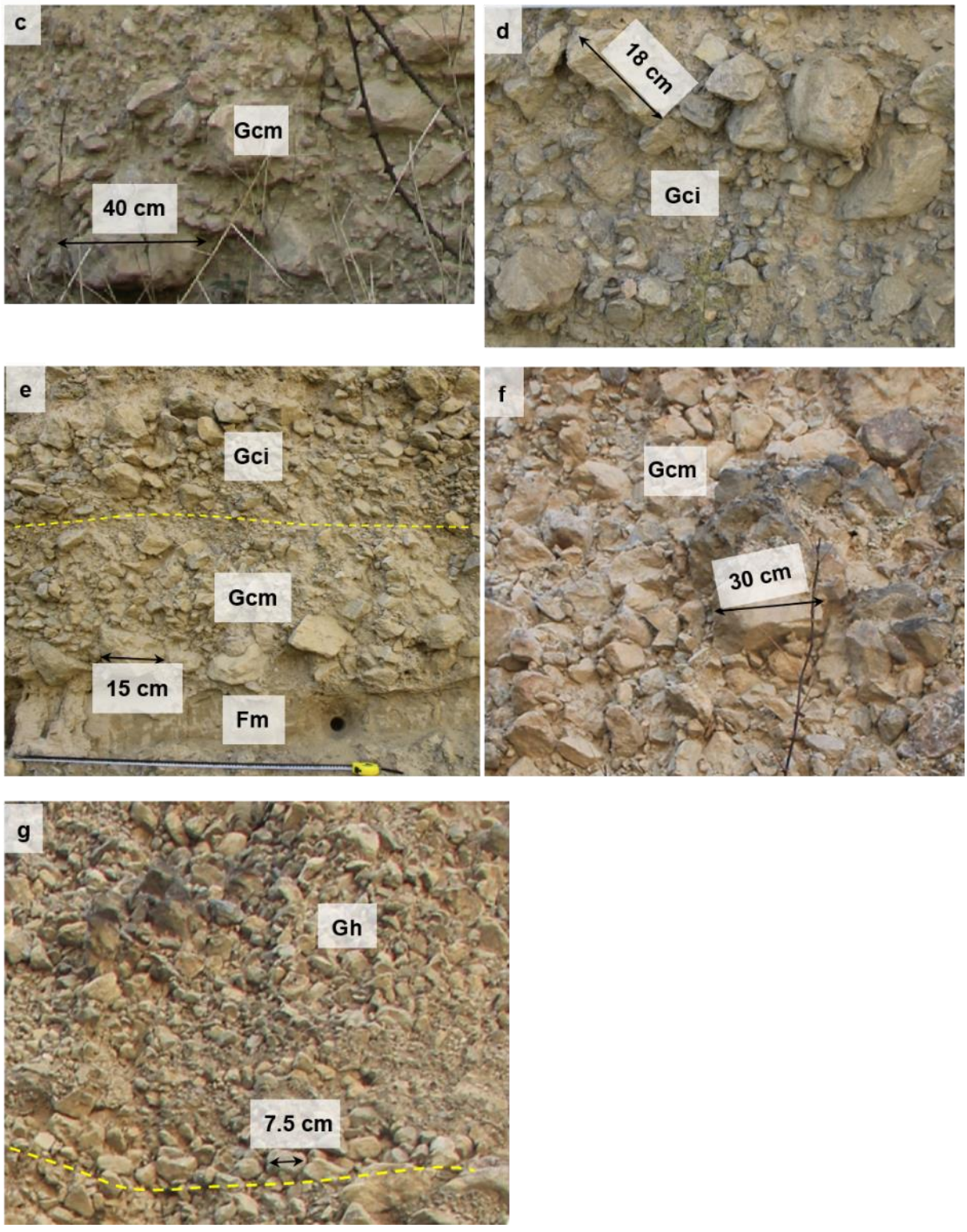

Fig. A5.21. Sedimentary characteristics of section T2S4. Close-up photographs of c, d, e, f and g.

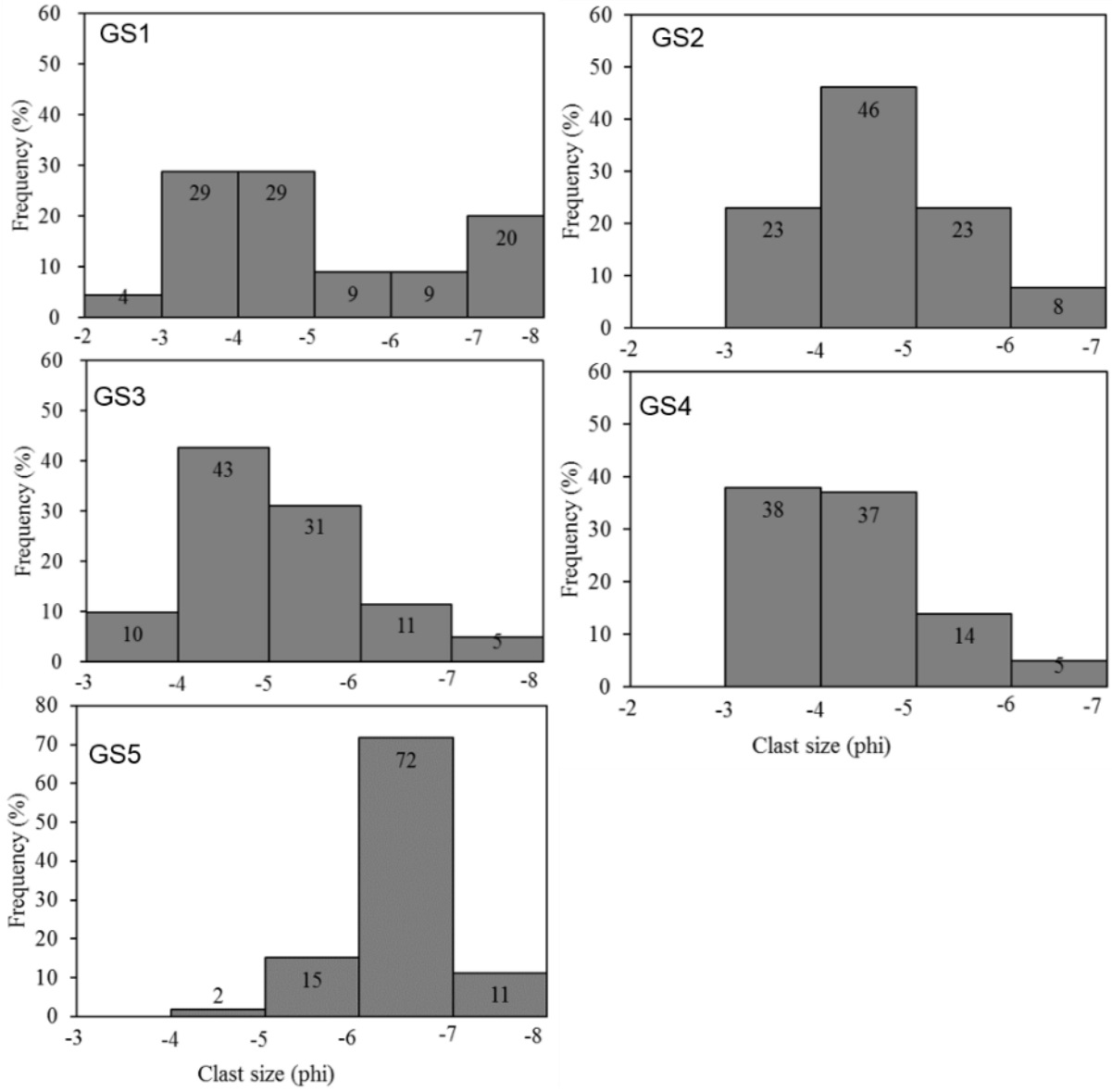

Fig. A5.22. Grain size distribution of the clasts at section T2S4 by Nano measurer 1.2.

Section T1S1

Section T1S1 is close to the fault of the GLP valley. Here, the alluvial sediments rest on the phyllite bedrock, which is higher than the surface of the T2 terrace (Fig. A5.23). The T1 terrace has been largely eroded leaving steep cliffs and few flat surfaces (Fig. A5.23). Since most T1 terrace profiles are inaccessible, only two sub-sections (T1S1_A and T1S1_B in Fig. A5.23) were available for detailed analyses. The detailed sedimentary characteristics of the two sections are present in Figs. A5.24 and A5.25.

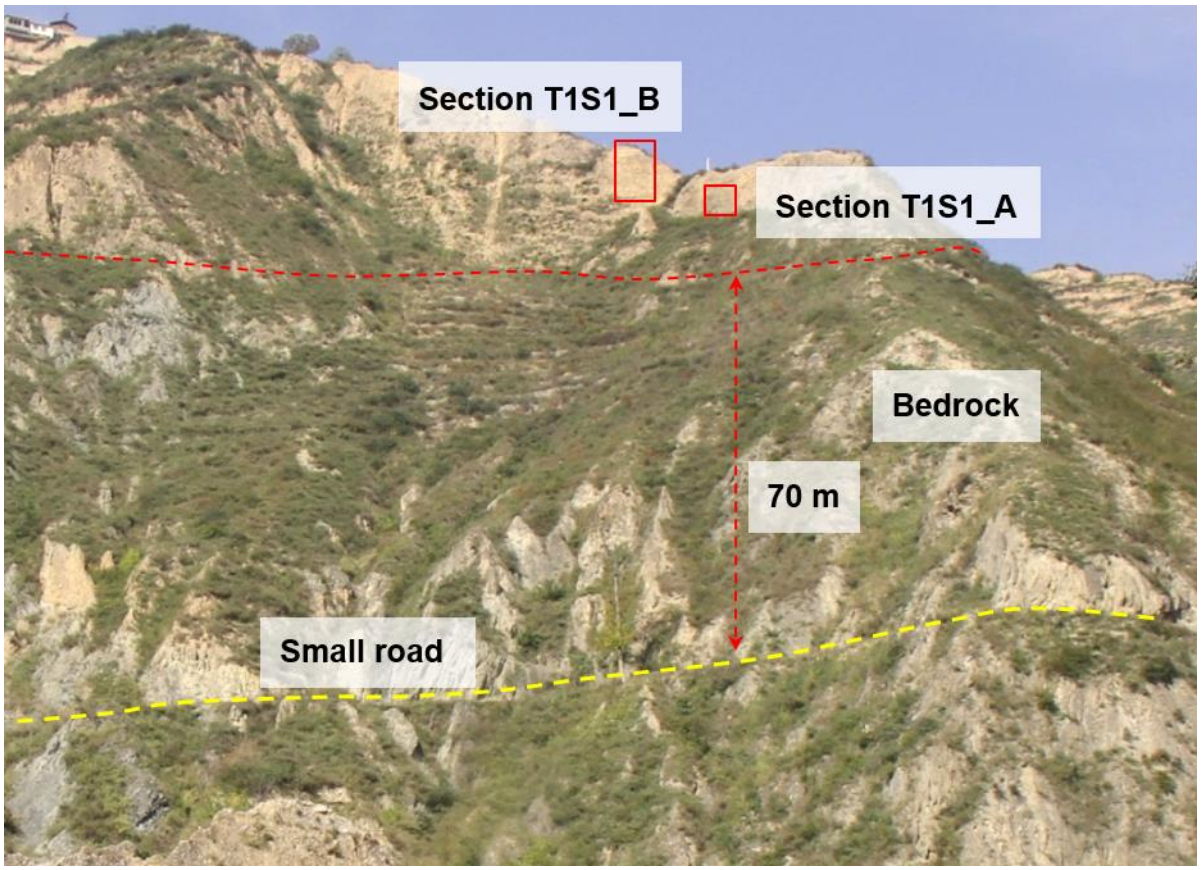

Fig. A5.23. Location of section T1S1, which is composed of two subsections: Section T1S1_ A and Section T1S1_B.

Section T1S1_A is selected because of its exposed face is clear and can be accessed. The logged section is only 1 m thick and is composed of lithofacies Gci and Gh' (Fig. A5.24).

The Gci sediments occur at section 0 – 0.42 m and 0.5 – 1 m (Fig. A5.24b). In each unit, clasts are mainly angular to sub-angular pebble- to cobble-sized limestones without phyllite. The clasts are inversely graded with the finer clasts distributed in the lower section and the coarser clasts in the upper section (Fig. A5.24a). The clasts develop weak fabrics with various dips and orientations, especially in the upper part of each unit (Fig. A5.24a). The Gh' sediment is in section 0.42 – 0.5 m (Fig. A5.24b), which is intercalated between the two Gci units. Clasts at this section are mainly well-bedded pebbly limestones (Fig. A5.24a).

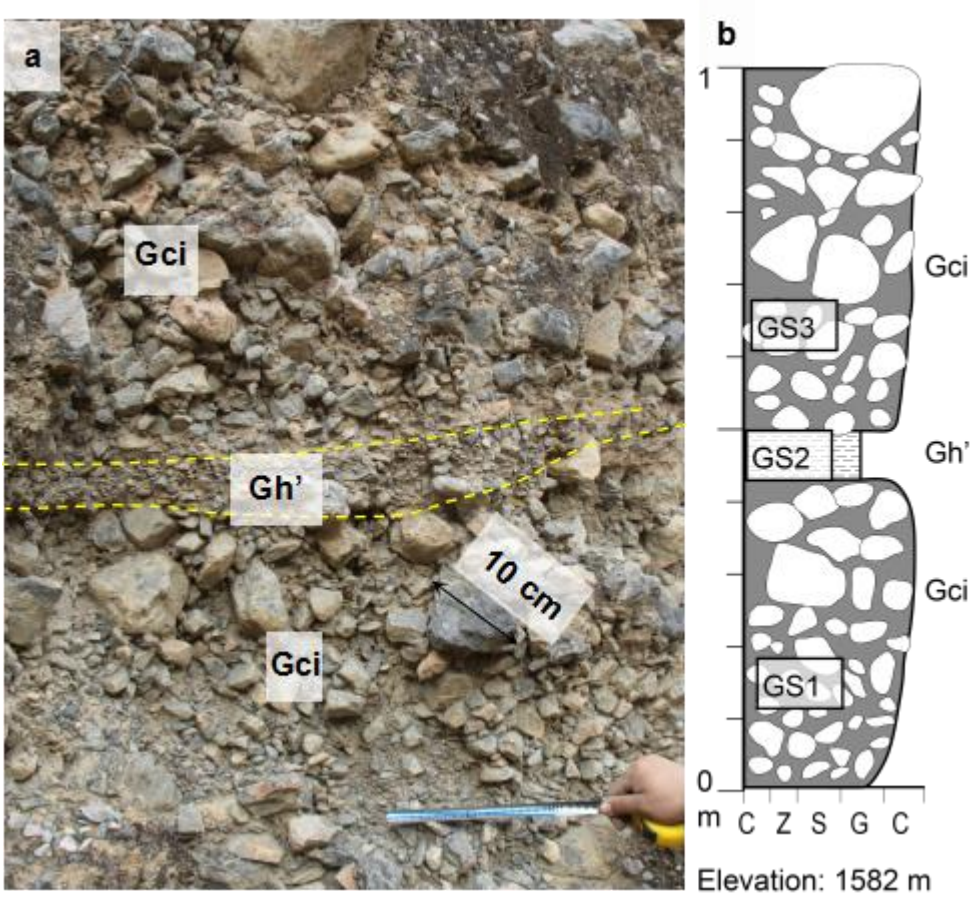

Fig. A5.24. Sedimentary characteristics of section T1S1_A. a. Photograph of section T1S1_A. b. Sedimentary log of section T1S1_A.

Section T1S1_B has an exposed thickness of 14 m (Fig. A5.25b), and it is formed by four types of sediments: thin massive silt (Fm), thick relatively homogeneous silt (Fm'), massive clast-supported pebble- to cobble-sized clasts (Gcm) and inversely graded clast-supported pebble- to cobble-sized clasts (Gci).

The Gci sediments are present at sections 0 – 1.3 m, 1.8 – 3.7 m, and the Gcm sediments are present at sections 10 - 12.5 m and 12.7 – 13.9 m (Fig. A5.25). Clasts of these two types of lithofacies both are poorly sorted angular to sub-angular limestones and develop weak fabrics with various dips and orientations (Fig. A5.25b). Clasts in the Gci sediments are inversely graded, while clasts in the Gcm sediments are massively distributed with no grading and stratification. The two units of Gci sediments are each capped by a layer of homogeneous silt (Fm'), while the two units of Gcm sediments are each capped by a layer of massive silt (Fm) (Fig. A5.25)

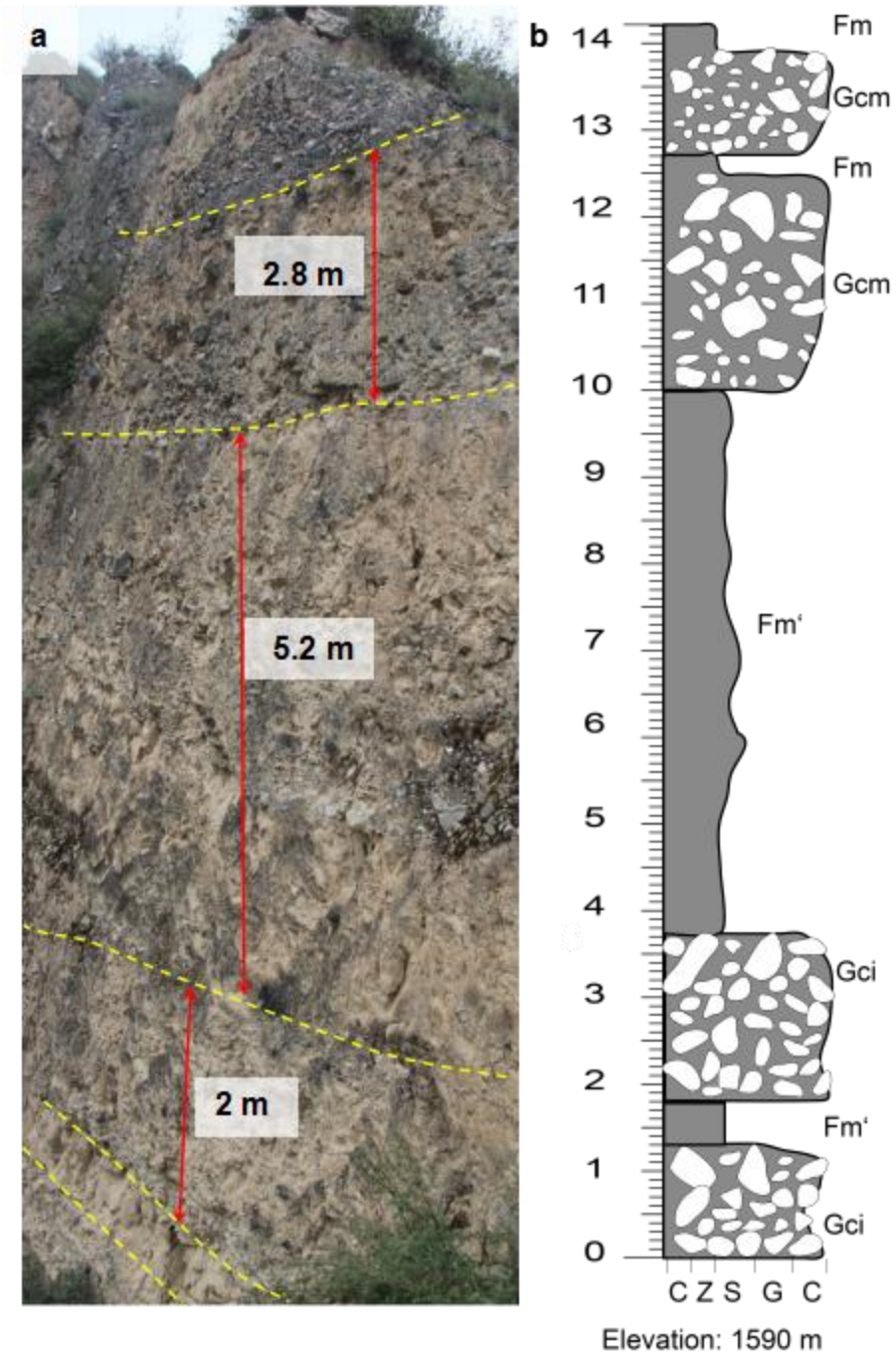

Fig. A5.25. Sedimentary characteristics of section T1S1_B. A. Photograph of section T1S1_B. B. Sedimentary log of section T1S1_B.

Section T1S2

Section T1S2 is located near the top of a T1 terrace in the midstream portion of the GLP valley (Fig. A5.26). The exposed thickness of the section is only 2.5 m. Detailed sedimentary characteristics is displayed in Fig. A5.27. The clast size

was measured using the software ‘Nano measurer 1.2’, and the result is displayed in Fig. A5.28.

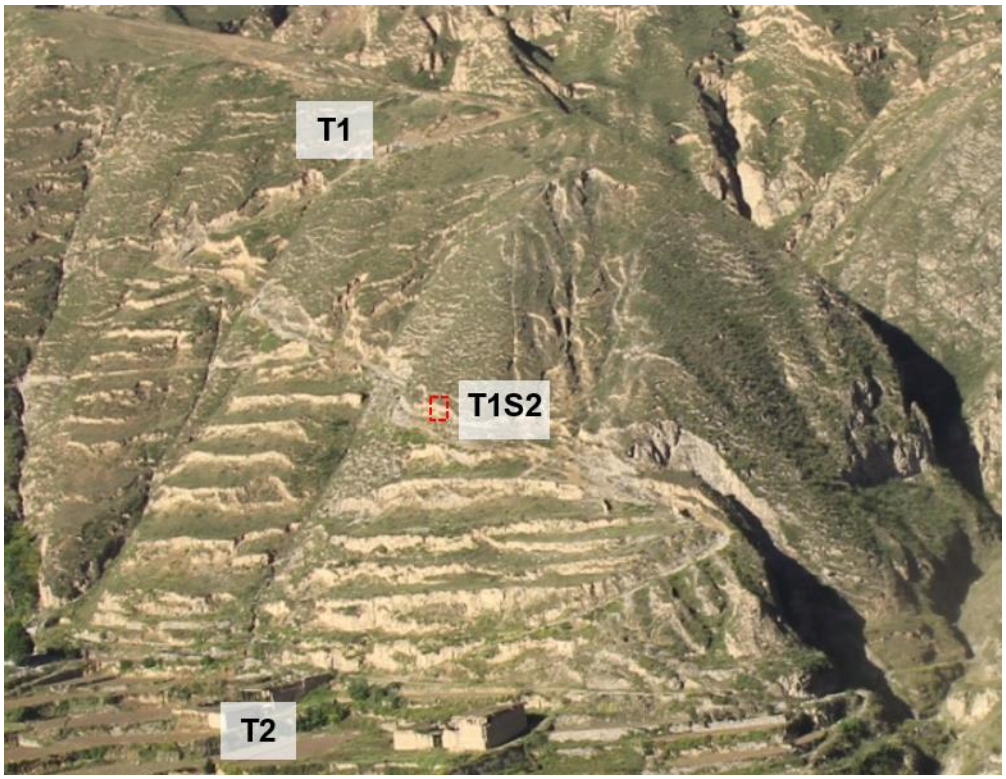

Fig. A5.26. Location (red box) of section T1S2.

This section is composed of lithofacies Gh, Gmm and Fm (Fig. A5.27). The Gh sediments are present at sections 0 – 0.3 m and 0.3 – 0.45 m. For each of the unit, the base is paved with imbricated clasts (Fig. A5.27a), while the upper part is formed by crudely bedded clasts. The Gmm sediments are present at sections 0.57 – 1 m, 1 – 1.15 m and 1.15 – 2 m. Sediments in these units are poorly sorted clast-to matrix-supported cobble clasts. Big boulders are present in these units (Fig. A5.27a), and these boulders generally dip with their a-b planes in shallow angles. Clasts close to each bed base are clast-supported, while clasts in the upper parts of each unit gradually changed to be matrix-supported. On top of each unit, a thin layer of massive silt drapes down the unit (Fig. A5.27 a).

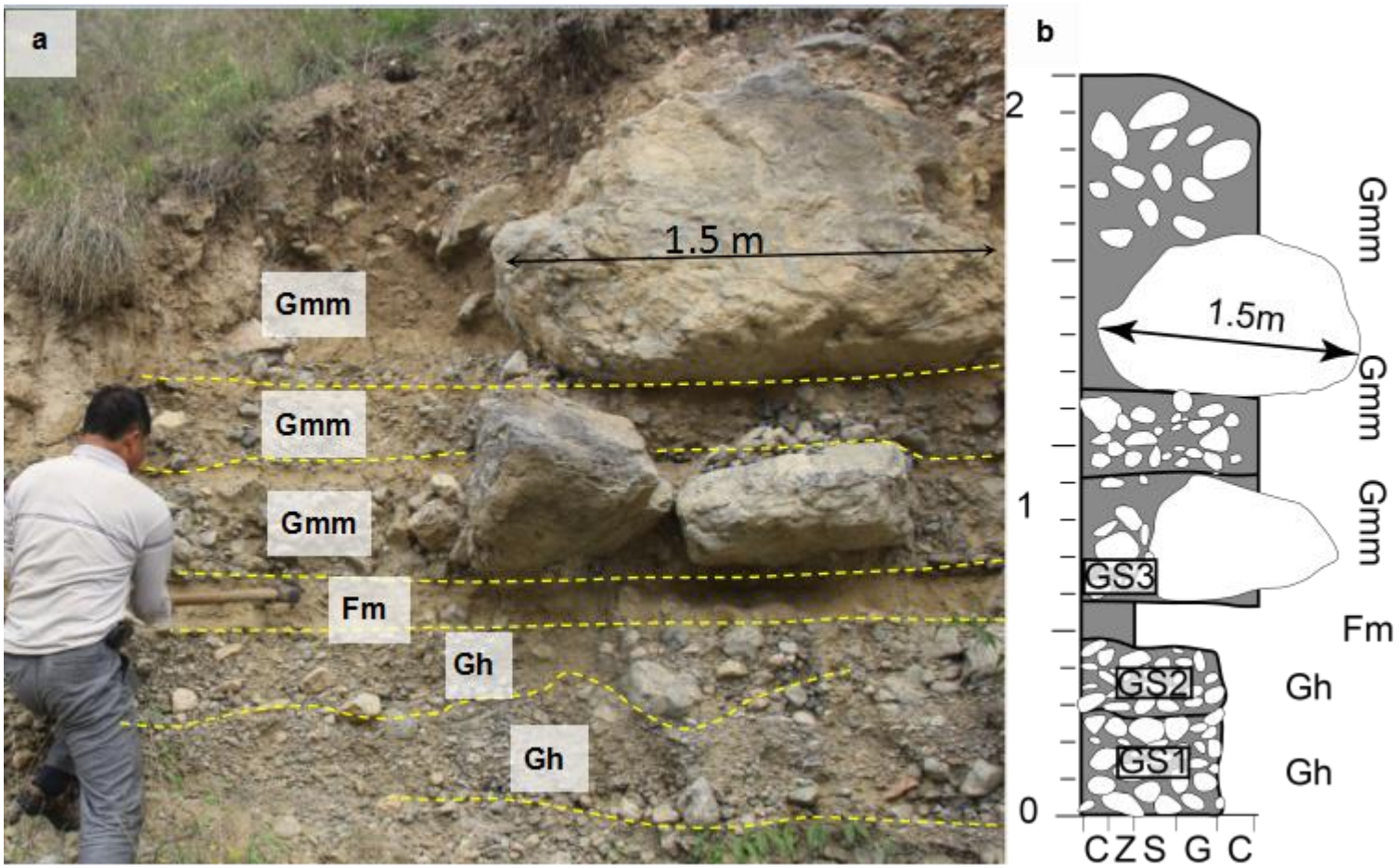

Fig. A5.27. Sedimentary characteristics of section T1S2. a. Photograph of section T1S2. The flow direction points into the page. b. Sedimentary log of section T1S2.

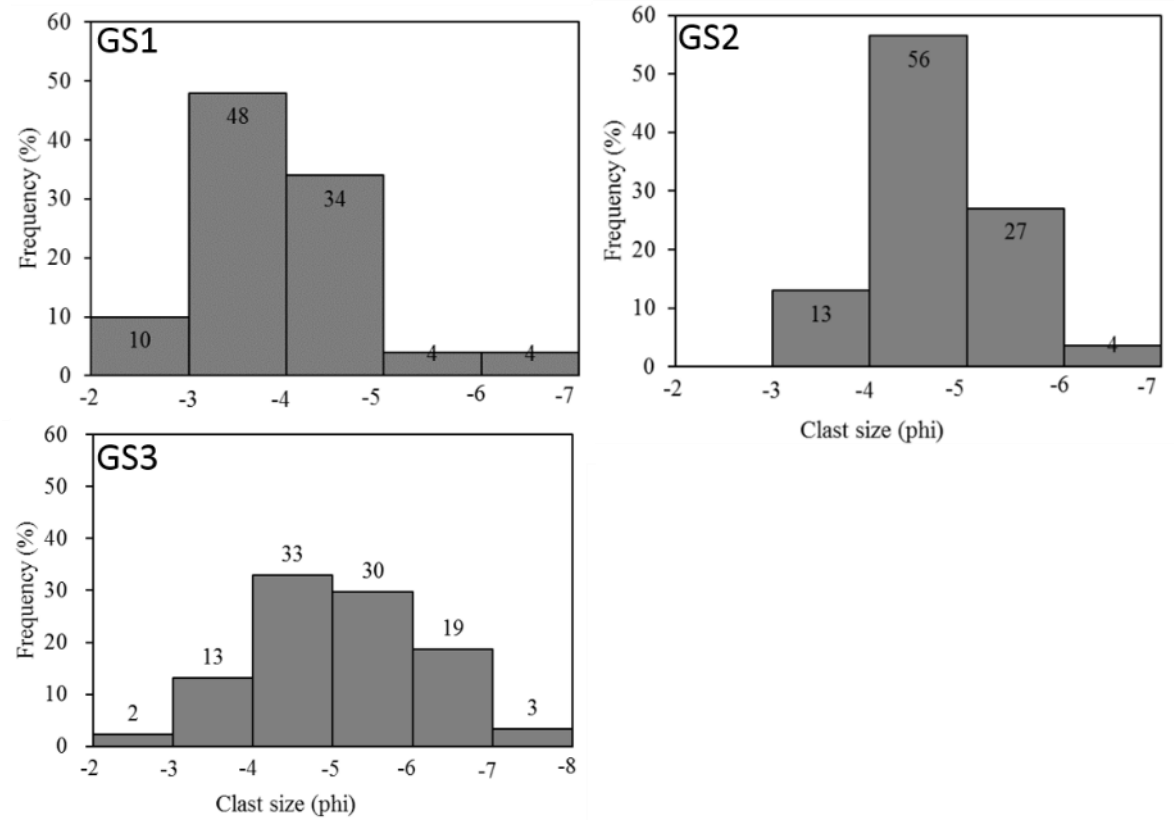

Fig. A5.28. Grain size distribution of the clasts at section T1S2 by Nano measurer 1.2.

Section T1S3

The position of section T1S3 is shown in Fig. A5.29. The vertical scale of the section was measured using a portable laser rangefinder (PKI 3100). Section T1S3 starts from the elevation of 1148 m, which is at the contact between the phyllite bedrock and the alluvial materials (Fig. A5.29). The whole thickness of the profile is 72 m. It is composed of three distinct parts. The lower part (1148 – 1173 m elevation) is composed of well-rounded clasts with sandy matrix, the middle part (1173 – 1206 m elevation) is formed by sub-angular to sub-rounded clasts with silty matrix, and the upper part (1206 – 1220 m elevation) is comprised of aeolian loess. The sedimentary characteristics of the gravelly sections (the lower and the middle parts) are examined by three sections. Section T1S3_A (1148 – 1156 m elevation) is composed of well rounded pebbles with sandy matrix;

Section T1S3_B (1169 – 1175 m elevation) is composed of both well rounded and sub-rounded pebbles. Section T1S3_C (1198 – 1201 m elevation) is composed of sub-rounded pebbles with silty matrix.

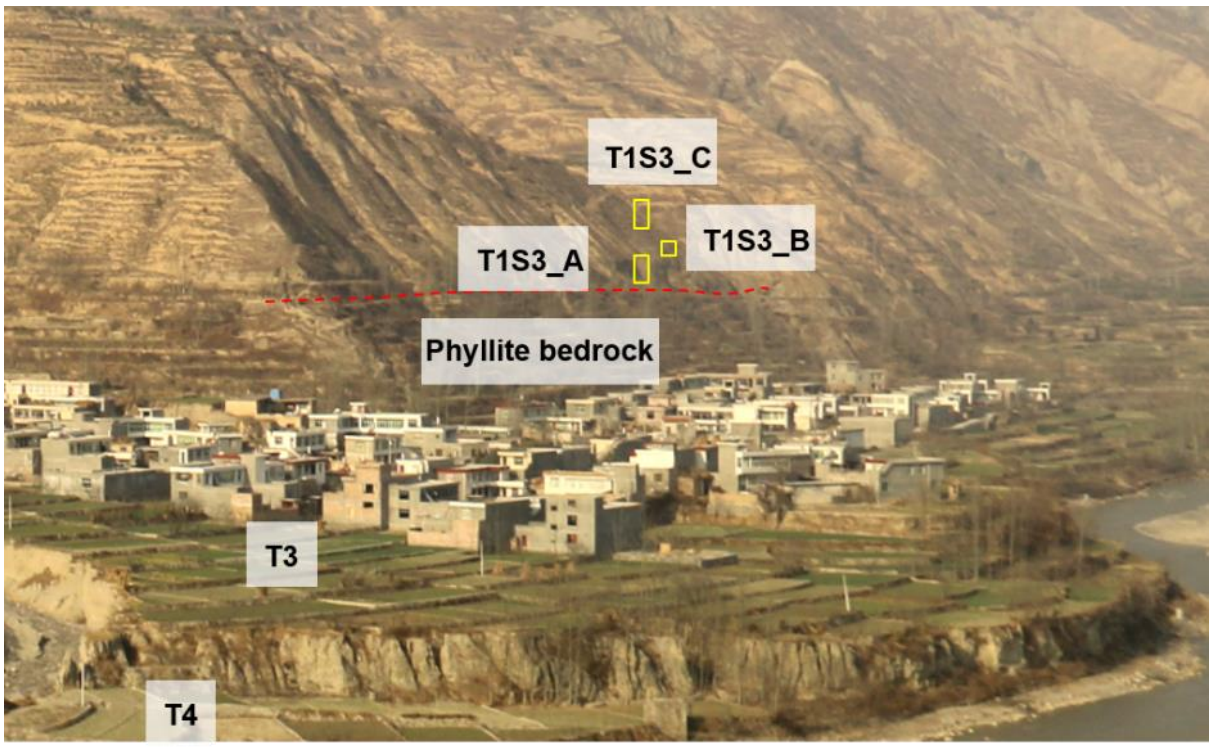

Fig. A5.29. Location of section T1S3. Dashed red line delineates the contact between the phyllite bedrock and the overlying alluvial sediment. Yellow boxes delineate the three sub-sections.

Section T1S3_A is in the basal part of section T1S3. It stands as a vertical cliff with an exposure thickness of ~ 8 m (Fig. A5.30). Two measurements of grain sizes were conducted for this section (Fig. A5.30b), and the results are displayed in Fig. A5.31.

Clasts in this section are generally rounded to well rounded. Except limestones and phyllites, sandstones and granites which are exotic to GLP, are present in the sediments. The section is generally formed by two types of lithofacies: (1) the moderately sorted well bedded granule- to pebble-sized clasts with sandy matrix (Gh (r)') and (2) the poorly sorted crudely bedded pebble-sized clasts with sandy matrix (Gh (r)). The Gh (r)' sediments form sections 0 – 0.8 m and 0.8 – 1.9 m (Fig. A5.30). In each of the unit, the clasts are aligned with their a-b planes horizontally forming planar beddings (Fig. A5.30a). Both the top and base of each unit are flat. The amount of the sandy matrix increases upward in each unit, and at the unit top, stratified sands are present (Fig. A5.30a). The Gh (r) sediment forms the remaining part of the section. The unit is composed of poorly sorted clast-supported cobble- to pebble-sized clasts with sandy to silty matrix. The base is occupied by imbricated cobble-sized clasts with their b-axes mostly parallel to the flow direction (Fig. A5.30a). The amount of matrix increases upwards (Fig. A5.30a).

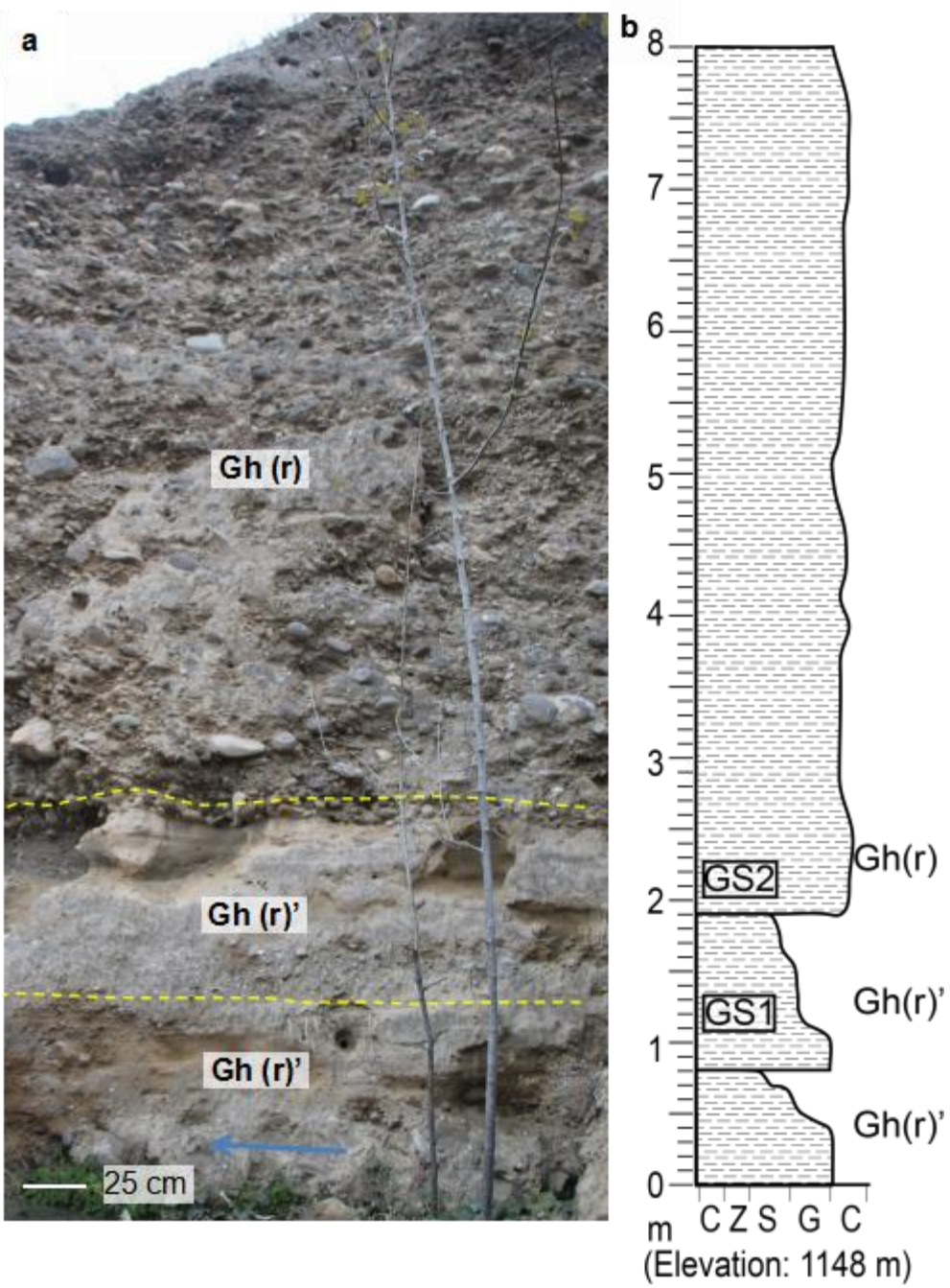

.

Fig. A5.30. Sedimentary characteristics of section T1S3_A. a. Photograph of section T1S3_A. b. Sedimentary log of section T1S3_A

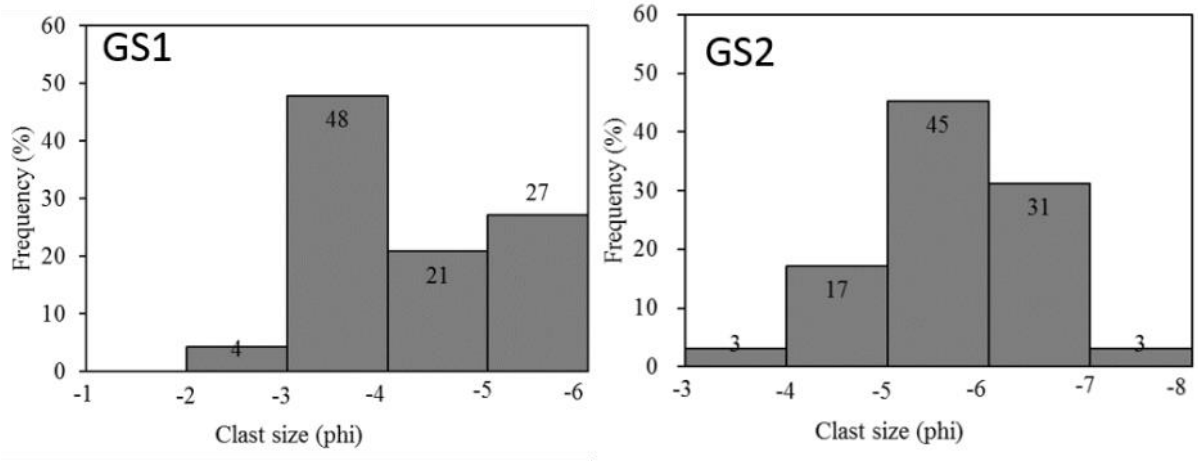

Fig. A5.31. Grain size distribution of the clasts at section T1S3_A by Nano measurer 1.2.

Section T1S3_B is present above section T1S3_A. The sedimentary characteristics are present in Fig. A5.32. At some locations with good exposure (Fig. A5.32a), the grain sizes were measured using Nano measurer 1.2, and the results are displayed in Fig. A5.33. The section is formed by lithofacies Sh, Gh, Gh', and Gh (r).

The Sh sediments occur in sections 0 – 1.1 m, 1.4 – 1.55 m and 3.3 – 3.9 m. In the middle part of section 0 – 1.1 m (Fig. A5.32a, b), a thin layer (15 cm) of rounded granule to pebbly clasts (Gh') is present. The lithology of these clasts is dominated by limestone and quartzite.

The Gh' sediments are present in sections 1.1 – 1.4 m and 1.55 – 1.7 m (Fig. A5.32a). These units are composed of well sorted well-bedded granule to pebble clasts with sandy matrix (Fig. A5.32c). The clast lithology is dominated by limestones, and clasts are sub-rounded to rounded. The clasts in each of the unit are normally graded (Fig. A5.32c).

The Gh sediments are present in sections 1.7 – 2.3 m and 3.9 – 6.2 m (Fig.

A5.32a). In each of the unit, the clasts are poorly sorted sub-rounded to rounded pebbly clasts. Limestone form the primary lithology of these clasts. The sediments are crudely bedded in these units (Fig. A5.32c, d).

The Gh (r) sediments are present in section 2.3 – 3.3 m (Fig. A5.32a). The sediments are formed by poorly sorted rounded to well rounded crudely bedded sandy-matrix-supported pebbly clasts (Fig. A5.32d). The clasts lithology includes limestone, phyllite, sandstone and quartzite.

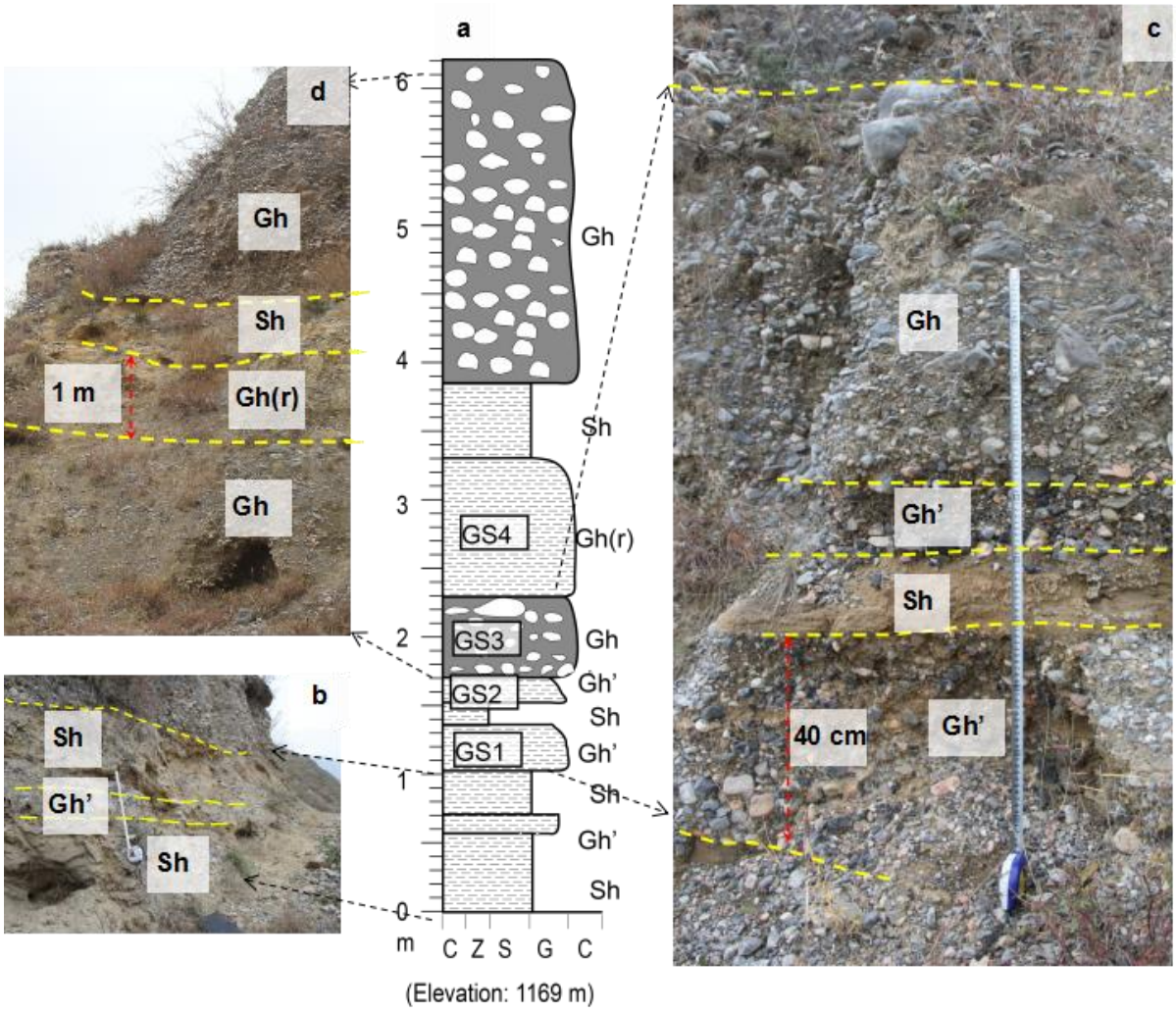

Fig. A5.32 Sedimentary characteristics of section T1S3_B. a. Sedimentary log of section T1S3_B. b, c and d. Photographs showing the details of different units.

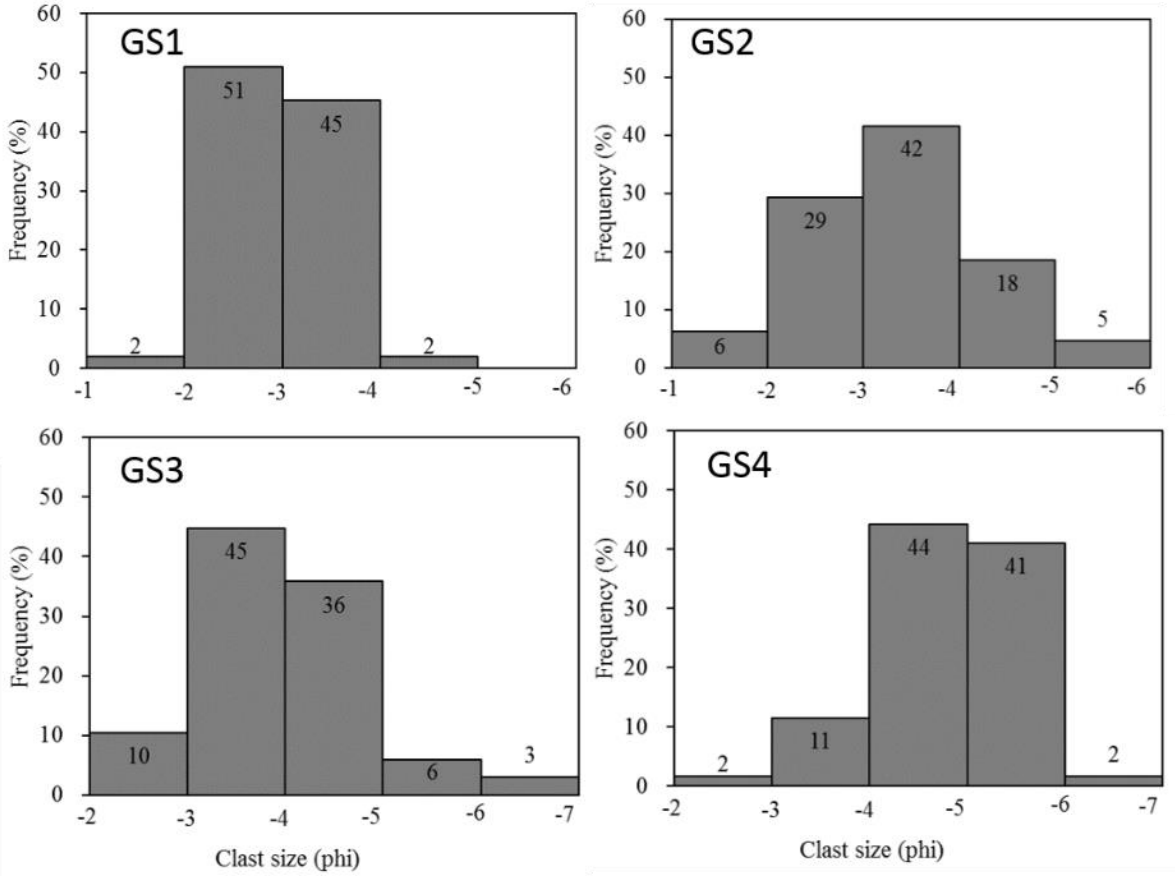

Fig. A5.33. Grain size distribution of the clasts at section T1S3_B by Nano measurer 1.2.

Section T1S3_C is 3.2 m thick, and the sedimentary characteristics are displayed in Fig. A5.34. Four measurements of grain sizes were conducted using “Nano measurer 1.2”, and the results are shown in Fig. A5.35.

The section was formed by lithofacies Gh’, Gcm, Gh and Fm (Fig. A5.34). The Gh’ sediments are present in section 0 – 0.2 m (Fig. A5.34b). This unit is composed of well sorted well-bedded pebble-sized clasts (Fig. A5.34a). The clasts are mainly sub-rounded limestones with some quartzites and are normally graded. The Gh sediments are present in sections 0.2 – 1.15 m and 1.25 – 2.5 m. These sediments are composed of poorly sorted clast-supported pebbly clasts with silty matrix (Fig. A5.34a). The clasts are mainly sub-rounded limestones with some quartzites. Each of the unit contains several sub-layers which are distinguished by a well-bedded imbricated layer, while the upper part of the layer contains crudely bedded clasts (Fig. A5.34a). The Gcm sediments are present at the top of the section (2.5 – 3.2 m, Fig. A5.34a). Sediments in this unit are poorly sorted clast-supported pebble clasts with silty matrix (Fig. A5.34a). The base of the unit is paved with large cobbles and boulders with their a-b planes imbricated. Clasts overlying the coarse sediments are smaller pebble- to cobble- sized clasts. At the unit top, a large boulder with an a-axis length of 80 cm is present. The amount of matrix increases from the unit base to the top, and clasts at the bed top are almost matrix-supported.

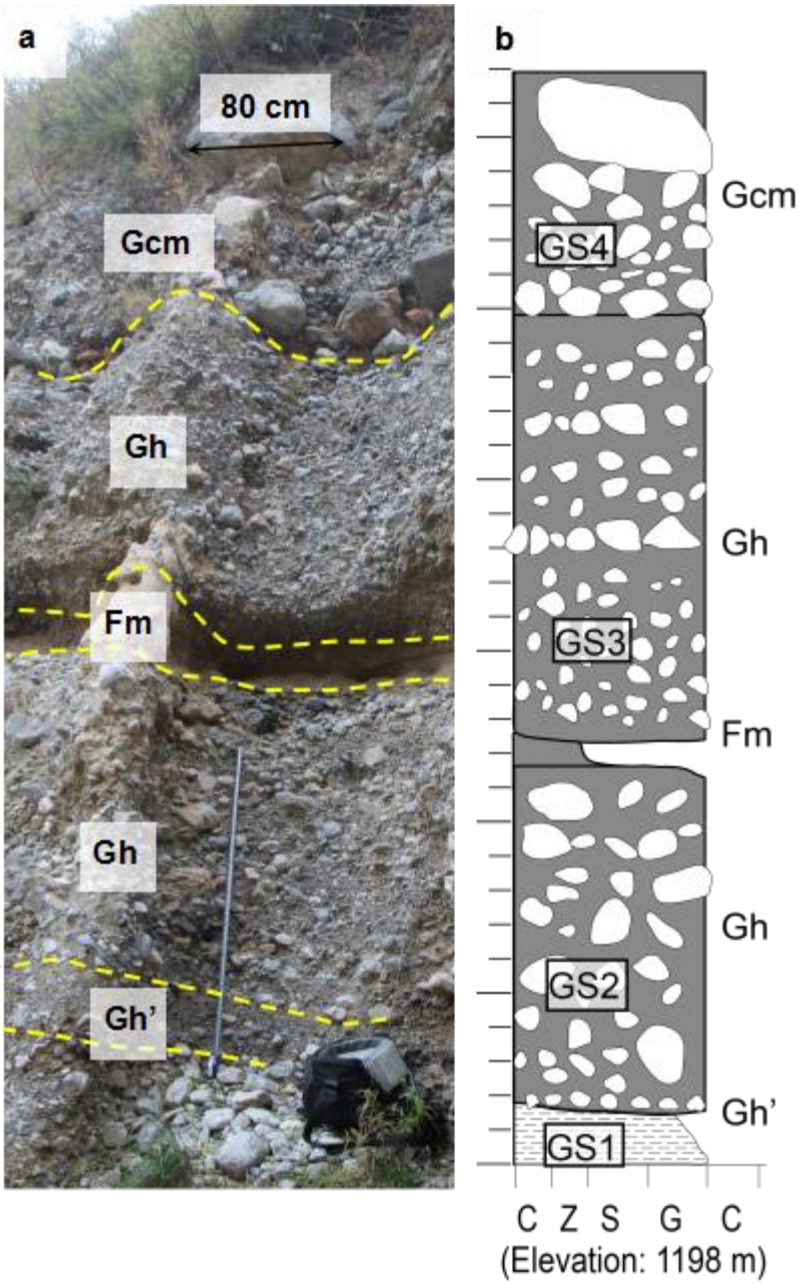

Fig. A5.34. Sedimentary characteristics of section T1S3_C. a. Photograph of section T1S3_C. b. Sedimentary log of section T1S3_C.

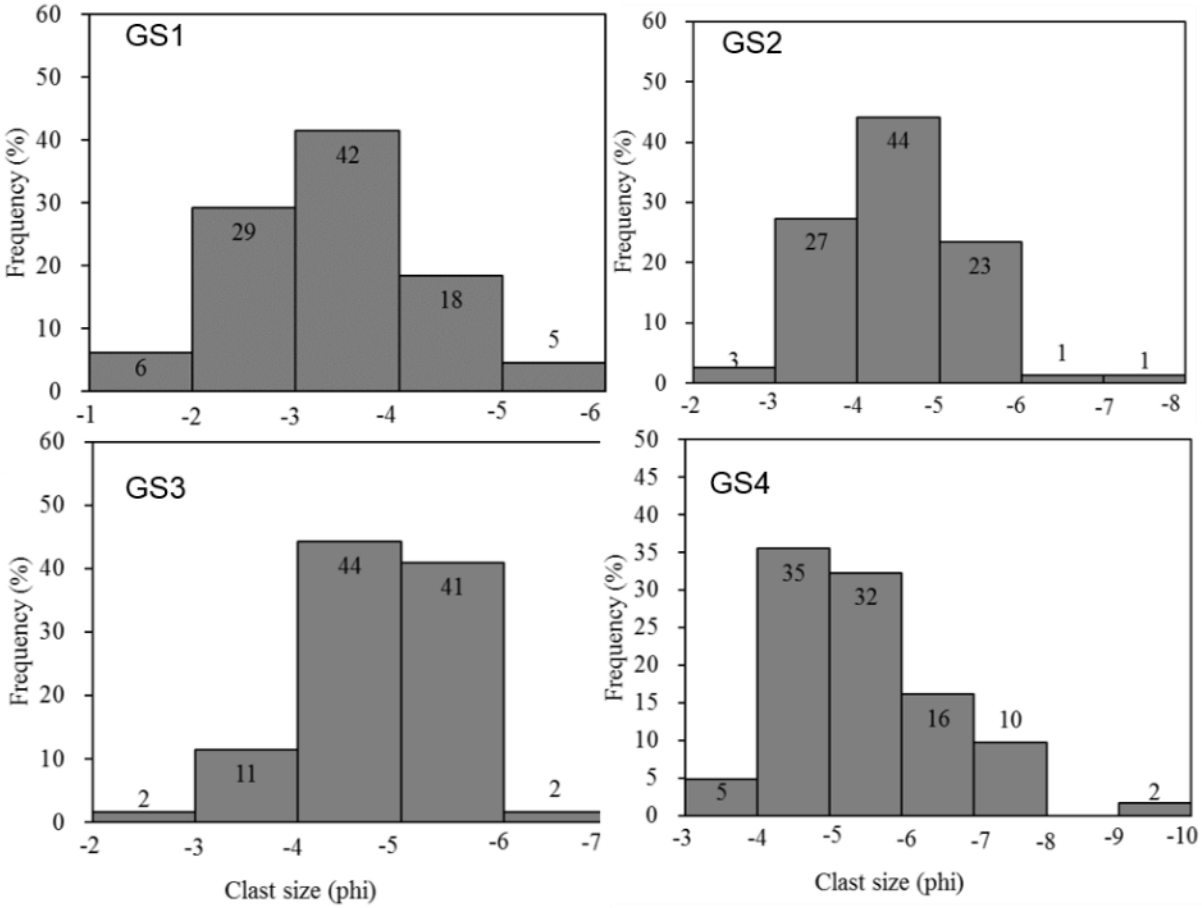

Fig. A5.35. Grain size distribution of the clasts at section T1S3_C by Nano measurer 1.2. The clast a-axes were measured

Appendix 6 Borehole Sedimentology

Table A6.1. Sedimentary characteristics of core D01 (section depth 0-34.4 m). Meaning of abbreviations: DGS = dominant grain sizes. Gr = granules; C = cobbles; P = pebbles; SA = sub-angular; SR = sub-rounded; WR = well rounded; R = rounded; PS = poorly sorted; MS = moderately sorted; WS = well sorted; VPS = very poorly sorted; L = limestone; P = phyllite; S = sandstone; Q = quartzite; G = granite; L&P means limestone and phyllite account for a relatively equal proportion in the sediment; L(P) means the sediment is dominated by limestone clasts with few phyllite clasts. L (P, S, G) means that the sediment is dominated by limestone clasts with some phyllite, sandstone and granite clasts. LFs = lithofacies. LFAs = lithofacies associations

Depth(m)	DGS	R	Sorting	Lithology	Matrix	LFs	LFAs
0-0.8	Gr	SA/SR	PS	L&P	sandy	Gr1	LFAc1
0.8-1	C	SA/SR	MS	L	no	C1	
1-3.9	P	SA/SR	PS	L(P)	silty	P1	
3.9-5	C	SA/SR	MS	L	no	C1	
5-6.6	P	SA/SR	PS	L(P)	silty	P1	
6.6-6.9	Gr	WR	WS	L(P)	sandy	Gr2	
6.9-8.9	C	SR	PS	L	silty	C1	
8.9-11	P	SR	PS	L(P)	silty	P1	
11-11.8	Gr	WR	WS	L&P&S&Q	sandy	Gr3	LFAc3
11.8-14.4	C	SA/SR	MS	L	silty	C1	LFAc1
14.4-15.4	P	R/WR	MS	L(P,S,G)	sandy	P3	LFAc3
15.4-15.7	Sand		WS		sandy	S1	
15.7–17.1	P	R/WR	MS	L(P,S,G)	sandy	P3	
17.1-18.8	C	SA/SR	MS	L	no	C1	LFAc1
18.8-19.3	P	SA/SR	PS	L(P)	silty	P1	
19.3-20	C	SA/SR	PS	L	no	C1	
20-22	Gr	SA/SR	MS	L(P)	no	Gr2	LFAc2
22-23.5	P	SA/SR	PS	L(P)	silty	P1	LFAc1
23.5-24. 7	Gr	SA/SR	WS	L(P)	sandy	Gr2	LFAc2
24.7-26	P	SA/SR	MS	L(P)	sandy	P2	
26-26.7	C	SA/SR	MS	L	sandy	C1	
26.7-30.6	P	SA/SR	PS	L(P)	silty	P1	LFAc1
30.6-30.8	Sand				sandy	S1	LFAc2
30.8-32	C	SR/R	MS	L	sandy	C1	
32-34	P	SR/R	MS	L(P)	sandy	P2	
34-35.4	C	SA/SR	PS	L	silty	C1	LFAc1

Table A6.2. Sedimentary characteristics of core D01 (section depth 35.4-62 m). Abbreviations follow the same meanings of those in Table A6.1

Depth(m)	DGS	R	Sorting	Lithology	Matrix	LFs	LFAs
35.4-36.5	P	R/WR	MS	L (P, S, G)	sandy	P3	LFAc3
36.5-36.9	Gr	R/WR	MS	L (P, S, G)	sandy	Gr3	
36.9-39	P	R/WR	WS	L(S)	no	P3	
39-40.7	Gr	R/WR	WS	L (S, P)	sandy	Gr3	
40.7-41.2	C	SA/SR	PS	L	silty	C1	LFAc1
41.2-46.2	P	R/WR	MS	L	sandy	P3	LFAc3
43.9-44.6	C	R/WR	MS	L(S,G)	sandy	C2	
44.6-46.2	P	R/WR	MS	L	sandy	P3	
46.2-46.8	Sand					S1	
46.8-48	Gr	WR	WS	L(S)	sandy	Gr3	
48-55	P	R/WR	MS	L	sandy	P3	
55-56.1	C	SA/SR	PS	L(S)	silty	C1	LFAc1
56.1-56.2	Gr	R/WR	MS	L	sandy	Gr3	LFAc3
56.2-57. 8	Gr	SR/R	PS	P	muddy	Gr4	LFAc4
57.8-62	Silt			P	silty	S2	Phyllite bedrock

Table A6.3. Sedimentary characteristics of core D01. Abbreviations follow the same meaning of those in Table A6.1.

Depth (m)	DGS	S	R	Lithology	Matrix	LFs	LFAs
0-0.7	P	PS	SA/SR	L, P	silty	P1	LFAc1
0.7-0.9	P	MS	SA/SR	L (P, Q)	no	P1	
0.9 -2	P	PS	SA/SR	L (P, Q)	silty	P1	
2-2.55	P	PS	SA/SR	L (P, Q)	no	P1	
2.55-6.2	P	PS	SA/SR	L (P, Q)	silty	P1	
6.2-7.4	Silt					S3	
7. 4-8.6	C	VPS	SA/SR	L (P, Q)	silty	C1	
8.6-9.2	P	VPS	SA/SR	L (P, Q)	silty	P1	
9.2-10.4	P	PS	SA/SR	L (P, Q)	silty	P1	
10.4-12.3	P	PS	SA/SR	L (P, Q)	sandy	P2	LFAc2
12.3-14	P	PS	SA/SR	L (P, Q)	silty	P1	LFAc1
14-14.8	P	PS	SA/SR	L (P, Q)	sandy	P2	LFAc2
14.8-15.3	P	PS	SA/SR	L (P, Q)	silty	P1	LFAc1
15.3-19.3	P	VPS	SA/SR	L (P, Q)	sandy	P2	LFAc2
19.3-19.6	Gr	PS	SA/SR	L (P, Q)	sandy	Gr2	
19.6-20.8	C	WS	SA/SR	L (P, Q)	no	C1	LFAc1
20.8-23	P	PS	SA/SR	L (P, Q)	silty	P1	
23-27.6	P	PS	SA/SR	L (P, Q)	sandy	P2	LFAc2
27.6-33.2	P	PS	SA/SR	L (P, Q)	silty	P1	LFAc1
33.2-34	C	MS	SA/SR	L (P, Q)	no	C1	LFAc2
34-38.2	P	PS	SA/SR	L (P, Q)	sandy	P2	
38.2-39.8	P	PS	SA/SR	L (P, Q)	silty	P1	LFAc1
39.8-41.6 :	P	PS	SA/SR	L (P, Q)	sandy	P2	LFAc2
41.6-43	P	PS	SA/SR	L (P, Q)	silty	P1	LFAc1
43-50.7	P	MS	SA/SR	L (P, Q)	sandy	P2	LFAc2
50.7-51.6	Silt						Phyllite bedrock

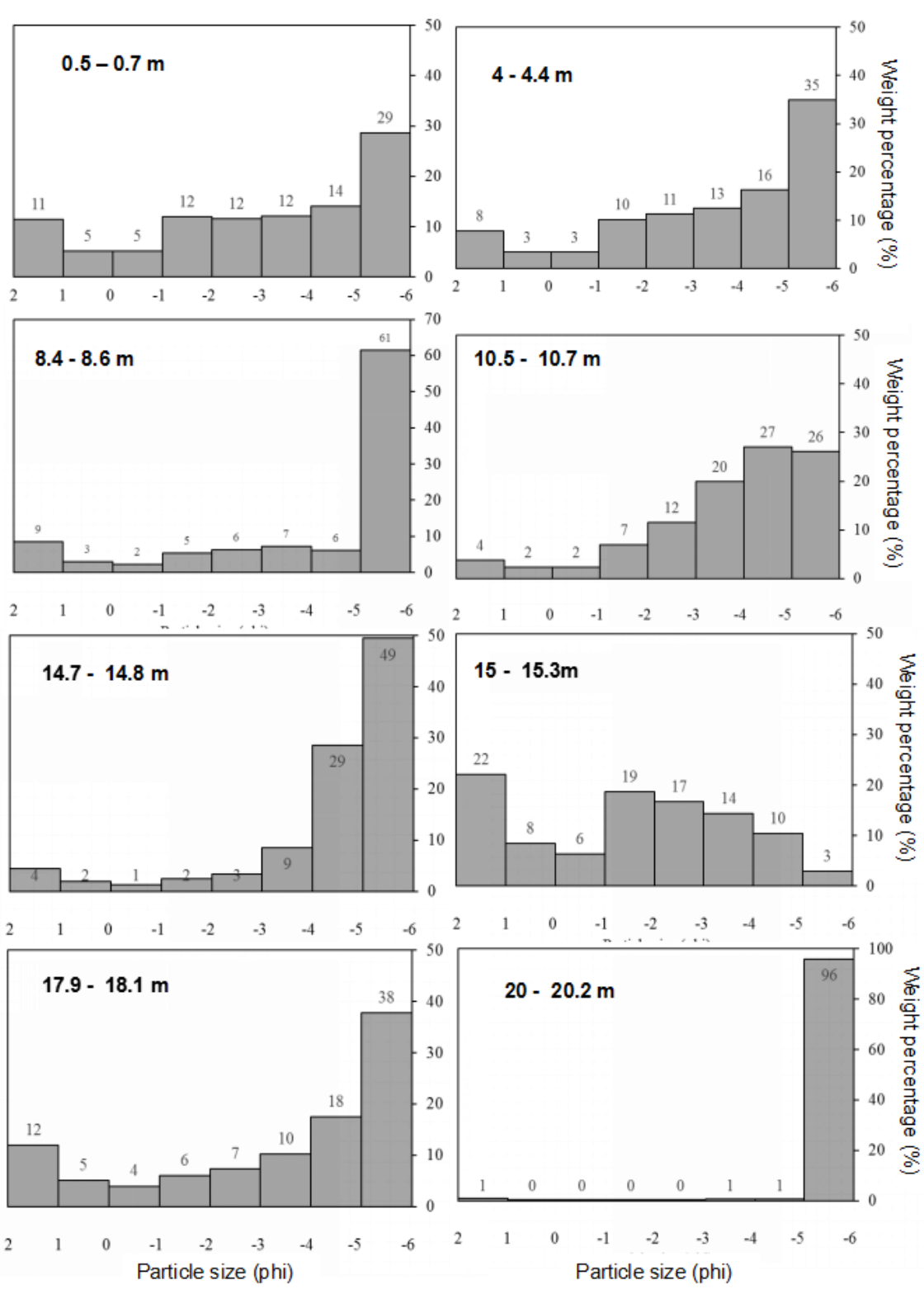

Fig. A6.1. Sieving results of grain size distribution for sediments in different depths of core D03

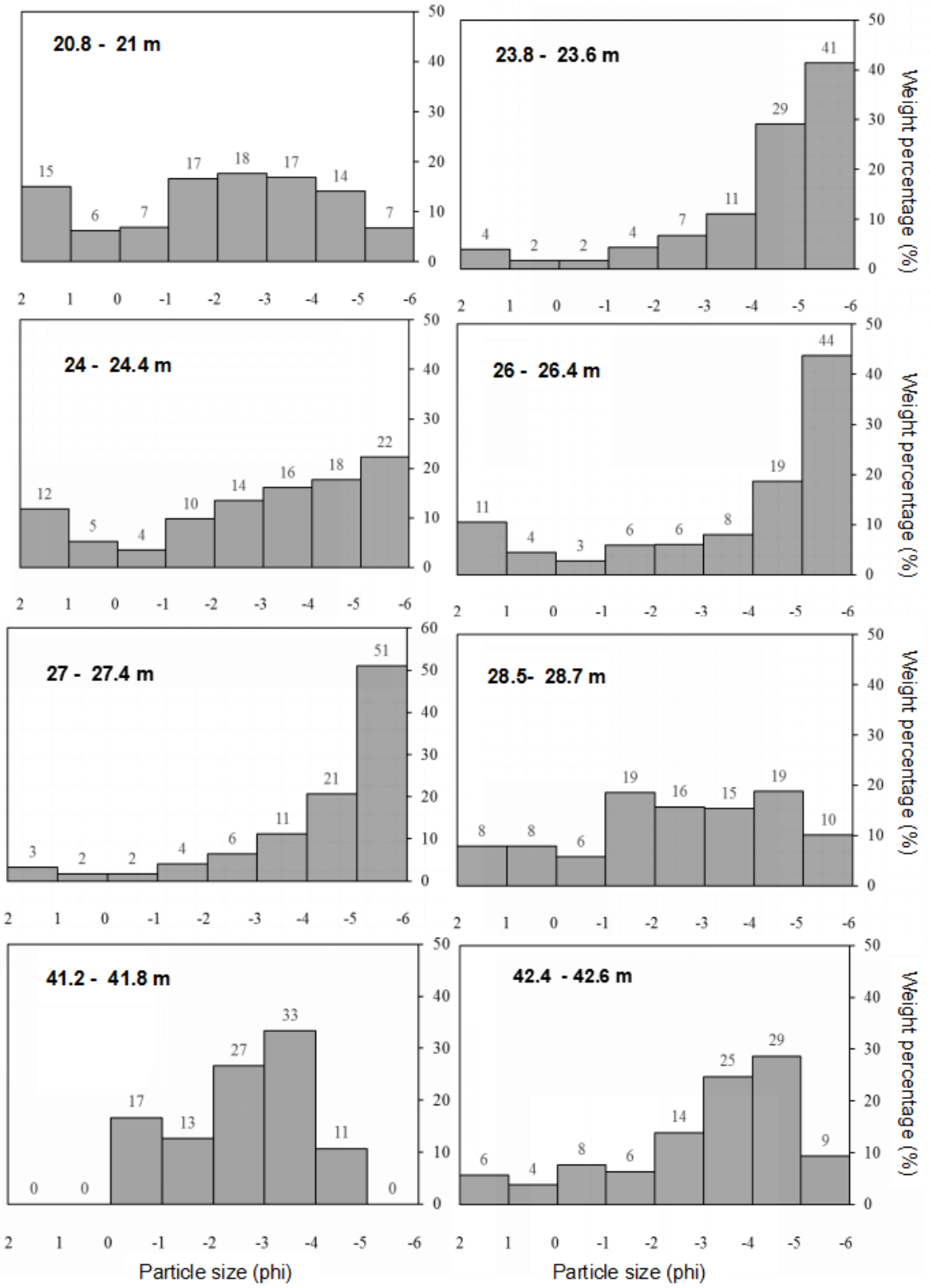

Fig. A6.2. Sieving results of grain size distribution for sediments in different depths of core D03